On the Fire Performance of Exterior Wall Materials and Assemblies

by

Vusal Ibrahimli

A thesis
presented to the University of Waterloo
in fulfillment of the
thesis requirement for the degree of
Master of Applied Science
in
Mechanical Engineering

Waterloo, Ontario, Canada, 2022

Author's Declaration

I hereby declare that I am the sole author of this thesis. This is a true copy of the thesis, including any required final revisions, as accepted by my examiners.

I understand that my thesis may be made electronically available to the public.

Abstract

Recent attempts at combating climate change have urged the developers, public authorities, and other building stakeholders to employ enhanced energy conservation initiatives as Canada's building sector accounts for 13% of national greenhouse gas emissions. These initiatives are often realized by using energy–efficient envelopes on the building exterior. As a physical barrier separating the controlled interior spaces of a structure from the exterior surroundings, the building envelopes are designed to provide effective vapour control while simultaneously being constructed with high thermal resistant materials in the façade. Consistent with this, modern energy–efficient envelopes are composed of four distinct layers (from outermost to innermost): decorative surface siding, exterior continuous insulation, weather resistant barrier, and exterior sheathing. Each layer addresses a specific design objective, and when assembled into the envelope, contributes to the overall performance of the exterior wall in meeting energy efficiency and hygrothermal requirements. Nowadays, multi–layered exterior envelopes are taking centre stage in construction, gradually replacing conventional monolithic concrete and masonry façades. Predicting fire performance of such assemblies, however, is challenging and should be carefully addressed to ensure occupant and firefighter safety as well as minimize property damage in the event of fire. The importance of this has been tragically demonstrated through recent massive fires around the globe in Turkey (Polat Tower, 2012), Australia (Lacrosse Building, 2014), England (Grenfell Tower, 2017) and even twice for the same residential building in the U.A.E. (Torch Tower, 2015 and 2017). It has become evident that while much emphasis is placed on improving energy and hygrothermal performance of exterior assemblies, next generation exterior wall designs must also exhibit superior fire resistance. For this, understanding the fire performance of exterior wall materials, alone and in combination with underlying layers, is critical since a broad selection of material combinations are possible when designing an envelope.

Assessment of the fire response of exterior wall assemblies usually involves expensive large–scale testing, that can only be conducted in a limited number of facilities, and which are often outfitted with the minimum instrumentation required by a given test standard. This has led to a dearth of detailed data, with consequent knowledge gaps, regarding the high temperature properties and fire behavior of many building materials. Further, it still poses a significant challenge to properly assess the effect of building envelope design features on the fire performance of exterior wall assemblies. Careful and detailed assessment of fire behaviour of such assemblies is therefore needed to advance performance–based engineering of new and innovative exterior wall designs.

The goal of the present research is to address these challenges through developing a consistent set of test methods where exterior wall materials are subjected, at small– through larger–scale, to temperature and heat flux conditions similar to those encountered in realistic fire exposures. More specifically, experiments are aimed toward characterizing and advancing current understanding of the impact of different exterior continuous insulation products on the fire performance and bulk–path heat transfer in wall assemblies. To achieve these objectives, representative samples of the main layers forming an energy–efficient, exterior building envelope in Canada were first identified. These layers are vinyl siding panels, stone wool insulation, polyisocyanurate insulation, extruded polystyrene insulation, non–woven house wrap, and oriented strand board. Their fire performance was then characterized via two complementary avenues of investigation. In Phase 1, small–scale fire testing of the selected materials was conducted by instrumenting representative specimens of each material with thermocouple probes and subjecting them to varying levels of radiant heat flux exposure to determine key parameters such as time variations in mass loss and heat release rate per unit area, time–histories of surface and bulk sample temperatures, as well as thermal degradation and damage (shrinking, charring, melting, self–heating). In Phase 2, 2,438 mm $\times$ 2,438 mm large exterior wall envelopes constructed using the same materials were instrumented with multiple sets of thermocouple probe rakes positioned across each layer of the test structure and subjected to temperature and heat flux from a realistic, but contained, fire. This allowed capture of the thermal response of the wall assemblies to the prescribed exposure and assessment of the observed thermal degradation phenomena relative to the temperatures measured in the degrading walls. Results show that temperatures measured in the small–scale fire tests may provide a good indication of temperature evolution and heat transfer within full–scale wall assemblies during large–scale fire tests. Further, comparable levels of fire damage and thermal degradation (shrinking, charring, melting, self–heating) of the studied building products were obtained across the two scales of fire testing. Thus, the utility of studying thermal degradation of building materials and construction assemblies in the context of energy–efficient building envelopes at both the small– and large–scales was demonstrated. In combination, the novel set of experimental data obtained via Phase 1 and 2 of this research may guide formulation of advanced numerical simulation and design tools for predicting fire performance of individual building materials and their interactions in exterior wall assemblies when subject to realistic fire exposures.

Acknowledgements

I would first like to express my sincere gratitude to my supervisor, Dr. Elizabeth Weckman, for her expertise, wisdom, guidance and patience over the course of my graduate studies. Thank you for teaching me the ropes of fire testing technology, and your continuous support in the sea of seemingly endless troubleshooting attempts of all kinds to keep the research progressing forward. Words cannot express how grateful I am for all the opportunities presented that have helped me grow as a student, early career researcher, team member and overall person. I look forward to continuing to work with you on the next chapter of my graduate journey.

I would also like to thank my colleagues: Bronwyn Forrest, Alexander DiPaola, Peter O'Hagan, Keon Senez, Liam Marshall, Ayaan Lakhani and Mohammad Ahmed for helping me throughout various stages of this study as well as other exciting projects along the way, with special acknowledgement to Andrew Barber for his technical expertise.

In addition, I would like to acknowledge the contributions of Alejandra Nieto and Richard Roos of ROCKWOOL® North America.

Thank you all for the priceless input that made this thesis possible.

Dedication

This is dedicated to my family and Veysal, thank you for always supporting me on all fronts and reminding me to maintain a positive outlook on life.

Table of Contents

List of Figures

List of Tables

Nomenclature

$(\rho C_p(T))_{ins}$	Volumetric heat capacity of metal felt insulation (MJ/(m^3°C))
$(\rho C_p(T))_{pl}$	Volumetric heat capacity of Inconel sensor plate (MJ/(m^3°C))
α	Volumetric expansion factor (= 1.105)
ΔP	The pressure drop in the exhaust stack (Pa)
$\dot{Q}''(t)$	Heat release rate per unit exposed surface area of a specimen at some test time, t, following the onset of exposure (kW/m^2)
ϕ	Oxygen depletion factor
C	The orifice plate coefficient, calibrated for a standard volume flow rate of 24 l/s
E	Heat release per unit mass of oxygen consumed ($\approx$ 13.1 kJ/g)
X_{CO_2}	Volume fraction of carbon dioxide in the sampled gas
$X^a_{CO_2}$	Volume fraction of carbon dioxide in the ambient air
X_{CO}	Volume fraction of carbon monoxide in the sampled gas
$X^a_{H_2O}$	Volume fraction of water vapour in the ambient air ($\approx$ 1–2%)
X_{O_2}	Volume fraction of oxygen in the sampled gas
$X^a_{O_2}$	Volume fraction of oxygen in the ambient air
A_s	Area of the exposed surface of the specimen (m^2)
L_{ins}	Metal felt insulation thickness (0.012 m)
L_{pl}	Inconel sensor plate thickness (0.0032 m)
M_{air}	Molecular weight of dry air ($\approx$ 29 g/mol)
M_{O_2}	Molecular weight of oxygen gas ($\approx$ 32 g/mol)
q_{net}	Net heat flux calculated with ASTM E3057–16 Energy Storage Method (kW/m^2)

T_e	The temperature of the hot gases in the exhaust stack (K)
$k_{ins}(T)$	Thermal conductivity of metal felt insulation (W/(m°C))
T_{back}	Thermocouple measurement on the back Inconel plate sensor (°C)
T_{front}	Thermocouple measurement on the front (fire–side) Inconel plate sensor (°C)
T_{ins}	Estimate of the metal felt insulation temperature (°C)

Chapter 1

Introduction

Climate change is one of the defining challenges of the 21st century and calls for collective action around the globe to mitigate further escalation of its devastating impacts. By curbing the quantity of greenhouse gases (GHG) emitted, reduction in their environmental footprint could be achieved. At present, it is estimated that construction and operation of buildings contribute as much as 38% of total global energy–related GHG emissions [1]. In Canada, homes and buildings account for 13% of national GHG emissions; when emissions associated with the combustion of fossil fuels for space and water heating, electricity use for cooling, lighting and appliances are included, energy–related building emissions share adds up to 18% of the country's total [2]. In order to achieve its 2030 emission reduction goals, Canada's building sector will require existing retrofit projects as well as new residential homes constructed between now and then to have improved energy use and emissions performance. Consistent with this, much emphasis has been placed on enhancing the energy performance of building envelopes due to the fact that over half of a building's energy demand is attributed to heat losses through its enclosure [3]. Research has shown that affixing a layer of weather resistant barrier in conjunction with continuous thermal insulation over a building's exterior sheathing is one of the most effective measures to decrease energy use for heating and cooling [4]. With such measures, it is predicted that multi–layered and highly–insulated building envelopes could potentially save 11.6 PJ of energy and 1.2 Mt of GHG emissions per year assuming a Canadian market share of 25% for new residential home construction and existing retrofits by year 2025 [5]. More recently, experimental and modelling results from an extensive study undertaken at NRC–FEWF[1] demonstrated that such exterior wall assemblies do not only meet energy efficiency and

[1]The National Research Council of Canada – Field Exposure of Walls Test Facility

hygrothermal requirements, but also ensure a building's expected longevity in the face of changing Canadian climate [6].

Nowadays, multi–layered and highly–insulated building envelopes are taking centre stage in construction, although their design is much more complex than the conventional monolithic stone, masonry, or concrete façades of earlier times [7]. Predicting fire performance of these complex assemblies is a particular challenge that must be carefully addressed to ensure occupant and firefighter safety as well as minimize property damage in the event of fire. The primary threat to a building and its occupants by a façade fire is the potential for the fire to spread vertically from floor to floor or horizontally across the façade impacting adjacent spaces. In residential buildings, for example, a fire could originate inside the building, spread to the façade via openings in the compartment, extend up the exterior side of the building, and consequently break into the floors above. Although strategies for fire safety design in buildings typically aim for the fire to be confined to its floor of origin, the frequency of fires involving flame spread along the building exterior is still on the rise. In fact, worldwide, the total number of fires spread via an exterior wall has increased by seven times in the past three decades [7]. One major factor contributing to this disturbing statistic is increased use of combustible components, such as polyurethane and polyisocyanurate insulation, within façade systems. These are often added to achieve improved building energy performance and reduction in water and air infiltration [8]. For instance, in Canada, the exterior walls of energy–efficient residential homes built in humid climates (Vancouver, St. John's) are often layered with extruded polystyrene foam insulation [9]. Since a growing number of building envelopes are constructed with varying amounts of such combustible components, there is an increased chance for them to be directly involved in a fire. When they are, they add to the fuel load and make it easier for flames to spread further up the building exterior, reaching storeys beyond the fire's floor of origin. This has been tragically demonstrated through recent massive fires around the globe: in Turkey (Polat Tower, 2012), Australia (Lacrosse Building, 2014), England (Grenfell Tower, 2017) and even twice for the same residential building in the U.A.E. (Torch Tower, 2015 and 2017) [10, 11]. Furthermore, the increased frequency of wildfires exacerbated by severe heatwaves due to climate change, makes modern high–performance building envelopes more susceptible to exposure from fires originating externally to the building. In these cases, a fire may ignite an exterior wall and then spread from the façade into the interior spaces. This too has been tragically demonstrated through devastating forest fires in the U.S. (Northern California, 2017) and closer to home, in Alberta (Fort McMurray, 2016) and more recently in British Columbia (White Rock Lake, 2021) [12–14].

The kinds of tragedies make it evident that in addition to the significant emphasis placed on improving energy and hygrothermal performance of exterior wall assemblies, next generation building envelopes must also exhibit superior fire resistance. For this, understanding the fire performance of exterior wall materials, alone and in combination with underlying layers, is critical since a broad selection of material combinations are possible when designing a modern building envelope. To begin to address this need, the present research outlines results from a series of experiments conducted to characterize the fire performance of common Canadian exterior building materials and their representative composite assemblies via complementary small– and large–scale experiments.

Specifically, the objectives of the research are:

1. to undertake a series of small–scale experiments to characterize the fire performance of building materials found in each layer of a typical Canadian exterior wall assembly,

2. to construct representative assemblies of the building materials and conduct comparative small–scale tests to examine the fire performance of the assembled composite samples, and

3. to complement the small-scale experiments with a limited set of larger–scale tests conducted to investigate the fire performance of full exterior walls under a more realistic fire exposure.

This thesis presents the background, key findings, conclusions and recommendations from the study. Background information and the literature review are included in Chapter 2 which begins by detailing the multi–objective design in construction of residential building envelopes and current measures taken to address fire safety in the design of modern energy–efficient exterior wall assemblies. This is then followed by a description of the layers used in the construction of exterior walls in present–day buildings, including the range of materials which are most commonly found in Canada. The construction products of interest are then presented along with a descriptive overview of these materials together with a more specific review of existing literature related to their thermal and fire properties. Understanding of thermal degradation phenomena of constituent wall components is then highlighted and current approaches adopted to systematically investigate this phenomena are presented. The state–of–the–art in fire testing following these methodologies are presented next and current gaps in research are identified.

Chapter 3 outlines the experimental methods and instrumentation used in the small–scale tests, along with materials selected and description of test assembly construction. The results obtained from the small–scale studies undertaken in this work are then presented and discussed, first for the individual construction products followed by experiments conducted on the assembled composite samples. Following presentation of results, the data from the small–scale tests are then related to what might be expected in a full–scale test of a similar assembly. Experimental design and results for the comparative large–scale fire performance tests are presented and discussed in Chapter 4, first for the assembly containing stone wool insulation followed by those for polyisocyanurate and extruded polystyrene foam insulation. Finally, conclusions and recommendations arising from the work are outlined in Chapter 5.

Chapter 2

Literature Review

2.1 Towards Optimal Design of Residential Building Envelopes

The design of modern residential building envelopes can be regarded as a multi–objective optimization challenge, in which several criteria are considered for finding the most favourable solutions. Some relevant criteria include:

- sustainability, such as meeting energy efficiency requirements [15, 16] and ensuring a building's expected longevity [17];
- occupant comfort, such as thermal [18, 19] and acoustical comfort [20, 21];
- space use [22] and structural design [23]; as well as
- fire safety [24, 25].

In order to perform a multi–objective design, evaluation of the cost of alternative solutions must be undertaken, which requires the criteria of interest to be quantifiable. Criteria such as energy performance, acoustics, comfort and utility of space, for instance, can be quantified as functions of certain parameters. For example, a widely used metric for rating energy efficiency in building envelopes is the Overall Thermal Transfer Value (OTTV), defined as the ratio of heat gain into the building through the building envelope to the total wall area and measured in (W/m^2) [26]. Similarly, acoustic levels could be expressed in sound pressure level (SPL) measured in decibels (dB) [27], while utility of space can be quantified as a function of the wall thickness (m) and total area (m^2).

Among the above listed criteria, however, fire safety is not included in terms of comparable parameters in the design of residential building envelopes. Instead, a regulatory framework outlines a set of prescriptive requirements for fire safety that must be met in buildings. In Canada, minimum acceptable measures for meeting fire safety requirements in the design and construction of residential building envelopes are provided in the National Building Code of Canada [28]. The National Building Code is an objective–based code with clearly stated objectives and functional statements for its requirements. Compliance with the code is achieved by directly applying the acceptable solutions (i.e. the prescriptive requirements outlined in Division B of the code) or by developing alternative solutions. According to the National Building Code, with respect to meeting fire safety requirements, the design and construction of exterior wall assemblies must satisfy the acceptance criteria when tested in accordance with CAN/ULC–S134–13, "Standard Method of Fire Test of Exterior Wall Assemblies", for limiting fire spread on or within the exterior wall assembly. This standard method was developed to evaluate the performance of an exterior wall assembly under test conditions representing a fire exposure resulting from a post–flashover fire inside a compartment venting through an opening, such as a window, in the wall [29]. This test method assesses comparative fire performance characteristics of exterior wall assemblies measuring 9,500 mm tall $\times$ 6,600 mm wide by evaluating fire spread over the exterior wall surface, heat flow from the fire plume to the exterior wall surface, and fire spread within the test wall. Visual fire propagation and heat flux measured at 3.5 m above the window opening are the primary variables used for assessing the fire performance of an exterior wall assembly. Specifically, meeting the fire safety requirements is based on two acceptance criteria: 1) no more than 5 m of vertical flame spread on the exterior of the test wall and 2) no more than 35 kW/m^2 heat flux on the exposed wall assembly face at the specified height above the vent opening.

While both the visual flame propagation along the exterior of the test assembly and heat flux measured on the exposed wall face are pertinent design parameters, they do not provide the adequate and complete data required to support detailed fire safety analyses of the performance of the walls (e.g. thermal penetration through the bulk of the wall). In addition, data from the tests may not reflect the actual performance of an exterior wall assembly under any but the test fire exposure conditions. To truly advance the design of exterior walls for fire safety, it is necessary to obtain new insight and develop better understanding of the physics underlying various thermal degradation mechanisms of exterior wall assemblies and their constituent components. This, in turn, will lead to development of a comprehensive data set capable of supporting detailed fire performance analyses. With this in mind, a brief description of the topology of exterior wall assemblies and common building products used in their construction is presented in the next section,

followed by a review of thermal degradation phenomena unique to these materials.

2.2 Overview of Wall Topology for Residential Building Envelopes

This section begins with a description of the layers used in constructing exterior walls in modern buildings, including the range of materials which are most commonly found in Canada. Exterior wall assemblies of Canadian residential buildings are typically composed of four distinct layers (from outermost to innermost): decorative surface siding, exterior continuous insulation, weather resistant barrier, and exterior sheathing [5, 6]. Together, these layers form the exterior envelope of the house, protecting the interior spaces from the variable ambient outdoor environment. Each layer addresses a specific design objective, and when assembled into the building envelope, contributes to the overall performance of the wall in meeting energy efficiency, hygrothermal, and acoustic requirements.

Decorative surface siding, often referred to as exterior cladding, is the outermost layer affixed to the building exterior. It is generally regarded as the first line of defense against bulk rainwater penetration and has an added value of aesthetics allowing for versatile design flexibility [4, 30]. While masonry, stucco and fiber cement siding may be found as exterior wall coverings and finishes, vinyl siding is one of the most popular decorative surface finishes encountered in modern construction due to its low cost, versatility and easy maintenance [31, 32].

The underlying layer of exterior continuous insulation plays a crucial role in achieving an energy efficient building envelope. When incorporated into a frame construction, this layer provides significant reduction in thermal bridging[1] at the studs leading to a higher overall RSI–value[2] for the wall assembly [35]. It also warms the sheathing surface beneath, reducing the potential for water condensation within the wall system [36]. In Canada, highly–insulated exterior wall assemblies are usually lined with two types of continuous thermal insulation based on the local climate: mineral fibre–based thermal insulation (such as stone wool) is commonly used for walls in dry climates (Edmonton, Yellowknife), while foam insulation (such as extruded polystyrene) is widely used in walls located in humid climates (Vancouver, St. John's) [6].

[1] A thermal bridge is a zone of the building envelope where the local thermal resistance is significantly reduced, allowing heat to flow through framing members [33].

[2] RSI–value is a measure of thermal resistance (opposition to heat flow) expressed in $m^2 \cdot K/W$ [34].

Moving further in to the building envelope, a weather resistant barrier is the next layer. Next to the decorative siding, the weather resistant barrier is considered to be the second line of defense against moisture infiltration into the building envelope [37]. Modern weather resistant barriers are designed to allow the water vapour to move freely within the exterior assembly, but to also trap liquid water, preventing it from reaching the underlying sheathing. Plastic house wrap is a popular choice for a weather resistant barrier in a typical residential house [38].

Finally, the innermost component of an exterior wall assembly is the exterior sheathing that is affixed to the exterior side of the framing members. It provides a solid nailing base for the above–mentioned layers, lending them structural support and increasing the overall integrity of a wall system. Plywood and oriented strand board sheets are building boards that are made of timber and glue, and have good structural strength making them two popular exterior sheathing products in contemporary construction practice [39].

In the present work, the following products were determined to be of interest for this thesis work based on their extensive use in construction of building envelopes in Canada:

- commercially available vinyl siding panels made of polyvinyl chloride compound were selected for the decorative surface siding;
- three exterior continuous insulation products were selected:
    1. rigid stone wool insulation with an RSI–value of 0.88,
    2. polyisocyanurate rigid foam insulation with the foam core bonded on each side to aluminum foil facers with an RSI–value of 1.1, and
    3. extruded polystyrene rigid foam insulation with an RSI–value of 0.88.
- a commercially available synthetic non–woven house wrap was selected for the weather resistant barrier; and
- commercially available oriented strand board sheet was selected for the exterior sheathing.

A descriptive overview of these materials is presented below, together with a more specific review of existing literature related to their thermal and fire properties.

2.3 Review of Thermal Degradation Phenomena of Exterior Wall Materials

Thermal degradation refers to the process by which a material degenerates under the influence of increased temperature. In the context of exterior wall assemblies, thermal degradation of the assembly subject to heating by exposure to fire is a complex process involving both chemical and structural changes to the constituent layers, as well as their subsequent impact on the interior temperature profiles within the assembly under continued exposure. The extent of these changes depends on the temperature or heat flux and the length of time of the thermal exposure. In this section, thermal degradation phenomena unique to the building products selected for this study are presented, first for the polyvinyl chloride siding, followed by the three insulation products (stone wool, polyisocyanurate, extruded polystyrene), the non–woven house wrap (i.e. weather resistant barrier), and finally, for the oriented strand board sheathing. Ignition phenomena are not included here to highlight degradation that might occur under heating in the absence of ignition.

2.3.1 Polyvinyl Chloride Siding

Vinyl siding is a decorative surface finish typically manufactured by co–extruding[3], in this case a highly stabilized polyvinyl chloride capstock (surface layer) over a differently formulated polyvinyl chloride substrate formulation. While stabilizers, pigments, impact modifiers and lubricants may be added in various proportions, polyvinyl chloride resin, usually constitutes approximately 80% of the raw materials used in production of vinyl siding [42, 43]. The thermal degradation of polyvinyl chloride has been the subject of numerous investigations and is generally considered to follow a multi–stage process which is outlined below [44–52]:

- When exposed to elevated temperatures, polyvinyl chloride siding tends to soften, buckle and deform; the distortion in siding geometry under thermal heating is associated with the bulk sample temperatures approaching the 61°C – 74°C glass transition temperature range;

[3]Co–extrusion is the process of forming an extruded material composed of more than one thermoplastic melt stream which requires separate extruders for each distinct material. The final product of this process is a thin plastic material containing two or more distinct plastic layers [40, 41].

- Under continued exposure, gaseous pyrolysis products are driven off the decomposing polyvinyl material and when temperatures reach about 200°C, loss of hydrogen chloride molecules begins. This results in the formation of polyene in competition with the formation of a cross–linked structure involving different chain radicals;
- At about 250°C, the onset of char formation begins;
- Between 350°C and 520°C, thermal decomposition of polyvinyl chloride continues wherein cracking of some carbon–carbon bonds of the previously formed polyene structures occurs;
- At temperatures above 520°C, nearly complete consumption of polyvinyl chloride mass occurs leaving behind a charred reside.

2.3.2 Rigid Stone Wool Insulation

Stone wool is an insulating material manufactured by melting volcanic basalt and diabase rocks, and spinning the molten matter to produce fibres. In this process, a thermoset binder (usually cured urea extended phenol–formaldehyde resin) and oils are used to keep the fibres together which are then assembled into batts. A typical by mass composition of stone wool is as follows: 94% – 99% of mineral fibre content and 1% – 6% binder [53]. The thermal decomposition of stone wool is commonly understood and characterized by different phenomena as the interior temperature within the material bulk is increased [54–61]:

- The onset of thermal decomposition (pyrolysis) of organic content (binder and associated additives) within the insulation commences at temperatures of around 250°C;
- When the interior temperatures reach above 500°C, gaseous pyrolysis products liberated from thermally decomposing binder are oxidized. This process is commonly known as binder burn–off;
- At 600°C, the binder is subjected to a mass loss of nearly 80%;
- Oxidation of organic matter in stone wool is associated with compromised stone wool rigidity, and at temperatures $\geq$ 650°C, crystallization of siliceous species occurs;
- Once the interior temperatures rise above 1,100°C, the fibres melt.

2.3.3 Polyisocyanurate Insulation

Polyisocyanurate insulation boards are made of a thermoset, closed–cell, rigid isocyanurate-based foam that is manufactured through a continuous lamination process. The raw materials that make up the foam formulation are mixed, causing a rapid chemical reaction that transforms them into a rigid, thermally stable polymeric structure. Details of this reaction can be found in [62]. While still in the lamination processor, face adhesion of the foam core occurs, wherein facing materials (facers) such as aluminium foil are laminated onto each side of the foam sheet. Adhesion of foil facers serves a number of functions during the service life of the finished insulation product, including reduced water absorption and increased thermal resistance. Thermal degradation phenomena unique to this material have been investigated with key results presented below [63–65]:

- The onset of pyrolysis of the polyisocyanurate foam core starts at around 200°C;
- Under continued exposure to elevated temperatures, the rate of pyrolysis intensifies and a peak rate is observed when the interior temperatures of the polyisocyanurate foam core reach 300°C – 370°C;
- At 350°C, dissociation of isocyanurate linkage occurs;
- Once interior temperatures rise above 500°C, oxidation of the pyrolysis gases liberated from thermally decomposing polisocyanurate foam takes place;
- Nearly complete consumption of polyisocyanurate mass occurs at around 600°C, after which a black and porous charred residue is left.

2.3.4 Extruded Polystyrene Insulation

Extruded polystyrene insulation boards are manufactured via an extrusion process wherein raw materials (general purpose polystyrene, polypropylene, recycled foam plastic resin and other additives) are combined and propelled continuously along a screw through regions of high temperature and pressure. The mixed, melted, and compacted plastic matter is then forced through a die into the desired shape. The resulting foam plastic is then cut and trimmed to the final product dimensions. Similar to the polyisocyanurate foam, extruded polystyrene is also rigid and has a closed–cell foam structure. Extruded polystyrene is thermoplastic and thus belongs to a class of polymers that are softened and melted by the application of heat. The thermal degradation of extruded polystyrene foam has been observed to follow a multi–stage process which is outlined below [66–68]:

- At the onset of thermal exposure, the bulk of the insulation starts to soften due to its thermoplastic nature;
- Under continued exposure to elevated temperatures, the polymer beads collapse at about 110°C – 120°C;
- When the interior temperatures reach 160°C threshold, the collapsed beads start to melt forming a viscous residue;
- As the temperature increases past 170°C, the viscosity of the polystyrene melt decreases until the vaporization point is reached at temperatures greater than about 275°C;
- Between 410°C and 460°C, the melted foam residue continues to decompose releasing volatile gaseous products (primarily styrene monomers); and
- By 480°C – 500°C, almost all of the sample is vaporized and no residue is left.

2.3.5 Non–Woven House Wrap

The synthetic house wrap selected to represent weather resistant barrier in this study is a non-woven, non-perforated sheet made by spinning fine continuous high–density polyethylene (HDPE) fibres that are fused together to form a strong uniform web. The fibrous structure of the house wrap is engineered to create small pores that resist bulk water penetration while allowing water vapour to pass freely through the sheet. Melting of HDPE is reported to occur around 127°C with the melting point of the house wrap having been previously reported as 135°C [69, 70].

2.3.6 Oriented Strand Board

Oriented strand board sheets are made of rectangular wood strands (typically 8 to 15 cm long) blended with waterproof adhesive (usually phenol–formaldehyde (PF) resin [71]) that are arranged into cross–directional layers. The average holocellulose[4] and lignin content of oriented strand board is approximately 45% and 29% by mass, respectively, while the remaining 26% of its composition is associated with the mass of the adhesive [73]. Similar to the other building materials described above, many aspects of the thermal decomposition of oriented strand board are commonly understood. Different phenomena have been observed to occur as the interior temperature of an oriented strand board slab is increased [74–79]:

- Dehydration of oriented strand board begins at around 100°C, while evaporation of chemically bound water occurs at slightly higher temperature, around 127°C;
- The thermal decomposition of hemicellulose starts at approximately 200°C – 220°C;
- When temperatures reach about 235°C, char formation commences;
- At around 300°C – 315°C, thermal decomposition of cellulose begins;
- In contrast to hemicellulose and cellulose, lignin decomposes at a slower rate and over a broader reported range of temperature between 160°C – 900°C;
- The PF resin starts to thermally decompose at around 200°C and once the temperatures rise to about 630°C the resin is fully volatilized.

The above presented discussion has outlined some of thermal degradation phenomena that have been observed for individual materials. However, when multiple materials are involved in an assembly, as in the case of exterior wall assemblies, the complexity of the coupled heat and mass transport (e.g. thermal penetration through the bulk of the assembly and migration of moisture) increases drastically [80]. One way to address this challenge is by conducting systematic tests of materials and composites on different scales, wherein specimen dimensions are progressively increased toward a final large (real) scale. This methodology is often referred to as a multi–scale (or scale–up) approach and has been repeatedly employed by the fire safety research community over the past decade [81–87].

[4]Holocellulose is a water–insoluble carbohydrate fraction of wood materials which includes cellulose and hemicellulose content of wood [72]

As the name suggests, the methodology involves conducting tests at multiple scales to investigate the inherently complex physical processes occurring at each scale and thus characterize the overall fire behaviour for a given material or composite by better understanding the phenomena that drive that behaviour across scales as well. Typical scales involved in such a multi–scale approach are presented below:

- *Micro–scale* involves analysis of material behaviour based on samples of the material with masses of a few milligrams. Testing at this scale can be performed by thermogravimetric analysis, differential scanning calorimetry, micro combustion calorimetry and other bench–scale methodologies. Test results typically provide information regarding chemical reactions occurring in the materials in different ranges of temperature in terms of mass consumed and energy released or absorbed as well as associated kinetic parameters. At this scale, the effects of heat and species transport into a bulk sample are minimized and the impact of increased temperature on the chemical formulation of the specimens can be studied accurately. Test samples at micro–scale are often assumed to have negligible mass and geometric dimension, as well as being subject to uniform and homogeneous temperatures.

- *Material–scale* analysis involves testing of specimens with masses around ten grams and measuring a few cm^2. At this scale, gradients of thermal penetration and species transport can be studied as the samples are usually irradiated on one surface which results in the displacement of decomposition and/or thermal fronts through the sample depth with time. The cone calorimeter is a prominent tool employed at this scale. The conditions of specimen degradation seen from cone calorimetry testing have been shown to be realistic, and can provide good sets of data with respect to the above mentioned thermal penetration phenomena. In the cone calorimeter, the surface of a specimen is subjected to varying levels of incident radiant heat flux and simultaneous measurements of mass loss, smoke production, and heat release rates are obtained in a timely and cost–effective fashion. A detailed description of the test apparatus, sample preparation and testing in the cone calorimeter as it was used in this research is presented in Chapter 3.

- *Composite–scale* analysis involves testing of layered composite assemblies referred to as "sandwiches" in this work. In the context of exterior wall assemblies, sandwiches present a layered design where representative materials of decorative surface siding, exterior continuous insulation, weather resistant barrier and exterior sheathing sheets are stacked in the order that they would be assembled in real walls (yet at a significantly reduced scale). The stacked assemblies are then subjected to varying levels of radiant exposure; the methodology is similar to that followed at the material–scale described above. Cone calorimeter testing can be performed at this scale as well to obtain additional insight into thermal penetration through the different layers of a sandwich assembly. In this way, the interactions of the constituent layers and their impact on the observed bulk–path heat transfer phenomena can be investigated. The layers used in construction of sandwich assemblies are typically the same products tested individually at the material–scale.

- *Large–* or *system–scale* refers to tests conducted at a size deemed to mimic the end use of products as they would appear in a building. In the context of residential building envelopes, large–scale analysis entails fire testing of full exterior wall sections. Conducting tests at such a scale is usually expensive and requires employing extensive instrumentation outfitted to measure various parameters of interest such as temperatures within the test wall assembly and heat fluxes experienced at the exposed wall face. The choice of fire exposure (specifically, temperature and heat flux conditions from a fire) and the extent of instrumentation involved is dependent on the specific objective of a test, but can often be adapted from instrumentation specified in either standard or custom test methodologies. In the present context, large–scale testing is aimed towards capturing the thermal response of exterior wall assemblies to temperature and heat flux conditions from a realistic fire exposure and thereby assessing the observed thermal degradation phenomena relative to the temperatures measured in the degrading walls.

Extending from this background, it is of interest to further explore the state–of–the–art in fire testing at each of these scales, as well as across the scales, as related to thermal penetration and fire performance of exterior wall assemblies. This forms the bases for the following section which outlines existing results first from the literature related to material–scale testing of the materials above, followed by what has been done in both composite– and large–scale testing of exterior wall assemblies similar to those outlined here.

2.4 State-of-the-Art on Multi-Scale Fire Testing of Exterior Wall Components and Assemblies

2.4.1 Fire Testing at Matter- and Material-Scale

Thermal degradation phenomena of constituent exterior wall components is often described in terms of critical temperatures at which certain degradation phenomena occur. Typically, at the matter–scale, these have been determined by means of thermogravimetric analysis which is a traditional method to investigate thermal degradation by measuring the relative change in the mass of a sample of material as a function of increasing temperature through tests conducted at different heating rates (e.g. 5 K/min, 10 K/min, 20 K/min) and atmospheres (e.g. in nitrogen and/or air) [88–94]. One of the advantages of the thermogravimetric analysis is that the test conditions driving the degradation processes are well controlled, due to the small mass of specimen being tested (near to one milligram) and the slow heating rates employed [95]. Conditions of decomposition during thermogravimetric analysis, however, are not representative of those that would occur in a real fire situation. For instance, the heating rates are considerably lower compared to the rate of heating imparted by the heat flux from a realistic fire and inhomogeneities, gradients of temperature and diffusion of species that may occur in a large sample of material are not necessarily captured during the test. This is supported by the observation that when a material is tested at slightly larger scales (e.g. when specimens weigh a few grams and are a few cm^2 large), the temperature of the material is often not uniform which can result in behaviour quite different than that seen in a thermogravimetric analysis. Due to this shortcoming, conducting tests at matter–scale is not pursued in this thesis work, however, it is important to note that an extensive body of research exists in the literature pertinent to thermogravimetric analysis of polyvinyl chloride [44–49, 51], stone wool [54, 55, 57, 58], polyisocyanurate [63–65], extruded polystyrene [66, 68], and oriented strand board [74–77] samples at the milligram scale.

On the other hand, at the material–scale, gradients of thermal penetration and species transport can be studied in the cone calorimeter wherein larger samples are subjected to varying levels of incident radiant heat flux close to those seen from a realistic fire exposure. There have been numerous studies on all of the individual materials of exterior wall assemblies, including polyvinyl chloride siding [96–102], stone wool [53, 103, 104], polyisocyanurate [62, 65, 105–109] and extruded polystyrene foam insulation [110–113], as well as oriented strand board sheathing [75, 77, 114–125]. The majority of authors conducted tests under external irradiation levels ranging from 20 kW/m^2 to 70 kW/m^2 heat flux. The focus of the vast majority of these studies was to obtain key parameters, such as

times to ignition, critical heat flux for ignition, heat release rate, mass loss rate, smoke production and toxicity, related to the reaction–to–fire behaviour of a given exterior wall material in response to various levels of external heat flux. In only a limited subset of these studies [53,65,115,125], were the samples instrumented with thermocouple probes to provide additional insight into thermal penetration through the bulk of the test materials. In general, proper evaluation of thermal degradation of exterior wall materials requires measurements of temperature evolution over time [80], which in turn can speak to the thermal penetration into and through the bulk of test materials. Therefore, it is crucial to undertake a series of small–scale experiments to characterize the thermal penetration and fire performance of exterior wall materials wherein samples are instrumented with thermocouple probes and temperature–time profiles are obtained concurrently with the decaying specimen mass and heat release rate under varying levels of radiant exposures. This thesis work aims to address this gap by instrumenting each exterior wall material with temperature probes and exposing them to eight levels of external heat flux, ranging from 15 kW/m^2 to 75 kW/m^2, in the cone calorimeter. Details of a series of small–scale experiments undertaken to characterize the thermal penetration and fire performance of vinyl siding, exterior continuous insulation, house wrap and oriented strand are presented in Chapter 3.

2.4.2 Fire Testing at Composite-Scale

Investigations into the thermal response of sandwich assemblies has conventionally been performed by conducting fire tests at large–scale on select components of a full structure under study [82]. Although these tests, when instrumented appropriately, could offer adequate information regarding thermal degradation of the layers of a test assembly as related to the heat transfer mechanisms through the assembly in response to a specified fire exposure, instrumenting and conducting such experiments is expensive and complex. More recently, evaluation of fire behaviour of scaled down sandwich assemblies has been carried out with a cone calorimeter, facilitating more timely and cost–effective investigation of some of the phenomena that might occur at larger scale. A set of such studies that relate to the present work are found in the literature [126–133] and are detailed below.

Chow [126] conducted fire hazard assessment on sandwich assemblies used in construction of temporary accommodation units in Hong Kong. The assemblies were made of polyurethane foam insulation slabs sandwiched between two sheets of galvanized steel, with one sheet on each side of the foam insulation core. The assemblies were tested in the cone calorimeter under four levels of incident radiant heat flux (20, 25, 50 and 65 kW/m^2) with one of the metal surfaces exposed to the prescribed level of external irradiation. Key parameters on thermal behaviour and smoke emission were collected at each heat flux level by measurements of heat release rate, mass loss rate, total smoke release, carbon monoxide and carbon dioxide yields. Although much useful information was obtained related to possibilities of flashover (e.g. time and propensity to flashover) as well as smoke emission, and related to what might be expected at a larger scale, no observations of thermal degradation mechanisms or measurements to determine thermal penetration through the layers of the sandwich were reported. Preliminary recommendations on what should be considered in specifying standardized fire tests for new regulations on the use of these sandwich panels were discussed as well.

Following the aftermath of the 2017 Grenfell Tower tragedy, increasing number of studies have been conducted on understanding fire behaviour of modern façade materials in combination with underlying layers. Much emphasis has been placed on studying the fire performance of lightweight composite cladding such as aluminium composite panels which were used in refurbishment of the Grenfell Tower and thus played a role in the ensuing fire [127–129]. These composite panels were constructed with an insulating slab core (such as polyethylene, polyisocyanurate, and phenolic foam insulation as well as stone and glass wool insulation) sandwiched between two thin layers of aluminium sheets. In these studies, conducted by McKenna et al. [127], Khan et al. [128], and Hossain et al. [129], sandwich assemblies were tested in the cone calorimeter under varying levels of external heat flux (50 kW/m^2 in [127, 129] and between 20 and 60 kW/m^2 in [128]) and measurements of time to ignition, heat release rate, total heat release, mass loss rate, and smoke production rate were collected for each test. Assessment of reaction–to–fire properties, structural failure of sandwich assemblies (such as bending, softening, cracking, and melting of insulation) and evolution of toxic products were discussed and the results were related to fire behaviour of these assemblies at a larger scale. Similar to the study conducted previously by Chow [126], no measurements to determine thermal penetration through the layers of the sandwich were reported in these studies.

External thermal insulation composite (sandwich) systems (ETICS) intended for use in energy–efficient building envelopes were also studied extensively in the cone calorimeter [130–133]. The principal design of an ETICS sandwich assembly includes insulation material (such as extruded and expanded polystyrene foam insulation) which is affixed to an exterior wall material, and forms the sandwich core, over which is applied a mesh and cement bound mortar and then a finishing layer. Due to the known flammability of some designs, certain installations also include embedded strips of stone wool or glass fibre which act as fire barriers [134]. Similar to the previous studies conducted on metal–insulation–metal sandwiches, scaled down ETICS sandwich assemblies were tested in the cone calorimeter under varying levels of external irradiation (30 kW/m^2 in [132, 133] and and 50 kW/m^2 in [130–132]) and measurements of time to ignition, heat release rate, total heat release, and mass loss rate were collected in each test. Results were then related to what might be expected in a larger scale installation to provide some insight into scale effects and fire hazard assessment in façade fires as well. Again, no information regarding thermal penetration through the layers of heated sandwich assemblies was presented in these above studies since the test specimens had not been instrumented in each layer with thermocouple probes. Consistent with this, no examination of the thermal degradation of the constituent layers and their impact on the bulk–path heat transfer phenomena in sandwich assemblies was discussed either.

In contrast, other work (for example, DiDomizio [80], Andrés Valiente [87] and Aire [135]), had indicated that in order to properly investigate the thermal degradation of composite assemblies, it is crucial to obtain information on the temperature–time history of the constituent components. Therefore, in experiments tailored for studying thermal degradation phenomena, temperatures of each material in a composite assembly should be measured during each test. Most importantly to the present research, there is no previously published research on fire testing, at the composite–scale, on exterior wall assemblies constructed with the layers identified in this work (vinyl siding, exterior continuous insulation, house wrap and oriented strand). The experiments that form one key element of this thesis research aim to address this gap. Constituent components of reduced scale exterior wall assemblies (representative of a typical residential building envelope in Canada) will be instrumented with temperature probes and exposed to low and higher levels of external heat flux in the cone calorimeter. Details of this series of composite–scale experiments are presented in Chapter 3.

2.4.3 Fire Testing at Large-Scale

There have been numerous studies on the assessment of fire hazard and fire performance of large exterior wall sections, with an increasing focus on assemblies representative of energy–efficient building envelopes, such as the exterior thermal insulation systems (ETICS) [136–147]. The majority of these studies were aimed towards identifying a harmonized test protocol (i.e. standard test method) conceived to be repeatable, versatile, and able to provide the relevant evaluation of fire hazards (such as flame spread, heat release rate, incident heat flux, and smoke obscuration) for use in fire risk assessment. In a small subset of these studies [138, 142, 146], the experiments were performed by following existing test methodology such as BS 8414–1 and BS 8414–2[5] where instrumentation and fire exposure are specified. The test configuration consists of a 8,000 mm tall × 2,600 mm wide main wall and a vertical 90° return wall (wing) measuring 8,000 mm tall and 1,500 mm wide, located at one side of (and adjacent to) the main test wall. Sets of external thermocouples are positioned in front of the main test wall face, on the centre line and at 500 mm and 1,000 mm each side of the centre line (five locations), at two levels: 4,500 mm and 7,000 mm above the base of the wall. Thermocouples are also positioned in front of the wing wall face at locations 150 mm, 600 mm, and 1,050 mm (three locations) away from the finished face of the main test wall and the same two heights above the base of the wall. Internal thermocouples are positioned at mid–depth within each layer of the test assembly (exterior continuous insulation, for instance) that exceeds 10 mm in thickness. These thermocouples are placed only at 7,000 mm above the base of the wall, on the centre line and at 500 mm and 1,000 mm to each side of the centre line of the main test wall, as well as on the wing wall at positions 150 mm, 600 mm and 1,050 mm away from the the main wall. The response of the wall assembly to fire exposure is captured by recording temperature–time profiles at all thermocouple locations. The primary focus of the studies was to investigate the impact of constituent wall components (e.g. nature and thickness of embedded fire barriers) on the overall fire behaviour of exterior wall assemblies, typically assessed on the basis of flame spread and temporal development of temperature along the exterior of the test wall assembly [138, 142, 146]. For instance, Xin et al. [138] and Bjegović et al. [142] demonstrated that incorporating fire barriers made of mineral wool insulation into ETICS assemblies can significantly mitigate fire spread along the exterior of the test walls, while Zhou et al. [144] and Čolić et al. [146] highlighted that with application of these mineral wool barriers, the relative position of the barriers also had a

[5]BS 8414, Fire Performance of Exterior Cladding Systems, is a test standard initially developed by the Building Research Establishment (BRE) in the United Kingdom, to evaluate whether a cladding system subjected to an interior fire breaking out of an opening (such as a window) in a multi–layer exterior wall will result in excessive vertical fire spread along the outside of the structure [148, 149].

large influence on mitigation of fire spread up the exterior. Interestingly, despite the test wall assemblies being instrumented with temperature probes, plate thermometers and heat flux gauges, no information regarding thermal penetration through the layers of the exterior assemblies was reported in these above studies. Consistent with this, no examination of the thermal degradation of the constituent layers and their impact on the bulk–path heat transfer phenomena in large sections of exterior wall assemblies was discussed either. It is important to note that despite any existing data on fire performance of large–scale exterior wall assemblies, predicting fire behaviour of entire wall assemblies remains challenging since new materials are continually being introduced into the marketplace and there is no single universal design for construction of residential building envelopes. These challenges are in addition to the dearth of data regarding thermal degradation of, and thermal penetration through, exterior wall components and their impact on the through–wall heat transfer phenomena. Most importantly to the present research, there is no previously published research on fire testing, at a large–scale, on exterior wall assemblies constructed with the layers identified in this work: vinyl siding, exterior continuous insulation, house wrap and oriented strand.

Moreover, nearly all of the published studies on the fire performance of exterior wall assemblies have been concerned with one type of fire exposure scenario. This is exposure to flames from a fully developed room (compartment) fire venting out and spreading through an opening, such as a window, in the wall. Subjecting exterior wall assemblies to such exposure has also been reflected in various test standards around the world including CAN/ULC–S134 in Canada [29], BS 8414–1 and BS 8414–2 in the United Kingdom [148, 149], NFPA 285 in the United States [150], JIS A 1310 in Japan [151], and in international standard ISO 13785–2 [152]. As mentioned previously, this is not the only mode of fire exposure that modern energy efficient building envelopes face, yet the impact of other fire scenarios (such as fires igniting externally to the building and radiating back towards the wall [7, 143]) unfortunately have been judged as less critical, leading to a widespread opinion that all other wall fire exposure scenarios are covered by the above listed fire test standards [137]. The experiments that form one key element of this thesis research aim to address this gap. Constituent components of large scale exterior wall assemblies (representative of a typical residential building envelope in Canada) will be instrumented with temperature probes and exposed to temperature and heat flux from a realistic, yet contained, fire ignited externally to the face of the wall. Details of this series of large–scale tests are presented in Chapter 4.

A final element of the research in this thesis is to investigate the suitability of applying a multi–scale (scale–up) approach for understanding the thermal penetration through, and thermal degradation of, exterior wall materials under exposure to fires in order to better understand their impact on the overall fire performance and bulk–path heat transfer phenomena in reduced– and large–scale wall assemblies. Although the use of reduced–scale experiments (such as those conducted in the cone calorimeter) in conjunction with full–scale tests for assessing the effect of variations in the composition and design of exterior wall assemblies was advocated more than two decades ago [153], to date, very few systematic studies of this nature have been conducted. At the same time, the suitability of the multi–scale approach has been shown to be effective in limited studies concerning the fire performance of interior wall partitions [69, 87, 154].

In the present work, detailed results from reduced– and large–scale experiments are presented in Chapters 3 and 4, respectively, while discussions regarding the suitability of the scale–up approach in predicting the overall fire performance of exterior wall assemblies constructed with the layers identified in this work are provided in Chapters 4 and 5. Through the combined results presented then, the present research aims to add to the existing knowledge on use of scaling approaches in fire research, focused here specifically on studies into the fire performance of exterior wall materials and assemblies encountered most commonly in construction of residential building envelopes in Canada.

Chapter 3

Small–Scale Fire Testing

In this Chapter, the experimental methods, instrumentation used in the small–scale tests, materials selected and test assembly construction are described. The results of the small–scale tests are then presented and discussed. Following presentation of results for the individual materials, data from the sandwich samples are outlined and related to what might be expected in a full-scale test of a similar assembly.

3.1 Test Apparatus

Bench–scale fire testing in this work was conducted by employing the cone calorimeter, as it is widely used and has been found suitable for obtaining comparative evaluations of the relative hazard posed by materials when subjected to fire. In the cone calorimeter, the performance of a material is determined on the basis of ignitability, heat release rate, total heat release, mass loss rate, effective heat of combustion and other derived parameters [155, 156]. A schematic diagram of the equipment is depicted in Figure 3.1.

A test specimen, measuring nominally 100 mm $\times$ 100 mm in size, is placed in the designated sample holder and mounted onto the load cell platform in the horizontal configuration, positioned such that the exposed surface is 25 mm below the base of the conical heater of the cone calorimeter apparatus. The heater is rated at 5,000 W at 240 V, and is capable of producing uniform levels of incident heat flux up to 100 kW/m^2 onto the exposed surface of the test specimen.

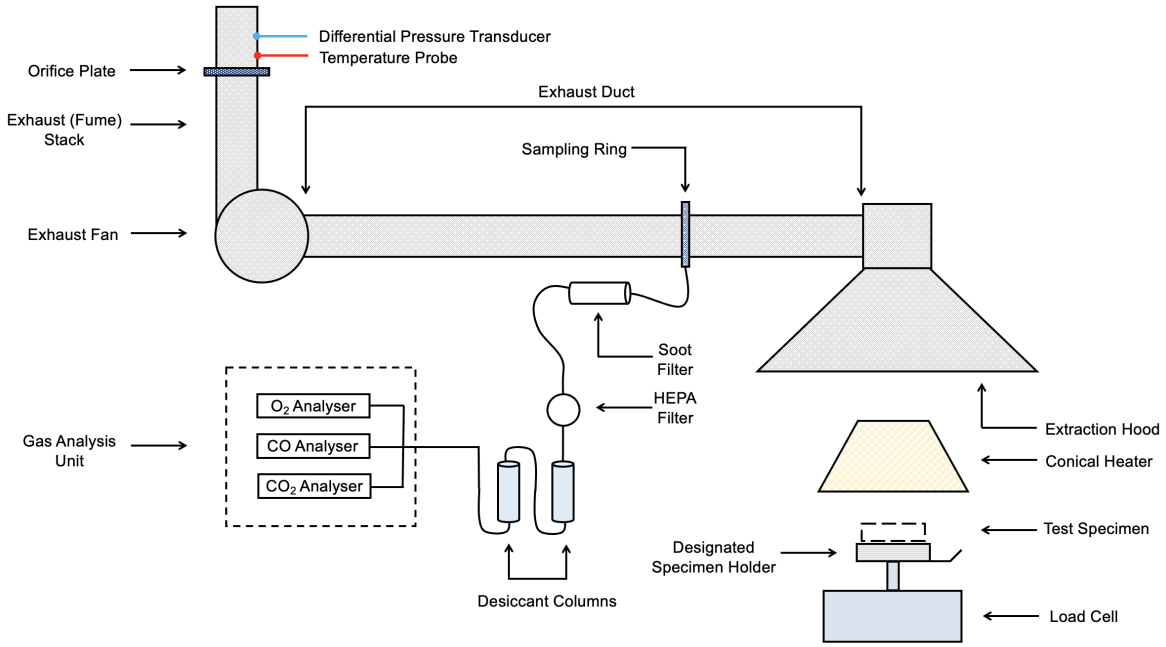

Figure 3.1: A schematic diagram of the cone calorimeter apparatus

As the specimen is subjected to a prescribed level of incident flux, it heats up and starts to release gaseous pyrolysis products, typically within a minute, following the onset of exposure. Once sufficient concentration of combustible pyrolysates are released, have mixed with ambient air and the mixture is heated sufficiently by the cone heater they ignite forming a flame above the surface of the test specimen. This event is registered as "time to ignition". The load cell, with an accuracy of 0.1 g, records the decaying mass of the burning specimen. Combustion gases are collected in the extraction hood located above the conical heater and are directed by an exhaust fan to the duct for extraction through the exhaust stack. A set of temperature probes and differential pressure transducers are located with an orifice plate in the exhaust stack to measure the volumetric flow rate of the hot gases as they are extracted.

In the exhaust duct before the stack, a sampling ring draws combustion gases through a series of soot and high–efficiency particulate arrestance filters, as well as a pair of desiccant columns loaded with sorbent drying agent before entering the Servomex Xentra 4100 gas analysis system of the cone calorimeter unit. These ensure that the sampled gas is soot–, particulate–, and moisture–free for adequate operation of the gas analysis system. The gas analysis system itself is equipped with paramagnetic oxygen (O_2) and non–dispersive

infrared carbon monoxide (CO) and carbon dioxide (CO_2) analyzers which measure the volume fractions of O_2, CO, and CO_2 in the sampled gas, respectively.

The end of the test occurs when flaming combustion ceases (visible flames are no longer observed). The extinction of visible flames marks "time to flame–out"; a test is concluded 120 seconds following this event.

During a test, the manufacturer–supplied cone calorimeter software, ConeCalc5 [157], registers a number of data channels including:

- user entered time to ignition and time to flame–out;
- differential pressure and temperature in the exhaust stack as functions of time;
- measured volume fractions of O_2, CO, and CO_2 in the sampled gas as functions of time; and
- the time varying mass of the test specimen.

At the end of a test, the software further reduces the data to estimate the following parameters:

- heat release rate per exposed specimen area and total heat release during the burning period, as well as
- mass remaining and total mass loss of the specimen from the start of the test, and during the burning period.

The theory behind these parameters, as well as calculation methods employed are presented in the next Section.

3.2 Calculation of Heat Release Rate and Derived Parameters

Heat release rate per unit exposed surface area of a burning specimen is determined using the first law of thermodynamics and the principle of oxygen consumption. This method was first proposed by Thornton in 1917, whose work demonstrated that for a majority

of organic liquids and gases undergoing complete combustion, an approximately constant net value of heat is released per unit mass of oxygen consumed [158]. In 1980, Huggett discovered this to be also true for a large number of organic solids, and determined an average constant value of 13.1 kJ of heat released per gram of oxygen consumed [159]. For practical applications, this value is considered to be accurate with very few exceptions to within ± 5% [160].

Thornton's work implies that in order to approximate the heat release rate of a burning specimen, it is sufficient to measure the change in the mass percentage of oxygen in the combustion gases. Additional measurements of CO and CO_2 content in the flue gases can also be considered in heat release rate calculations to account for incomplete combustion. Heat release rate per unit exposed surface area of a specimen at some test time, t, following the onset of exposure, $\dot{Q}''(t)$ (kW/m^2), is therefore estimated using Equation 3.1.

$$\dot{Q}''(t) = \frac{E}{A_s}\left(\frac{\phi}{1+\phi(\alpha-1)}\right) C\sqrt{\frac{\Delta P}{T_e}}\frac{M_{O_2}}{M_{air}}\left(1 - X^a_{H_2O} - X^a_{CO_2}\right) X^a_{O_2} \tag{3.1}$$

with

$$\phi = \frac{X^a_{O_2}\left(1 - X_{CO} - X_{CO_2}\right) - X_{O_2}\left(1 - X^a_{CO_2}\right)}{X^a_{O_2}\left(1 - X_{O_2} - X_{CO} - X_{CO_2}\right)} \tag{3.2}$$

The specimen mass remaining at some test time, t, following the onset of exposure, is presented as a non–dimensional variable normalized by the initial mass of the sample prior to testing, $m_{specimen}(t_0)$, and is expressed as percent mass remaining as outlined in Equation 3.3.

$$m(t) = 100\% \times \frac{m_{specimen}(t)}{m_{specimen}(t_0)} \tag{3.3}$$

The parameters estimated using the equations above (Equation 3.1–3.3) are used for examining the rates of thermal decomposition and temporal evolution of heat release throughout the remainder of this thesis to demonstrate the underlying physics of material behaviour in response to radiant heating.

3.3 Specimen Preparation and Testing

Based on the literature review of exterior wall topology, construction practices and research to date on fire performance of exterior wall construction, the assemblies for this study consisted of four distinct layers: decorative surface siding, exterior continuous insulation, weather resistant barrier, and exterior sheathing.

Since the main objective was to assess heat transfer through wall assemblies lined with different insulation materials, the exterior of all walls were clad with the same decorative surface siding: 1.02 mm thick, commercially available polyvinyl chloride siding panels.

For the next layer, three exterior continuous insulation layers were chosen:

1. rigid stone wool insulation (31.75 mm thick),
2. polyisocyanurate foam insulation (25.4 mm thick), and
3. extruded polystyrene insulation (25.4 mm thick).

Again since emphasis was on understanding the impact of different insulation products on fire performance and heat transfer in wall assemblies, a single commercially available house wrap made of 0.17 mm thick fused (non–woven) high–density polyethylene fibres was selected to represent the weather resistant barrier for all walls investigated. Likewise, the sheathing was the same across all walls. A typical sheathing material, 12.7 mm thick oriented strand board made of rectangular wood strands blended with waterproof adhesive and arranged into cross–directional layers, was selected.

All materials were purchased in bulk from a local home improvement store in attempts to minimize lot to lot variation in materials due to differing times of purchase.

Specimens of each material were prepared for bench–scale fire testing using the cone calorimeter by cutting square specimens measuring 100 mm $\pm$ 2 mm on a side. Each was conditioned to moisture equilibrium at 23°C $\pm$ 2°C and 50% $\pm$ 10% relative humidity for at least 24 hours prior to testing, in accordance with ASTM E1354–17 standard [161]. All tests were conducted in a draft–free environment at an ambient temperature of 23°C $\pm$ 3°C and relative humidity between 20% and 60%.

Cone calorimeter testing was conducted in two stages. First, each material in the wall assembly was tested individually. Specimens were instrumented with 22–gauge Type–K thermocouples connected to a National Instruments distributed 16–channel data acquisition system to measure and record the thermal response of each material during a test. Independent tests were conducted on each sample type at each of eight levels of incident heat flux (15, 20, 25, 30, 40, 50, 60, and 75 kW/m^2), comprising 145 tests in total.

For vinyl siding tests, thermocouples were installed on the unexposed surface of each sample of vinyl siding. For polyisocyanurate and extruded polystyrene insulation, due to the additional thickness of the samples, thermocouples were installed along the bulk–path of heat transfer through the insulation slab with one thermocouple placed at the mid–depth of the insulating board to measure the thermal response of the material under differing levels of incident heat flux. Due to the known self–heating phenomena of stone wool material [53], samples of this insulation were probed with three thermocouples instead, centrally positioned at three depths within the bulk of the specimen slab to monitor the differences in the interior temperature rise rates along stone wool bulk under exposure to radiant heating:

- 3 mm below the surface exposed to the conical heater (i.e. exposed surface);
- at the slab's mid–depth of 16 mm (i.e. centre); and
- 3 mm above the backside unexposed surface of the slab (i.e. unexposed surface).

In the case of oriented strand board sheets, thermocouples were mounted at the specimen mid–depth only due to the confined slab thickness.

For all tests, the data acquisition system was configured using FieldPoint and temperature data was logged using custom LabView software at a sampling frequency of 0.9 Hz. The response of each specimen to thermal exposure (time–histories of temperature changes) was simultaneously recorded using the cone calorimeter and data logging software while visual observations of their behaviour were concurrently captured with video recordings.

Once the ignition threshold, in terms of heat flux, of each exterior wall component was identified, the layers were tested in combination to form a scaled wall assembly, referred to as "sandwich" in this work. These sandwich assemblies were:

- Sandwich #1, lined with rigid stone wool insulation;
- Sandwich #2, lined with polyisocyanurate insulation; and
- Sandwich #3, lined with extruded polystyrene insulation.

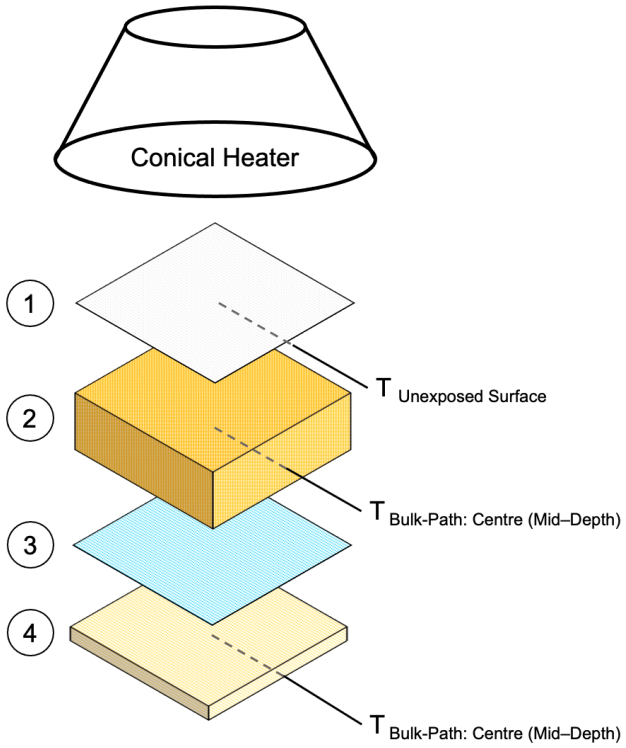

Figure 3.2: Layered design of a scaled wall assembly for cone calorimeter testing: 1) vinyl siding; 2) exterior continuous insulation; 3) weather resistant barrier; and 4) oriented strand board

Each sandwich assembly was lined with one type of exterior insulation (rigid stone wool, polyisocyanurate, or extruded polystyrene) while exposed (vinyl siding) and unexposed (weather–resistant barrier and oriented strand board) layers were kept the same. The layers of each material were stacked as shown in Figure 3.2 with thermocouples placed in the following positions: on the unexposed side of vinyl siding and at the mid–depth of underlying insulation and oriented strand board sheets. The sandwich face lined with vinyl siding was exposed to the conical heater of the cone calorimeter. The sandwich assemblies were tested at two irradiance levels: 15 kW/m^2 and 50 kW/m^2 to capture the difference in thermal response of these assemblies to low and high levels of external heat flux. The response of each sandwich was documented and comparative results regarding thermal behaviour and fire performance of the layered designs were obtained from measured thermocouple data paired with the calculated parameters from the cone calorimeter software. At least 3 samples of each exterior wall material and each scaled assembly were tested at each irradiance level, with results reported here averaged across each set.

3.4 Results and Discussions

In this section, the results of the small–scale tests are presented and discussed. Following presentation of results for the individual materials, data from the sandwich samples are outlined and related to what might be expected in a large–scale test of a similar assembly.

3.4.1 Performance of Individual Wall Components

Polyvinyl Chloride Siding

Results of cone calorimeter tests conducted on polyvinyl chloride siding samples are presented in Figures 3.3 through 3.5. The specimens were subjected to eight levels of incident heat flux and measurements of mass remaining versus time, time–resolved heat release rate per unit area as well as time–histories of unexposed temperature were recorded during each test. The vinyl siding samples did not ignite when subjected to heat flux levels below 50 kW/m^2. As a result, measured heat release rates from tests conducted at 15, 20, 25, 30 and 40 kW/m^2 flux were very low; for a large portion of the tests, they were below the threshold of 30 kW/m^2 heat release rate per unit area (HRRPUA) resolution of the cone calorimeter [162]. Time–resolved profiles of HRRPUA are therefore only shown for tests performed under 50, 60, and 75 kW/m^2 external heat flux (Figure 3.5c). Time–varying plots of mass remaining and unexposed surface temperatures are also presented separately for tests conducted at incident heat flux below and above 50 kW/m^2; these are given in Figures 3.4a–3.4b and 3.5a–3.5b, respectively. For tests conducted at less than 50 kW/m^2 heat flux, specimens were subjected to 10 minutes (600 seconds) of radiant heating, whereas for cases of flaming combustion of vinyl siding material, the tests were concluded 120 seconds after extinction of the visible flames as previously outlined in Section 3.1. In the latter case, the test duration was at most 300 seconds.

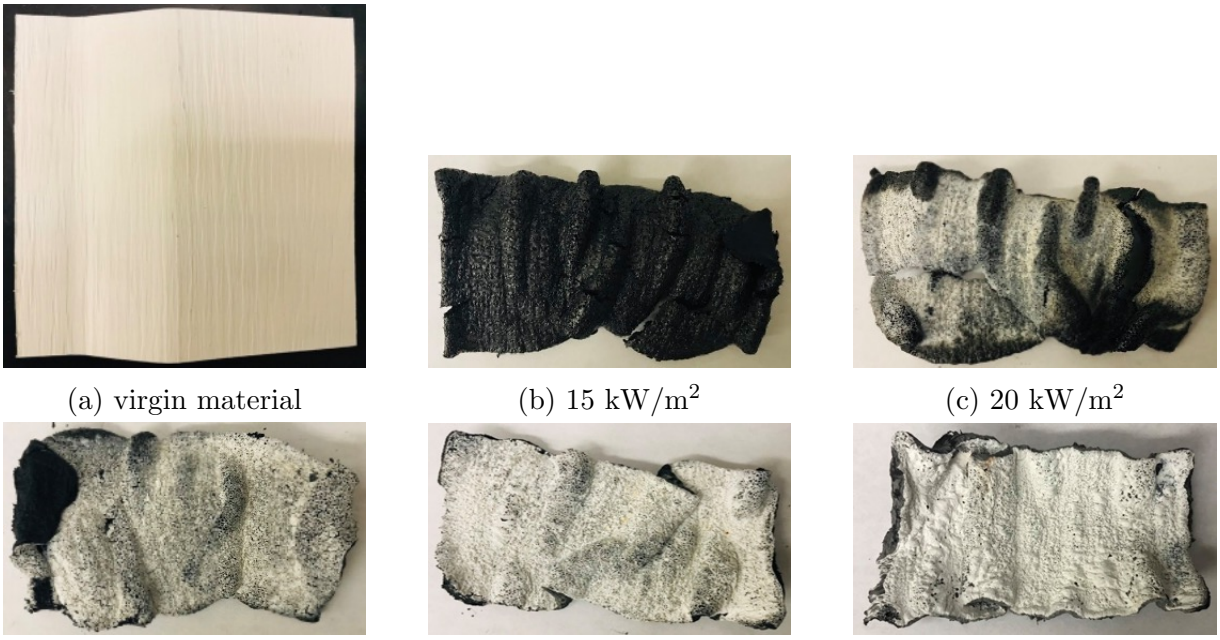

(a) virgin material (b) 15 kW/m^2 (c) 20 kW/m^2

(d) 25 kW/m^2 (e) 30 kW/m^2 (f) 40 kW/m^2

Figure 3.3: The state of vinyl siding samples a) before and after exposure to b) 15 kW/m^2, c) 20 kW/m^2, d) 25 kW/m^2, e) 30 kW/m^2, and f) 40 kW/m^2 heat flux in the cone calorimeter

The post–exposure state of vinyl siding samples subjected to incident heat flux levels of 15 kW/m^2 through 40 kW/m^2 is shown in Figure 3.3. Upon examination of these after test samples, it can be seen that all of the specimens charred leaving behind a carbon–rich residue. After exposure to 30 kW/m^2 and 40 kW/m^2 heat flux, the entire exposed sample surface appears to be covered with ash. Moreover, the size of the post–exposure samples is considerably smaller than 100 mm $\times$ 100 mm dimension of the virgin specimens because immediately as they were heated, the samples buckled and deformed and subsequently shrinking in size as the test progressed. The distortion in sample geometry under thermal heating, is likely associated with the bulk sample temperature approaching the glass transition temperature which for vinyl siding has been reported to be between 61°C and 74°C [52]. Referring to Figure 3.4b, this temperature range was attained very early into the test, in fact, immediately after exposure to the prescribed level of incident heat flux. The extent of geometric distortion (buckling, wrinkling, and shrinking) of the siding material depended on both the level of applied external heat flux as well as duration of exposure. This is demonstrated in Table 3.1, where the total areas of post–exposure

samples are tabulated. These values were calculated by approximating the shape of the charred residue as a trapezoid and computing the area. The percent loss in area was then determined by computing the difference between the sample areas before and after exposure. As anticipated, the total area loss increased with increasing level of thermal exposure from about 56% for 15 kW/m^2 to 63%, 68% and 70% at 20, 30 and 40 kW/m^2 heat flux, respectively.

Table 3.1: End–of–test total area loss of vinyl siding samples subjected to below 50 kW/m^2 heat flux exposure in the cone calorimeter

Incident Heat Flux (kW/m^2)	Total Area Post–Exposure (cm^2)	Total Area Loss Post–Exposure (%)
15	43.70	56.30
20	37.40	62.60
25	33.06	66.94
30	32.19	67.81
40	30.60	69.40

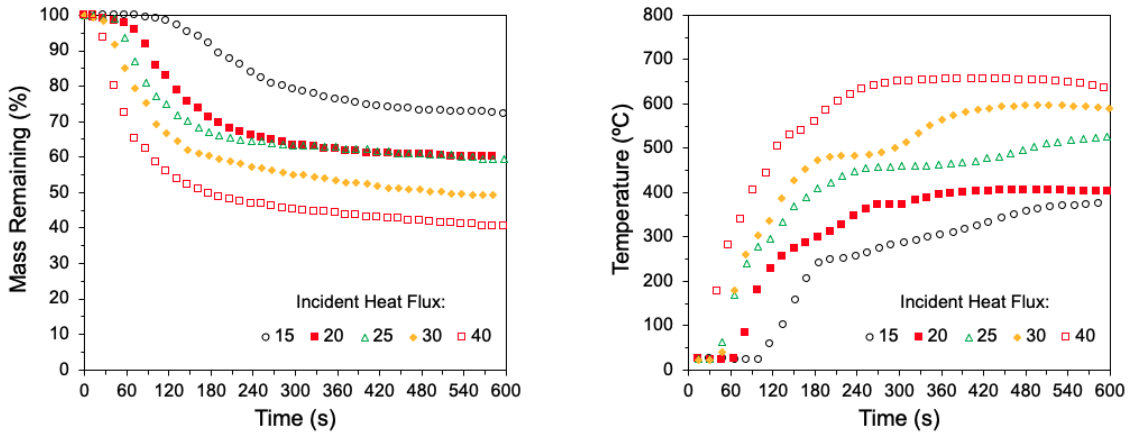

(a) (b)

Figure 3.4: Averaged time–resolved traces of a) mass remaining and b) unexposed temperature profiles for vinyl siding tested in the cone calorimeter below 50 kW/m^2 flux

Figure 3.4a presents mass remaining versus time for vinyl siding samples tested at incident heat flux levels below 50 kW/m^2. From Figure 3.4a, it can be seen that the mass loss and mass loss rate of the siding specimens increased with increasing external heat flux. Regardless of exposure, however, not all the mass was consumed during these tests. Final results are summarized in Table 3.2 in the form of percent mass loss recorded at the end of each test. As can be seen from Table 3.2, the total mass loss increased from about 28% under an incident heat flux of 15 kW/m^2 to 60% at 40 kW/m^2 heat flux, with intermediate values of 40% and 51% for heat flux levels of 20 kW/m^2 and 30 kW/m^2, respectively.

Table 3.2: End–of–test total mass loss of vinyl siding samples subjected to below 50 kW/m^2 heat flux exposure in the cone calorimeter

Incident Heat Flux (kW/m^2)	Total Mass Loss (%)
15	27.9 ± 0.3
20	39.9 ± 0.1
25	40.6 ± 0.3
30	50.8 ± 0.3
40	60.0 ± 0.2

According to the literature [49,50], thermal decomposition of a polyvinyl chloride specimen undergoes a two–step process. First, gaseous pyrolysis products, primarily hydrogen chloride gas, are driven off the decomposing specimen bulk; this event is often referred to as chain stripping. Consequently, liberation of gaseous pyrolysate leaves much of the carbon content in the original sample behind as a solid char residue. Similar observations as reported in Table 3.2 were also made by Wen [101], who studied fire performance of polymers in the cone calorimeter and further noted that not all of the mass of a polyvinyl chloride sample was completely consumed by the end of the thermal exposure due to the char that remained.

The release of pyrolysis gases and subsequent char formation is further explored by analyzing the varying rates of mass loss and temperature rise from the plots shown in Figures 3.4a and 3.4b:

For the case of 15 kW/m^2 heat flux, the release of pyrolysis products commenced at around 120 seconds following the onset of exposure. Between 120 and 210 seconds, the polyvinyl chloride sample continued to thermally decompose, losing mass at a rate of 0.018 g/s. The temperature rise within this 90–second window was 2.66°C/s. After 210 seconds and until the end of the test, the rate of mass loss and rate of temperature increase both slowed considerably to approximately 0.004 g/s and 0.38°C/s, respectively. These slow rates of decomposition and temperature increase are attributed to the formation of a stable char layer with a low thermal conductivity. At the end of the test, the total mass loss was about 28% while the unexposed temperature reached a quasi–steady value of 364.5°C ± 3.5°C.

Under radiant heating at 20 kW/m^2, sample pyrolysis began earlier, at around 72 seconds after exposure. Between 72 and 160 seconds, the mass loss rate of the pyrolyzing sample was also higher than at lower levels of exposure, around 0.034 g/s. The unexposed surface temperature rose at a rate of 3.02°C/s. After 160 seconds, char formation commenced. From this time until the end of the test, the rate of mass loss decreased to 0.004 g/s while the unexposed temperature continued to rise at a rate of 0.53°C/s. The total mass loss at the end of the test was just below 40% and the steady–state temperature of the unexposed surface was 401.1°C ± 0.6°C.

As expected, under exposure to 25 kW/m^2 incident flux, the release of pyrolysis products started even sooner, at around 60 seconds following the exposure. Between 60 and 130 seconds, the rate at which the pyrolysis gases were driven off the thermally degrading vinyl siding specimen was approximately 0.043 g/s and the unexposed side temperature rose at a rate of 3.13°C/s. As char formed, the rates of mass loss and unexposed temperature decreased to 0.003 g/s and 0.78°C/s, respectively. The total mass loss at the end of the test was about 41% and the quasi steady–state temperature of the unexposed surface was 542.8°C ± 2.2°C.

When subjected to 30 kW/m^2 incident heat flux, the sample pyrolysis began at around 30 seconds following the onset of exposure. Between 30 and 120 seconds, the heated vinyl siding sample pyrolyzed at a rate of about 0.052 g/s and the unexposed surface temperature rose at a rate of 3.55°C/s. After 120 seconds, char formation dominated and mass loss rate again decreased to 0.004 g/s. Due to the higher incident flux, the temperature on the unexposed surface rose at a higher rate of 0.82°C/s. The total mass loss at the end of the test was about 51% and the steady–state temperature plateaued at a value of 596.0°C ± 1.3°C.

Under exposure to 40 kW/m^2 incident heat flux, pyrolysis again began at around 30 seconds after the exposure. In this case pyrolysis products were liberated from the specimen bulk at a rate of approximately 0.075 g/s for times between 30 and 90 seconds after exposure, while the unexposed surface temperature increased at a rate of 4.64°C/s. After 90 seconds, char formation dominated and the mass loss rate decreased to 0.004 g/s while the unexposed side temperature continued to rise at a rate of 0.86°C/s. At the end of the test, the total mass loss and quasi–steady temperature achieved on the unexposed specimen surface were 60% and 653.4°C ± 2.4°C, respectively.

From the above results, it can be concluded that the rate of release of gaseous pyrolysis products from thermally decomposing vinyl siding material increases with increasing external heat flux from about 0.018 g/s for 15 kW/m^2 to approximately 0.075 g/s at 40 kW/m^2. Similarly, the rate of temperature rise at the unexposed sample surface increases with higher levels of radiant exposure: from 2.66°C/s at 15 kW/m^2 to 4.64°C/s under 40 kW/m^2 heat flux. In terms of char formation, the onset of charring for vinyl siding samples occurs earlier in the test with increasing incident heat flux; however, the mass loss rate during char formation appears to remain relatively constant at around 0.004 g/s irrespective of imposed irradiance. The temperature rise on the unexposed siding surface also tends to increase with higher levels of external irradiance, from 0.38°C/s at 15 kW/m^2 to about 0.86°C/s at 40 kW/m^2 with lower differences in rate observed for external irradiances of 25 kW/m^2 through 40 kW/m^2, where the average rate of temperature rise rate was 0.082°C/s ± 0.04°C/s.

In contrast to heating with the lower heat fluxes discussed above, vinyl siding samples ignited and burned when subjected to incident heat flux levels above 50 kW/m^2. Cone calorimeter test results from these experiments are presented in Figure 3.5, where time–histories of sample mass remaining, unexposed side temperature, and heat release rate per unit exposed specimen area are shown in Figures 3.5a, 3.5b, and 3.5c, respectively.

The overall behaviour of the vinyl siding samples under exposure to external heat flux levels $\geq$ 50 kW/m^2 was similar to that discussed previously for the cases of 15 kW/m^2 – 40 kW/m^2 irradiance: at the onset of exposure to radiant heat, the specimens started to soften, buckle, and shrink while releasing gaseous pyrolysis products. Shortly afterwards, char formation began. Under continued exposure to incident heat flux, the heated pyrolysis gases ignited and formed a flame above the exposed surface of the specimen. The samples continued to char throughout the flaming combustion period and by the end of the test, a charred residue, completely covered with ash, was left behind on the exposed surface of the specimen. Post–test samples following exposure to 50 kW/m^2, 60 kW/m^2, and 75 kW/m^2 heat flux were practically indistinguishable from the post–test specimen shown in Figure 3.3f so are not included here. Again, due to charring of the vinyl siding, not all of the sample mass was consumed by completion of the test. Referring to Figure 3.5a, the percentage mass loss calculated post–exposure to 50 kW/m^2, 60 kW/m^2, and 75 kW/m^2 incident heat flux were 61.4% $\pm$ 0.4%, 60.9% $\pm$ 0.4%, and 62.0% $\pm$ 0.5%, respectively; on average, 61.4% $\pm$ 0.6% across these experiments. The carbon–rich char remaining from the vinyl siding material was therefore approximately 38.6% by mass, consistent with findings for similar vinyl siding products reported in the literature [163, 164].

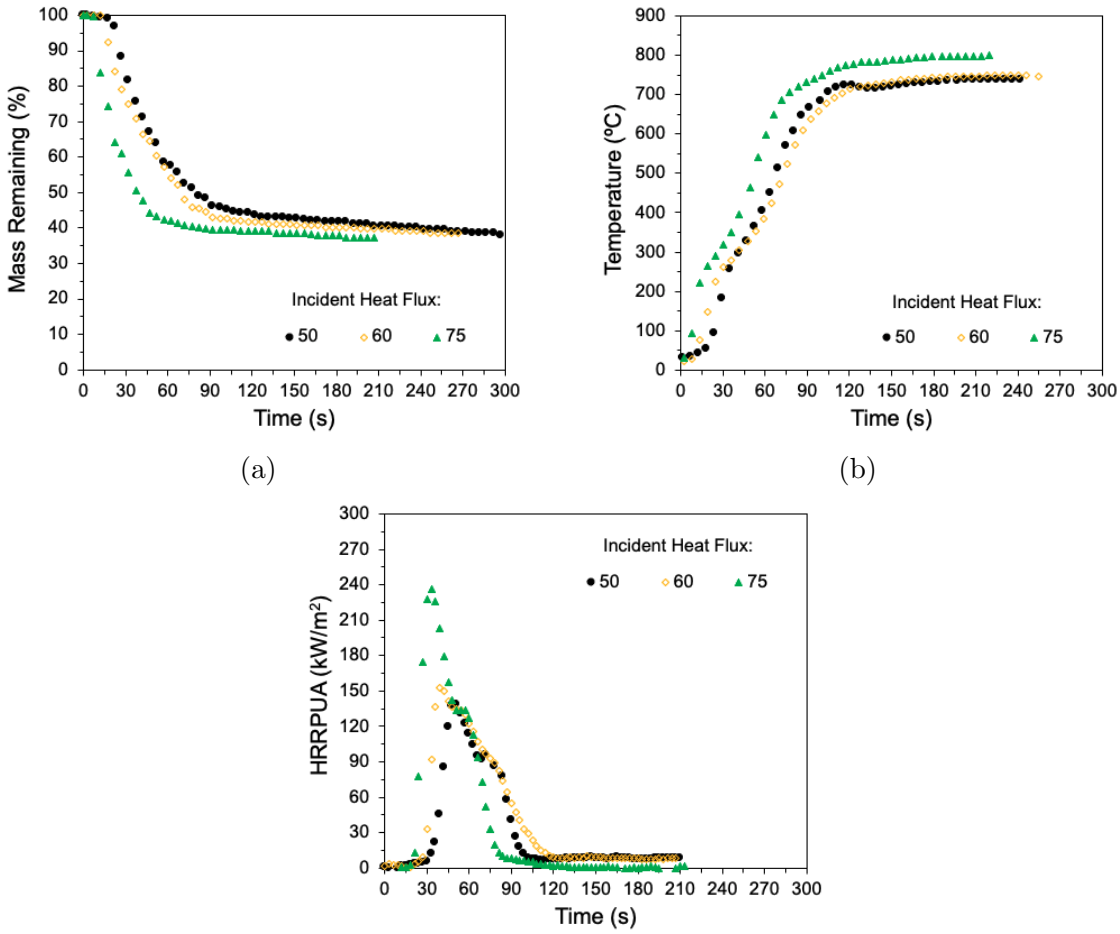

Figure 3.5: Averaged time–resolved traces of a) mass remaining, b) unexposed temperature and c) heat release rate per unit area profiles for vinyl siding tested in the cone calorimeter above 50 kW/m^2 flux

An analysis of the total area loss across the experiments suggests an average end–of–test area loss of 68.50% ± 3.52% for exposures of 50 kW/m^2 – 75 kW/m^2 incident heat flux. Interestingly, total area loss observed for both 30 kW/m^2 (67.81%) and 40 kW/m^2 (69.40%) flux exposure are also within that range. This suggests that past a critical exposure level, 31.5% of the sample (by volume) remains as char, while the remaining 68.5 vol.% of the sample feeds the pyrolysis process, regardless whether those pyrolysis products underwent flaming combustion.

The release of pyrolysis gases, their combustion characteristics and charring of vinyl siding specimens is further explored by analyzing the varying rates of mass loss, temperature rise and heat release per unit exposed sample area from time–resolved traces of mass remaining, unexposed temperature and HRRPUA profiles shown in Figures 3.5a, 3.5b, and 3.5c, respectively. The times to ignition recorded during exposure to 50 kW/m^2, 60 kW/m^2, and 75 kW/m^2 heat flux were 31, 24, and 12 seconds, respectively. Prior to ignition of specimen bulk, the mass loss rates attributed to the initial release of gaseous products were 1.36 g/s for 50 kW/m^2, 1.74 g/s for 60 kW/m^2, and 2.89 g/s at 75 kW/m^2 heat flux exposures. At the same time, sample unexposed surface temperatures rose at rates of 10.88°C/s, 10.90°C/s and 11.39°C/s for exposures of 50 kW/m^2, 60 kW/m^2, and 75 kW/m^2, respectively. Both these rates of increase were considerably higher than those reported for the tests conducted at below 50 kW/m^2 flux. Subsequently, when the pyrolysis gases above the specimen bulk ignited, the heat release rate from burning sample increased sharply, as can be seen from Figure 3.5c, attaining peak values of 138.63 kW/m^2, 152.46 kW/m^2, and 236.37 kW/m^2 under radiant heating to 50 kW/m^2, 60 kW/m^2, and 75 kW/m^2 flux, respectively. As anticipated, the durations of sustained flaming, i.e. from time to ignition to time when all visible flames were out, also decreased with increase in external incident heat flux with values of 100 seconds at 50 kW/m^2, 90 seconds at 60 kW/m^2, and 64 seconds for 75 kW/m^2 heat flux. During this period, the rates of mass loss and unexposed side temperature rise also increased as:

- 0.081 g/s and 5.48°C/s for the case of 50 kW/m^2 heat flux exposure;
- 0.095 g/s and 7.36°C/s for the case of 60 kW/m^2 heat flux exposure; and
- 0.125 g/s and 9.44°C/s for the case of 75 kW/m^2 heat flux exposure.

The rates of mass loss and temperature increase over the duration of sustained flaming were lower compared to those observed in the period prior to ignition. This was likely due to the formation and subsequent insulating effect of the char, which was continuously formed across the surface and through the thickness of the specimen throughout the test duration. Finally, for experiments performed under 50 kW/m^2 – 75 kW/m^2 radiant heating, the end–of–test total mass loss and unexposed temperatures attained were 61.4% and 735.8°C for 50 kW/m^2, 60.9% and 747.8°C for 60 kW/m^2, and 62.0% and 795.3°C for 75 kW/m^2 flux.

Rigid Stone Wool Insulation

Results of cone calorimeter tests conducted on rigid stone wool insulation slabs are presented in Figures 3.6 through 3.8 in the following paragraphs. The rigid stone wool insulation did not ignite at any incident heat flux. As a result, the measured heat release rate remained very low; for a large portion of the tests, it was below the threshold of 30 kW/m^2 heat release rate per unit area resolution of the cone calorimeter [162]. Thus, for stone wool insulation, time–resolved profiles of heat release rate per unit area are not presented in this section. Measurements of mass loss versus time, as well as time–histories of temperature at three locations along the bulk–path of a slab were recorded during each test. Since none of the samples ignited, tests were concluded five minutes after the temperature profiles at all three locations within the bulk insulation material reached quasi–steady values.

The total mass loss of the rigid stone wool insulation increased with increasing level of external incident heat flux starting at approximately 1% for 15 kW/m^2 flux to approximately 7% at 75 kW/m^2. Intermediate values of 2.5% and 3.6% were observed for 25 kW/m^2 and 50 kW/m^2, respectively. The change in the mass loss is most likely attributed to the quantity of organic binder and sample impurities, such as dust binding oil in the sample, that thermally decompose under heating. This is consistent with the notion that as temperatures in the sample increase, from lower to higher levels of incident heat flux (<40 kW/m^2 to >40 kW/m^2), more pyrolysis of the binder is likely to occur resulting in a greater mass loss in the specimen [54]. The values seen in these tests are consistent with an assumption that it is mainly the binder and associated additives that significantly contribute to mass loss of stone wool insulation. This would suggest that the organic content of these stone wool insulation samples would be between 1% and 7% by mass consistent with results presented by Nagy [53] who reported mineral fibre and organic binder contents of 94%–99% and 1%–6% by mass, respectively, in similar samples.

That the differences in measured mass loss are related to binder composition is further supported by visual observations of the tested insulation specimens. Different grades of discolouration were observed for stone wool specimens heated at the varying levels of external incident heat flux. This is illustrated in images of the stone wool specimens exposed to three levels of incident heat flux (15, 40 and 75 kW/m^2) in Figure 3.6. These heat fluxes were selected to demonstrate the extent of (exposed) surface and interior cross–sectional discolouration observed for stone wool specimens after exposure to lower (<40 kW/m^2), moderate (40 kW/m^2), and higher (>40 kW/m^2) levels of incident heat flux. The post–exposure samples were cut along the two mid–lines of the square specimen sides, yielding four equal cubic pieces measuring 51 mm long × 51 mm wide × 32 mm thick. This allowed the author to explore potential symmetry in the patterns of discolouration along the two lines of symmetry of the original post–test specimen and to evaluate the depth of the heat affected zone within the sample interior. Two pieces of 51 mm × 51 mm × 32 mm dimensions were then put side by side forming one of the lines of symmetry of the original post–test sample, measuring 102 mm long × 51 mm wide × 32 mm thick, as depicted in Figure 3.6. The cut lines along the center of the half–specimens shown in Figure 3.6 are artifacts of the post–exposure examination of samples as discussed above. A virgin sample of stone wool insulation material (prior to testing) was also cut into four equal cubic pieces and was used as a reference for identifying the discolouration patterns on the post–exposure specimens. The sample section depicted in Figure 3.6a shows the yellow and light khaki tint of a virgin stone wool specimen before testing.

The state of the sample following exposure to 15 kW/m^2 external incident heat flux is shown in Figure 3.6b. No noticeable changes in colour were evident on the unexposed surface and the four sides of the sample after heating at this exposure. On the other hand, the colour of the exposed specimen surface changed from its initial yellow tint to brown, with a brown to orange transition zone penetrating into the bulk of the sample. This transition zone appears to be parabolic (concave up) in shape, deepest at the geometric centre of the slab and symmetrically lessening in depth towards the edges and top of the sample. It extended to a depth of about 13 mm into the sample thickness at its point of farthest advance, as measured from the exposed sample surface. In contrast, near the edges close to the exposed surface, the heat affected zone advanced approximately 5 mm into the sample thickness from the exposed sample surface. The shape of this heat–affected zone suggests that the there was a considerable thermal gradient in the sample in the radial direction as the sample was heated under 15 kW/m^2 exposure. Similar observations were recorded by Nagy [53] who investigated thermal penetration in disc–shaped stone wool insulation specimens subjected to radiant heating in the cone calorimeter.

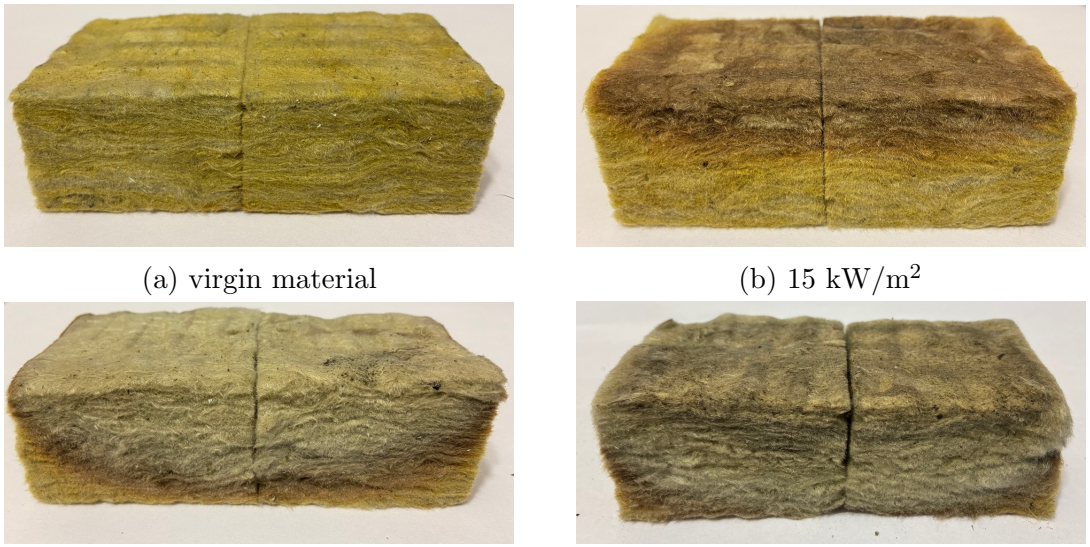

(a) virgin material (b) 15 kW/m^2

(c) 40 kW/m^2 (d) 75 kW/m^2

Figure 3.6: The state of exposed surface and interior cross section of stone wool insulation samples (a) before a test and after exposure to (b) 15 kW/m^2, (c) 40 kW/m^2, and (d) 75 kW/m^2 of external incident heat flux in the cone calorimeter

The post–exposure condition of a stone wool sample subjected to 40 kW/m^2 incident heat flux is shown in Figure 3.6c. Examination of the exposed surface and the outer (unexposed) sides of the sample indicated the presence of a light brown discoloured strip, measuring about 6 mm in thickness, surrounding the sides of the sample close to its exposed surface (not depicted in the figure). No colour changes were observed on the underside of the specimen. Similar to the experiment conducted under 15 kW/m^2 incident flux, the exposed surface completely changed in colour, in this case, from an initial light yellow tone to light grey. In addition to surface discolouration, a pattern of light grey to brown to orange discolouration can be seen in the sample cross section. The parabolic (concave up) shape of this zone resembles the heat affected region discussed above for the 15 kW/m^2 case. The light grey portion of discoloration extended 22.5 mm from the exposed surface into the sample thickness at its farthest advance while the underlying brown strip (approximately 8 mm in thickness) reached the bottom of the specimen. Minor orange discolouration can be noticed near the edges of the sample close to the unexposed side.

Upon exposure to 40 kW/m^2 heat flux, the sample appears to lose some of its original rigidity, especially in the areas having light grey tones. The light grey areas of the sample were soft to the touch and layers of mineral fibres from this region could be easily separated from the rest of the sample bulk. No further investigations were conducted to explore the impact of varying heating rates on characteristics such as the compressibility of the heated stone wool insulation, but the loosely stacked structure of mineral fibres in the heat affected zone was likely due to thermal decomposition of the binding agent and associated additives that had originally held the strings of mineral fibres together in the rigid insulation block. Similar observations were reported by Karamanos et al. [165] who investigated the performance of stone wool under elevated temperatures.

The sample section depicted in Figure 3.6d shows the state of stone wool sample after exposure to 75 kW/m^2 incident heat flux. A strip of three discoloured regions (light grey to brown to orange), measuring 22 mm in thickness, was seen around the outer perimeter of the sample close to the exposed surface. Slight discolouration from light yellow (initial colour) to light brown was found on the underside (unexposed surface) of this specimen suggesting that the heat had penetrated entirely through the sample during the exposure. Similar to previous observations, the exposed surface of the sample underwent a distinct colour change from light yellow (virgin material) to taupe. A taupe to light grey to brown pattern of discolouration can also be seen in the interior cross section of the sample. Unlike the above samples, the interior heat affected zone for this specimen appears to encompass the entire internal volume of the specimen bulk. The rigidity of the post–exposure sample was significantly compromised, throughout the thickness of the original slab.

The variations in colour and the sequence of discolouration patterns (from light yellow to orange to brown to light grey to taupe) are possibly linked to a series of thermal degradation processes that have previously been observed during thermal degradation of the organic binder in stone wool samples [154]. To further understand the relation between binder decomposition and mass loss in the samples, it is of interest to examine the time–histories of temperatures that were recorded at the three measurement positions within the stone wool for increasing levels of incident heat flux as well. These are shown for the cone calorimeter stone wool insulation samples tested at lower ($<$40 kW/m^2) and higher ($\geq$ 40kW/m^2) levels of external heat flux in Figures 3.7 and 3.8, respectively.

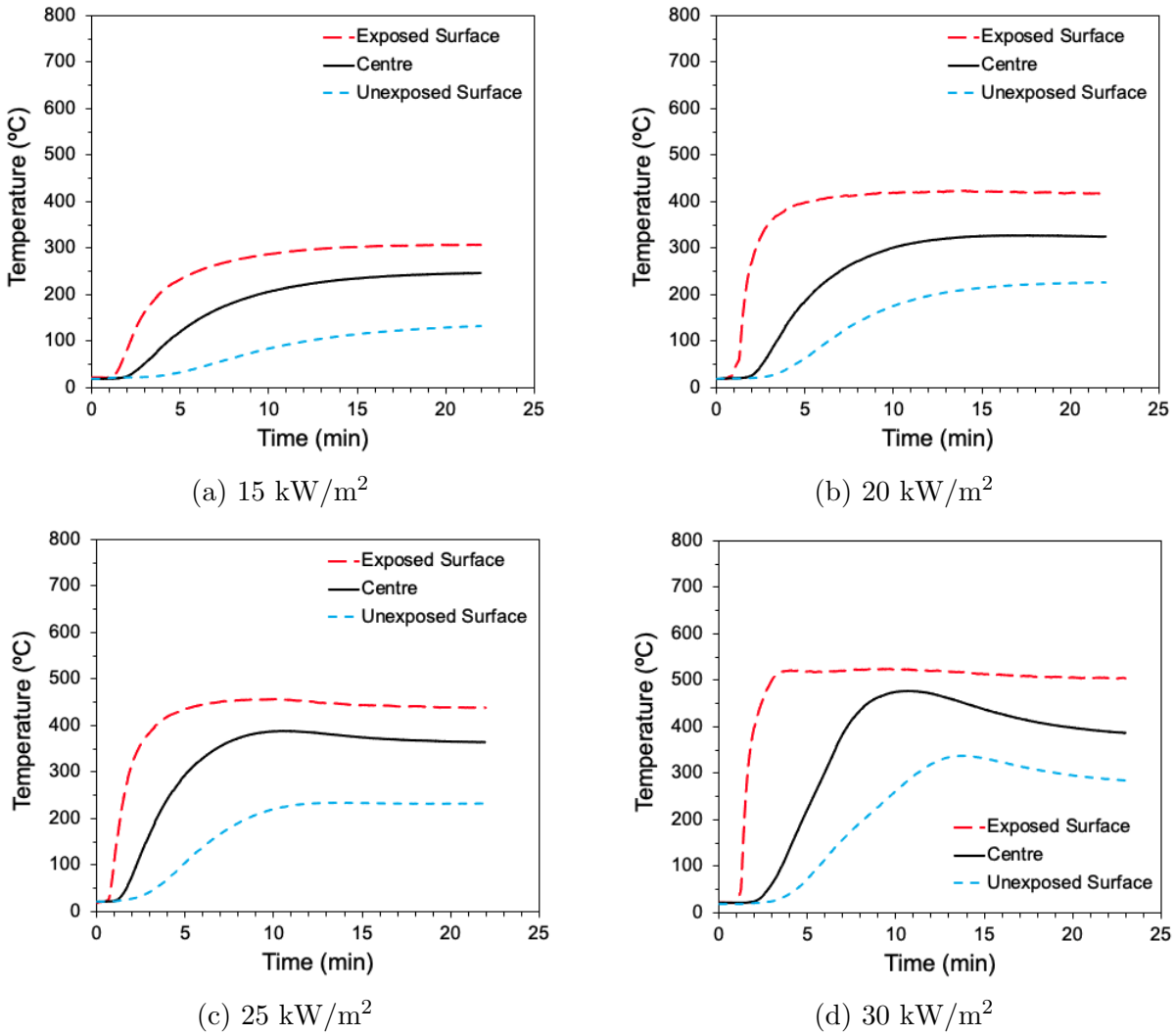

(a) 15 kW/m^2 (b) 20 kW/m^2

(c) 25 kW/m^2 (d) 30 kW/m^2

Figure 3.7: Temperature–time profiles along the bulk–path of rigid stone wool insulation exposed to (a) 15, (b) 20, (c) 25, and (d) 30 kW/m^2 of external incident heat flux

Figure 3.7a presents average temperature–time profiles through the bulk of a stone wool sample subjected to 15 kW/m^2 external incident heat flux. Following the onset of exposure, the temperature of the exposed surface gradually increased to a steady–state value of 306°C ± 0.1°C after 10 minutes of heating. The centre of the slab exhibited a similar pattern of temperature increase with a rate of temperature rise of 0.6°C/s. The centre of the specimen and the unexposed surface reached steady–state temperatures of 247°C ± 0.2°C and 133°C ± 0.4°C after 13 and 15 minutes of heating, respectively. Recalling the extent of discolouration (Figure 3.6b) observed for the interior of the sample exposed to 15 kW/m^2 heat flux, the interface between the discoloured (brown to orange) and virgin (light yellow) regions can be associated with an interface temperature of 247°C, suggesting that binder decomposition commenced at temperatures around 250°C. Similar temperature thresholds for binder decomposition were reported by Nagy [53] and Sjöström et al. [54] during thermogravimetric measurements on stone wool insulation at several heating rates in air. Since only a partial volume of the specimen slab reached the binder decomposition threshold by the end of the test, the total mass loss associated with thermal degradation of organic content is expected to be relatively small. Consistent with this, the total mass loss recorded for stone wool insulation under 15 kW/m^2 heat flux exposure was 1%, as discussed previously.

Figures 3.7b and 3.7c present the time–histories of average temperatures recorded for a stone wool sample during exposure to 20 kW/m^2 and 25 kW/m^2 heat flux. At these exposures, temperatures close to the surface reached steady–state values of 418°C ± 0.5°C and 438°C ± 0.9°C, respectively. In the case of 20 kW/m^2 exposure, the centre of the slab gradually increased to a steady–state of value 324°C ± 0.4°C after about 12 minutes of heating with a rate of temperature rise of 1.1°C/s, higher than that observed for 15 kW/m^2 exposure. A slightly higher rate of temperature rise (1.5°C/s) was calculated for the centre thermocouple during heating of the stone wool sample subjected to 25 kW/m^2 external radiant heat flux. Consistent with this, the quasi steady–state temperature at the centre of the slab exposed to a flux of 25 kW/m^2 was also higher than that at 20 kW/m^2, plateauing at 367°C ± 1.1°C. Unlike the previous exposures (15 kW/m^2 and 20 kW/m^2) for the 25 kW/m^2 heat flux exposure, a peak temperature of 389°C was recorded by the centre thermocouple at around 10 minutes into the test but decayed thereafter as can be seen in Figure 3.7c. This behaviour could possibly be attributed to the thermocouple measuring temperatures in an accumulation of hot pyrolysis gases released from thermally decomposing organic content in stone wool insulation. Between 250°C and 500°C, the rate at which the binder thermally degrades increased and had been associated with elevated temperatures recorded within the specimen bulk [53, 165].

When the rate of generation of pyrolysis gases from thermally decomposing binder surpassed the rate at which they could escape from the specimen body, some of the hot gases were thought to remain locally trapped within the sample volume until they gradually dispersed within the volume or out of the bulk material. For tests conducted at both 20 kW/m^2 and 25 kW/m^2 heat flux, the unexposed surfaces plateaued smoothly to steady–state temperatures. The end–of–test values on the bottom (unexposed) surfaces of the samples were 226°C ± 0.3°C and 232°C ± 0.2°C for 20 kW/m^2 and 25 kW/m^2 heat flux, respectively.

Average temperature–time profiles recorded through the thickness of the stone wool insulation slabs under heating at 30 kW/m^2 incident flux are presented Figure 3.7d. A rapid increase in temperature was recorded by the surface thermocouple, reaching a steady–state value of 505°C ± 0.6°C within about one minute after exposure. At the centre of the specimen, the temperature reached a peak value of 477°C ± 0.2°C in 9 minutes and remained stable at that value for about 60 seconds followed by a gradual decrease in temperature to a value of 392°C ± 3.6°C towards the end of the test. While the peak temperature recorded at the centre of the specimen was approximately 90°C higher than that recorded for the 25 kW/m^2 exposure, it could also be associated with the thermocouple measuring temperatures in a localized pocket of accumulated hot pyrolysis gases from the thermally decomposing binder since it lied in the 250°C – 500°C decomposition temperature range seen for similar stone wool materials. Unlike observations for 15 kW/m^2 through 25 kW/m^2 heat flux exposures, when the sample was exposed to 30 kW/m^2, a peak in temperature was also measured on the unexposed side of the sample. In this case, a peak temperature of 337°C occurred on the unexposed surface temperature about half–way into the test following which it decayed to a value of 286°C ± 1.3°C towards the test completion.

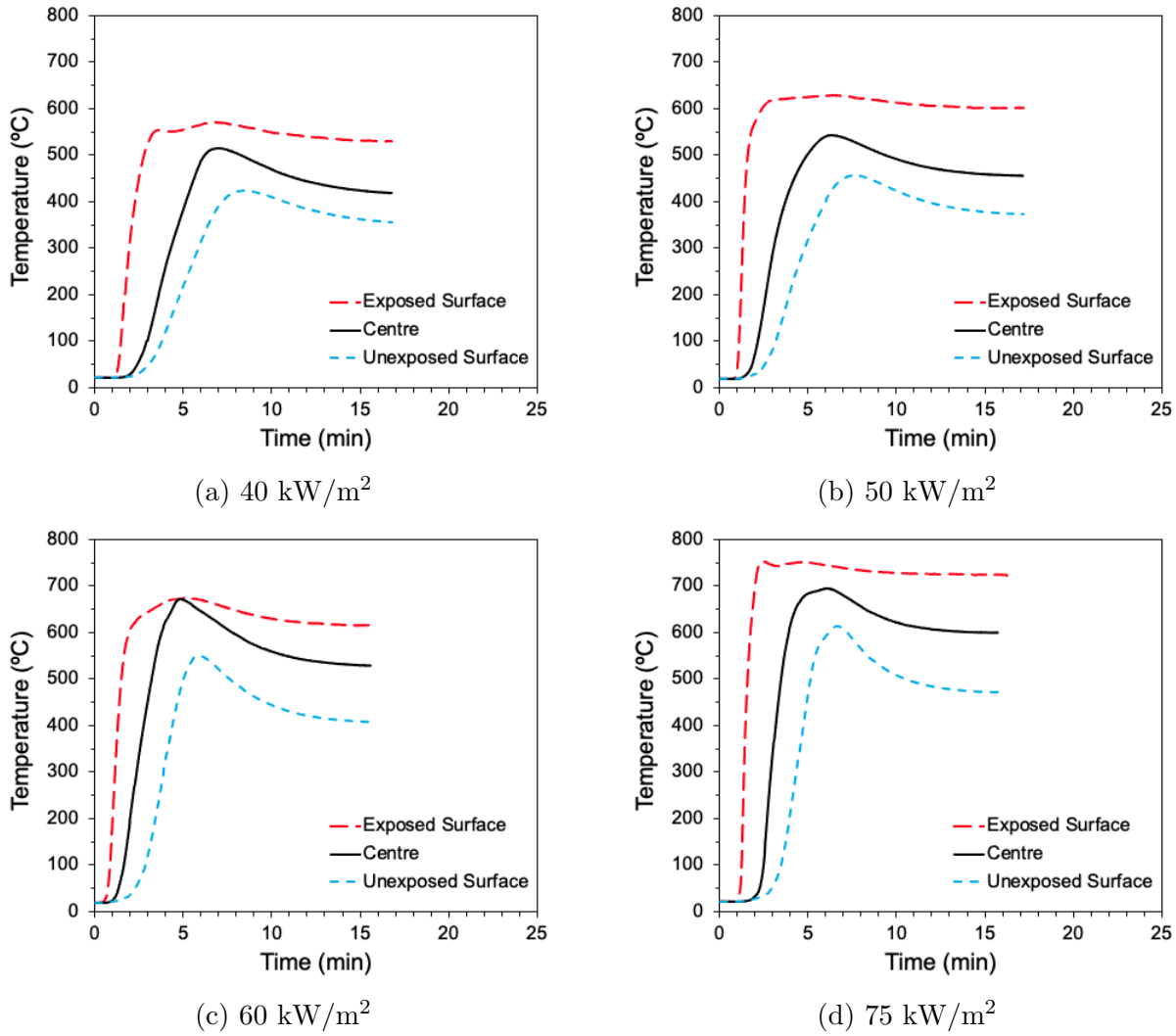

(a) 40 kW/m^2 (b) 50 kW/m^2

(c) 60 kW/m^2 (d) 75 kW/m^2

Figure 3.8: Temperature–time profiles along the bulk–path of rigid stone wool insulation exposed to (a) 40, (b) 50, (c) 60, and (d) 75 kW/m^2 of external incident heat flux

Figure 3.8a presents the average time–histories of temperatures recorded through the thickness of stone wool samples during exposure to 40 kW/m^2 heat flux. The exposed surface thermocouple again showed an initial sharp increase in temperature and subsequently reached a maximum value of 571°C six minutes after the onset of exposure. Following this, there was a slight temperature decrease which finally plateaued to a value of 531°C ± 0.5°C toward the end of the test. At the centre of the specimen, interior temperatures increased at a rate of 2.7°C/s to peak temperatures of 515°C, also approximately six minutes after the onset of exposure. The centre temperature then gradually decreased to a a steady value of 420°C ± 1.3°C. A similar temperature–time profile can be observed on the unexposed surface with peak and steady–state temperatures of 425°C and 359°C ± 1.6°C, respectively. The temperature maxima of 571°C and 515°C registered close to the exposed surface and at the centre of the stone wool samples, respectively, are associated with oxidation of gaseous pyrolysis products liberated from the thermally decomposing resins in the insulation binders. The threshold temperature for initiation of this oxidation reaction is reported to be ≥ 500°C [53, 57, 165]. Further, according to Paudel et al. [166], a bell shaped profile at temperatures above 500°C on a temperature–time curve for heated stone wool represents a region affected by energy (heat) released from these oxidation reactions. Figure 3.8a shows such a bell–shaped temperature region for the centre of the sample between 6 and 8 minutes into the test. Recalling the grade, pattern and extent of discolouration observed for the exposed surface and interior cross section of stone wool sample exposed to 40 kW/m^2 heat flux (Figure 3.6c), the light grey colour of the heat affected zone was consistent with a chemical reaction and could be linked to the residues from binder pyrolysis and oxidation, whereas the brown to orange tints more likely indicated zones undergoing only thermal pyrolysis. It is also interesting to note that at temperatures above 500°C, in addition to potential oxidation of the binders, the binder resins could be polymerized. In either case, they no longer connected the mineral fibres [56] which then resulted in decreased material density [165] observed here and noted above when discussing the compromised rigidity of stone wool samples in the light grey heat affected zones after exposure to 40 kW/m^2 heat flux.

Figure 3.8b shows temperature–time histories for a stone wool sample tested at 50 kW/m^2 incident heat flux. Similar to the previous case for exposure to 40 kW/m^2 incident flux, the exposed surface again experienced a sharp increase in temperature, almost instantaneously reaching 601°C and remaining at that value ± 0.3°C for the duration of the test. The centre of the specimen heated at a rate of about 4°C/s reaching a peak value of 544°C five minutes after the onset of exposure which was then followed by a gradual decrease in temperature to a relatively steady value of 457°C ± 0.4°C. A similar profile is seen for the temperature of the unexposed surface with time, where a peak value of 457°C was achieved and subsequently decreased to a value of 374°C ± 0.6°C.

Time–histories of measured temperature through the bulk of stone wool insulation sample subjected to external radiant heating of 60 kW/m^2 are presented in Figure 3.8c. Similar to the previous case of 50 kW/m^2 flux, the exposed surface thermocouple showed an initial sharp increase in temperature to a peak value of 676°C by four minutes into the test. This was followed by a gradual decrease in temperature to a steady value of 617°C ± 0.2°C. In contrast to any of the tests conducted at lower levels of incident flux, for 60 kW/m^2 exposure, the peak temperature measured at the centre of the specimen was only slightly lower, 673°C, and occurred at about the same time as the peak measured by the thermocouple at the exposed surface. According to Moesgaard et al. [59], who studied crystallization of stone wool fibres, the oxidation of siliceous species occurs at temperatures above 650°C. Consistent with this, the regions on the temperature–time curves between 650°C and 673°C – 676°C peaks may relate to crystallization taking place across a broad volume in the top half of the sample. Following the peaks, it is interesting that the decay in temperature was different for the exposed surface than in the specimen centre as they decreased to values of 617°C ± 0.2°C and 530°C ± 0.3°C, respectively, toward the end of the test. A bell–shaped profile of temperature with time, with a peak of 551°C, was registered on the unexposed surface six minutes following the onset of exposure suggesting that binder oxidation might had occurred through the bulk of the sample at this level of incident heat flux [53,57,165,166]. As in the cases above, following the peak, temperatures decreased again, in this case to values of 408°C ± 0.3°C which were higher than for any previous tests.

Time–histories of measured exposed surface, specimen center and unexposed surface temperatures for the case of stone wool samples subjected to 75 kW/m^2 incident heat flux are presented in Figure 3.8d. The shapes of these temperature–time profiles were very similar to those discussed for exposures of 50 kW/m^2 and 60 kW/m^2 heat flux. The exposed surface rapidly rose in temperature after exposure, reaching steady–state values of 735°C ± 0.4°C. At the centre of the specimen body, a peak temperature of 695°C was attained five minutes after the onset of exposure, which was then followed by a gradual decrease in temperature plateauing at a value of 600°C ± 0.3°C. The time–history of temperature for the unexposed surface was very similar, albeit with a sharper peak in temperature reaching 614°C, and subsequently leveling to 472°C ± 0.4°C. Taking 500°C as a threshold value for commencement of binder oxidation reactions, it appears that the binder in the entire interior volume of the stone wool sample oxidized in under four minutes after exposure, consistent with the extent of the light grey discolouration patterns discussed previously for visual observations of samples after exposure to 75 kW/m^2 heat flux. Referring to the colours observed in the stone wool insulation sections depicted in Figure 3.6d, the taupe tint covering the exposed surface and portions of the interior cross section (up to the sample's mid–depth) could be attributed to the crystallization of siliceous species at temperatures above 650°C [59], since these temperature levels were attained on the exposed surface and at the centre of the sample early in the test, at one and three minutes after exposure, respectively. Since the unexposed surface temperature did not reach 650°C, no taupe discolouration was observed between the mid–depth and bottom of the specimen and colours there were more consistent with binder oxidation seen in samples under lower exposure levels. Either way, the original rigidity of stone wool was significantly compromised, especially in regions corresponding to highest temperatures (taupe colour).

Table 3.3 summarizes measured values of end-of-test and peak temperatures reached at the exposed surface, center and unexposed surfaces of the stone wool insulation samples across the eight levels of external incident heat flux tested. These values were presented individually when discussing time–histories of recorded temperatures within the stone wool samples at different heat fluxes but are summarized here to illustrate trends across tests. As can be seen from Table 3.3, both end–of–test and peak temperatures recorded at the three measurement locations increased with increasing external incident heat flux. The onset of thermal decomposition (pyrolysis) of organic content (binder and associated additives) within the insulation commenced at temperatures of around 250°C; this could be seen via visual observations and measurements in tests conducted at external heat fluxes as low as 15 kW/m^2 (see end–of–test temperature at centre of sample in Table 3.3).

Table 3.3: End–of–test and peak temperatures of stone wool insulation measured at three depths across eight levels of external incident heat flux

Incident Heat Flux (kW/m^2)	End–of–Test Temperature (°C)			Peak Temperature (°C)		
	Exposed Surface	Slab Centre	Unexposed Surface	Exposed Surface	Slab Centre	Unexposed Surface
15	305.9 ± 0.1	246.9 ± 0.2	132.7 ± 0.4	306.2	247.4	133.4
20	418.1 ± 0.5	324.4 ± 0.4	225.5 ± 0.3	424.1	326.3	226.1
25	438.0 ± 0.9	366.5 ± 1.1	231.6 ± 0.2	455.4	389.1	233.5
30	504.7 ± 0.6	392.4 ± 3.6	286.0 ± 1.3	524.6	477.1	337.0
40	530.6 ± 0.5	420.2 ± 1.3	358.6 ± 1.6	570.9	514.9	424.5
50	601.0 ± 0.3	456.8 ± 0.4	373.6 ± 0.6	628.3	543.8	456.6
60	616.6 ± 0.2	529.7 ± 0.3	408.3 ± 0.3	675.6	672.6	550.5
75	734.5 ± 0.4	599.7 ± 0.3	472.4 ± 0.4	755.3	694.6	614.3

Between 250°C and 500°C, the rate of binder decomposition increased with increasing external heat flux, suggesting that at external heat fluxes of 20 kW/m^2 to 30 kW/m^2, pyrolysis of binder in stone wool samples was the major contributor for increased total mass loss and internal temperature rise (see peak temperatures at 25 kW/m^2 and 30 kW/m^2 in Table 3.3). Physical evidence of binder pyrolysis was also demarcated by the brown to orange tint seen on post–exposure samples depicted in Figure 3.6. Above 500°C, gaseous pyrolysis products liberated from thermally decomposing binder were oxidized. This threshold temperature appeared in peak and end–of–test exposed surface temperatures for 30 kW/m^2 through 50 kW/m^2 heat flux, and as end–of–test temperature for even at the centre of the specimen for 60 kW/m^2 exposure. Oxidation of organic matter was associated with compromised stone wool rigidity; this was extensively demonstrated for the case of post 40 kW/m^2 heat flux exposure. At temperatures $\geq$ 650°C, crystallization of siliceous species occurred. This could be seen in the peak temperatures tabulated in Table 3.3 for the cases of 60 kW/m^2 and 75 kW/m^2. The mineral fibres in the affected regions were characterized by the taupe colour and were easily disintegrated as previously discussed in greater detail.

Polyisocyanurate Insulation

Results of cone calorimeter tests conducted on polyisocyanurate insulation samples are presented in Figures 3.9 through 3.12. The specimens were subjected to eight levels of incident heat flux and measurements of mass remaining versus time, time–resolved heat release rate per unit area as well as time–histories of specimen centre temperature profiles were recorded during each test. Polyisocyanurate samples did not ignite when subjected to heat flux levels below 50 kW/m^2. As a result, the measured heat release rate from tests conducted at 15, 20, 25, 30 and 40 kW/m^2 flux was below the threshold of 30 kW/m^2 heat release rate per unit area (HRRPUA) resolution of the cone calorimeter [162] for most of the test. Thus, time–resolved profiles of HRRPUA are only shown for tests performed under 50, 60, and 75 kW/m^2 external heat flux (Figure 3.11c). Time–varying plots of mass remaining and specimen mid–depth temperatures are presented separately for tests conducted at below and above 50 kW/m^2 heat flux; these are given in Figures 3.9a–3.9b and 3.11a–3.11b, respectively. For tests conducted at $<$ 50 kW/m^2 heat flux, specimens were subjected to 10 minutes (600 seconds) of radiant heating, whereas for cases of flaming combustion of polyisocyanurate insulation, the tests were concluded 120 seconds after extinction of visible flames as previously outlined in Section 3.1. In the latter case, the test duration was at most 300 seconds.

In this section, the cone calorimeter test results are first discussed for experiments conducted under $<$ 50 kW/m^2 exposure, while subsequent paragraphs present data pertaining to the tests performed under radiant heating of above 50 kW/m^2 heat flux.

The results of cone calorimeter testing of polyisocyanurate insulation specimens under incident heat flux exposures of 15 kW/m^2 through 40 kW/m^2 are presented in Figure 3.9, where time–histories of mass loss and temperatures recorded at the specimen's mid–depth are shown separately in Figures 3.9a and 3.9b, respectively.

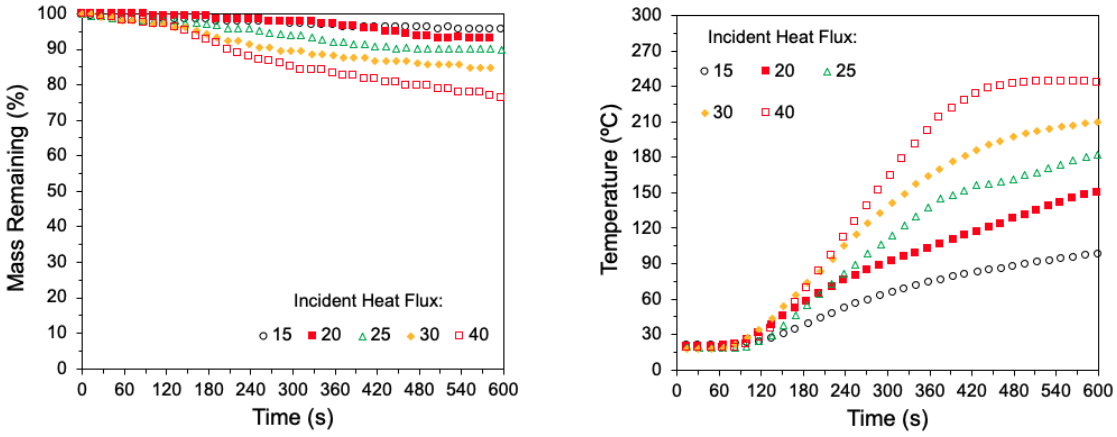

(a) (b)

Figure 3.9: Averaged time–resolved traces of a) mass remaining and b) slab centre temperature profiles for polyisocyanurate insulation tested in the cone calorimeter below 50 kW/m^2 flux

Table 3.4: End–of–test total mass loss of polyisocyanurate insulation samples subjected to below 50 kW/m^2 heat flux exposure in the cone calorimeter

Incident Heat Flux (kW/m^2)	Total Mass Loss (%)
15	4.3 ± 0.4
20	6.9 ± 0.3
25	9.7 ± 0.3
30	14.6 ± 0.5
40	22.5 ± 0.9

As can be seen from Figure 3.9a, only a small portion of the initial mass of the sample was consumed upon completion of tests conducted at below 50 kW/m^2 incident heat flux. As shown in Table 3.4, the total mass loss increased with increasing level of imposed heat flux from about 4% for 15 kW/m^2 to 23% at 40 kW/m^2 heat flux. Intermediate values of approximately 7% and 15% were computed for 20 kW/m^2 and 30 kW/m^2, respectively. These values of mass loss likely occurred for the following two reasons:

- first, due to the presence of the protective layer (foil facer) the foam core was shielded from the incident heat flux, an effect that was more pronounced throughout radiant heating under 15 kW/m^2 – 25 kW/m^2 heat flux, and in the early stages of the tests conducted at 30 kW/m^2 and 40 kW/m^2 flux; and
- secondly, due to charring of the foam core of the samples, and effect observed for experiments under exposure to 30 kW/m^2 and 40 kW/m^2 incident heat flux.

As can be seen from Figure 3.9, after an initial period of exposure, the mass loss of the sample and the temperature at the centre of the sample exhibited fairly linear profiles with increasing time. As anticipated, both increased with increasing level of external heat flux as well:

- for the case of 15 kW/m^2 flux, the mass loss rate was 0.0008 g/s and rate of temperature rise was 0.15°C/s;
- for exposure to 20 kW/m^2 heat flux, the rates of mass loss and temperature rise were 0.0014 g/s and 0.24°C/s, respectively; and
- for heat flux of 25 kW/m^2, the specimen mass loss and temperature rise rates of 0.0021 g/s and 0.32°C/s were calculated.

Under the steady increases in temperature shown in Figure 3.9b, temperatures at the centre of the polyisocyanurate slab by the end of the 600–second heating period under exposure to 15 kW/m^2, 20 kW/m^2, and 25 kW/m^2 flux were still fairly low, approximately 95°C, 148°C, and 180°C, respectively. Since the overall intensity of gaseous pyrolysate generation was low at lower internal sample temperatures, the total mass loss associated with thermal degradation of foam and subsequent liberation of volatiles from specimen body was expected to be relatively small at these lower levels of incident heat flux. This was consistent with the low values of total mass loss noted above.

The low observed rates of mass loss also result from secondary effects related to the structure of the foam itself, as well as the protective foil layer on the exposed surface of the polyisocyanurate sample. When subjected to an external radiant heat flux, as the interior of the polyisocyanurate samples heated up they did not reach the 300°C – 370°C temperatures that have been associated with the onset of significant pyrolysis [154]. Further,the closed–cell structure of polyisocyanurate insulation tended to limit the circulation of the small quantities of gases that might be generated within the specimen as well. Finally, the protective foil layer, which remained intact under incident heat flux from 15 kW/m^2 through 25 kW/m^2, might had trapped any gases that were generated within the sample core. Should the integrity of the protective layer be compromised, which tended to occur at $\geq$ 30 kW/m^2 heat flux, the closed–cell structure of the foam core may still inhibit escape of accumulated gases, but without the foil covering the potential for escape would be less restricted. In all cases, under continued exposure, some volatiles could escape through the open sides of the foam layer of the present samples under exposure to 15 kW/m^2 – 25 kW/m^2 heat flux, this was likely what resulted in the recorded mass loss.

When subjected to incident heat flux levels of 30 kW/m^2 and 40 kW/m^2, the behaviour of polyisocyanurate samples during the early stages of the tests was similar to that described for the 15 kW/m^2 – 25 kW/m^2 heat flux cases. The samples heated up and volatile gases were initially trapped between the protective foil layer and the surface of the foam. As the interior temperature of the sample further increased, the rate of vaporization intensified and the volume of gas accumulated within the sample volume increased. Trapped gases increased in pressure within the foam core and under the foil leading to lifting, detaching and cracking of the facer as seen in Figure 3.10 which illustrates the post–test state of polyisocyanurate specimens exposed to 30 kW/m^2 and 40 kW/m^2 heat flux. As can be seen from Figure 3.10b, large sub–surface bubbles formed on the left side of the exposed foil facer surface due to pressure exerted by the accumulation of pyrolysis gases. The size and frequency of such bubbles across the foil facer increased with increasing heat flux as more pockets of accumulated hot volatile gases appeared. This can be seen for the case of exposure of a sample to 40 kW/m^2 in Figure 3.10c. At the same time, the integrity of the foil facer also deteriorated with increasing external heat flux, as shown in Figure 3.10 for exposures to 30 kW/m^2 flux, and which was further exacerbated and manifested also by cracking of the bubbled regions at 40 kW/m^2 heat flux. For both 30 kW/m^2 and 40 kW/m^2 heat flux exposures, discolouration of polyisocyanurate specimens was also observed as shown in the lateral side images presented in Figure 3.10.

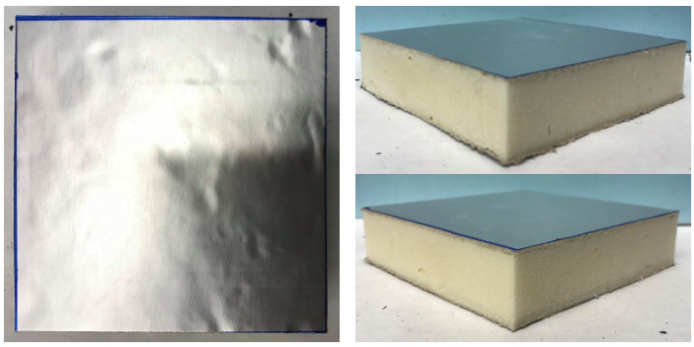

(a) virgin material

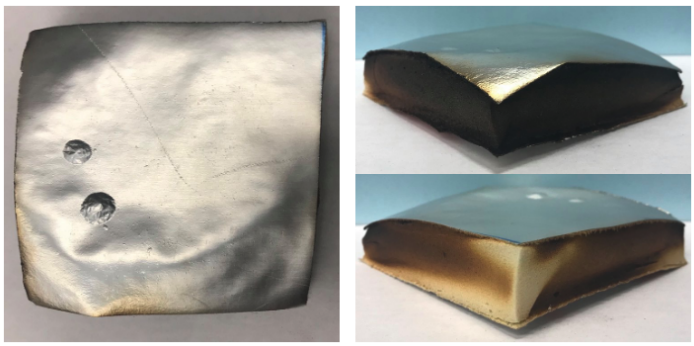

(b) 30 kW/m^2

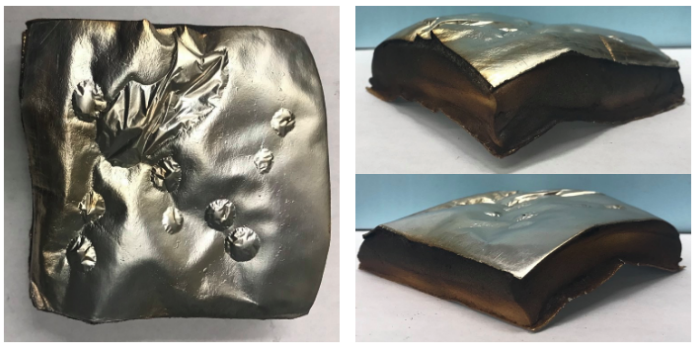

(c) 40 kW/m^2

Figure 3.10: The state of exposed surface and lateral sides of polyisocyanurate insulation samples (a) before a test and after exposure to (b) 30 kW/m^2 and (c) 40 kW/m^2 of external incident heat flux in the cone calorimeter

The residues remaining after the experiments suggest a black, porous char structure, typical for polyisocyanurate insulation [154]. Due to the formation of char, the entire mass of the polyisocyanurate samples was not consumed at the completion of the test. Instead, the total mass loss for 30 kW/m^2 was about 15% and for 40 kW/m^2 heat flux was around 23%. Similar to the cases of 15 kW/m^2 – 25 kW/m^2 heat flux exposures, the mass loss for 30 kW/m^2 and 40 kW/m^2 exposures tended to follow a fairly linear decrease with time, with mass loss rates of 0.0029 g/s and 0.0045 g/s, respectively. The rate of temperature rise recorded by the centre thermocouple was also fairly constant: 0.49°C/s and 0.72°C/s for the cases of 30 kW/m^2 and 40 kW/m^2 flux, respectively. Referring to Figure 3.9b, the quasi–steady state temperatures attained at the centre of the polyisocyanurate slab after a 600–second long heating period under exposure to 30 kW/m^2 and 40 kW/m^2 flux were higher than those at the lower levels of flux, approximately 205.8°C ± 1.6°C and 243.9°C ± 0.4°C, respectively.

The polyisocyanurate insulation samples ignited and burned when subjected to external heat flux levels of 50 kW/m^2 through 75 kW/m^2 in the cone calorimeter. The results from these experiments (time–dependent traces of mass remaining, slab centre temperature, and heat release rate) are presented in Figure 3.11.

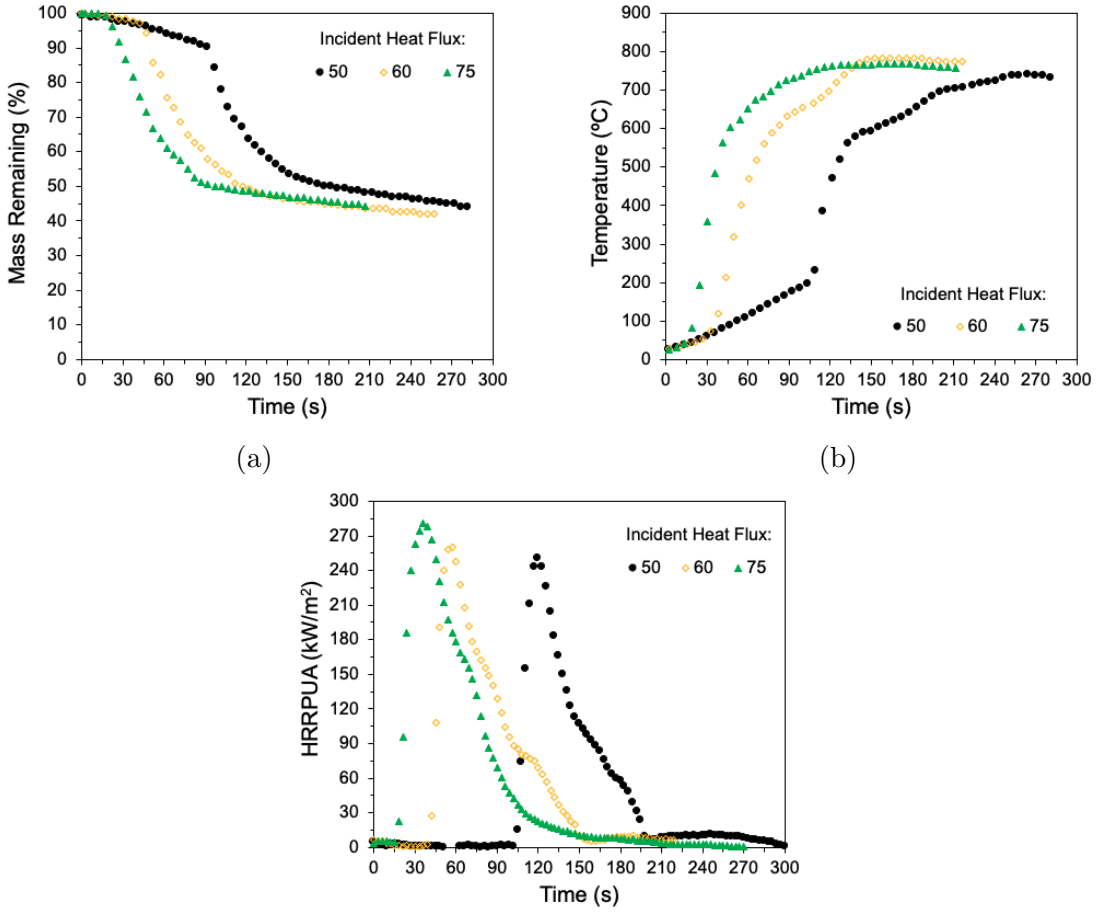

Figure 3.11: Averaged time–resolved traces of a) mass remaining, b) slab centre temperature and c) heat release rate per unit area profiles for polyisocyanurate insulation tested in the cone calorimeter above 50 kW/m^2 flux

The polyisocyanurate specimens ignited at 108, 42, and 18 seconds following the onset of exposure for tests performed at 50 kW/m^2, 60 kW/m^2, and 75 kW/m^2 heat flux. The duration of sustained burning shortened with increasing levels of external irradiation: 119 seconds for 50 kW/m^2, 110 seconds at 60 kW/m^2, and 102 seconds under 75 kW/m^2 irradiance.

During the early stages of exposure (prior to ignition), the behaviour of polyisocyanurate samples was similar to that discussed for tests conducted at below 50 kW/m^2 flux. After initial heating, the integrity of the foil facer covering the exposed sample surface was severely compromised allowing the accumulated pyrolysis gases to freely escape the sample bulk. Interestingly, irrespective of the external irradiance imposed across the range of incident heat flux from 50 kW/m^2 – 75 kW/m^2, the liberation of volatile gases from the specimen body occurred at a similar, relatively steady rate of 0.011 g/s on average prior to ignition of the sample. Consistent with this, as can be seen from Figure 3.11a, comparable slopes (within 3.2%) of mass remaining traces with time were obtained up to the time of ignition. Similarly, the temperature–time profiles (Figure 3.11b) recorded at the specimen mid–depth for tests performed at 50 kW/m^2 – 75 kW/m^2 flux followed each other closely, indicating that the increase in temperature at the slab centre also occurred at a relatively steady rate of 1.02°C/s ± 0.03°C/s. When the pyrolysis gases ignited, the rates of mass loss and heat release per unit area rapidly increased. At this point also, the heat release rate sharply increased (seen in Figure 3.11c), attaining peak values around 15 seconds after ignition, followed by a progressive decay until extinction of visible flames. During the burning period:

- mass loss rates of 0.046 g/s, 0.071 g/s, and 0.076 g/s were calculated for 50 kW/m^2, 60 kW/m^2 and 75 kW/m^2 heat flux; and
- peak HRRPUA values of 250.07 kW/m^2 for 50 kW/m^2, 260.90 kW/m^2 at 60 kW/m^2, and 280.65 kW/m^2 at 75 kW/m^2 exposure were achieved.

From thermal profiles at the centre of the samples, it is seen that the slopes of temperature vs. time traces are not linear throughout the burning period: the rate of temperature rise was larger from ignition until peak HRRPUA, and then decreased during the decay phase until completion of the test at which quasi–steady state values were achieved. Rates of temperature rise during both periods, as well as the steady–state temperatures measured at the end of the test are compiled in Table 3.5.

Table 3.5: Temperature rise rates and end–of–test quasi–steady temperatures of polyisocyanurate insulation measured at the sample mid–depth above 50 kW/m^2 incident heat flux

Incident Heat Flux (kW/m^2)	Rate of Temperature Rise (°C/s)		End–of–Test Temperature (°C)
	During HRRPUA Growth Phase	During HRRPUA Decay Phase	
50	8.34	1.44	737.5 ± 2.7
60	10.94	2.30	782.4 ± 0.9
75	16.77	2.78	766.5 ± 2.0

As can be seen from Table 3.5, the rates of temperature rise during both phases increased with increasing external heat flux, from about 8°C/s for 50 kW/m^2 to around 17°C/s at 75 kW/m^2 during the fire growth phase, and doubled from 1.4°C/s to 2.8°C/s during the decay phase for 50 kW/m^2 and 75 kW/m^2 flux, respectively. Upon completion of the tests, charred carbonaceous residues were left behind from burning polyisocyanurate specimen as can be seen from the post–experiment state of the samples presented in Figure 3.12. Again due to char formation with the polyisocyanurate insulation material, not all of the initial sample mass was consumed by the end of the test. End–of–test total mass loss values of 55.2%, 57.5%, and 55.3% were calculated for heat exposures under 50 kW/m^2, 60 kW/m^2 and 75 kW/m^2 incident flux, respectively.

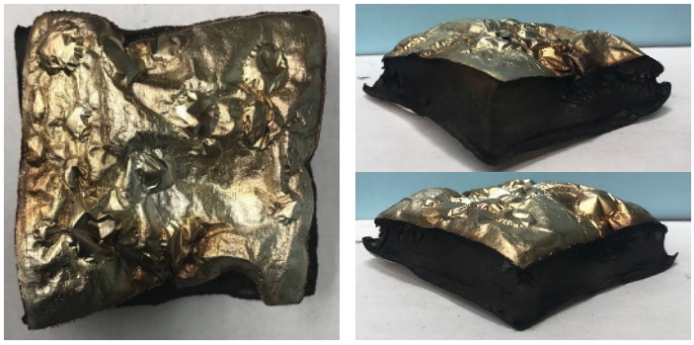

(a) 50 kW/m^2

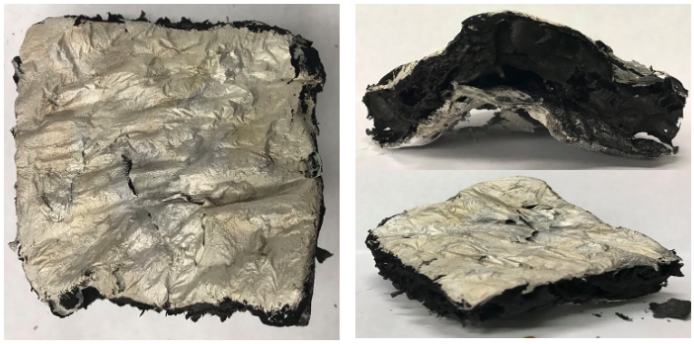

(b) 60 kW/m^2

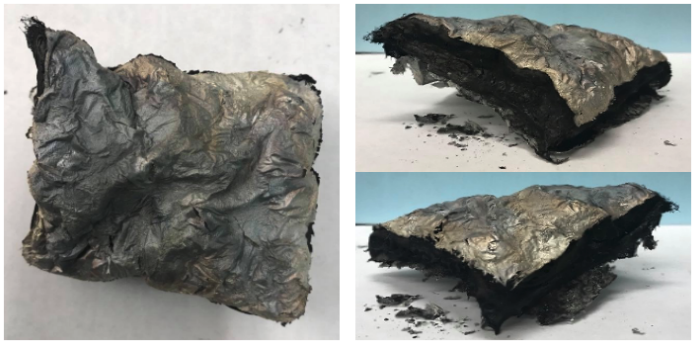

(c) 75 kW/m^2

Figure 3.12: The state of exposed surface and lateral sides of polyisocyanurate insulation samples after exposure to (a) 50 kW/m^2, (b) 60 kW/m^2 and (c) 75 kW/m^2 of external incident heat flux in the cone calorimeter

Extruded Polystyrene Insulation

Results of cone calorimeter tests conducted on extruded polystyrene insulation samples are presented in Figures 3.13 through 3.15. The specimens were subjected to eight levels of incident heat flux and measurements of mass remaining versus time, time–resolved heat release rate per unit area as well as time–histories of specimen centre temperature profiles were recorded during each test. The bulk of extruded polystyrene specimens did not ignite when subjected to heat flux levels below 40 kW/m^2. As a result, the measured heat release rate from tests conducted at 15, 20, 25, and 30 kW/m^2 flux remained below the threshold of 30 kW/m^2 heat release rate per unit area (HRRPUA) resolution of the cone calorimeter [162] for a large portion of each test. Thus, for extruded polystyrene insulation samples, time–resolved profiles of HRRPUA are only shown for tests performed under 40, 50, 60, and 75 kW/m^2 external heat flux (Figure 3.15c). The time–varying plots of mass remaining and specimen mid–depth temperatures are presented separately for tests conducted at below and above 40 kW/m^2 heat flux; these are given in Figures 3.13a–3.13b and 3.15a–3.15b, respectively. For tests conducted at $<$ 40 kW/m^2 heat flux, specimens were subjected to 10 minutes (600 seconds) of radiant heating, whereas for cases of flaming combustion of extruded polystyrene insulation samples, the tests were concluded 120 seconds after extinction of visible flames as previously outlined in Section 3.1. In the latter case, the test duration was at most 200 seconds.

In this section, the cone calorimeter test results are first discussed for experiments conducted under $<$ 40 kW/m^2 exposure, while subsequent paragraphs present data pertaining to the tests performed under radiant heating of above 40 kW/m^2 heat flux.

The results of cone calorimeter testing of extruded polystyrene specimens under incident heat flux exposures of 15 kW/m^2 through 30 kW/m^2 are presented in Figure 3.13, where time–histories of mass loss and temperatures recorded at the specimen's mid–depth are shown separately in Figures 3.13a and 3.13b, respectively.

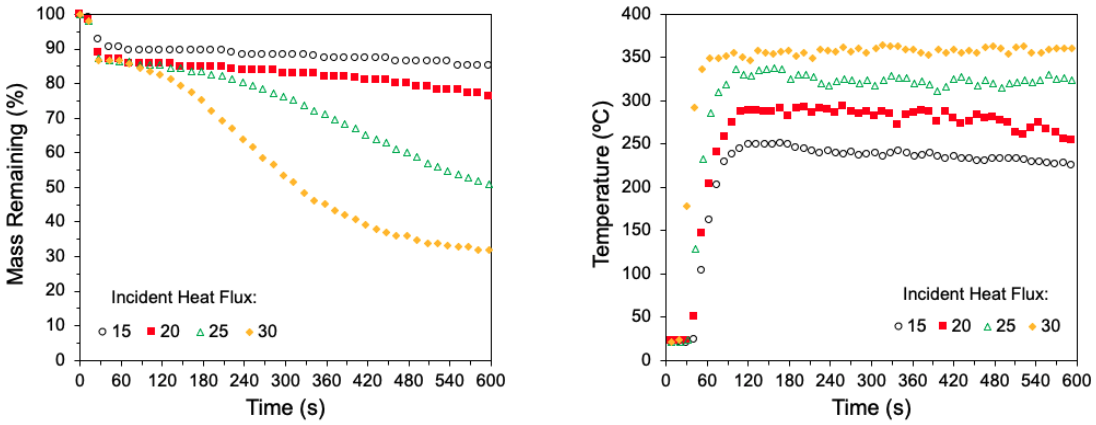

(a) (b)

Figure 3.13: Averaged time–resolved traces of a) mass remaining and b) slab centre temperature for extruded polystyrene insulation samples tested in the cone calorimeter below 40 kW/m^2 flux

When subjected to a prescribed level of irradiance from the conical heater of the cone calorimeter, extruded polystyrene insulation material softened, reduced in thickness and melted into a viscous fluid which pyrolyzed from the bottom of the sample holder. The release of volatile gases from thermally decomposing extruded polystyrene melt fluid continued until the shutters on the cone heater were closed and the specimen was removed. Consistent with there being residue from the pyrolyzing fluid melt, seen in Figure 3.14 for a sample after exposure to 15 kW/m^2 incident heat flux, not all of the sample mass was consumed by the end of a test. Instead, the total mass loss recorded for exposures to heat flux of 15 kW/m^2, 20 kW/m^2, 25 kW/m^2, and 30 kW/m^2 were 14.9%, 23.7%, 49.2%, and 68.2%, respectively. The remaining mass was in the form of a hardened residue from the melted extruded polystyrene, likely due to the transition of polystyrene to a glass state as its temperature was reduced after melting [154].

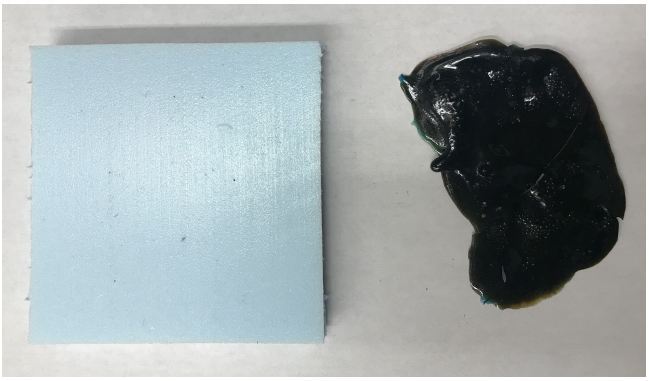

Figure 3.14: The state of the extruded polystyrene insulation sample before (left) and post–exposure (right) to 15 kW/m^2 incident heat flux in the cone calorimeter

Since extruded polystyrene samples were found to shrink very quickly when exposed to external irradiances as low as 15 kW/m^2, the measurements of temperature recorded at the mid–depth of the specimen were only relevant for a short period, primarily in the early stages of the tests. Following exposure, the solid foam reduced in thickness and the exposed surface receded towards the bottom of the sample holder. When the receding surface of the sample reached the mid–depth level, the thermocouple detached and thereafter measuring changes in the gas temperatures above the melted sample, as well as temperatures due to radiation from the cone heater. As can be seen from Figure 3.13b, the initial rise in temperature values with time are indicative of the solid–phase temperature rise while the thermocouple remains in the receding solid foam. The later portions of the temperature–time curves, where on average the temperature has reached an approximately constant value, instead provide estimates of gas–phase temperatures. The rates of temperature increase within the solid–phase before thermocouple detachment and subsequent measurements of gas–phase temperatures are complied in Table 3.6. As can be seen, the solid–phase temperature rose at rates which increased with increasing levels of external irradiance from 4.4°C/s for 15 kW/m^2 to 7.2°C/s at 30 kW/m^2 flux. Average gas–phase temperatures also increased with increasing heat flux, indicative of increasing radiation heat flux to the exposed thermocouple from the conical heater of the cone calorimeter. Consistent with this as well, the rate of reduction in sample thickness also increased with increasing incident heat flux such that the detachment of thermocouple occurred twice as fast under 30 kW/m^2 heat flux than at 15 kW/m^2.

Table 3.6: Measured solid– and gas–phase temperatures from thermally decomposing extruded polystyrene samples subjected to external incident heat flux levels of 15 kW/m^2 – 30 kW/m^2

Incident Heat Flux (kW/m^2)	Time to Thermocouple Detachment (s)	Rate of Temperature Rise in Solid–Phase (°C/s)	Temperature of Gas–Phase (°C)
15	120	4.4	233.6 ± 4.8
20	107	5.1	278.1 ± 11.3
25	98	6.5	323.9 ± 5.6
30	60	7.2	357.6 ± 3.8

As mentioned previously, the bulk of extruded polystyrene insulation ignited and burned when subjected to external heat flux levels above 40 kW/m^2. The cone calorimeter results from these experiments are presented in Figure 3.15.

The behaviour of extruded polystyrene upon exposure to external irradiance levels of $\geq$ 40 kW/m^2 flux was similar to that previously noted for the cases of 15 kW/m^2 – 30 kW/m^2. Following the onset of exposure and prior to ignition, the foam specimens collapsed and reduced in thickness as they melted and formed a viscous liquid film at the bottom of the specimen holder. The mid–depth thermocouples again detached and recorded gas–phase temperatures when the sample surface receded past their position. The rates of temperature rise prior to thermocouple detachment are presented in Table 3.7 and again increased with increasing levels of incident heat flux. As anticipated, times to centre thermocouple detachment were also considerably shorter than those for the cases of 15 kW/m^2 – 30 kW/m^2 heat flux (Table 3.6) while the rates of temperature rise were much higher.

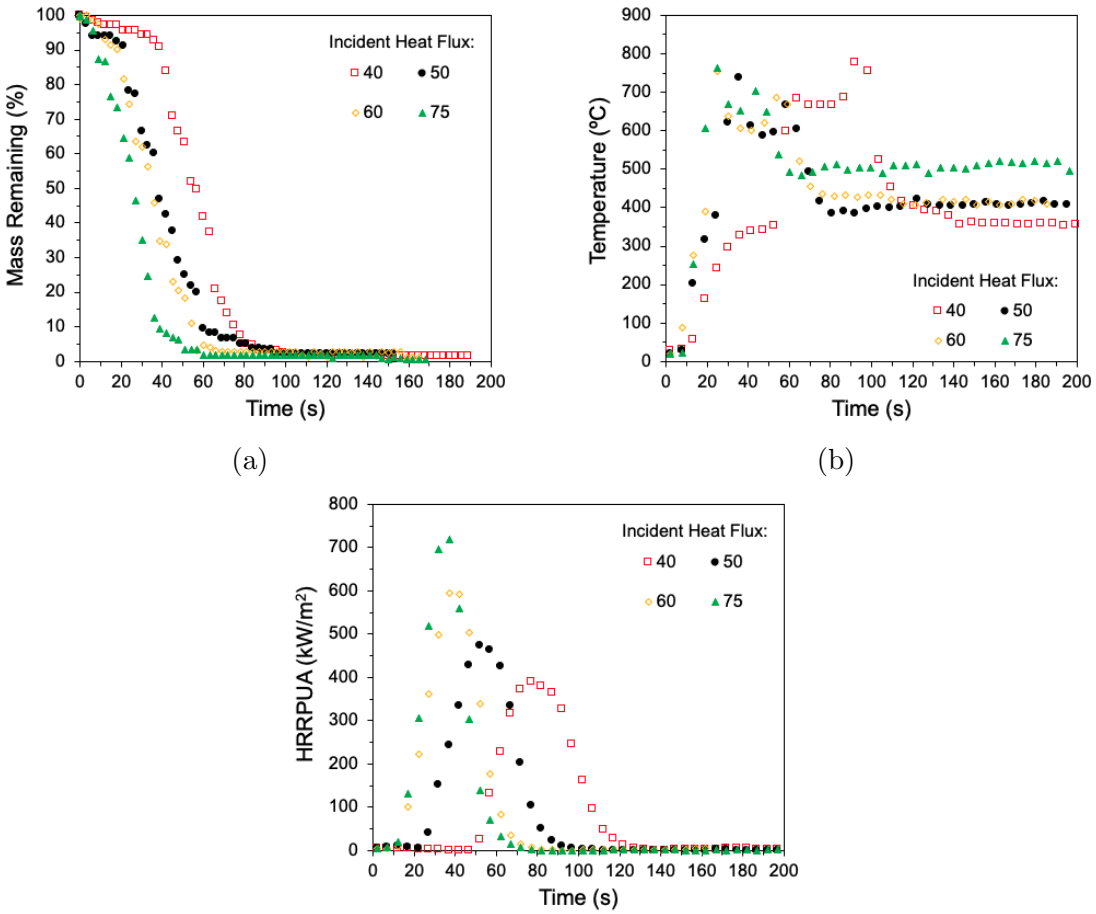

Figure 3.15: Averaged time–resolved traces of a) mass remaining, b) slab centre temperature and c) heat release rate per unit area profiles for extruded polystyrene insulation samples tested in the cone calorimeter above 40 kW/m^2 flux

Table 3.7: The temperature rise rates in the solid–phase of thermally decomposing extruded polystyrene samples as a function of external heat flux prior to detachment of centre thermocouple

Incident Heat Flux (kW/m^2)	Time to Thermocouple Detachment (s)	Rate of Temperature Rise in Solid–Phase (°C/s)
40	42	10.1
50	25	13.8
60	19	17.7
75	13	36.4

As the sample melted, it released volatile gases and, once a sufficient concentration had been liberated, they ignited above the surface of the test specimen. Times to ignition and duration of sustained flaming of extruded polystyrene samples exposed to each heat flux between 40 kW/m^2 and 75 kW/m^2 are tabulated in Table 3.8. The onset of ignition shortened with increasing level of imposed irradiance from 43 seconds at 40 kW/m^2 to 11 seconds for 75 kW/m^2. Similarly, the duration of sustained burning decreased with increasing external irradiance from 75 seconds to 36 seconds for heat flux levels of 40 kW/m^2 and 75 kW/m^2, respectively. The mid–depth thermocouple had already detached from the solid foam when ignition occurred, so was suspended in the flames that established above the burning viscous liquid. Therefore, as can be seen in Figure 3.15b, this thermocouple initially registered flame temperatures of between 600°C and 800°C during the sustained flaming period, followed by the decay in gas–phase temperatures down to quasi–steady values of 358.5°C ± 4.4°C, 405.5°C ± 9.7°C, 418.7°C ± 9.0°C, and 505.8°C ± 11.3°C under heat exposures of 40 kW/m^2, 50 kW/m^2, 60 kW/m^2, and 75 kW/m^2, respectively.

Table 3.8: Details of ignition and sustained flaming time histories from extruded polystyrene tests conducted under 40 kW/m^2 – 75 kW/m^2 heat flux exposures in the cone calorimeter

Incident Heat Flux (kW/m^2)	Time to Ignition (s)	Time to Flame–Out (s)	Duration of Sustained Flaming (s)
40	43	118	75
50	23	84	61
60	15	60	45
75	11	47	36

The time–resolved profiles of mass remaining and heat release rate per unit area of burning extruded polystyrene samples are shown in Figures 3.15a and 3.15c. Referring to these figures, the following observations can be made related to the characteristics of the sustained burning period:

- under exposure to 40 kW/m^2 heat flux, the extruded polystyrene samples burned with a mass loss rate of 0.14 g/s and reached a peak HRRPUA of 389.84 kW/m^2;
- when exposed to 50 kW/m^2 incident heat flux, the mass loss rate was 0.15 g/s and peak HRRPUA was 472.95 kW/m^2;
- for the case of 60 kW/m^2 flux, the mass loss rate and peak HRRPUA were 0.16 g/s and 595.38 kW/m^2, respectively; and
- when subjected to incident irradiance of 75 kW/m^2, the mass loss rate of the specimen was 0.19 g/s while a maximum HRRPUA of 719.58 kW/m^2 was registered shortly after the onset of ignition.

Consistent with expectations, both the mass loss rate and the peak HRRPUA increased with increasing external heat flux. As can be seen from Figure 3.15a, virtually all of the sample mass (98.6% on average) was consumed during burning of the specimens, leaving a residue of only 0.1 g in mass. Observations in this work are in good agreement with literature values for thermal degradation and flaming combustion of extruded polystyrene [110, 167].

Weather Resistant Barrier and Oriented Strand Board

It was originally intended to subject individual samples of weather resistant barrier (house wrap) and oriented strand board to the eight prescribed levels of incident heat flux separately. However, upon completion of the preliminary round of testing, it was found that the house wrap used in this study shrank immediately following the onset of exposure leaving only a teardrop of material as shown in Figure 3.16 for the case of 40 kW/m^2 heat flux exposure. Since minimal effluent was released from the thermally decomposing house wrap, no ignition was observed in tests conducted at external irradiances of 15 kW/m^2 through 75 kW/m^2 heat flux. Thus, the house wrap and oriented strand board samples were tested together as a composite. Consistent with their intended end use in construction, a layer of house wrap was placed over an oriented strand board slab and secured around the sides with sheathing tape as depicted in Figure 3.17. The composite samples were then subjected to prescribed levels of external incident heat flux with the house wrap side facing the conical heater of the cone calorimeter. Results of cone calorimeter tests conducted on weather resistant barrier and oriented strand board composites are presented in Figures 3.18 through 3.20. The composite specimens were subjected to eight levels of incident heat flux, 15 kW/m^2 through 75 kW/m^2, and measurements of mass remaining versus time, time–resolved heat release rate per unit area as well as time–histories of oriented strand board specimen centre temperature profiles were recorded during each test. Composite samples did not ignite when subjected to heat flux levels below 30 kW/m^2. As a result, the measured heat release rate from tests conducted at 15, 20, and 25 kW/m^2 flux were below the threshold of 30 kW/m^2 heat release rate per unit area (HRRPUA) resolution of the cone calorimeter [162]. Time–resolved profiles of HRRPUA are thus only shown for tests performed under 30, 40, 50, 60, and 75 kW/m^2 external heat flux (Figure 3.20c). The time–varying plots of mass remaining and oriented strand board mid–depth temperatures are presented separately for tests conducted at below and above 30 kW/m^2 heat flux; these are given in Figures 3.18a–3.18b and 3.20a–3.20b, respectively. For tests conducted at < 30 kW/m^2 heat flux, specimens were subjected to 15 minutes (900 seconds) of radiant heating, whereas for cases of flaming combustion of house wrap and oriented strand board composites, the tests were concluded 120 seconds after extinction of visible flames as previously outlined in Section 3.1. In the latter case, the test duration was at most 900 seconds.

In this section, the cone calorimeter test results are first discussed for experiments conducted under < 30 kW/m^2 exposure, while subsequent paragraphs present data pertaining to the tests performed under radiant heating of above 30 kW/m^2 heat flux.

Figure 3.16: The state of the weather resistant barrier sample before (left) and post–exposure (right) to 40 kW/m^2 incident heat flux in the cone calorimeter

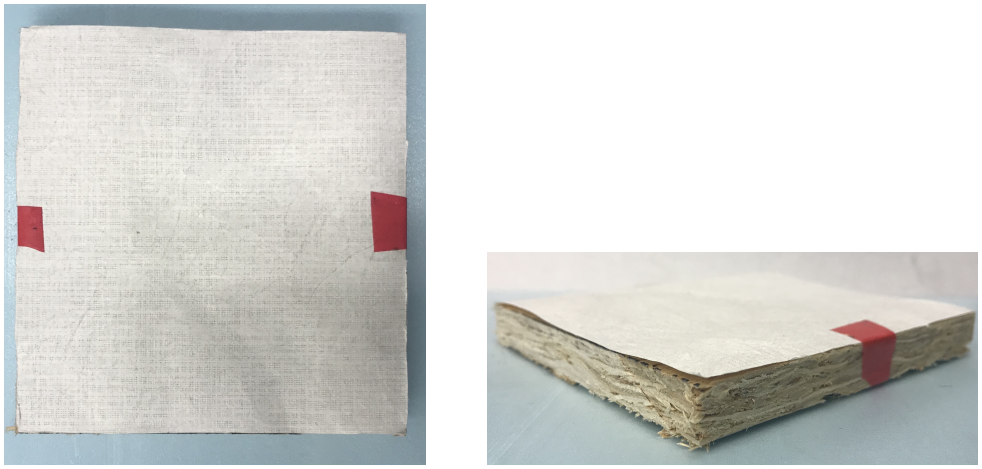

(a) (b)

Figure 3.17: Photograph of a house wrap and oriented strand board composite sample before testing: a) top (exposed surface) and b) side views

The results of cone calorimeter testing of house wrap and oriented strand board composite specimens under incident heat flux exposures of 15 kW/m^2 through 25 kW/m^2 are presented in Figure 3.18, where time–histories of mass loss and temperatures recorded at the oriented strand board slab mid–depth are shown separately in Figures 3.18a and 3.18b, respectively.

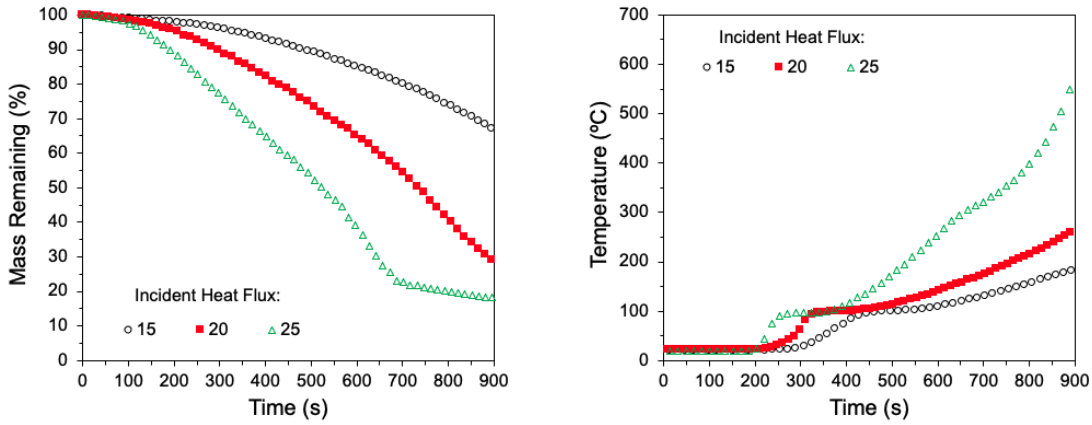

(a) (b)

Figure 3.18: Averaged time–resolved traces of a) mass remaining and b) slab centre temperature for house wrap and oriented strand board composites tested in the cone calorimeter below 30 kW/m^2 flux

When subjected to 15 kW/m^2 through 25 kW/m^2 of external irradiance, the layer of weather resistant barrier quickly shrank and melted away from the centre toward the edges of the composite sample. This left the underlying oriented strand board face exposed to the conical heater within seconds following the onset of exposure. The oriented strand board slab then began to heat with the midpoint thermocouple registering rates of temperature rise of 0.51°C/s for 15 kW/m^2, 0.78°C/s for 20 kW/m^2, and 1.11°C/s for 25 kW/m^2 heat flux until the temperatures reached a value of 98.3°C $\pm$ 1.4°C independent of the imposed external heat flux. The plateau, which corresponded to liberation of moisture from the sample, is clearly seen in Figure 3.18b, between test times of 440–560 seconds, 320–420 seconds, and 270–350 seconds for radiant heat flux levels of 15 kW/m^2, 20 kW/m^2, and 25 kW/m^2, respectively. The rate of evaporation of entrained water intensified with increasing incident heat flux and resulted in a mass loss of approximately 2% for each sample. This was consistent with levels of moisture content seen in oriented strand board specimens conditioned in similar environments prior to testing in the cone calorimeter [115].

After dehydration, the strand board samples thermally decomposed, releasing pyrolysis gases from both the wood strands and the water–resistant adhesive resin that held the strands together. During decomposition, the following rates of mass loss and interior temperature rise were recorded:

- 0.03 g/s and 0.32°C/s for the case of 15 kW/m^2 heat flux;
- 0.05 g/s and 0.39°C/s under exposure to 20 kW/m^2 irradiance; and
- 0.08 g/s and 0.73°C/s when subjected to 25 kW/m^2 incident heat flux.

As the test progressed, degradation of the oriented strand board sample surface continued, marked by partial delamination of wood strands on the exposed face and dark brown and black discolouration. Near the end of the 900–second radiant heating period, a carbon layer had also formed on the exposed face of the strand board, leading to post–test samples similar to that depicted in Figure 3.19 for exposure to 25 kW/m^2 heat flux. The residual char encompassed almost all of the exposed surface; due to this, not all of the specimen mass was consumed by the end of the experiments. Instead, the total mass loss calculated at the end of each test was 64.6%, 80.2%, and 87.6% for exposure to 15 kW/m^2, 20 kW/m^2, and 25 kW/m^2 heat flux, respectively.

Figure 3.19: The state of the oriented strand board sample post exposure to 25 kW/m^2 incident heat flux in the cone calorimeter

Ignition of house wrap and oriented strand board composite samples occurred during exposure to external irradiance levels of $\geq$ 30 kW/m^2 heat flux. Time dependent traces of mass remaining, measured temperature at the strand board mid–depth, as well as heat release rate per unit exposed specimen area are presented in Figures 3.20a, 3.20b, and 3.20c, respectively.

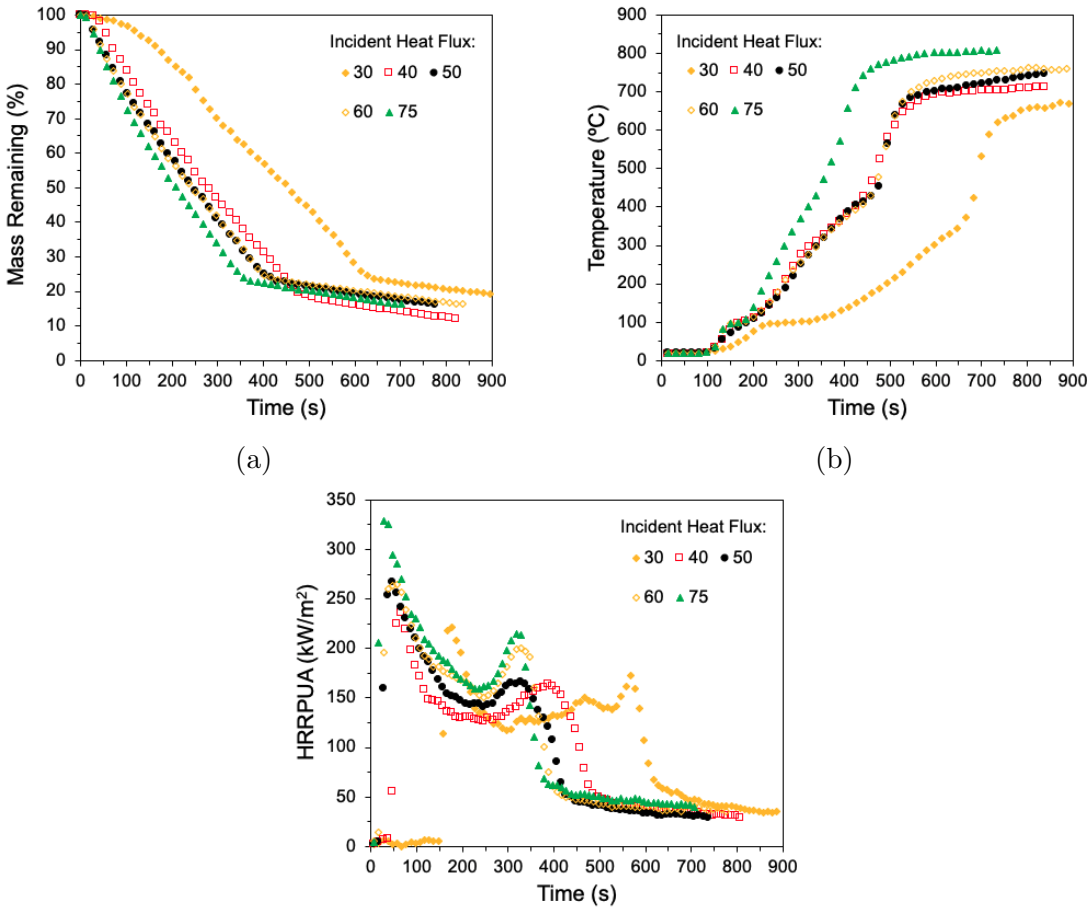

Figure 3.20: Averaged time–resolved traces of a) mass remaining, b) slab centre temperature and c) heat release rate per unit area profiles for house wrap and oriented strand board assemblies tested in the cone calorimeter above 30 kW/m^2 flux

Under radiant heating levels of 30 kW/m^2 – 75 kW/m^2, the weather resistant barrier again quickly shrunk away leaving the oriented strand board sample surface exposed as noted for heat flux exposures of 15 kW/m^2 through 25 kW/m^2. The interior temperature of the sample then increased to 98.4°C ± 2.1°C leading to evaporation of moisture in the sample. The dehydration period lasted for about 70 seconds at 30 kW/m^2 heat flux and around 40 seconds at 75 kW/m^2 and again resulted in approximately 2% decrease in the sample mass. Pyrolysis gases subsequently formed and ignited as tabulated in Table 3.9. As expected, the onset of ignition shortened with increasing level of imposed irradiance from 152 seconds at 30 kW/m^2 to 7 seconds for 75 kW/m^2 heat flux. Similarly, the duration of sustained burning also decreased from 475 seconds to 360 seconds with increasing external irradiance levels of 30 kW/m^2 and 75 kW/m^2, respectively.

Table 3.9: Details of ignition and sustained flaming time histories from house wrap and oriented strand board composite tests conducted under 30 kW/m^2 – 75 kW/m^2 heat flux exposures in the cone calorimeter

Incident Heat Flux (kW/m^2)	Time to Ignition (s)	Time to Flame–Out (s)	Duration of Sustained Flaming (s)
30	152	627	475
40	45	501	456
50	21	427	406
60	16	398	382
75	7	367	360

Time–resolved heat release rate curves shown in Figure 3.20c exhibit sharp increases in measured HRRPUA to initial peak values within 29 ± 7 seconds of ignition across exposures from 30 kW/m^2 – 75 kW/m^2 flux. The initial sharp peak was followed by a period of decay and then quasi–steady burning, which shortened with increasing levels of incident heat flux. After this, a second peak occurred before extinction of visible flames. Peak values of measured heat release rate (PHRRPUA) and times to peak values after ignition, as well as average heat release rate calculated for the period of quasi–steady burning, are presented in Table 3.10 below. As can be seen, the magnitude of the initial peak tended to increase with increasing external irradiance from about 222 kW/m^2 for 30 kW/m^2 heat flux to around 325 kW/m^2 at 75 kW/m^2. Similarly, the average HRRPUA during the quasi–steady burning period also increased with increasing heat flux from 133 kW/m^2 to 167 kW/m^2 at 30 kW/m^2 and 75 kW/m^2 heat flux, respectively.

Table 3.10: Details of measured heat release rates from oriented strand board specimens undergoing flaming combustion in the cone calorimeter

Incident Heat Flux (kW/m^2)	Peak HRRPUA (kW/m^2)		Time to PHRRPUA After Ignition (s)		Average HRRPUA Quasi–Steady Burning (kW/m^2)
	Peak 1	Peak 2	Peak 1	Peak 2	
30	221.8	173.1	25	415	132.8 ± 9.1
40	235.7	163.4	22	342	133.6 ± 6.1
50	266.9	166.2	26	306	145.0 ± 4.4
60	264.1	200.7	41	311	164.0 ± 9.7
75	325.3	214.7	30	310	167.2 ± 7.5

The initial peak observed on time–resolved traces of HRRPUA was generally attributed to the rapid increase in heat release rate due to initial combustion of uncharred wood. This then reduced as the protective char layer formed on the surface of the oriented strand board [114]. Enough flammable gases were still produced during surface charring to support a period of quasi–steady flaming combustion. As the depth of char penetrated further into the pyrolyzing strand board bulk, the insulating effect resulted in decreased generation and flow of pyrolysis gases coupled to impeded mixing of those gases with the ambient oxygen needed to support combustion.

As time progressed, however, the equilibrium shifted and ambient oxygen was better able penetrate through the cracks formed within the carbonized layer on the specimen surface. This increased influx of oxygen and its reaction with the remaining pyrolysis gases resulted in the increase in measured HRRPUA corresponding to the second peak observed in the time dependent traces of recorded heat release rates. This was not sufficient to sustain additional formation of pyrolysis gases nor mixing with oxygen, and led to the subsequent extinction of the flames over the sample.

Rates of mass loss and temperature rise at the strand board specimen mid–depth, tabulated in Table 3.11, vary in a manner consistent with the changes in the magnitude of the measured HRRPUA throughout the sustained flaming period.

Table 3.11: Mass loss rates and specimen centre temperature rise rates of oriented strand board samples undergoing flaming combustion in the cone calorimeter

Incident Heat Flux (kW/m^2)	Mass Loss Rate (g/s) During			Rate of Temperature Rise (°C/s) During		
	Uncharred Wood Oxidation	Quasi Steady Burning	Charred Wood Oxidation	Uncharred Wood Oxidation	Quasi Steady Burning	Charred Wood Oxidation
30	0.102	0.091	0.098	0.99	0.76	2.31
40	0.144	0.092	0.109	1.45	0.91	2.49
50	0.168	0.101	0.121	1.53	1.03	3.13
60	0.175	0.108	0.122	1.57	1.11	3.19
75	0.205	0.113	0.132	2.26	2.00	3.33

As can be seen from Table 3.11, the rates of mass loss and temperature rise during each period increased with increasing level of external incident heat flux: from 0.102 g/s and 0.99°C/s at 30 kW/m^2 to 0.205 g/s and 2.26°C/s at 75 kW/m^2 during uncharred wood oxidation; from 0.091 g/s and 0.76°C/s at 30 kW/m^2 to 0.113 g/s and 2.0°C/s at 75 kW/m^2 during quasi–steady burning; and from 0.098 g/s and 2.31°C/s at 30 kW/m^2 to 0.132 g/s and 3.33°C/s at 75 kW/m^2 during char oxidation. In general, the following relationships in measured mass loss rate ($\dot{m}$) and specimen centre temperature rise rate $\left(\frac{dT}{dt}\right)$ are true irrespective of the imposed external irradiation:

- $\dot{m}_{\text{uncharred wood oxidation}} > \dot{m}_{\text{quasi–steady burning}} > \dot{m}_{\text{char oxidation}}$, and
- $\frac{dT}{dt}_{\text{uncharred wood oxidation}} > \frac{dT}{dt}_{\text{quasi–steady burning}} > \frac{dT}{dt}_{\text{char oxidation}}$

Upon extinction of visible flames, the charred residues continued to support glowing combustion until specimens were removed from the load cell of the cone calorimeter and extinguished manually in the fume hood. Through this smouldering period a relatively stable rate of heat release (37 kW/m^2 ± 3.8 kW/m^2) was recorded across all tests conducted at external incident heat flux levels of 30 kW/m^2 through 75 kW/m^2. The resulting post–exposure states of all oriented strand board specimens were practically indistinguishable from one another and were well represented by the photograph in Figure 3.19. Despite this, some differences were seen in terms of the total quantity of sample mass consumed and interior sample temperatures across the tests. The total mass loss and quasi–steady slab centre temperatures recorded at the end of the heating periods were 80.6% and 667.4°C ± 6.2°C for the case of 30 kW/m^2 heat flux exposure and higher at 83.7% and 803.8°C ± 3.8°C for 75 kW/m^2 flux with intermediate values of 84.0% and 735.0°C ± 8.2°C registered for the 50 kW/m^2 heat flux case.

3.4.2 Performance of Stacked Wall Sandwiches

Sandwich #1 – Rigid Stone Wool Insulation

Results of cone calorimeter tests conducted on Sandwich #1 samples are presented in Figures 3.21 through 3.24. Vinyl siding, stone wool insulation, weather resistant barrier and oriented strand board were stacked to form a (scaled) section of an exterior wall assembly and instrumented as outlined in Section 3.3. Separate instrumented sandwich samples were then subjected to low (15 kW/m^2) and high (50 kW/m^2) levels of incident heat flux in the cone calorimeter. Temperature–time histories through the sandwich assemblies were recorded during each test at three locations: on the unexposed side of vinyl siding, at the mid-depth in the centre of the stone wool and at the mid-depth in the centre of the oriented strand board. The sandwich assemblies did not ignite when exposed to 15 kW/m^2 incident flux for 30 minutes. On the contrary, sandwich assemblies exposed to 50 kW/m^2 did ignite so that these tests continued for 20 minutes, beyond extinction of the visible flames to capture thermal profiles through the sandwich after it underwent flame combustion.

The post–exposure state of a Sandwich #1 sample subjected to an incident heat flux of 15 kW/m^2 is shown in Figure 3.21. Consistent with results seen for vinyl siding when tested as an individual material, Figure 3.3b, the layer of vinyl siding on the exposed surface charred leaving behind a carbon–rich residue. Under heating, the siding material shrunk, buckling towards the centre of the exposed sandwich surface. This left the underlying stone wool partially exposed to incident heat flux from the conical heater within a minute after the onset of exposure. As a result, the stone wool insulation discoloured across the exposed slab and down the sides, seen as tones of light yellow to orange to brown in Figure 3.21b and indicating thermal degradation following the exposure. This was again consistent with signs of thermal exposure and binder decomposition noted previously in after test samples of single–layer stone wool insulation following exposure to 15 kW/m^2 flux (Figure 3.6b). No noticeable changes in colour, geometry or charring were evident in the post–exposure state of either the weather resistant barrier or oriented strand board layers as a result of these layers being insulated from the incident radiation by the 32 mm thick stone wool slab of insulation.

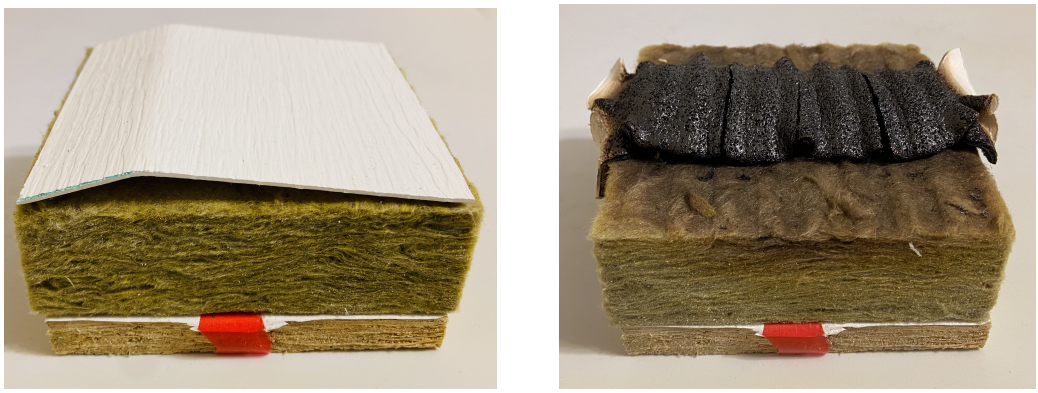

(a) (b)

Figure 3.21: The state of Sandwich #1 samples (a) before and (b) after exposure to 15 kW/m^2 external incident heat flux in the cone calorimeter

To further understand the effects of each layer on the overall thermal performance of the sandwich assembly under exposure to 15 kW/m^2 incident heat flux, it is of interest to examine the time–histories of temperature that were recorded at the three measurement positions within the sandwich bulk. These are shown in Figure 3.22a with overplots of the temperature–time profiles obtained for the layer materials in individual tests (Figures 3.22b, 3.22c, and 3.22d for vinyl siding, stone wool insulation, and oriented strand board, respectively). Discussions regarding the thermal decomposition of each layer, their impact on recorded rates of temperature rise and subsequent temperature profiles of the heated sandwich components are presented below.

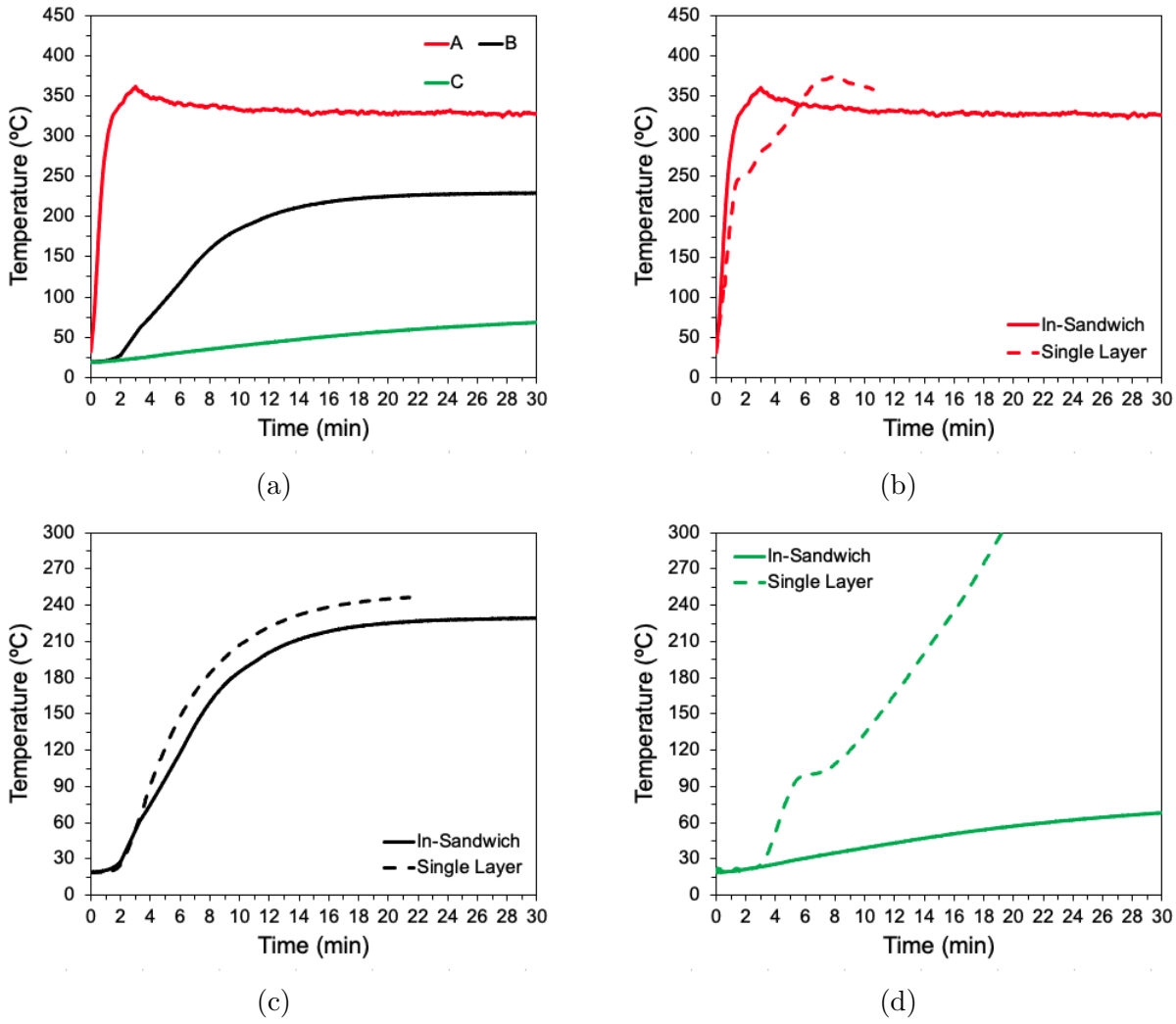

Figure 3.22: Averaged time–resolved profiles of temperatures measured a) along the bulk–path of Sandwich #1 assembly (A – unexposed surface of vinyl siding, B – centre/mid–depth of stone wool insulation bulk, C – centre/mid–depth of oriented strand board slab) and comparison of temperature–time profiles across each layer of b) vinyl siding, c) stone wool insulation, and d) oriented strand board when tested individually versus in combination with underlying layers in sandwich assemblies under external irradiance of 15 kW/m^2 flux in the cone calorimeter

As can be seen Figure 3.22a, the thermocouple affixed to the unexposed vinyl siding surface registered a rapid increase in temperature shortly after the onset of exposure, with a temperature rise rate of 4.97°C/s until charring of vinyl siding was observed at around 250°C. Yu et al. reported similar threshold temperatures flagging the onset of char promotion in polyvinyl chloride samples [51]. Upon initiation of charring, the rate of temperature rise slowed considerably, to around 0.74°C/s, due to the insulating effect of the char layer. When the char extended through the thickness of the siding material, the backside temperature plateaued at 327.4°C ± 2.2°C for the remainder of the radiant heat exposure. While similar processes were observed in small–scale testing of the single–layer vinyl siding material under 15 kW/m^2 heat flux exposure, when the material was incorporated into a sandwich assembly, the rates of temperature rise on the unexposed surface were twice as high for periods prior to and after the onset of char formation. This can also be seen from the differences in the slopes of temperature–time traces shown in Figure 3.22b. In the sandwich configuration, the underlying layer of stone wool would provide increased insulation to the backside of the vinyl siding, causing the unexposed surface temperatures to increase more quickly compared to the results from single–layer tests.

The increase in measured temperature at the centre of the stone wool slab begins about two minutes following the onset of temperature rise on the unexposed vinyl siding surface. Temperature gradually increased at a rate of 0.35°C/s, and reached a plateau of 228.7°C ± 2.0°C after 16 minutes of heating. Despite the similarity in the shapes of recorded temperature–time traces between tests on individual insulation samples and in–sandwich insulation layers shown in Figure 3.22c, the rate of temperature rise at the centre of stone wool insulation was 1.7 times lower when it was incorporated into a sandwich assembly. Similarly, the steady–state temperatures measured at the slab centre near the end of the radiant heating period during in–sandwich tests were also lower, by 18°C on average. The observed differences were likely attributed to the shielding effect of the charred vinyl siding residue located centrally on the exposed surface of the stone wool insulation (Figure 3.21b) which in the case of the sandwich assembly tests partially covered and insulated the exposed face.

Beneath the stone wool insulation lay a layer of weather resistant barrier and oriented strand board sheathing. As can be seen in Figure 3.22d where temperature–time profiles for strand board slabs are compared across individual and in–sandwich test series, the interface temperatures between the stone wool insulation, weather resistant barrier and oriented strand board remained below the 135°C melting point of the house wrap used in this study [69]. Further, the time–history of temperature measured at the mid–depth of the oriented strand board (Figure 3.22a) exhibited a fairly linear increase with time that began about 3 minutes after the onset of exposure and continued at a rate of 0.029°C/s until the end of the test. The peak value of temperature was about 68°C after 30 minutes of exposure. In contrast, the rate of temperature rise (0.51°C/s) was almost 18 times higher for the case of an individual sample of oriented strand board tested under 15 kW/m^2 heat flux. In fact, due to the increased insulation provided to the oriented strand board by the presence of the stone wool layer, temperatures did not increase to the $\sim$ 98°C that would trigger onset of evaporation of water from the oriented strand board layer.

In contrast to heating with the lower heat fluxes discussed above, Sandwich #1 samples ignited and burned when subjected to an incident heat flux of 50 kW/m^2. At these levels of heat flux, the vinyl siding first softened, buckled, and shrunk while releasing pyrolysis gases. Under continued exposure char began to form. Subsequently, the pyrolysis gases ignited with sustained flaming confined to the vinyl siding layer of the sandwich. Thus, the sequence of events leading to ignition of the siding material was identical to that discussed for tests conducted on individual samples of the siding material under the same external irradiance. Following ignition, the vinyl siding continued to char and by the end of the test, a charred residue was left behind on the exposed sandwich surface as depicted in Figure 3.23a. Under the combined influence of increased external irradiation and flame heat feedback from the burning vinyl siding above, the underlying layer of stone wool insulation discoloured significantly, with brown–to–taupe tones across the exposed surface and down the sides. This can be seen in Figures 3.23a and 3.23b. The variations in colour and sequence of discolouration patterns were indicative of thermal degradation processes such as binder decomposition and oxidation of organic and siliceous content in the insulation. Due to the higher level of heating throughout the sandwich, the weather resistant barrier melted significantly, depicted in Figure 3.23c, although no noticeable changes were observed on the exposed surface of the underlying oriented strand board sheet. Thus, it appears that the levels of thermal penetration through stone wool insulation were high enough to result in melting of house wrap, but still too low to promote surface charring in the underlying oriented strand board.

(a)

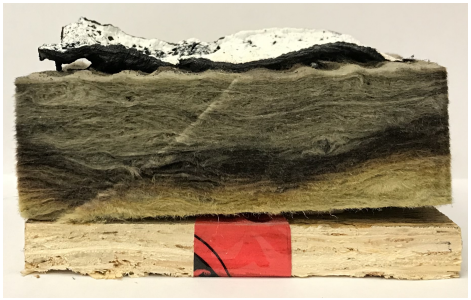

(b)

(c)

Figure 3.23: The state of Sandwich #1 assembly following the exposure 50 kW/m^2 flux in the cone calorimeter, photographs of a) the exposed sandwich surface, b) its lateral side, and c) exposed surface of the underlying house wrap and oriented strand board

To further understand the effects of each layer on the overall fire performance of the sandwich assemblies under exposure to 50 kW/m^2 incident heat flux, it is of interest to examine the time–histories of temperature recorded within the bulk sandwich materials. These are shown in Figure 3.24a, again with overplots of temperature–time profiles obtained during testing of each individual material in the sandwich (Figures 3.24b, 3.24c, and 3.24d).

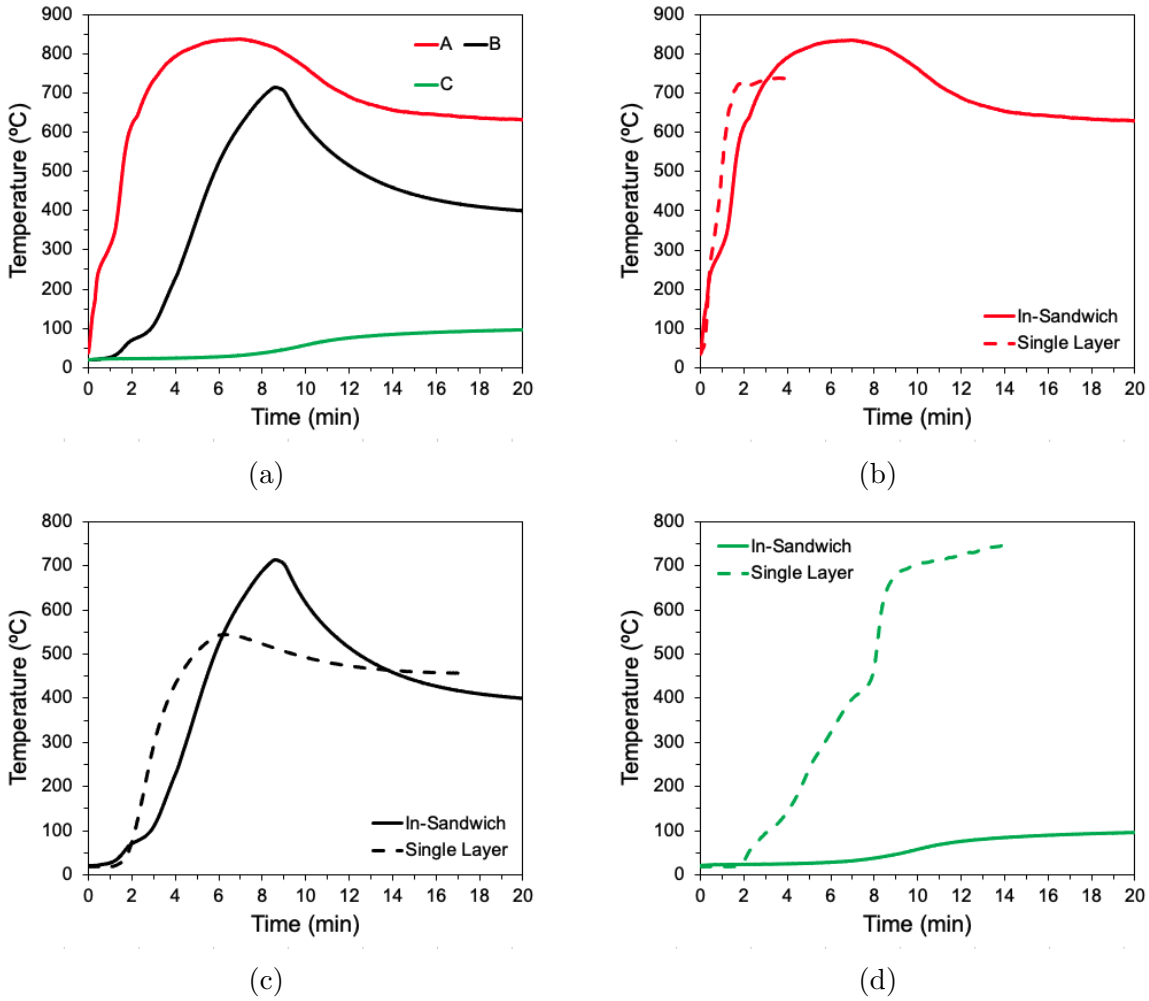

Figure 3.24: Averaged time–resolved profiles of temperatures measured a) along the bulk–path of Sandwich #1 assembly (A – unexposed surface of vinyl siding, B – centre/mid–depth of stone wool insulation bulk, C – centre/mid–depth of oriented strand board slab) and comparison of temperature–time profiles across each layer of b) vinyl siding, c) stone wool insulation, and d) oriented strand board when tested individually versus in combination with underlying layers in sandwich assemblies under external irradiance of 50 kW/m^2 flux in the cone calorimeter

Figure 3.24a compares temperatures measured in the three layers comprising the Sandwich #1 scaled wall assembly tested under 50 kW/m^2 incident heat flux. Even prior to ignition, which occurred at around 33 seconds following the onset of exposure, the thermocouple affixed to the unexposed vinyl siding surface registered a rapid rate of increase in temperature of 8.78°C/s. Following ignition, the duration of sustained flaming was 95 seconds. During this period, the rate of temperature rise on the unexposed surface was 4.33°C/s which was lower compared to that in the period prior to ignition. This was likely due to the formation and subsequent insulating effect of the char layer which was continuously formed across the surface and through the thickness of the vinyl siding throughout the test similar to behaviour seen for the individual vinyl siding material tests at the same incident heat flux levels. When incorporated into a sandwich assembly, rates of unexposed temperature rise appeared to be lower, by 1.2 and 1.3 times, than those recorded from individual vinyl siding test series for periods prior to ignition and during sustained flaming, respectively as shown in Figure 3.24b.

As can be seen from Figure 3.24a, the increase in measured temperature at the stone wool slab mid–depth occurred one minute after the onset of exposure. The centre of stone wool heated at a rate of about 2.17°C/s and reached a peak value of 714°C which was then followed by a gradual decrease in temperature to value of 400°C at the end of the test. In contrast, the rate of mid–depth temperature rise and peak temperature attained from the test of an individual stone wool sample at 50 kW/m^2 incident heat flux were 4°C/s and 544°C, respectively. Interestingly, although the rate of temperature rise was initially 1.8 times lower for in–sandwich tests than for tests on the individual material, the peak temperature at the stone wool mid–depth in the sandwich tests reached values 170°C higher compared to the individual tests. The observed differences likely occurred for the following reasons:

- When an individual stone wool sample was subjected to 50 kW/m^2 incident heat flux, thermal penetration into the sample led to a temperature rise at the sample mid–depth with resultant decomposition of the binder in the insulation. When temperatures increased to high enough values, the heating continued, driven partly by the heat of binder decomposition in combination with the imposed irradiance.

- In the case of in–sandwich tests, the vinyl siding centrally shielded the underlying stone wool from the full impact of the imposed external heat flux, which led initially to a slower rate of interior temperature rise (2.17°C/s) with resultant binder decomposition but not necessarily oxidation. However, once the vinyl siding ignited such that its flame was established on the surface of the insulation, the heat feedback from the flame accelerated decomposition and oxidation of the binder and even promoted oxidation of the siliceous species since the heat from the first reaction raised the interior temperatures to above 500°C, while the second reaction occurred at temperatures above 650°C. Thus, the insulating effect of the vinyl siding initially yielded lower rates of overall temperature rise, while the flame heat feedback combined with internal decomposition and oxidation reactions within the insulation raised the interior temperatures in excess of 700°C regardless of the rate of initial temperature rise.

Beneath the stone wool insulation lay a layer of weather resistant barrier and oriented strand board sheathing. The observed melting of the house wrap suggested that the interface temperature between the stone wool insulation and weather resistant barrier had reached or exceeded temperatures of 135°C for some period during the test. For the oriented strand board, the time–history of temperature measured at the slab's mid–depth (Figure 3.24a) exhibited a fairly linear increase with time that began about 8 minutes after the onset of exposure and rose at a rate of 0.14°C/s until the end of the test subsequently reaching a temperature plateau of 96.2°C $\pm$ 0.4°C. Although the onset of oriented strand board dehydration appeared to have occurred at the mid–depth of the slab, the rate of temperature rise that led to this plateau was 8 times slower for in–sandwich tests compared to that from tests on individual oriented strand board samples. The difference seen spoke to the insulating effect of the stone wool as noted previously.

Sandwich #2 – Polyisocyanurate Insulation

Results of cone calorimeter tests conducted on Sandwich #2 samples are presented in Figures 3.25 through 3.28. Layers of vinyl siding, polyisocyanurate insulation, weather resistant barrier, and oriented strand board were instrumented with thermocouples and stacked to form a (scaled) section of an exterior wall assembly as previously outlined in Section 3.3. The instrumented sandwich samples were then exposed to low (15 kW/m^2) and high (50 kW/m^2) levels of external irradiation in the cone calorimeter. Measurements of temperature–time histories along the bulk–path through the sandwich assemblies were recorded during each test at three locations: on the unexposed side of vinyl siding and at the centre and mid-depth of the polyisocyanurate and oriented strand board slabs. None of the sandwich assemblies ignited when subjected to the low level of external heat flux, 15 kW/m^2 flux, for 30 minutes. Under exposure to 50 kW/m^2 incident heat flux, however, the sample did ignite and burn. As such, the tests were concluded 120 seconds after extinction of the visible flames (Section 3.1) which normally took 20 minutes.

The after test state of a Sandwich #2 sample following exposure to incident heat flux of 15 kW/m^2 is shown in Figure 3.25. Consistent with expectations, the layer of vinyl siding on the exposed sandwich surface charred leaving behind a carbon–rich residue similar to that presented for tests on individual samples of vinyl siding under the same imposed irradiance. The behaviour of the siding material under thermal heating was consistent in both cases as well. The siding initially shrunk buckling towards the centre of the exposed sandwich surface as can be seen from Figure 3.25b. This left the underlying polyisocyanurate insulation face partially exposed to heating from the conical heater within a minute after the onset of exposure. As the test progressed, thermal degradation of the polyisocyanurate intensified and the material expanded, creating a series of gaps in the foam core under the exposed foil facer. Interestingly, the integrity of the foil layer was not compromised as it was still attached to the foam core beneath. Upon closer examination of the after test state of the insulation, it was found that the foam expanded by about 10.5 mm (on–average) beyond the perimeter of the foil; this is shown in Figure 3.26 where the perimeter of the foil layer is marked with the thick white border. In addition to cracking and expansion of the foam, significant orange–to–brown tones of discolouration were observed within an area measuring approximately 45 mm $\times$ 100 mm at the centre of the exposed insulation surface. This area matched the footprint of the charred residue from the vinyl siding above, suggesting that the heat conducted through the upper layers was sufficient to initiate and sustain pyrolysis of the foam just below the foil facer. Slight surface charring of the polyisocyanurate foam can also be noticed at each end of the discoloured strip where the expanded foam was in direct contact with (and under) the edges of the charred siding residue.

Unlike the vinyl siding and polyisocyanurate insulation, there were no noticeable changes in the weather resistant barrier and oriented strand board layers, again likely due to the insulating effect of the polyisocyanurate foam which slowed the rate of thermal penetration to those bottom layers.

(a) (b)

Figure 3.25: The state of Sandwich #2 samples (a) before and (b) after exposure to 15 kW/m^2 external incident heat flux in the cone calorimeter

Figure 3.26: The state of the exposed in–sandwich polyisocyanurate surface (after removal of the vinyl siding and foil facer) following exposure to 15 kW/m^2 incident heat flux in the cone calorimeter

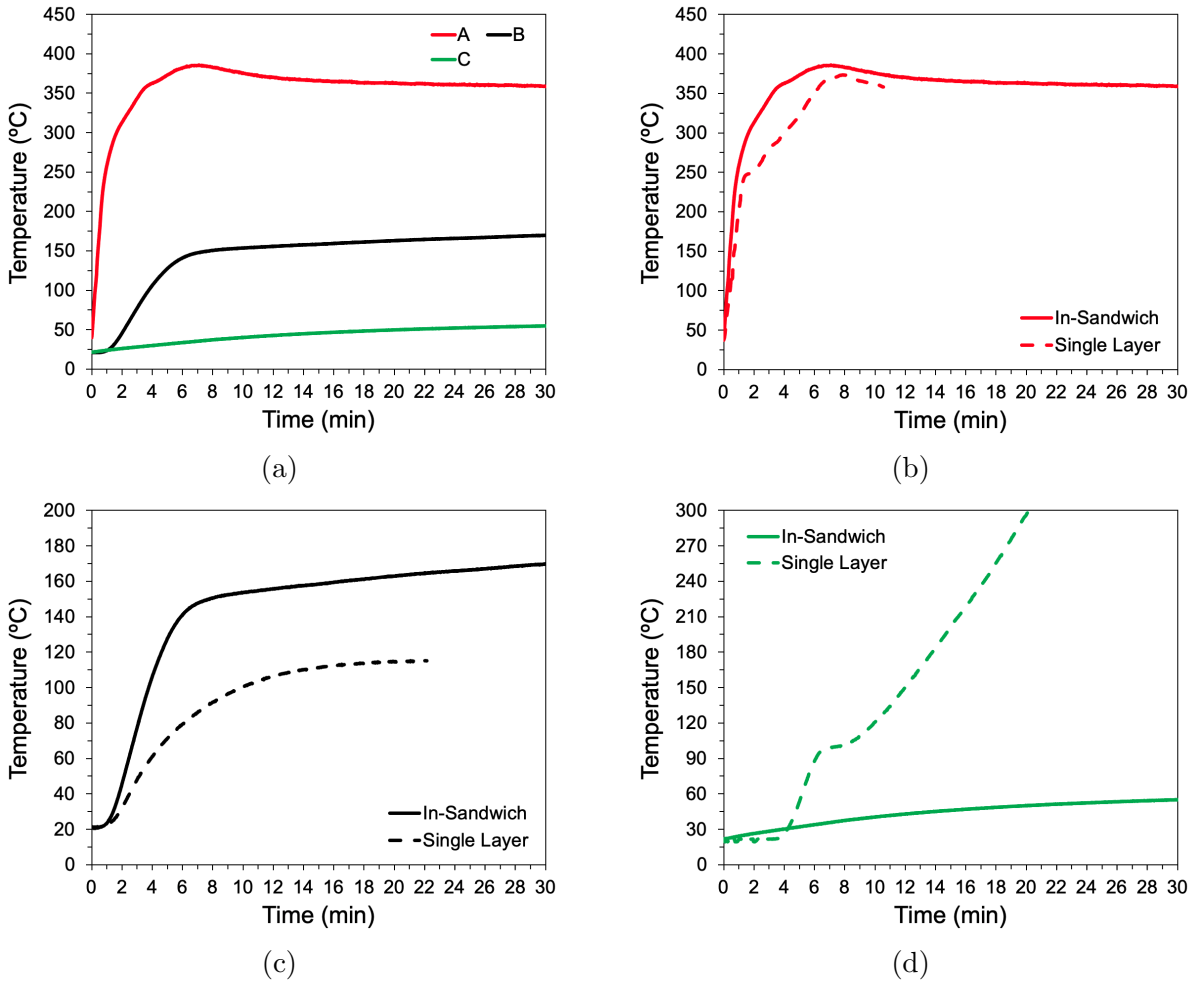

Figure 3.27: Averaged time–resolved profiles of temperatures measured a) along the bulk–path of Sandwich #2 assembly (A – unexposed surface of vinyl siding, B – centre/mid–depth of polyisocyanurate insulation bulk, C – centre/mid–depth of oriented strand board slab) and comparison of temperature–time profiles across each layer of b) vinyl siding, c) polyisocyanurate insulation, and d) oriented strand board when tested individually versus in combination with underlying layers in sandwich assemblies under external irradiance of 15 kW/m^2 flux in the cone calorimeter

To further understand the effects of each layer on the overall thermal performance of the sandwich assembly under exposure to 15 kW/m^2 incident heat flux, it is of interest to examine the time–histories of temperature that were recorded at the three measurement positions within the bulk assembly. These are shown in Figure 3.27a overplotted with the temperature–time profiles obtained during individual test on each sandwich layer (Figures 3.27b, 3.27c, and 3.27d for vinyl siding, polyisocyanurate insulation, and oriented strand board, respectively) and discussed further below.

Figure 3.27a compares temperatures measured at three locations through Sandwich #2 wall assemblies tested under 15 kW/m^2 incident heat flux. The thermocouple affixed to the unexposed surface of the vinyl siding registered a rapid increase in temperature shortly after the onset of exposure and rose at a rate of 3.79°C/s until charring of vinyl siding was observed around 250°C. Upon initiation of charring, the rate of temperature rise slowed considerably, to about 0.64°C/s, likely due to the insulating effect of the carbonized layer. A quasi–steady temperature of 360.4°C ± 0.8°C was reached when the char had penetrated through to the backside of the siding layer. The rates of temperature rise on the unexposed surface in the sandwich assemble were 1.4 and 1.7 times higher than those seen in tests of the individual material for periods prior to and after the onset of char formation, respectively. This can be seen from the differences in the slopes of temperature–time traces shown in Figure 3.27b. The discrepancy was consistent with the presence of the polyisocyanurate insulation below the vinyl siding in the sandwich, since it would insulate the backside of the vinyl siding leading to higher increases in temperature.

An increase in measured temperature at the polyisocyanurate mid–depth occurred 90 seconds following the onset of temperature rise on the unexposed vinyl siding surface. Temperatures at this location rose at a rate of 0.48°C/s, and reached quasi–steady temperatures of 162.6°C ± 4.7°C after 10 minutes of heating. This rate of temperature rise was 3.2 times higher, and steady–state temperatures were 66°C higher on average, in the sandwich assembly than for tests with the individual material. Due to the close contact between the hot charred siding residue and the underlying insulation slab it appeared that heat conducted from the degrading siding material was sufficient to initiate and sustain pyrolysis of the polyisocyanurate foam at the surface of the insulation slab as shown previously in Figure 3.26. The heat from the foam pyrolysis at the exposed insulation surface would then have penetrated into the bulk of the insulation slab, raising its interior temperature at the slab's mid–depth.

Upon examination of the post–exposure state of the layers below the polyisocyanurate insulation, there were no visual signs of melting of the house wrap or charring of the underlying strand board were observed. This suggested that the interface temperature between the polyisocyanurate insulation and weather resistant barrier remained below 135°C throughout the entire test duration. The time–history of temperature measured at the oriented strand board mid–depth (Figure 3.27a) exhibited a fairly linear profile with increasing time that began about 3 minutes after the onset of exposure and was still rising at a rate of 0.018°C/s until the end of the test when it had reached about 55°C. This rate of temperature rise was 28 times lower than for the case of individual oriented strand board sheet exposed to 15 kW/m^2 flux due to insulation from heat by the layers above.

In contrast to the thermal penetration which occurred in Sandwich #2 samples exposed to the lower heat flux discussed above, Sandwich #2 samples ignited and burned when subjected to incident heat flux of 50 kW/m^2. The time–histories of measured temperature recorded through the layers in Sandwich #2 during exposure to 50 kW/m^2 heat flux are presented in Figure 3.28a. At the onset of exposure, the vinyl siding started to soften, buckle, and shrink while releasing gaseous pyrolysis products. Shortly afterwards, the underlying polyisocyanurate insulation also started to expand while liberating gaseous pyrolysis products along the lateral sides of its foam core. At around 90 seconds following the onset of exposure, pyrolysis gases released from the vinyl siding ignited and a flame formed over the exposed insulation surface. This could be noticed from the steep increase in temperature to characteristic flame temperatures of 700°C – 800°C on the unexposed vinyl siding (trace "A" in Figure 3.28a). Approximately two minutes after the ignition of the vinyl siding, the flames weakened yet were able to descend further into the bulk of the sandwich, now anchoring and burning along the lateral sides of the polyisocyanurate foam. The heat feedback from the flames appeared to result in accelerated rate of thermal decomposition at the insulation mid–depth as can be seen from the temperature–time trace "B" in Figure 3.28a. The sustained flaming of polyisocyanurate foam continued for about 17 minutes. During this period, the flames continuously regressed further towards the bottom of the sample holder and engulfed the exposed surface of the underlying oriented strand board such that it ignited and burned. Upon extinction of the visible flames, layers of charred vinyl siding, polyisocyanurate insulation, and oriented strand board residues were left as was shown in previous sections.

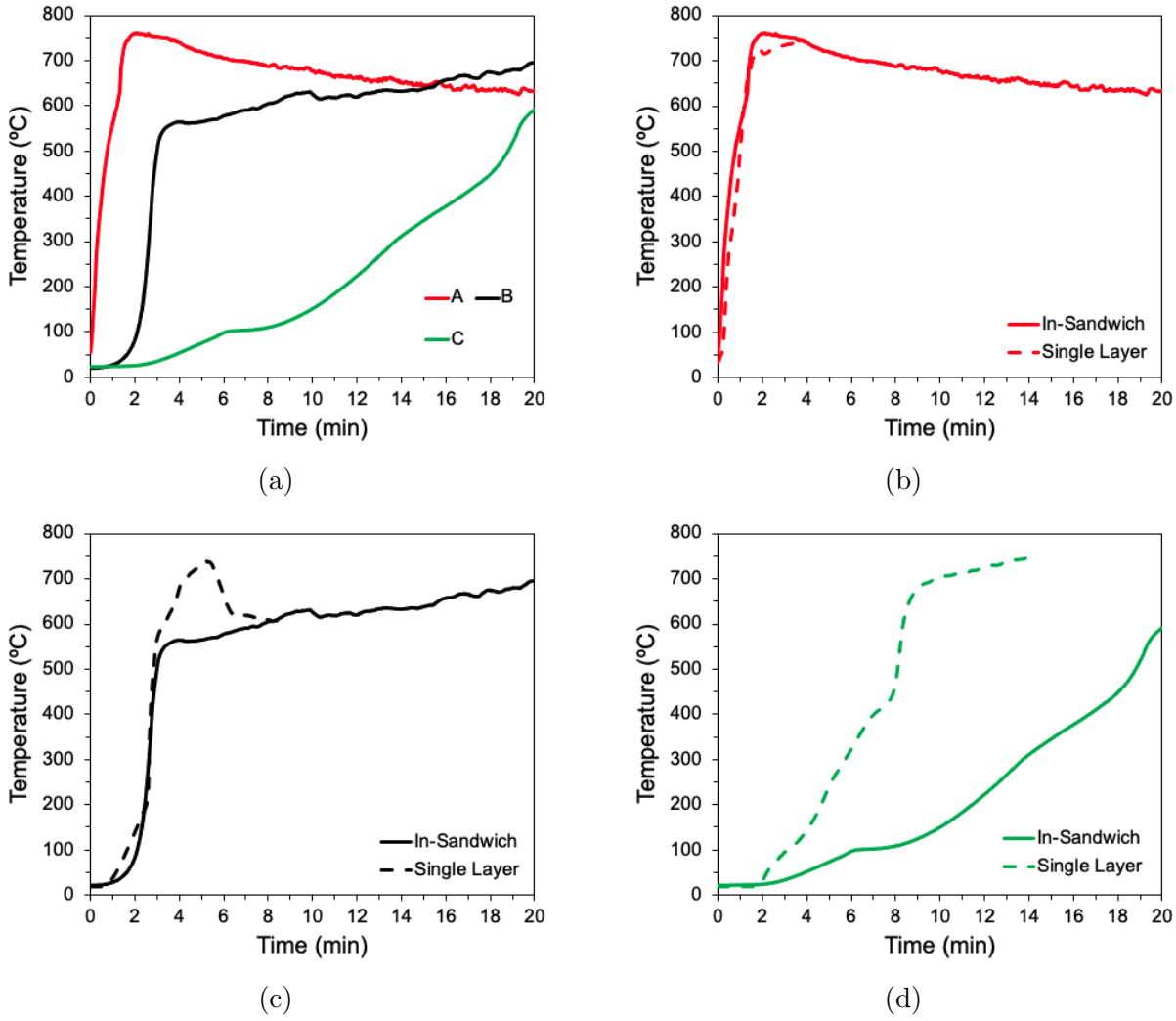

Figure 3.28: Averaged time–resolved profiles of temperatures measured a) along the bulk–path of Sandwich #2 assembly (A – unexposed surface of vinyl siding, B – centre/mid–depth of polyisocyanurate insulation bulk, C – centre/mid–depth of oriented strand board slab) and comparison of temperature–time profiles across each layer of b) vinyl siding, c) polyisocyanurate insulation, and d) oriented strand board when tested individually versus in combination with underlying layers in sandwich assemblies under external irradiance of 50 kW/m^2 flux in the cone calorimeter

Sandwich #3 – Extruded Polystyrene Insulation

Results of cone calorimeter tests conducted on Sandwich #3 samples are presented in Figures 3.29 through 3.31. Layers of vinyl siding, extruded polystyrene insulation, weather resistant barrier, and oriented strand board were instrumented with thermocouples and stacked to form a (scaled) section of an exterior wall assembly as previously outlined in Section 3.3. The instrumented sandwich samples were then exposed to low (15 kW/m^2) and high (50 kW/m^2) levels of external irradiation in the cone calorimeter. Measurements of temperature–time histories along the bulk–path through the sandwich assemblies were recorded during each test at three locations: on the unexposed side of vinyl siding and at the centre and mid-depth of the extruded polystyrene insulation and oriented strand board slabs. The sandwich assemblies did not ignite when subjected to low level of external heat flux for tests of 30 minute duration. Under exposure to 50 kW/m^2 incident heat flux, however, all Sandwich #3 assemblies did ignite, so tests were concluded 120 seconds after extinction of the visible flames leading to typical test duration of 10 minutes.

The after test state of a Sandwich #3 sample following exposure to incident heat flux of 15 kW/m^2 is shown in Figure 3.29. The layer of vinyl siding again shrunk and the underlying extruded polystyrene insulation started to soften, recede and collapsed onto the house wrap/oriented strand board layer forming a viscous liquid melt pool. In the meantime, char began to form through the shrunk vinyl siding, which was now 25 mm further away from the conical heater following the collapse of polystyrene insulation. The thermally decomposing polystyrene fluid melt continued to release gases until no polystyrene residue was left beyond the area shielded beneath the charred vinyl siding as can be seen in Figure 3.29b. The underlying house wrap and oriented strand board face were now partially exposed to the cone heater, leading to presumed melting of the house wrap and significant surface charring of the oriented strand board as well. Some hardened house wrap residue is indicated with the white circle in Figure 3.29b underneath the charred vinyl siding residue.

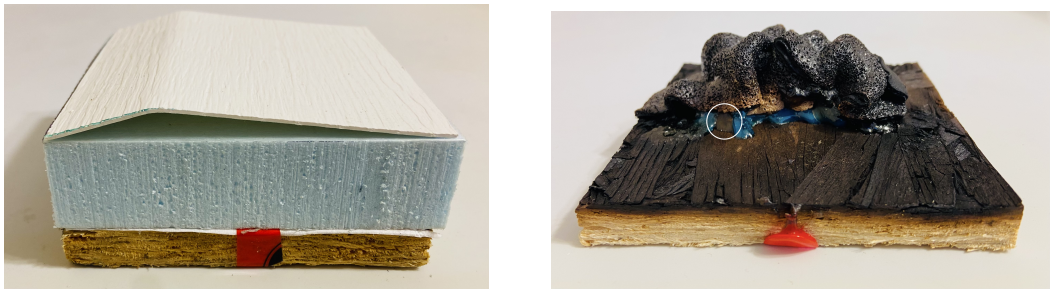

(a) (b)

Figure 3.29: The state of Sandwich #3 samples (a) before and (b) after exposure to 15 kW/m^2 external incident heat flux in the cone calorimeter

To further understand the effects of each layer on the overall thermal performance of the sandwich assembly under exposure to 15 kW/m^2 incident heat flux, it is of interest to examine the time–histories of temperature that were recorded at the three measurement positions within the sandwich bulk. These are shown in Figure 3.27a overplotted with temperature–time profiles obtained from individual testing of each layer material (Figures 3.27b, 3.27c, and 3.27d for vinyl siding, extruded polystyrene insulation, and oriented strand board, respectively). Discussion of the thermal decomposition, recorded rates of temperature rise and subsequent temperature profiles of the heated sandwich components are below.

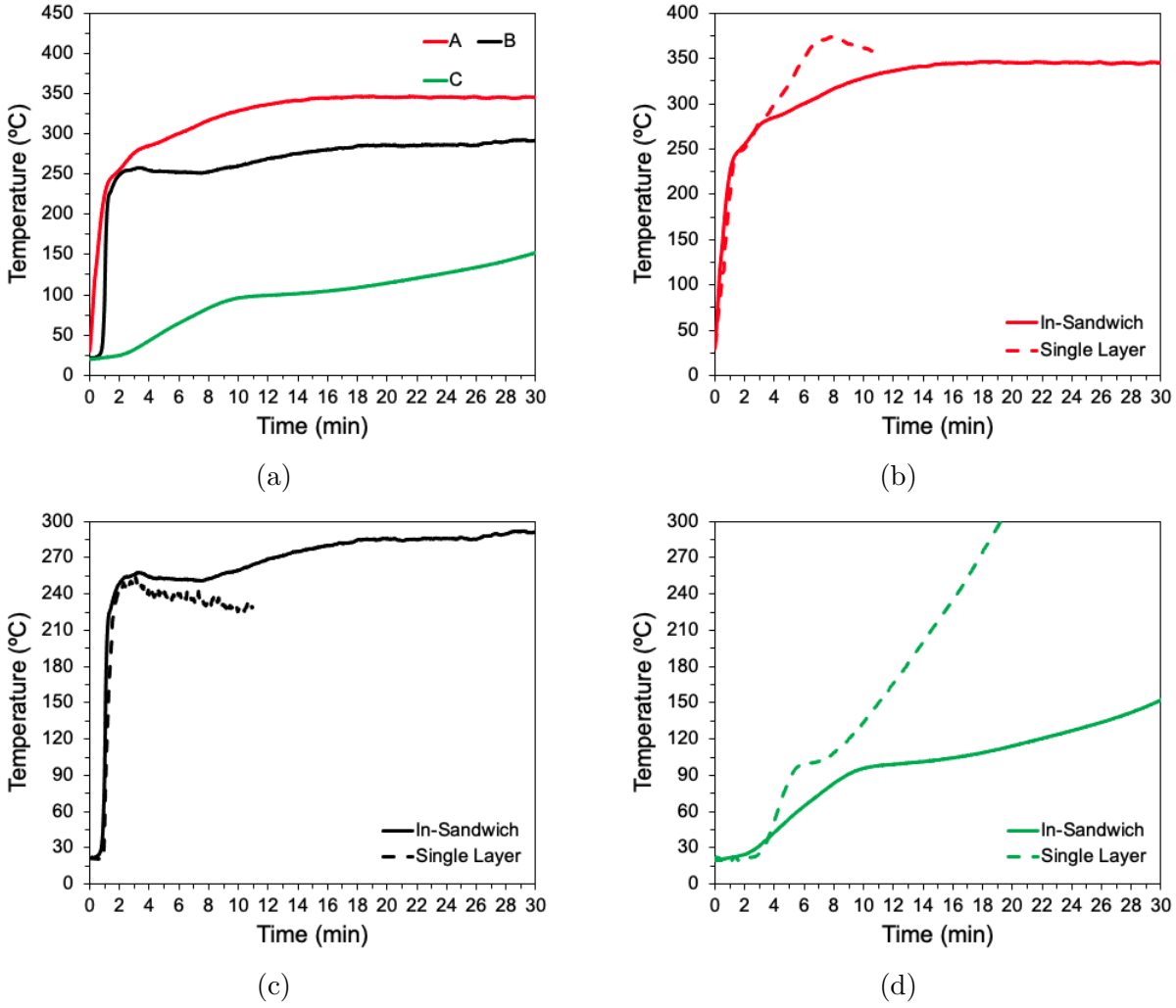

Figure 3.30: Averaged time–resolved profiles of temperatures measured a) along the bulk–path of Sandwich #3 assembly (A – unexposed surface of vinyl siding, B – centre/mid–depth of extruded polystyrene insulation bulk, C – centre/mid–depth of oriented strand board slab) and comparison of temperature–time profiles across each layer of b) vinyl siding, c) extruded polystyrene insulation, and d) oriented strand board when tested individually versus in combination with underlying layers in sandwich assemblies under external irradiance of 15 kW/m^2 flux in the cone calorimeter

Figure 3.30a compares temperatures measured at three locations within Sandwich #3 under exposure to 15 kW/m^2 incident heat flux. The thermocouple affixed to the unexposed vinyl siding surface registered a rapid increase in temperature shortly after the onset of exposure, initially rising at a rate of 2.64°C/s until char formation was observed around 250°C. Upon initiation of charring, the rate of temperature rise slowed considerably, to around 0.12°C/s, again due to the insulating effect of the carbonized layer. After 15 minutes of heating, the vinyl siding had charred through the thickness that led to backside temperatures of 345.3°C ± 0.5°C. In comparison to the results of testing of individual siding samples, at 15 kW/m^2 heat flux exposure, the rates of temperature rise prior to the onset of char formation were very similar, to within 0.76%, across the two test series. This was likely because the extruded polystyrene foam insulation collapsed and therefore failed to provide the increased insulation to the backside of the siding noted above for Sandwich #1 and #2. The rate of temperature rise after the onset of charring, however, was 3.2 times lower for the in–sandwich test. This was possibly because the charring of vinyl siding occurred after this layer dropped to the bottom of the sandwich assembly and further away from the cone heater, so the total incident heat flux was significantly lower than 15 kW/m^2. Previously, it was demonstrated that the rate of temperature rise during char formation decreased with lower external external heat flux, so the lower rate of 0.12°C/s would be consistent with the total heat flux being below 15 kW/m^2.

The increase in measured temperature at the extruded polystyrene mid–depth occurred 45 seconds following the onset of temperature rise on the unexposed surface of the vinyl siding as can be seen from Figure 3.30a. At the centre of the solid foam slab, the thermocouple registered a rapid rise in temperature with a rate of 4.7°C/s until around 230°C at which point the extruded polystyrene insulation collapses onto the house wrap/oriented strand board layer. Similar observations were made for the case of individual extruded polystyrene tests (Figure 3.30c) where the rates of temperature rise were very similar, to within 4.2%, across the two test series. At this stage, the extruded polystyrene had melted into a viscous fluid and thermocouple continued to measure the temperature of melted residue. Pyrolysis of the melted polystyrene foam continued for the remaining duration of heating.

It was previously noted that the collapse and subsequent melting of the polystyrene insulation resulted in the underlying oriented strand board face to be partially exposed to the cone heater. This in turn promoted significant surface charring of the oriented strand board which typically occurs at around 235°C [78]. At the centre of the strand board slab, however, the measured temperature attained 98.2°C ± 0.7°C plateau followed by a gradual increase to about 152°C as can be seen Figure 3.30a. Although dehydration of oriented strand board appeared to had occurred at the mid–depth of the oriented strand board, the rate of temperature rise leading to this temperature (0.17°C/s) was three times slower for in–sandwich tests compared to that from tests on individual strand board samples. This again pointed to the insulating effect of the charred vinyl siding that laid above the exposed oriented strand board surface, as well as decreased amount of total incident heat flux to this layer which was further away from the cone heater in the sandwich assembly.

In contrast to the thermal penetration and melting which occurred in Sandwich #3 samples exposed to the lower heat flux discussed above, Sandwich #3 samples ignited and burned when subjected to incident heat flux of 50 kW/m^2. The time–histories of measured temperatures recorded through the layers in Sandwich #3 during exposure to 50 kW/m^2 heat flux are presented in Figure 3.31a. At the onset of exposure, the vinyl siding started to soften, buckle, and shrink while releasing gaseous pyrolysis products. Shortly afterwards, the underlying extruded polystyrene insulation also started to soften, melt and collapse; due to the melting foam, the vinyl siding dropped from its original position to the top of the oriented strand board. At around 45 seconds following the onset of exposure, pyrolysis gases released from both the vinyl siding and polystyrene melt ignited and a flame formed over the melted extruded polystyrene pool, shown by the steep increase in temperature to characteristic flame temperatures of 700°C – 800°C on those two thermocouples (traces "A" and "B" in Figure 3.31a). The duration of sustained flaming was 560 seconds, during which the flames also engulfed the exposed surface of the underlying oriented strand board such that it ignited and burned as marked by the steep increase in temperature in Figure 3.31a as well. Upon extinction of the visible flames, a layer of charred vinyl siding residue and charred oriented strand board were left as was shown in previous sections.

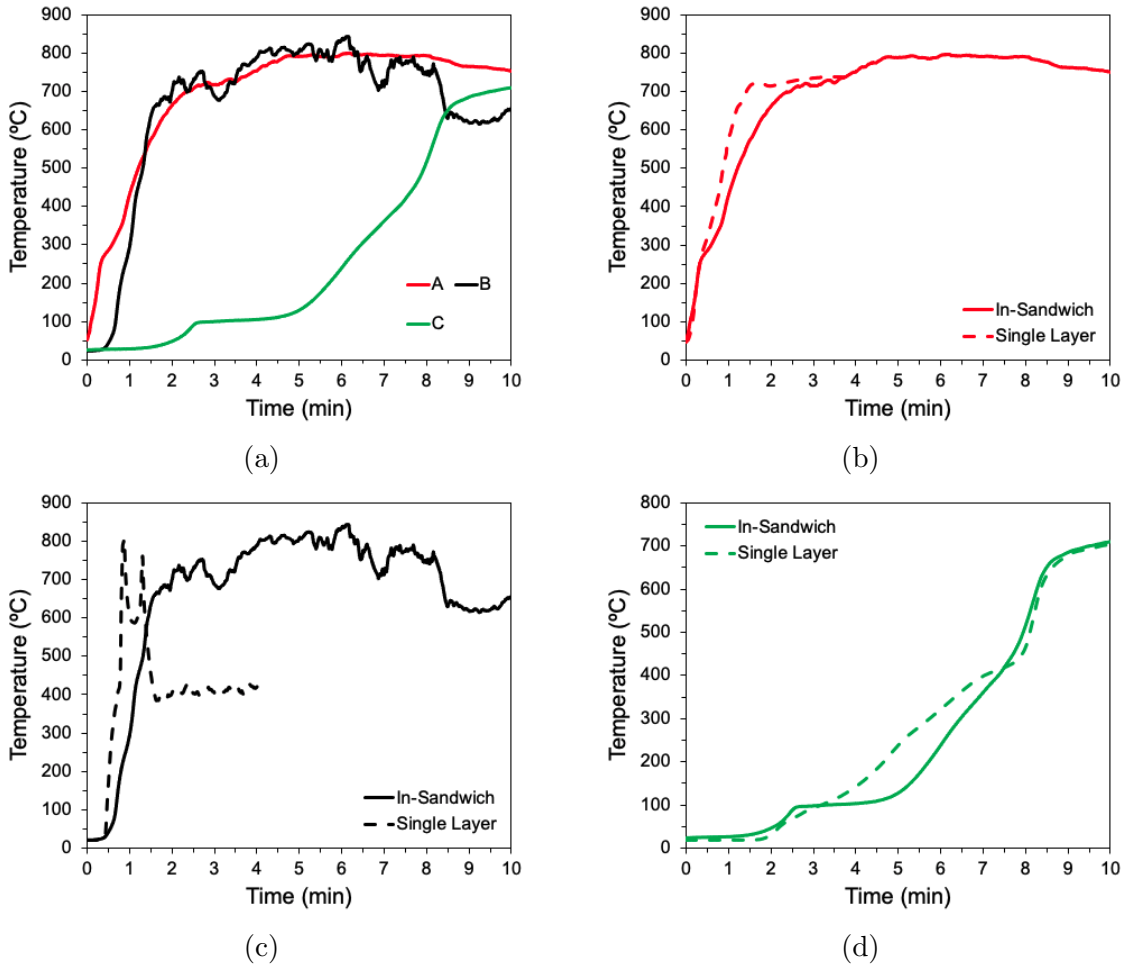

Figure 3.31: Averaged time–resolved profiles of temperatures measured a) along the bulk–path of Sandwich #3 assembly (A – unexposed surface of vinyl siding, B – centre/mid–depth of extruded polystyrene insulation bulk, C – centre/mid–depth of oriented strand board slab) and comparison of temperature–time profiles across each layer of b) vinyl siding, c) extruded polystyrene insulation, and d) oriented strand board when tested individually versus in combination with underlying layers in sandwich assemblies under external irradiance of 50 kW/m^2 flux in the cone calorimeter

Comparison of Bulk–Path Temperature Profiles in Sandwich Assemblies

One of the main objectives of this work was to conduct comparative small–scale tests to examine the fire performance of the composite sandwich assemblies. Therefore, in addition to the time evolution of temperatures measured within the sandwich assemblies, it was also of interest to compare the thermal penetration into the bulk of these composite samples. For this, first, a line plot of temperature versus time is shown in Figure 3.32a where temperatures recorded at the mid–depth of insulation (stone wool for Sandwich #1, polyisocyanurate for Sandwich #2, and extruded polystyrene for Sandwich #3) and at the mid–depth of the underlying oriented strand board sheets are overlaid across all three sandwich tests conducted under exposure to 15 kW/m^2 incident heat flux. These line plots were previously presented separately for Sandwich #1, #2 and #3 assemblies in Figures 3.22a, 3.27a and 3.30a, respectively. The lower level of external heat flux exposure was selected to allow for better comparison of the through–sandwich thermal penetration without the added complexity and impact of the flame heat feedback as seen previously for the tests performed under 50 kW/m^2 heat flux. To further illustrate through–sandwich heat transfer, the time–histories of temperature differences (taken as the difference in temperature across the mid–depth of insulation and the mid–depth of the oriented strand board) are plotted in Figure 3.32b. For both sets of plots in Figure 3.32, the time–resolved traces of measured temperature and temperature difference are presented for periods during which the thermocouple affixed at the mid–depth extruded polystyrene (Sandwich #3) was measuring the temperature of the solid foam. Thus, temperature–time profiles for Sandwich #3 are shown until a minute and a half (90 seconds) following the onset of exposure.

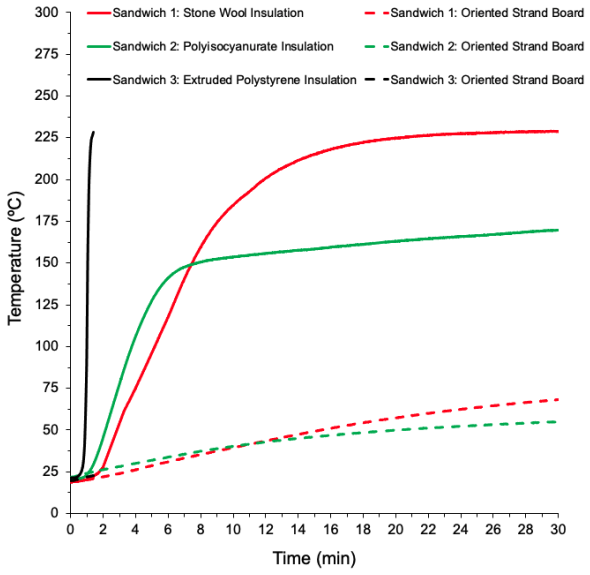

(a)

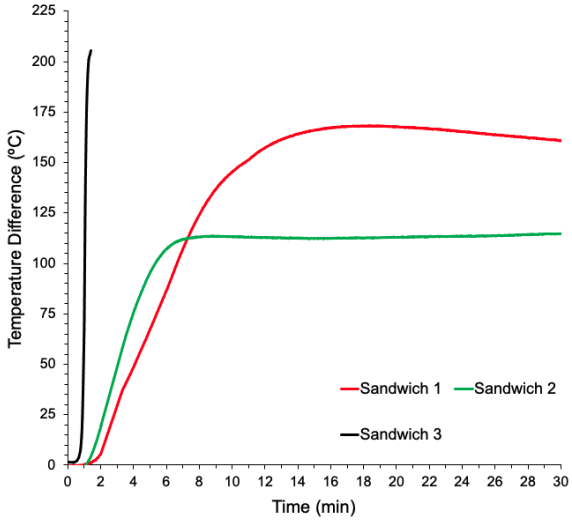

(b)

Figure 3.32: Time–histories of (a) temperatures measured at the mid–depth of insulation and mid–depth of oriented strand board across Sandwich #1, #2, #3 tests, and (b) their difference across the three sets of experiments

Table 3.12: Details of interior temperature rise dynamics across three sandwich assemblies tested under 15 kW/m^2 incident heat flux in the cone calorimeter

Sandwich Assembly	Onset of Temperature Rise Following Exposure (s)		Rate of Temperature Rise Following Exposure (°C/s)		Peak Temperature (°C)	
	Insulation Mid–Depth	Strand Board Mid–Depth	Insulation Mid–Depth	Strand Board Mid–Depth	Insulation Mid–Depth	Strand Board Mid–Depth
# 1	120	180	0.35	0.029	229	68
# 2	90	180	0.48	0.018	163	55
# 3	45	N/A	4.7	N/A	228	23

Table 3.12 summarizes the details pertaining to interior temperature–time profiles shown Figure 3.32a, specifically, data regarding the onset of temperature increase measured at the mid–depth of insulation and oriented strand board sheets, as well as the rates of temperature rise and subsequent peak temperatures attained at those locations. As can be seen, the earliest onset of increase in temperature measured at the centre of an insulation slab occurred for Sandwich #3 assembly followed by Sandwich #2 and Sandwich #1 assemblies at 45, 90, and 120 seconds following exposure, respectively. Under continued exposure, the mid–depth insulation temperatures continued to increase with the highest rate of temperature rise of 4.7°C/s observed for Sandwich #3, followed by 0.48°C/s for Sandwich #2, and 0.35°C/s for Sandwich #1. Consistent with the observed varying rates of interior temperature rise at the insulation mid–depth, peak temperatures recorded at this locations were also attained at different times: for Sandwich #1, a peak temperature of about 229°C was reached after 16 minutes of heating, while for Sandwich #2 and #3 assemblies peak temperatures of around 163°C and 228°C were measured after 10 and 1.5 minutes following the onset of exposure, respectively. The observed differences in interior temperature rise rates and subsequent peaks attained spoke to the differing dynamics of thermal decomposition and overall behaviour of each insulating material to radiant heat exposure such as self–heating of stone wool insulation, melting of extruded polystyrene foam, and expansion of polyisocyanurate foam core. These were previously discussed in greater detail for each sandwich assembly above.

In contrast to the temperature rise rates measured at the centre of insulating sheets, the rate of temperature rise at the mid–depth of oriented strand board layers were significantly lower across all sandwich assemblies. In fact, for Sandwich #3, this rate was minimal prior to melting of extruded polystyrene foam beyond its original mid–depth level, and the recorded temperatures were practically the same as those recorded at the onset exposure measuring only 23°C at the time of thermocouple detachment in the above–lying extruded polystyrene foam. For Sandwich #1 and #2 assemblies, however, the time–histories of temperature exhibited a fairly linear increase with time that began 180 seconds after the onset of exposure and continued at rates of 0.029°C/s and 0.018°C/s, respectively. The peak values of temperature were about 68°C for Sandwich #1 and 55°C for Sandwich #2 after 30 minutes of exposure. Due to the increased insulation provided to the oriented strand board by the presence of the stone wool and polyisocyanurate insulation layers in Sandwiches #1 and #2, respectively, temperatures at the strand board mid–depth did not increase to the $\sim$ 98°C threshold temperature that would trigger onset of evaporation of water from the oriented strand board layer. This, however, was not the case for Sandwich #3 assembly after complete collapse and melting of extruded polystyrene foam, as under continued exposure the temperature measured at the mid–depth of oriented strand board

increased to about 152°C after 30 minutes of heating; this was previously shown in Figure 3.30a, but is not presented in Figure 3.32a as the insulation in Sandwich #3 had already leading to heating phenomena that are not comparable to the bulk–path heat transfer in the other sandwich configurations.

Consistent with the slow rates of temperature rise and lower values of peak temperatures measured at the mid–depth of oriented strand board slabs, the time–resolved traces of temperature differences across the two measurement points within an assembly bulk (mid–depth of insulation and mid–depth of strand board) followed a similar shape to that of mid–depth insulation temperature–time curve across all sandwich tests. The largest temperature difference was recorded for Sandwich #3 assembly where a peak difference of 205°C was achieved around 1.5 minutes after the onset of exposure as the insulation melted. This was then followed by Sandwich #1 and Sandwich #2 where peak differences of 168°C and 113°C were measured around 18 and 8 minutes into the test, respectively, consistent with the differing time–resolved thermal profiles for both insulation and oriented strand board layers discussed above.

Chapter 4

Large–Scale Fire Testing

In this Chapter, the experimental methods, instrumentation and test assembly construction used in the large–scale tests are described. The fire exposure used and how it was measured are then outlined, followed by results of the tests and discussion of their implications in terms of fire exposure on exterior walls.

4.1 Overview of the Test Rig

A series of large–scale fire experiments were conducted outside, in a designated test area, at the University of Waterloo Live Fire Research Facility. In these experiments, a well–instrumented multi–layer exterior wall assembly was subjected to temperature and heat flux conditions similar to those encountered in a realistic (but contained) fire exposure. Details of the layered design and instrumentation of the test wall assembly as well as the fire exposure are presented in Sections 4.3 and 4.4, respectively. Results of the tests are then discussed in Section 4.6.

The test wall assembly was constructed on a raised fire brick platform and instrumented with thermocouples 24 hours prior to testing. The platform, measuring 3,658 mm $\times$ 3,658 mm, was large enough to accommodate the wall and the design fire. It was lined with a layer of 57 mm thick fire clay bricks to ensure negligible heat loss from the design fire to the ground. After construction and instrumentation of a test wall, the assembly was sheltered overnight under a wind rated mobile tent covered with waterproof rip–stop weave fabric. On the test day, the tent was removed and mobile screens were positioned along the perimeter of the raised platform to protect the test area from environmental perturbations

such as wind and dust. The fuel load was arranged (as described in Section 4.4) and the thermocouples in the test wall were connected to the National Instruments distributed data acquisition (NI DAQ) system. Signals from the NI DAQ were digitally transmitted back to the main computer system via 100 Mbps ethernet connection. Three cameras were placed at locations outside the platform to capture the state of the wall from various angles during a test. The live recordings were stored to a digital video recorder (DVR). The data acquisition system and DVR, along with corresponding computers, were housed in a steel control room located behind the test wall assembly. An aerial view of the test area including the control room, test wall, wind screens, raised platform, and cameras is depicted schematically in Figure 4.1.

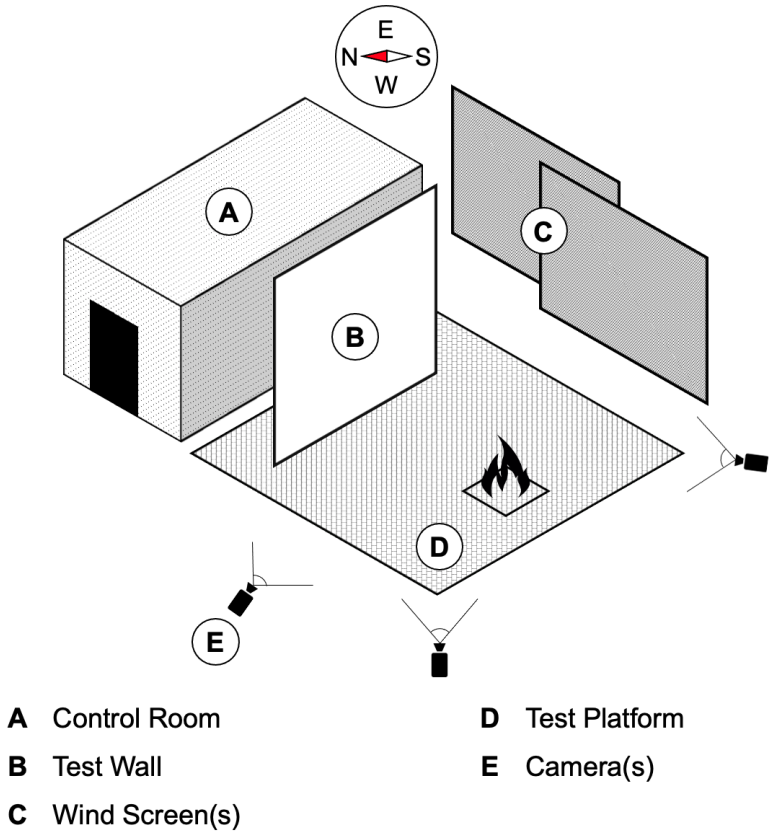

Figure 4.1: A schematic diagram of the large–scale test area

In the present work, large–scale tests were conducted to investigate the overall fire performance of three wall assemblies. As discussed in Section 2.2, the exterior envelope of the wall assemblies consisted of four distinct layers: decorative surface siding, exterior continuous insulation, weather resistant barrier, and exterior sheathing. Since the main objective was to assess heat transfer through different wall insulation materials at large-scale, each assembly incorporated one of the three types of exterior insulation studied:

- Wall #1, lined with 32 mm thick continuous rigid stone wool insulation;
- Wall #2, lined with 25 mm thick rigid polyisocyanurate insulation; and
- Wall #3, lined with 25 mm thick rigid extruded polystyrene foam insulation.

The construction and instrumentation details for the test walls are outlined below.

4.2 Test Wall Assembly Construction

The large–scale test wall assemblies were constructed with materials already discussed in Section 3.3. A schematic diagram of the assembly is presented in Figure 4.2. First, a frame for the wall was constructed with four lumber pieces, each 2,438 mm long × 152 mm wide × 50 mm thick. Five 2,438 mm long × 152 mm wide × 50 mm thick wood studs, spaced 406 mm on center, were installed in the frame, resulting in a six cavity configuration for the wall. The unexposed side of the wall was faced with two sheets of Type X fire resistant gypsum board each measuring 2,438 mm long × 1,219 mm wide × 16 mm thick. The gypsum board sheets were installed horizontally per standard construction practice and attached to the studs and frame using self–threading plasterboard screws. Building the wall from inside to the exterior, twelve 1,219 mm long × 406 mm wide × 140 mm thick stone wool insulation batts were then installed in the wall cavities, with two batts per cavity. The in–cavity batt insulation was rated at an RSI–value of 3.87. Next, two 2,438 mm long × 1,219 mm oriented strand board sheets were installed horizontally on the fire side of the wall, covering the studs, frames and in–cavity insulation. Weather resistant barrier (house wrap) was cut to 2,438 mm × 2,438 mm square and placed over the exterior oriented strand board sheathing, secured along the wall perimeter using a hammer tacker stapler. The exterior continuous insulation (one of the following: stone wool, polyisocyanurate, and extruded polystyrene insulation) was then then mounted over the house wrap sheet, and fastened to the underlying oriented strand board layer using 12–gauge cap nails.

Before mounting the decorative surface siding (i.e. vinyl siding panels), seven pieces of 2,438 mm $\times$ 76 mm $\times$ 25 mm wood furring strips were placed over the exterior continuous insulation layer, spaced at 406 mm on center, and fastened into the oriented strand board sheet. Such an arrangement provided a solid base for attaching the vinyl siding panels and resulted in an air gap of 64 mm (nominal depth) between the siding panels and exterior continuous insulation. The materials used in each test wall were conditioned to moisture equilibrium at $23°C \pm 2°C$ and $50\% \pm 10\%$ relative humidity for at least 72 hours prior to construction.

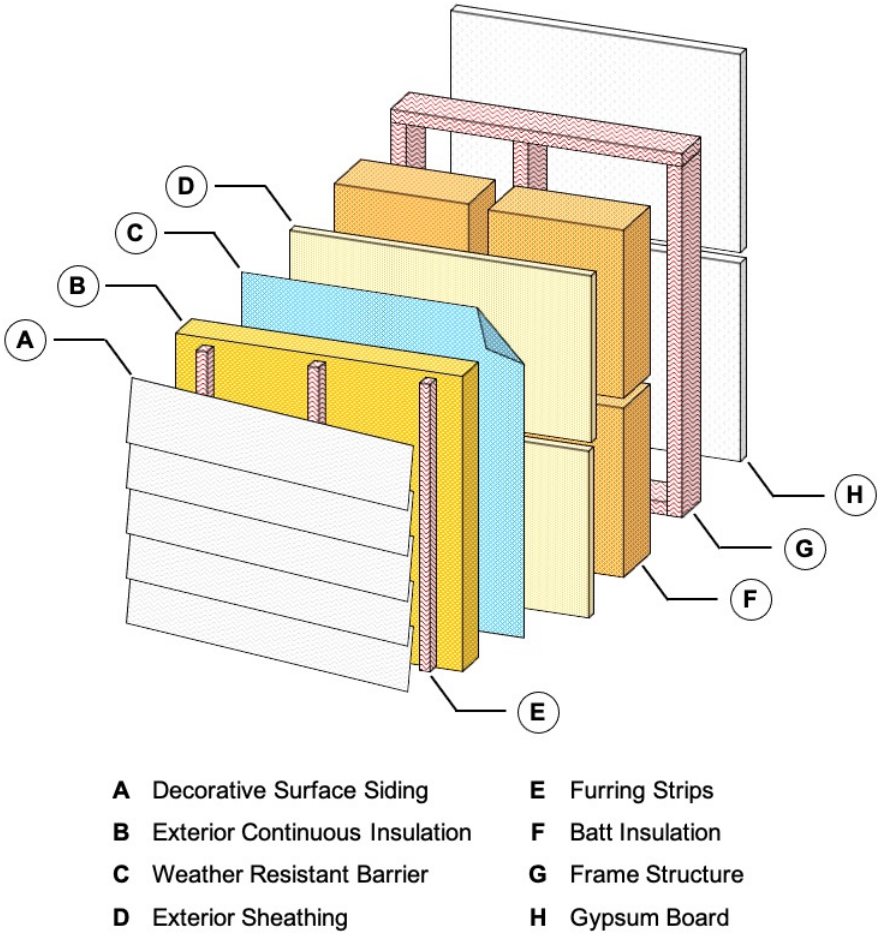

Figure 4.2: A schematic diagram of the large–scale test wall assembly

4.3 Test Wall Assembly Instrumentation

It was necessary to instrument the wall assembly appropriately to study its thermal response when subjected to a realistic (but contained) fire exposure. The test rig, therefore, needed to be instrumented sufficiently to monitor spatial and temporal temperature profiles within and across each layer throughout fire exposure. The instrumentation used here, and described in more detail below, was adapted from that specified in previous large–scale test rigs as outlined in Section 2.4.3.

The air gap and exterior gas temperatures adjacent to the decorative surface siding were instrumented by mounting a total of 39 Type–K (22–gauge) thermocouples (TC) on 11 rakes (denoted as T1–T11) as shown in Figure 4.3. TC trees T2, T4, T8, and T10, each having two probes, were suspended vertically along the mid–depth of the air gap between the vinyl siding and exterior continuous insulation, registering gas temperatures in the air cavity during a test. For the remaining rakes (T1, T3, T5, T6, T7, T9, and T11), each thermocouple probe was suspended 25 mm away from the exposed surface of the vinyl siding, measuring time variant air temperatures in the vicinity of the fire–side wall assembly face.

The underlying layer of exterior continuous insulation was instrumented with a total of 33 TC probes distributed over 11 rakes (T1–T11) as depicted in Figure 4.4. As the wall was being constructed, each thermocouple probe was placed half–way into the depth of the insulation core and mounted on the back face (unexposed side) of the layer.

A similar installation method was applied when instrumenting the exterior sheathing layer. A total of 25 thermocouples distributed over 9 rakes (T1, T3–T9, and T11) were placed half–way in to the oriented strand board sheet as outlined in Figure 4.5.

Finally, to instrument the back end (unexposed side) of the test wall 6 TC probes, distributed across 4 rakes, T3, T5, T7, and T9, were placed into the mid–depth of the interior layer of batt insulation and additional 5 TC probes, distributed across 3 rakes, T4, T6, and T8, into the half depth of wood stud frame bulk as shown in Figure 4.6.

Please note that the test wall dimensions and spacing between thermocouple locations shown in Figures 4.3 through 4.6 are expressed in mm.

All thermocouples were connected to back planes of a National Instruments distributed data acquisition system configured using the FieldPoint application. Temperature data was collected at a rate of 1.1 sample per second and logged, via ethernet connection, to a computer using a custom LabView script.

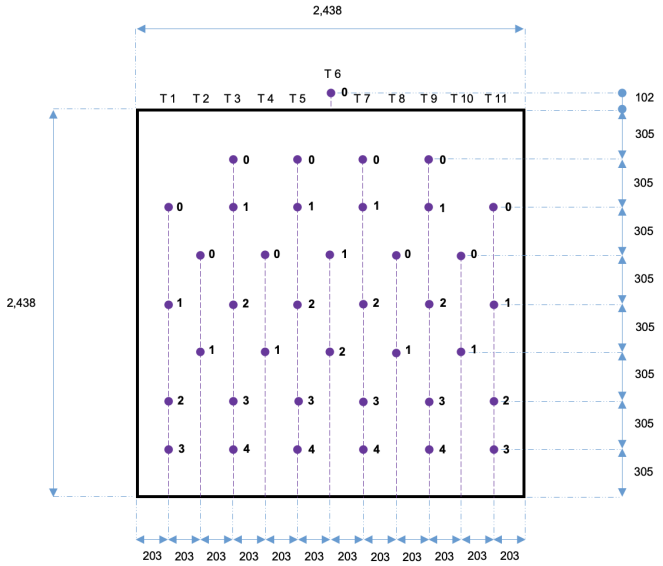

Figure 4.3: Details of instrumentation for the decorative surface siding layer

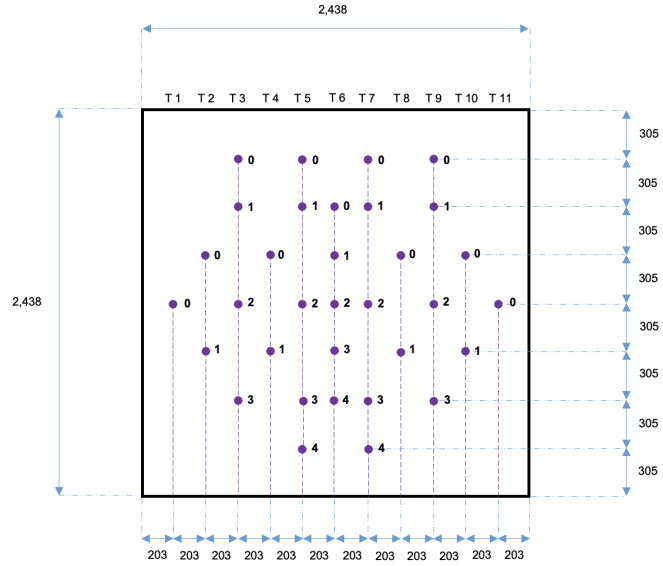

Figure 4.4: Details of instrumentation for the exterior continuous insulation layer

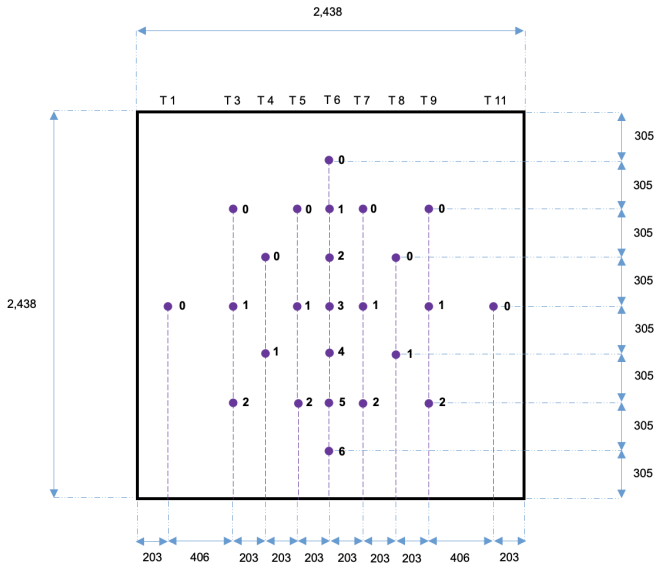

Figure 4.5: Details of instrumentation for the exterior sheathing layer

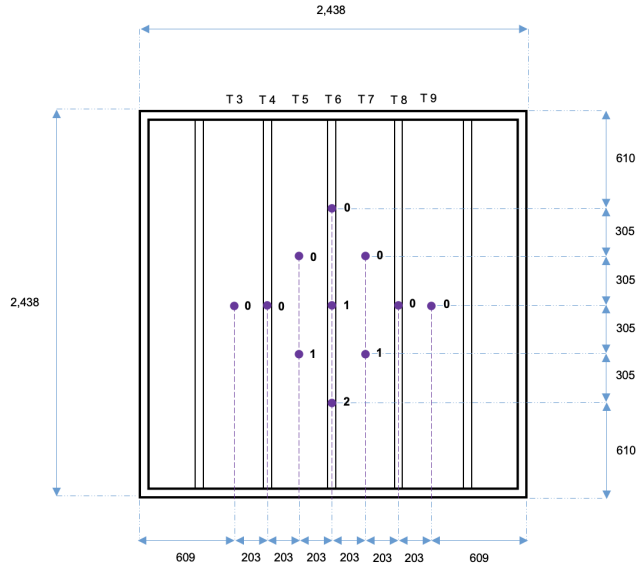

Figure 4.6: Details of instrumentation for the unexposed face of a test wall assembly

4.4 Fire Exposure

A major design consideration for the large–scale experiment is that the exterior wall section be subjected to a realistic, yet contained, fire exposure. In order to determine an appropriate severity of exposure, the guidelines of the Australian Standard, AS 3959:2018: Construction of Buildings in Bushfire–Prone Areas, were consulted in the absence of a national Candian equivalent [168]. The standard provides a regulatory framework for establishing construction requirements that achieve improved protection of building components from bushfires. In this regard, bushfire attack level, BAL, can be used to determine heat flux exposure levels, incident to the building's fire–side face, that correspond with potential severity of exposure from bushfire ember attack, radiant heat and direct flame contact. The various levels are summarized below:

- BAL–Low: There is insufficient risk to warrant any specific construction requirements;
- BAL–12.5: There is a risk of ember attack. The construction components are expected to be subjected to a maximum incident heat flux level of 12.5 kW/m^2;
- BAL–19: There is a risk of ember attack and a likelihood of exposure to radiant heat. The construction components are expected to be subjected to a maximum incident heat flux level of 19 kW/m^2;
- BAL–29: There is an increased risk of ember attack and a likelihood of exposure to an increased level of radiant heat. The construction components are expected to be subjected to a maximum incident heat flux level of 29 kW/m^2;
- BAL–40: There is a much increased risk of ember attack, a likelihood of exposure to a high level of radiant heat, and some likelihood of direct exposure to flames from the fire front. The construction components are expected to be subjected to an incident heat flux level no greater than 40 kW/m^2;
- BAL–FZ: There is an extremely high risk of ember attack, a likelihood of exposure to an extreme level of radiant heat, and direct exposure to flames from the fire front. The construction components are expected to be subjected to an incident heat flux level greater than 40 kW/m^2.

Incident heat flux levels corresponding to BAL–19 were selected in this study as an adequate level of exposure since the main objective was to gain preliminary insight into the extent of thermal penetration, and possibly damage, that an exterior wall assembly would experience when subjected to radiant heat from a realistic fire without direct flame impingement.

In order to achieve burning conditions and levels of incident heat flux needed in this research, wood cribs were constructed of 38 mm square softwood lumber pieces cut to 610 mm in length. Six pieces were placed in a row, equally spaced at 76 mm apart with the following row placed perpendicular to the adjacent row. Each crib contained six rows yielding a total stack height of 228 mm, and weighed on average around 15 kg. Two wood cribs were placed side by side to represent an approximate 500 kW design fire [169]. The fuel configuration is depicted in Figure 4.7. All lumber pieces were conditioned to moisture equilibrium in an environment at $21°C \pm 2°C$ and $50\% \pm 5\%$ relative humidity for at least 48 hours prior to testing. The average moisture content of the lumber pieces after conditioning was around 6%. The wood cribs were centrally positioned relative to the test wall and set at 1,000 mm away from its base.

Before each test, the wood cribs were placed on a raised support consisting of eight softwood lumber pieces, with two (2×2) stacks supporting a crib on each end, as shown in Figure 4.7. Such arrangement allowed for placement of fuel trays beneath the cribs and provided unconfined access for the ambient air to flow into the interior of the crib as it burned. The wood cribs were ignited by lighting 250 ml of ethyl alcohol (starter fuel) in small fuel trays under each crib.

Figure 4.7: Two wood cribs placed side by side representing a 500 kW design fire

4.5 Measurement of Heat Flux

In order to confirm the level of experimental heat flux and how it corresponded to levels indicated in BAL–19, a "blank" wall assembly was erected and exposed to the radiant heat from a typical 500 kW wood crib design fire positioned 1,000 mm away from the base of the wall.

The "blank" wall assembly was constructed with four 2,438 mm long × 152 mm wide × 50 mm thick wood frame pieces and five wood studs of the same dimensions spaced at 406 mm on center forming a six cavity configuration. Two sheets of cement board each measuring 2,438 mm long × 1,219 mm wide × 12 mm thick were mounted horizontally on the fire–side face of the wall. The seam between the two mounted sheets of cement board was covered with high temperature mortar. The fire–side surface of the "blank" wall assembly was then instrumented with eight heat flux gauges (HFG) positioned at locations determined through analysis of post–fire damage to the test walls.

Locations were chosen to correspond with the area that experienced the largest extent of damage and thermal penetration in the three large–scale wall assembly tests. These areas are presented in Figures 4.8, 4.9, and 4.10 for Walls #1, #2, and #3, respectively, wherein each red square (darker red squares correspond to the largest extent of observed thermal damage) represents a 305 mm × 305 mm area of mapped damage.

The contours from all three tests were overlaid in Figure 4.11 to identify the region with largest extent of damage and thermal penetration. The region was determined to be an area measuring 610 mm × 610 mm located centrally on the wall face and sitting 305 mm above its base as outlined with thick black border on Figure 4.11. Based on the analysis, the eight heat flux gauges were placed within and around the perimeter of this damage region as represented by white dots in Figure 4.11.

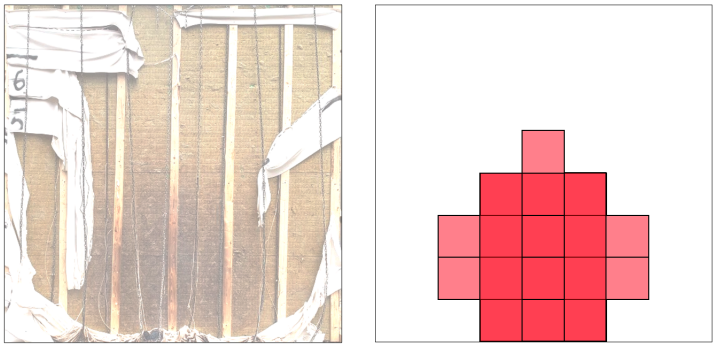

Figure 4.8: Damage contour observed on Wall #1

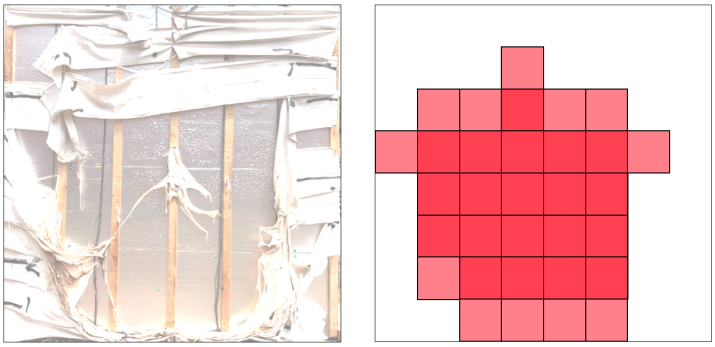

Figure 4.9: Damage contour observed on Wall #2

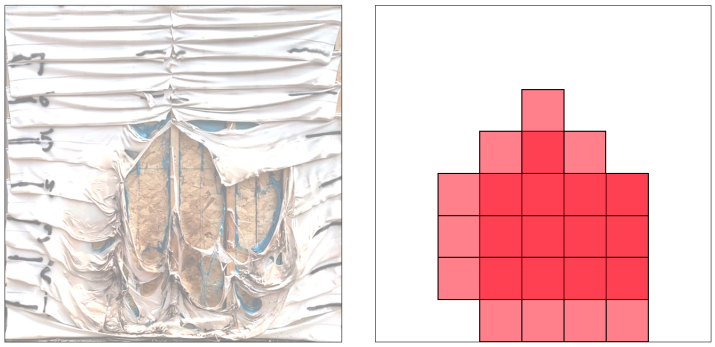

Figure 4.10: Damage contour observed on Wall #3

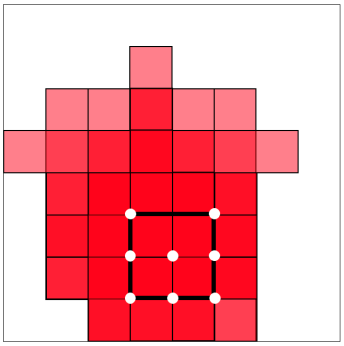

Figure 4.11: Damage contour mapped over Walls #1, #2, and #3

Eight heat flux gauges of two different types were used in this test: two Gardon gauges and six directional flame thermometer (DFT). The heat flux gauge budget was dictated by the number of available and operational sensors at the test facility.

The Gardon gauge (Figure 4.13a) employed in this work was a water–cooled sensor measuring 25 mm in diameter and 25 mm tall. It had a sensing foil (4.7 mm in diameter and 0.013 mm thick) that produced a voltage output linearly related to the incident heat flux through a calibration curve (Equation 4.1). The sensing surface of the gauge had an emissivity of 0.94 with the full–scale output of 150 kW/m^2.

$$\text{Incident Heat Flux}\left(\text{kW/m}^2\right) = 9.17\times\text{Signal}\left(\text{mV}\right) + 0.12 \tag{4.1}$$

The calibration curve presented in Equation 4.1 was obtained by correlating the raw voltage output from the gauge against varying levels of known incident heat flux. To achieve this, the Gardon gauge was exposed to ten levels of external heat flux, from 5 kW/m^2 to 75 kW/m^2, imposed by the conical heater of the cone calorimeter. Prior to exposure, the target incident heat flux was confirmed (measured) independently via the cone calorimeter's water–cooled heat flux gauge with manufacturer specified calibration parameters. Once the prescribed level of radiant heat flux was achieved, the concerning Gardon gauge was subjected to the imposed external irradiance. At each incident heat flux, the output signal from the gauge was logged until at least 20 seconds of quasi steady–state response was acquired. The obtained signal output was then averaged across the duration of steady–state response. The results of the calibration procedure are presented in Table 4.1. By obtaining several output signals at varying levels of external heat flux, a linear trend–line was fit to a scatter plot of the measured quasi–steady irradiance (kW/m^2) versus average Gardon gauge output signal (mV); this is shown in Figure 4.12. The gauge's calibration curve (Equation 4.1) is then represented by the slope of this trend–line.

Table 4.1: Average signal output from Gardon gauge at each set level of irradiance

Target Irradiance (kW/m^2)	Measured Irradiance (kW/m^2)	Gardon Gauge Signal Output (mV)
5 ± 0.5	5.3	0.61 ± 0.01
8 ± 0.5	8.2	0.86 ± 0.01
11 ± 0.5	11.2	1.13 ± 0.02
14 ± 0.5	14.4	1.53 ± 0.02
19 ± 0.5	19.4	2.08 ± 0.03
29 ± 0.5	28.8	3.29 ± 0.04
42 ± 0.5	41.7	4.57 ± 0.02
49 ± 0.5	49.4	5.39 ± 0.05
60 ± 0.5	60.1	6.42 ± 0.06
75 ± 0.5	74.7	8.15 ± 0.02

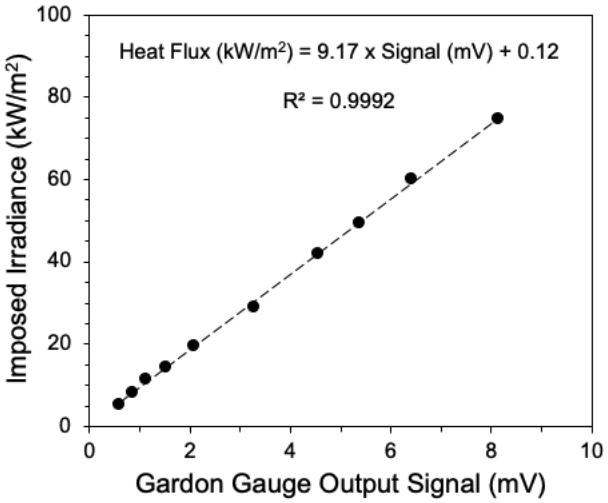

Figure 4.12: Linear trend–line fit to the scatter plot of imposed irradiance versus average gauge signal output

(a) Gardon gauge

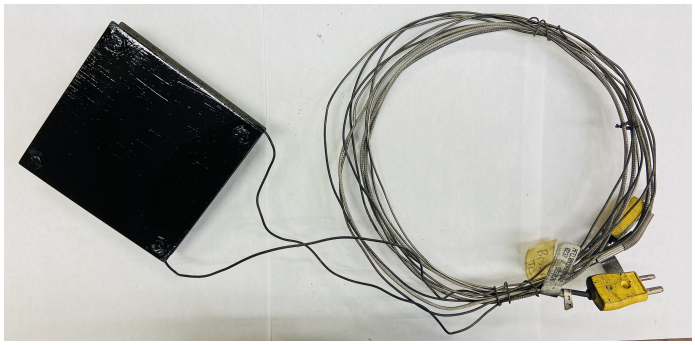

(b) directional flame thermometer

Figure 4.13: Photograph of (a) Gardon gauge and (b) directional flame thermometer

In contrast, the directional flame thermometers (Figure 4.13b) were not water–cooled and required use of an inverse heat conduction analysis to estimate the total incident heat flux. The DFT's were of sandwich construction with two 120 mm × 120 mm × 3.2 mm thick outer Inconel sensor plates separated by a 12 mm thick layer of 7% dense FeCrAIM metal felt insulation. Each Inconel sensor plate was instrumented with a Type–K thermocouple (1.6 mm in diameter) attached to the centre of its unexposed face. The exposed (fire–side) faces of the sensor plates were coated with a thin layer of Pyromark Series 2500 flat black paint to achieve a uniform gray surface with an emissivity of 0.85. The thermocouples attached to the unexposed side of the sensor plates were connected to a data acquisition system and the collected data was reduced to net heat flux following the Energy Storage Method outlined in ASTM E3057–16 [170] which is presented in Equation 4.2 below.

$$q_{net} = (\rho C_p(T))_{pl} L_{pl} \frac{dT_{front}}{dt} + k_{ins}(T) \frac{T_{front} - T_{back}}{L_{ins}} + (\rho C_p(T))_{ins} L_{ins} \frac{dT_{ins}}{dt} \tag{4.2}$$

with

$$(\rho C_p(T))_{pl} = 0.0018 \times T(^\circ C) + 3.7006 \tag{4.3}$$

$$k_{ins}(T) = 0.0011 \times T(^\circ C) - 0.0876 \tag{4.4}$$

$$(\rho C_p(T))_{ins} = 0.0004 \times T(^\circ C) + 0.2794 \tag{4.5}$$

$$T_{ins} = \frac{T_{front} + T_{back}}{2} \tag{4.6}$$

The final placement of heat flux gauges on the "blank" wall surface is schematically depicted in Figure 4.14a, where heat flux gauges (HFG's) 1, 2, 3, 5, 6, and 8 are the six DFT's and HFG's 4 and 7 are the two Gardon gauges. Please note that the "blank" wall dimensions and spacing between heat flux gauge locations shown in Figure 4.14a are expressed in mm. The photograph of the instrumented "blank" wall assembly is shown in Figure 4.14b.

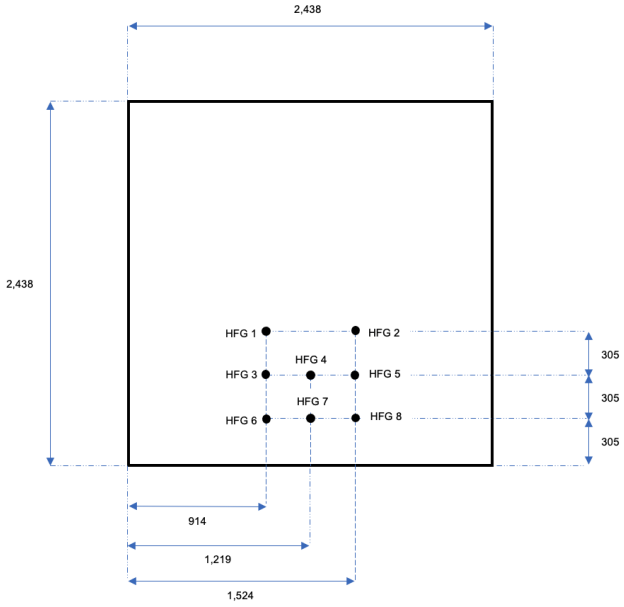

(a) Schematic Diagram

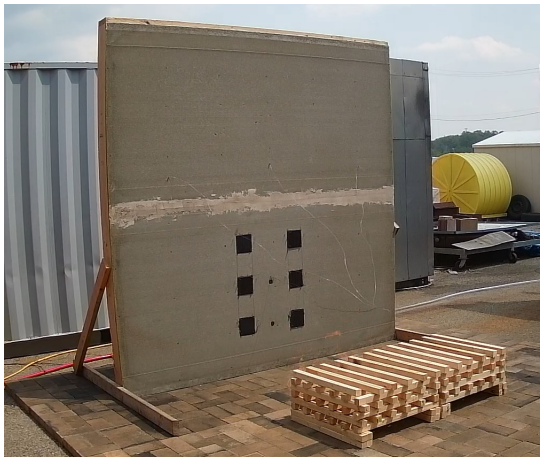

(b) "Blank" Wall Photograph

Figure 4.14: Placement of heat flux gauges on the fire-side surface of the "blank" wall: a) schematic diagram and b) photograph of the instrumented wall

Time–resolved traces of measured total heat flux from the fire incident to the exposed blank wall face are presented in Section 4.6.1 below.

4.6 Results and Discussions

In this section, the results of the large–scale tests are presented and discussed. First, the fire exposure symmetry and the total heat flux incident to the fire–side wall surface are examined, followed by presentation of results for the three large–scale wall tests, wherein each wall was lined with one type of exterior continuous thermal insulation. Comparison of through–wall heat transfer across the large– and composite–scale (sandwich) tests is then outlined for each wall and sandwich configuration of a similar assembly along with discussions of the scale effects from the obtained temperature–time data.

4.6.1 Total Heat Flux Incident to Fire–Side Wall Surface

The "blank" wall assembly, covered with one layer of non–combustible (cement board) cladding on its fire–side surface, was instrumented with eight heat flux gauges and exposed to the radiant heat from a 500 kW design fire positioned 1,000 mm away from the base of the wall. The fire was fuelled by two wood cribs, weighing 13.37 kg and 14.75 kg with 0%–6% moisture content, placed side by side and ignited with starter fuel as described in Section 4.4. The test was conducted to confirm the level of incident heat flux to the wall during the exposure experiments and determine how well it corresponded to the selected level of exposure indicated in BAL–19 in Section 4.4. Measurements of total heat flux incident on the fire–side wall surface were collected by the data acquisition system from all heat flux gauges. The distance between the flame front and the exposed wall surface was concurrently captured with video cameras throughout the test duration. Key parameters describing the local ambient environment (temperature, relative humidity, wind speed and direction) were also logged at five–minute intervals throughout the test and are presented in Table 4.2. From the logged data tabulated in Table 4.2, it can be seen that the ambient environment did not change significantly throughout the experiment. The average ambient temperature, relative humidity and wind speed remained as 25°C, 53%, and 8 km/h, respectively. The test was concluded 30 minutes after ignition, corresponding to nearly complete consumption of the wood cribs and extinction of visible design fire flames. The remaining smouldering fuel was manually extinguished. Data logging was stopped ten minutes following visible flame extinction. This was done to capture information related to the background irradiance seen by the gauges at the wall after exposure.

Table 4.2: Local ambient environment logged throughout "blank" wall test duration

Test Time (mm:ss)	Ambient Temperature (°C)	Relative Humidity (%)	Wind Speed, Direction (km/h), Cardinal Direction
00:00	25	53	8, East–Southeast
05:00	25	53	8, East–Southeast
10:00	25	53	8, East–Southeast
15:00	25	54	8, East–Southeast
20:00	25	52	8, East–Southeast
25:00	25	54	8, Southeast
30:00	25	54	8, Southeast

Details of construction and instrumentation of the "blank" wall were previously presented in Section 4.5. The locations of the heat flux gauges depicted schematically in Figure 4.14, their types and distances relative to the left edge and bottom of the "blank" wall face are reiterated in Table 4.3 for convenience in drawing comparisons when discussing the results.

Table 4.3: Heat flux gauge locations relative to the left edge and bottom of the fire–side "blank" wall face

Heat Flux Gauge #	Heat Flux Gauge Type	Distance from Left Edge (mm)	Distance from Bottom (mm)
1	Directional Flame Thermometer	914	915
2	Directional Flame Thermometer	1,524	915
3	Directional Flame Thermometer	914	610
4	Gardon Gauge	1,219	610
5	Directional Flame Thermometer	1,524	610
6	Directional Flame Thermometer	914	305
7	Gardon Gauge	1,219	305
8	Directional Flame Thermometer	1,524	305

Vertical distributions of total heat flux due to the fire incident on the exposed wall assembly surface were examined initially. For this, the measurements from the heat flux sensors on the wall are grouped into three clusters dependent on their location relative to the wall centre line such that:

- heat flux gauges 1, 3 and 6 are collectively referred to as "left" heat flux gauges;
- heat flux gauges 4 and 7 are collectively referred to as "centre" heat flux gauges; and
- heat flux gauges 2, 5 and 8 are collectively referred to as "right" heat flux gauges.

Figures 4.15, 4.16, and 4.18 show time–histories of measured total heat flux from gauges at locations 1 through 8, grouped into the three clusters: "left", "centre", and "right", respectively.

Time–varying total heat flux profiles for the "left" gauges are presented in Figure 4.15 which shows an overlay of traces from the three locations 1, 3 and 6. The time–resolved profiles of measured total heat flux were very similar (to within 6.2%) at locations 1 and 3, the highest and middle locations on the left side of the wall with maximum values of 9.6 kW/m^2 and 10 kW/m^2, respectively. In comparison, the maximum total heat flux measured at the lowest location on the wall, location 6, was only half that, peaking at a value of about 5.5 kW/m^2.

Values of total heat flux measured at the two centre heat flux gauge locations are overlaid and presented in Figure 4.16. Similar to the measured heat flux profiles at locations 1 and 3, the total heat flux traces for the "centre" heat flux gauges appeared to closely follow each other to within 4.3%. Also as anticipated, the maximum heat flux measured at the wall centre line was slightly higher (by approximately 3–4 kW/m^2) than that recorded on the left side of the wall. Twin–peaks in heat flux (with nearly identical localized peak values) can be seen in Figure 4.16 at test times of 10 and 15 minutes, with a local minimum at 12.5 minutes, for both locations 4 and 7. These were linked to flame tilt which brought the fire plume closer in proximity to the exposed wall surface. The angles of the flames from the fire relative to the fire–side wall surface are shown in Figure 4.17 for test times of 10, 12.5 and 15 minutes. This clearly illustrates that when the flame tilted towards the centre of the wall at times of 10 and 15 minutes into the test (Figures 4.17a and 4.17c) a higher incident heat flux was registered due to the decreased distance between the fire and measurement gauges, with lower incident flux at a time of 12.5 minutes when the flame tilted away from the exposed wall surface (Figure 4.17b).

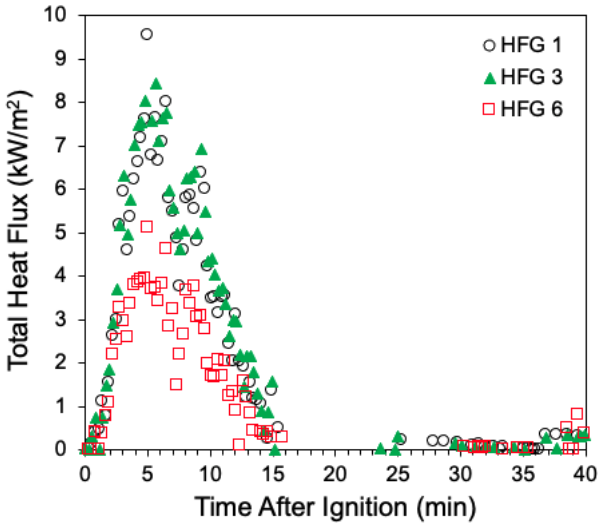

Figure 4.15: Time–resolved total heat flux profiles measured on the "blank" wall from "left" heat flux gauges cluster

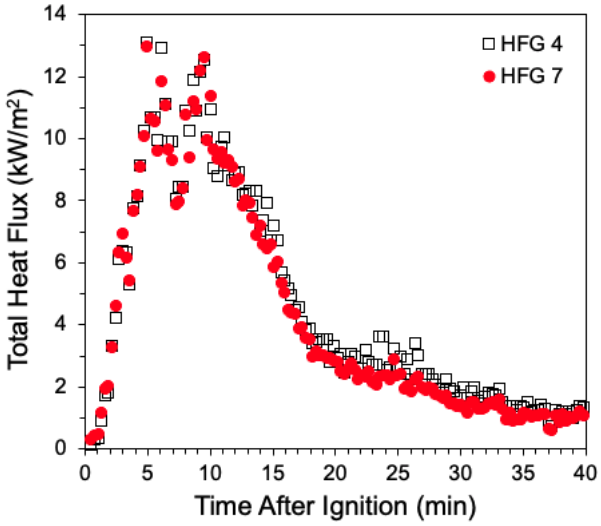

Figure 4.16: Time–resolved total heat flux profiles measured on the "blank" wall from "centre" heat flux gauges cluster

(a) Test Time = 10:00

(b) Test Time = 12:30

(c) Test Time = 15:00

Figure 4.17: The proximity of the design fire flame tilt relative to the fire–side wall face at test times of a) 10 minutes, b) 12.5 minutes, and c) 15 minutes

Time–dependent traces of total heat flux measured for the "right" heat flux gauges are overlaid and presented in Figure 4.18 for heat flux gauge positions 2, 5, and 8 in the "right" cluster. The time–resolved profiles of measured total heat flux were very similar, to within 11.5%, at all three locations exhibiting peak values of approximately 8.4 kW/m^2, 8.8 kW/m^2 and 8.4 kW/m^2, at locations 2, 5, and 8, respectively. These values were slightly lower (by approximately 1.2 kW/m^2) than those measured at corresponding heights on the left side of the wall, with the exception of the lowest gauge, where the peak total heat flux on the right side (location 8) was about 3 kW/m^2 higher than the maximum at location 6 on the left side. The discrepancy in values between the left and right heat flux gauges at similar heights suggested that there might be an asymmetry in the fire plume, albeit not too large, as heat fluxes measured by both left and right clusters were lower than at the centre.

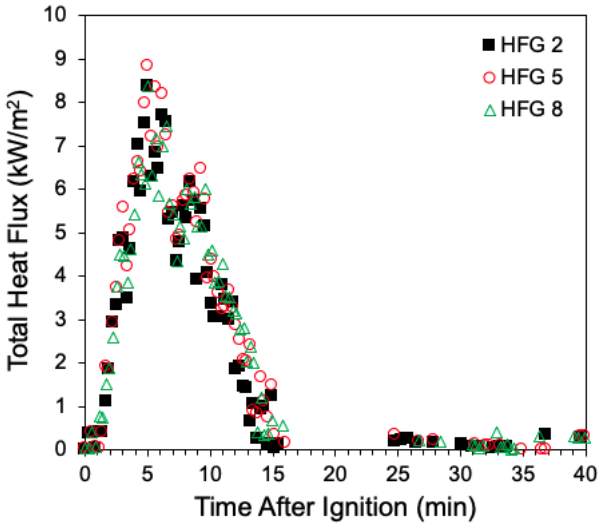

Figure 4.18: Time–resolved total heat flux profiles measured on the "blank" wall from "right" heat flux gauges cluster

In order to explain the discrepancies in heat flux values observed above, and to further examine any connection between the size and position of the fire plume and measured heat flux at the wall, horizontal distributions of measured total heat flux were compiled from the gauges at each height above the ground as:

- the "upper" group refers to heat flux gauges at positions 1 and 2;
- the "middle" group refers to heat flux gauges at positions 3, 4, and 5; and
- the "lower" group refers to heat flux gauges at positions 6, 7, and 8.

These groups were selected based on the relative distances of the heat flux gauges to the centre of the flame, as well as to the damage contour outlined with the thick black border in Figure 4.11. Overlays of measured results from gauges in the "top", "middle", and "bottom" groups are shown in Figures 4.19a, 4.19b, and 4.19c, respectively.

As shown by the higher values of total measured heat flux at central locations of 4 and 7 in comparison to those recorded at other positions, it is clear that the fire plume was anchored to the center of the fuel bed for a large portion of the test. Moreover, the total incident heat flux on the exposed wall was highest across the "middle" heat flux gauges as anticipated when looking at the projection of the flame core onto the wall surface as shown in Figure 4.20. Heat flux gauges 4 and 7 were located in the core of the projected area with heat flux gauges 3 and 5 being closer to outer edges of the projection consistent with observations in comparing across gauges within the "left" and "right" groups in Figures 4.15 and 4.18, respectively, as well. Further, the total heat flux measured at "upper" locations (HFG's 1 and 2) was slightly higher than from "lower" locations (HFG's 6 and 8). This was most likely because the heat flux gauges at locations 6 and 8 were aligned with the top of the fuel crib, which was less–emissive than the open flames since it was compromised of a mix of flame and charred wood, while the "upper" heat flux gauges were directly exposed to the fire plume above the fuel bed as depicted in Figure 4.20. Overall, the total heat flux measured on the surface of the fire–side wall mirrored the geometry of the flaming fire plume with highest incident flux at the "middle–centre" and "lower–centre" locations, followed by "upper–left" and "upper–right", "lower-right" and finally "lower–left". At the centre of the wall, levels of measured heat flux corresponded to the selected level of exposures indicated in BAL–19 in Section 4.4 so the described design fire was used in the remainder of the wall exposure tests.

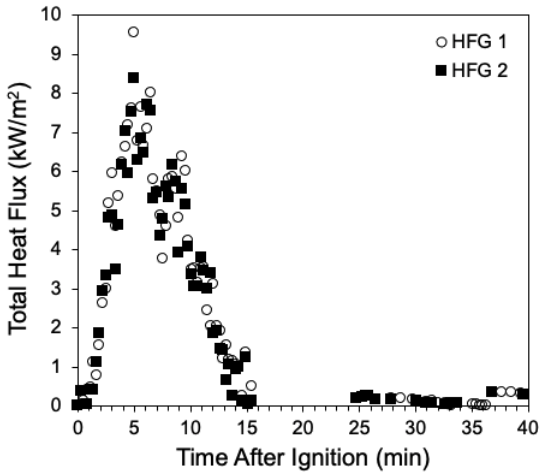

(a) Heat Flux Gauges 1 and 2

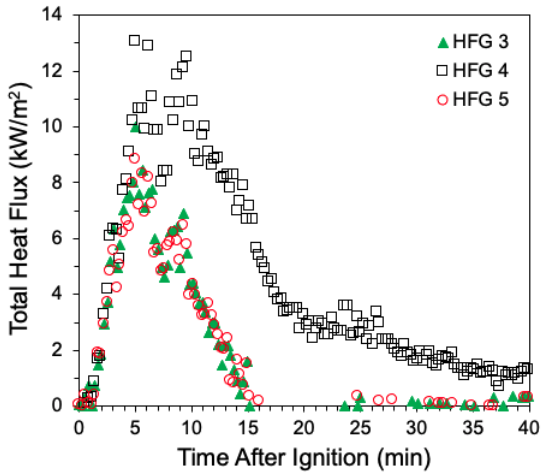

(b) Heat Flux Gauges 3, 4, and 5

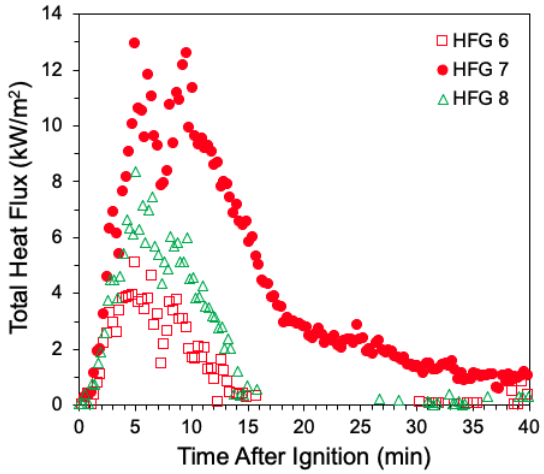

(c) Heat Flux Gauges 6, 7, and 8

Figure 4.19: Exposure symmetry: time–histories of total heat flux incident to the exposed "blank" wall measured at heat flux gauge locations of a) 1 and 2, b) 3, 4, and 5, and c) 6, 7, and 8 as shown in Figure 4.14

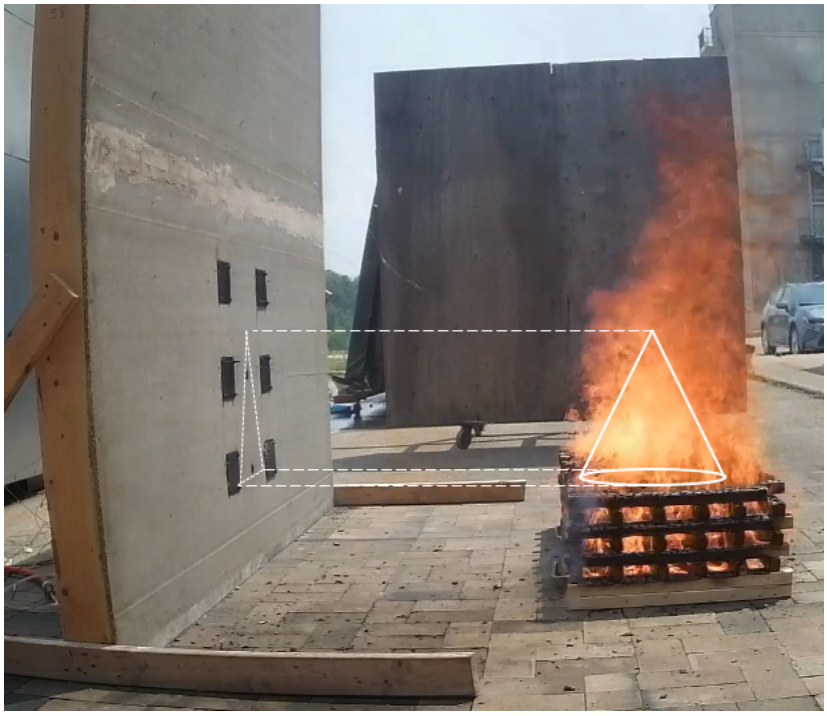

Figure 4.20: The design fire plume core and its projection onto the exposed wall surface

4.6.2 Wall #1 – Rigid Stone Wool Insulation

Test 1 involved an exterior wall assembly lined with rigid stone wool insulation. The wall was instrumented as described in Section 4.3. The exposure fire was fuelled by two wood cribs, weighing 14.02 kg and 14.33 kg with 0%–6% moisture content, placed side by side and ignited with the starter fuel as described in Section 4.4. Following ignition, temperature data was collected to the NI DAQ from all of the thermocouple trees concurrently with video capture of the visual state of the wall. Local ambient environment (temperature, relative humidity, wind speed and direction) was also logged at five–minute intervals throughout the test. From the results in Table 4.4, it can be seen that the ambient environment did not change significantly throughout the experiment. The average ambient temperature, relative humidity and wind speed remained as 24°C, 40%, and 17 km/h, respectively. The test was concluded 30 minutes after ignition, corresponding to nearly complete consumption of the wood cribs and visible flame extinction. The remaining smouldering fuel was manually extinguished.

Table 4.4: Local ambient environment throughout Wall #1 test duration

Test Time (mm:ss)	Ambient Temperature (°C)	Relative Humidity (%)	Wind Speed, Direction (km/h), Cardinal Direction
00:00	24	40	18, East
05:00	24	40	18, East
10:00	24	39	18, East
15:00	24	39	18, East
20:00	24	39	18, East
25:00	24	40	16, East
30:00	24	41	16, East

Table 4.5 lists the timeline of experimental observations (events) recorded during the test to describe the thermal response of the wall as observed on the fire–side surface. Events marked in **bold** in Table 4.5 are paired with video images and still camera photographs that depict the extent of thermal damage in Figure 4.21.

Table 4.5: Timeline of events recorded during Wall #1 test

Test Time (mm:ss)	Event
00:00	Ignition of fuel trays marked the beginning of the test. The initial state of the wall assembly is depicted in Figure 4.21a.
02:14	Softening of vinyl siding panels affixed 610 mm above the base of the wall.
02:35	Softening of vinyl siding panels affixed 915 mm above the base of the wall.
02:52	Softening of vinyl siding panels affixed at mid level (1,220 mm) of the wall. Onset of buckling of siding panels at 610 mm height.
05:50	Siding panels affixed at 1,220 mm and 1,525 mm above the wall base started to warp.
06:30	Softening of vinyl siding panels affixed 1,830 mm above the base of the wall.
06:57	Softening of vinyl siding panels affixed 2,135 mm above the base of the wall. Siding panels installed up to 915 mm above the wall base buckled along their length from edge to edge between the horizontal extremes of the wall.
07:05	Softening of the siding panels at the top of the wall assembly. Edge–to–edge buckling of all siding panels affixed up to 1,525 mm height of the wall assembly.
07:47	Detachment and partial collapse of siding panel at mid–level of the wall. This partial collapse exposed a 812 mm long strip of the underlying layer of stone wool insulation from the right edge of the wall. The state of the wall at this time is depicted in Figure 4.21b.
08:22	Edge–to–edge buckling of all siding panels affixed up to 2,135 mm of wall height.
09:21	Mid–level siding panel collapsed further revealing an additional 406 mm long strip of the underlying stone wool insulation face. The melted siding panels at the center of the wall collapsed sagging towards the base of the wall under gravity. The state of the wall at this time is depicted in Figure 4.21c.
09:35	Siding panel affixed at 915 mm height partially collapsed under the weight imposed by above hanging panel.
09:41	Detachment and partial collapse of siding panel originally affixed 1,525 mm above the wall base. This partial collapse exposed a 812 mm long strip of the underlying layer of stone wool insulation from the right edge of the wall assembly.

Test Time (mm:ss)	Event
10:28	Siding panel at wall mid–level height partially detached from its nailing base revealing an additional 406 mm strip of underlying stone wool insulation face. This panel collapsed onto thermocouple tree T3 upon detachment.
11:04	Siding panels at 915 mm and 2,135 mm heights partially collapsed onto thermocouple trees T11 and T9, respectively. Apparent surface discolouration of the exposed underlying stone wool insulation due to increased radiant heat from the fire. Charring of melted vinyl siding panels at the bottom of the wall. The state of the wall at this time is depicted in Figure 4.21d.
11:37	Partial collapse of siding panels at 1,525 mm and 2,135 mm wall heights.
12:11	Siding panel at 2,135 mm wall height detached from its nailing base, and collapsed onto thermocouple tree T7.
12:59	Siding panel originally affixed at 2,135 mm height fell to the ground.
13:22	Siding panel affixed at 1,830 mm height detached from the mid–level furring strip, and collapsed onto thermocouple tree T5. Considerable surface discolouration of exposed stone wool face up to wall mid–level. Slight charring of exposed wood furring strips at the center of the wall. The state of the wall at this time is depicted in Figure 4.21e.
14:13	Further detachment and significant melting of siding panels affixed to the wood furring strips at the edges of the wall.
15:48	No further change in the state of the wall regarding thermal damage. The final state of the wall assembly is depicted in Figure 4.21f.

(a) Test Time = 00:00 (Ignition)

(b) Time after Ignition = 07:47

(c) Time after Ignition = 09:21

(d) Time after Ignition = 11:04

(e) Time after Ignition = 13:22

(f) Time after Ignition = 15:48

Figure 4.21: The extent of damage on fire–side Wall #1 face at select times for events listed in Table 4.5

(a)

(b)

Figure 4.22: The state of exposed Wall #1 face (a) before and (b) after exposure to the total incident heat flux from the design fire

The state of the fire–side (exposed) face of Wall #1 before and after exposure is shown in Figure 4.22. Consistent with small–scale results seen for vinyl siding when tested in Sandwich #1 (Section 3.4.2) scaled assemblies, the layer of vinyl siding on the exposed wall surface softened and buckled shortly after the onset of exposure to radiant heat from the wood crib fire. Under continued exposure, the siding material started to melt and sag towards the bottom of the wall assembly, detaching at the nails. This left the underlying stone wool partially exposed to the incident heat flux from the design fire. As a result, the bottom central portion of stone wool insulation face discoloured on the fire–side, seen as tones of orange to brown in Figure 4.22 and indicating significant thermal degradation following the exposure. The thermal damage was consistent with signs of binder decomposition noted previously in post exposure samples of stone wool insulation tested in the cone calorimeter under similar values of heat flux. As can be seen from Figure 4.22, thermal damage for both the siding material and stone wool insulation was greatest across the bottom half of the exposed wall surface. This was because the value of total heat flux from the fire to the exposed wall face, around 14 kW/m^2 at the peak, was highest across this region (Section 4.6.1). There were no noticeable changes in colour or geometry and charring was not evident in the post–exposure state of either the weather resistant barrier or oriented strand board layers due to the presence of the 32 mm thick continuous slab of stone wool insulation that remained intact throughout the test and shielded these under layers from exposure to the fire.

To further understand the effects of each layer on the overall thermal performance of the wall assembly under exposure from the design fire, it is of interest to examine the time–histories of temperature that were measured through the bulk wall layers. For this, a line plot of temperature versus time is shown in Figure 4.23 for thermocouples T6–2 of the siding layer (Figure 4.3) positioned 25 mm away from its exposed surface, T6–4 positioned at the mid–depth of the stone wool insulation (Figure 4.4), and T6–5 at the mid–depth of the oriented strand board (Figure 4.5) where the latter two probes were installed 1,219 mm and 610 mm away from the left edge and bottom of the wall assembly, respectively, locations where highest total incident heat flux to the wall was registered (Section 4.6.1). The total heat flux from the fire incident on the wall face at that position is overlaid with temperature–time traces. It should be noted that thermocouple T6–2 for the siding layer (Figure 4.3) was positioned 1,219 mm and 915 mm away from the left edge and bottom of the wall assembly, respectively, since there was no thermocouple located 1,219 mm and 610 mm on that rake. Discussions regarding the thermal penetration through each layer, its impact on recorded rates of temperature rise and subsequent temperature profiles of the heated exterior wall components are presented and compared with results from the small–scale tests below.

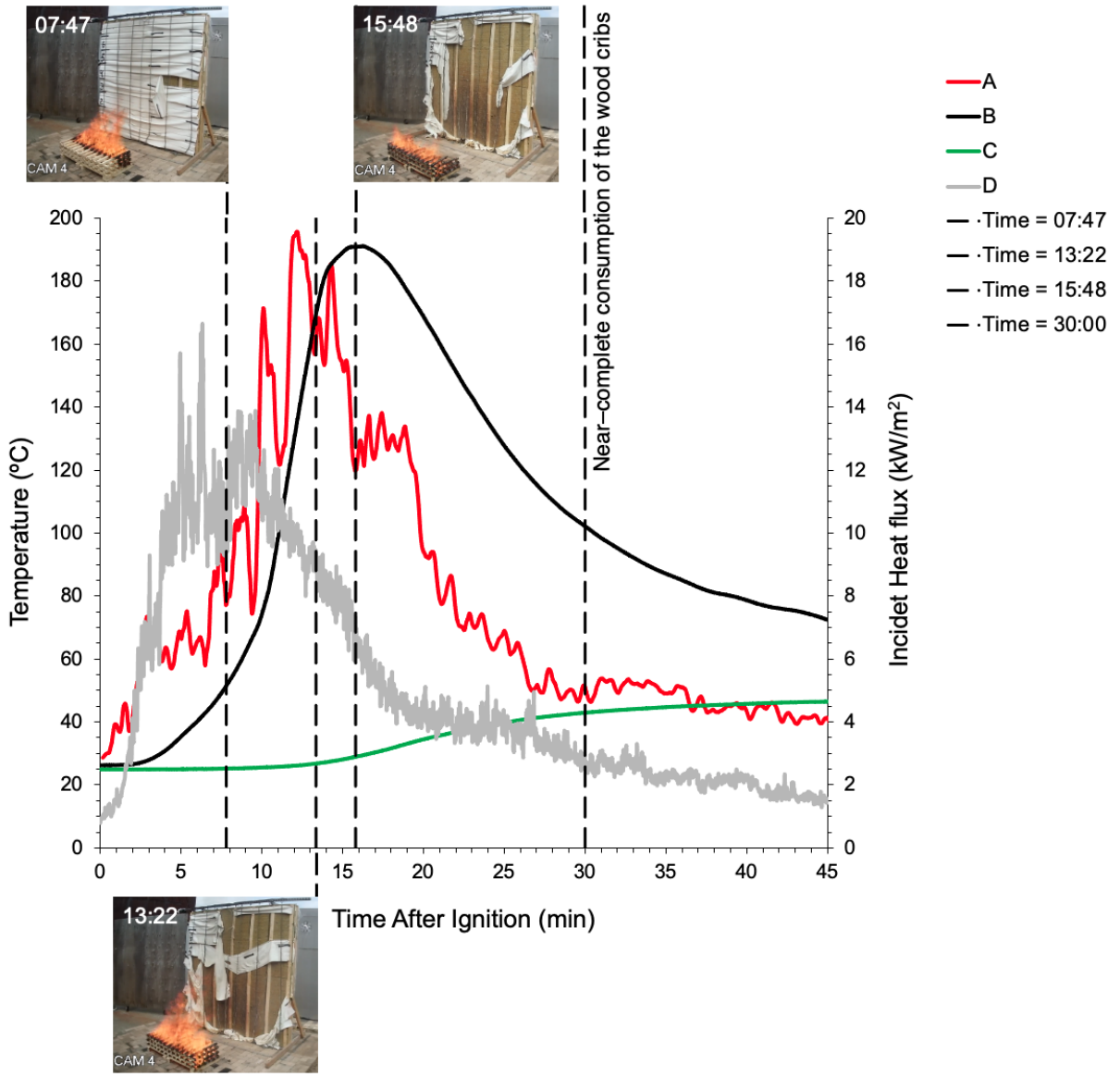

Figure 4.23: Wall #1: Temperature–time traces after ignition recorded from thermocouples T6–2 of the siding layer (A), T6–4 of the stone wool insulation (B), and T6–5 of the oriented strand board (C) overlaid with total incident heat flux profile from HFG #4 (D)

As can be seen from trace "D" in Figure 4.23, after ignition of starter fuel, the design fire grew in size to a peak of about 13 kW/m^2 $\pm$ 3 kW/m^2 between 5 and 10 minutes following ignition. During this time, significant warping of vinyl siding panels was observed, especially along the centre line of the wall. At about 7 minutes and 47 seconds into the test, detachment and partial collapse of vinyl siding panel at mid–level of the wall was noted (Table 4.5). Over this time, the thermocouple at the mid–depth of the stone wool registered a gradual increase in temperature, reaching around 75°C at 10 minutes. The rate of temperature rise then intensified, with that location in the stone wool insulation reaching a peak temperature of about 191°C at 15 minutes and 48 seconds following ignition. A contour plot of temperatures measured by thermocouples positioned across the mid–depth of the stone wool insulation is shown in Figure 4.24 for this time. As can be seen by the vertical and horizontal temperature gradients throughout the mid–depth of the stone wool insulation, thermal penetration into the depth of the wall was very location dependent. As expected, maximum thermal penetration occurred in the lower region of the wall where the incident heat flux was greatest. In contrast, in the middle and upper regions, temperature gradients varied both with height above the bottom of the wall and horizontally across the mid–plane insulation face marking the three-dimensional nature of heat penetration into the insulation layer.

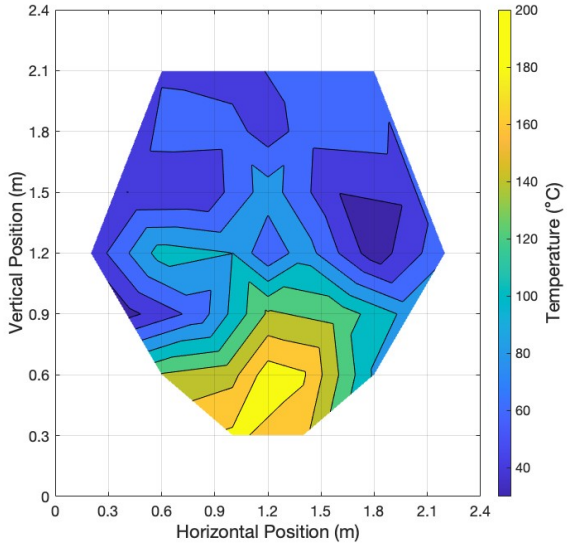

Figure 4.24: Wall #1: Contour plot of peak temperatures measured across the mid–depth face of stone wool insulation at Time = 15:48 after ignition

The accelerated increase in temperature at the mid–depth of the stone wool which began at 10 minutes following ignition corresponded with the collapse of the vinyl siding panels on the outer face of the wall and resulted in the stone wool face being exposed to the fire. This was supported by the photograph of the fire–side wall face taken at 13 minutes and 22 seconds after ignition (Figure 4.21e). Interestingly, this time also marked the onset of temperature rise at the mid–depth of the underlying oriented strand board, possibly suggesting that heat conducted into and retained in the stone wool began slowly penetrating further into the bulk of the wall assembly towards the unexposed side. This was further supported by the temperature–time traces "B" and "C" in Figure 4.23 recorded after 15 minutes and 48 seconds, where temperatures measured at the stone wool mid–depth gradually decayed due to decay of the fire, while the interior temperature of oriented strand board continued to rise. Thermal penetration through the bulk of the wall assembly appeared to continue after nearly complete consumption of the wood cribs (30 minute mark), as the stone wool temperature dropped from 102°C to 72°C, while temperature in the oriented strand board rose from around 42°C to 47°C between 30 and 45 minutes following ignition, respectively. To further visualize the two dimensional variation of temperature at various depths into the wall, contour plots of temperature are contained in Figures 4.25a and 4.25b for the mid–planes of the stone wool insulation and oriented strand board, respectively, at 45 minutes following ignition. Please note the difference in the colourbar scale limits on the subplots of Figure 4.25. As can be seen, maximum thermal penetration into all layers of wall assembly aligned with the highest incident heat flux across the lower region of the wall and temperatures varied both horizontally and vertically across both planes. On the backside of the wall, at the mid–depth of the in–cavity batt insulation and mid–depth of the wood studs, average temperature increases were minimal; at the end of the test these temperatures had risen only 0.4°C and 0.6°C, respectively, consistent with these layers remaining insulated from any incident radiation by the stone wool insulation.

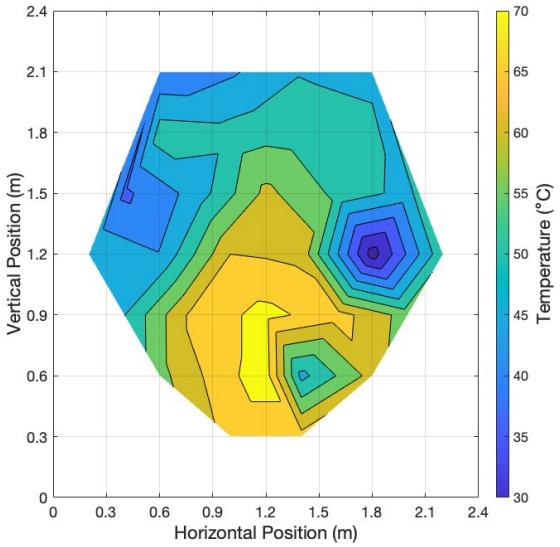

(a)

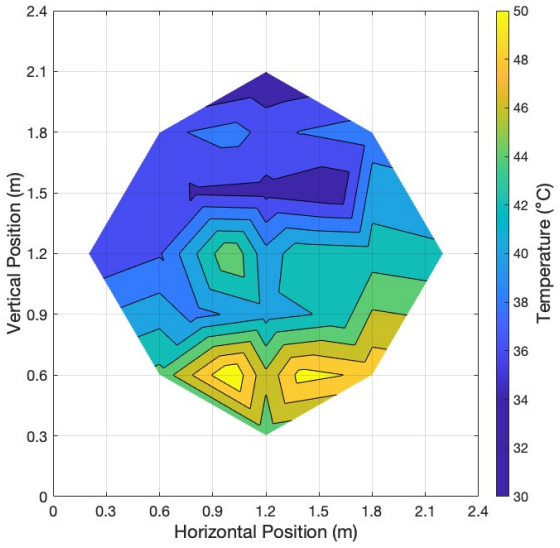

(b)

Figure 4.25: Wall #1: Contour plots of temperatures measured across the mid–depth face of (a) stone wool insulation and (b) oriented strand board at Time = 45:00 after ignition

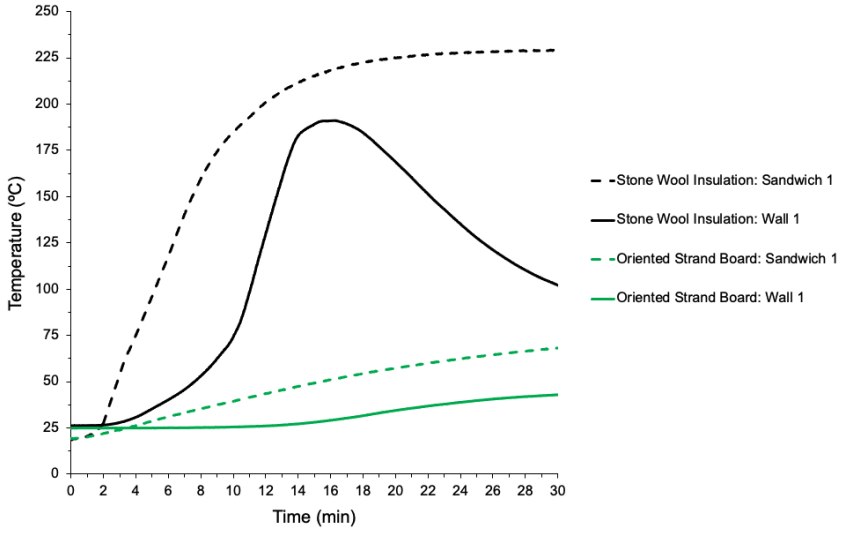

(a)

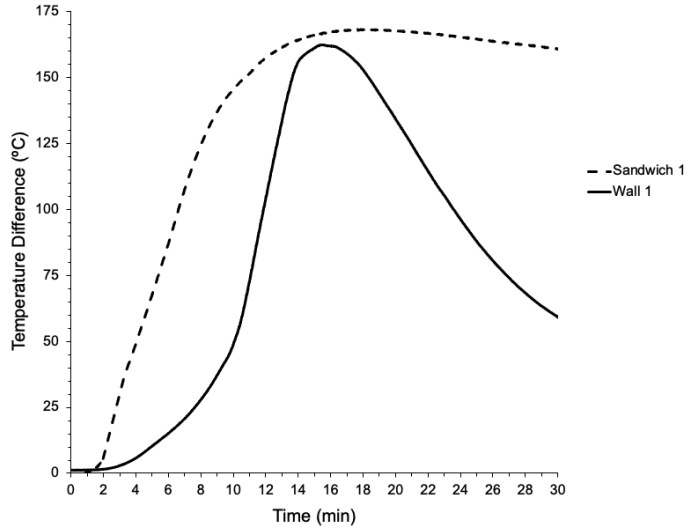

(b)

Figure 4.26: Time–histories of (a) temperatures measured at the mid–depth of extruded polystyrene foam and mid–depth of oriented strand board across Sandwich #1 and Wall #1 tests, and (b) their difference across the two sets of experiments

One of the main objectives of this work was to complement the previously conducted small–scale experiments with a limited set of larger–scale tests in order to investigate the fire performance of full exterior walls under a more realistic fire exposure. Therefore, in addition to the time evolution of temperatures measured within the wall assembly, it was also of interest to compare the thermal penetration into the bulk of the wall assemblies across the two scales. For this, first, a line plot of temperature versus time is shown in Figure 4.26a where temperatures recorded at the mid–depth of stone wool insulation and at the mid–depth of the underlying oriented strand board sheet are overlaid for Sandwich #1 and Wall #1 tests conducted under similar levels of incident radiant heat flux exposure; that is 15 kW/m^2 for Sandwich #1 and 13 kW/m^2 $\pm$ 3 kW/m^2 for Wall #1 experiments. These line plots were previously presented separately for Sandwich #1 and Wall #1 in Figures 3.22a and 4.23, respectively. To further illustrate through–wall heat transfer, the time–histories of temperature differences (taken as the difference in temperature across the mid–depth of stone wool insulation and the mid–depth of the oriented strand board) are plotted in Figure 4.26b.

As can be seen from Figure 4.26a, for the Sandwich #1 assembly, the increase in temperature at the centre of stone wool slab began around two minutes following the onset of exposure, gradually rose at a rate of 0.35°C/s and reached a plateau of 228.7°C $\pm$ 2.0°C after 16 minutes of heating. This profile of thermal penetration and temperature rise is consistent since the heat flux incident on the sample was uniform in both space and time. For Wall #1 assembly, the onset of temperature increase at the centre of stone wool slab occurred around 2 minutes after ignition of the wood cribs similar to the timing seen for heating of the sandwich assembly. Following this, however, the insulation in the wall assembly underwent varying rates of interior temperature rise until reaching a peak temperature of about 191°C at 15 minutes and 48 seconds following ignition of wood cribs. These rates were: 0.046°C/s between 2 and 5 minutes, 0.127°C/s between 5 and 10 minutes, and lastly 0.5°C/s between 10 minutes and 15 minutes after ignition. It is important to note that these differing rates of interior temperature rise at the mid–depth of stone wool were expected. The low rate of 0.046°C/s occurred while the design fire grew in size to its peak quasi–steady burning phase at around 5 minutes after ignition. This was followed by an increased rate of temperature rise of 0.127°C/s until about 10 minutes into the test when the vinyl siding melted, directly exposing the underlying stone wool insulation face to the radiant heat from the fire. After this time, the interior temperature of the now exposed insulation increased rapidly at a rate of 0.5°C/s until reaching a peak temperature of 191°C, after which the temperatures measured at the stone wool mid–depth gradually decayed due to decay of the fire.

The observed differences in the measured rates of interior temperature rise across the two scales of testing (Sandwich #1 vs. Wall #1) could therefore be attributed to differences in fire exposure profiles with time. In fact, the changes were consistent with results in Section 3.4.1 for individual stone wool insulation samples heated under different levels of external irradiance, where rates of temperature rise were 0.6°C/s for 15 kW/m^2 and 4°C/s at 50 kW/m^2 for example. Further, due to spatial gradients in exposure to the large Wall #1, any heat penetrating into the bulk of stone wool insulation from the fire was conducted in three dimensions. In contrast for Sandwich #1 assemblies under uniform exposure, heat transfer through the assembly was closer to one–dimensional and thus the insulation would heat at a higher rate than in the multi–dimensional wall situation.

The time–history of temperatures measured at the mid–depth of the oriented strand sheets for both Sandwich #1 and Wall #1 experiments are overlaid in Figure 4.26a. As can be seen, for Sandwich #1, the temperature at the centre of the slab increased with a fairly linear profile with increasing time, beginning about 3 minutes after the onset of exposure and continuing to rise at a rate of 0.031°C/s until the end of the test when a peak temperature value of 68°C was achieved. On the contrary, for Wall #1, the onset of temperature rise at the mid–depth of strand board occurred around 13 minutes after ignition of wood cribs and rose steadily at a rate of 0.017°C/s to a value of 42°C when the wood cribs were largely consumed (30 minute mark). For both sets of experiments, the lower rates of interior temperature rise at the mid–depth of oriented strand board was attributed to the increased insulation provided by the presence of the stone wool layer. Consistent with this, the time–resolved traces of temperature difference across the two measurement points within the assembly bulk (mid–depth of insulation and mid–depth of strand board) followed a similar shape to that of mid–depth insulation temperature–time curve. For Sandwich #1 assembly, the temperature difference curve increased gradually with time (Figure 4.40b) reaching a peak difference of 168°C around 18 minutes after the onset of exposure. For Wall #1, the measured difference initially followed a shallower climb, then became steeper after 10 minutes following ignition; a maximum difference in temperature of 162°C was achieved around 16 minutes into the test after which it progressively decayed, consistent with the differing exposure profiles discussed above.

4.6.3 Wall #2 – Polyisocyanurate Insulation

Test 2 investigated the thermal response of Wall #2 which had polyisocyanurate continuous exterior insulation instead of rigid stone wool. Before the test, the fire–side of the wall assembly was rebuilt with new oriented strand board sheets, wood furring strips and vinyl siding panels. The unexposed side of the wall (wood frame structure, in–cavity batt insulation, and gypsum board finish) was not renewed since it sustained no thermal or structural damage in Test 1. The instrumentation of the test rig was as described previously in Section 4.3. The exposure fuel load again consisted of two wood cribs placed side by side, this time weighing 14.32 kg and 14.72 kg and having 6%–11% moisture content. The fire was lit using starter fuel and time–resolved thermocouple data were recorded concurrently with video capture of the state of the wall. Local ambient environmental parameters (temperature, relative humidity, wind speed and direction) were logged at five–minute intervals and are presented in Table 4.6. As can be seen from Table 4.6 the ambient environment remained relatively stable and the average ambient temperature, relative humidity and wind speed throughout the test were 23°C, 79%, and 14 km/h, respectively. The test was concluded 33 minutes after ignition, at the time of extinction of the design fire. The remaining smouldering fuel was then manually extinguished.

Table 4.6: Local ambient environment throughout Wall #2 test duration

Test Time (mm:ss)	Ambient Temperature (°C)	Relative Humidity (%)	Wind Speed, Direction (km/h), Cardinal Direction
00:00	23	76	14, East
05:00	23	79	14, East
10:00	22	79	14, East
15:00	22	79	14, East
20:00	22	79	14, East
25:00	22	79	14, East
30:00	22	79	14, East

Table 4.7 lists the timeline of experimental observations (events) recorded during the test. These describe the thermal response of the wall as observed on the fire–side surface. Events marked in **bold** in Table 4.7 are paired with video images and still camera photographs that depict the extent of thermal damage in Figure 4.27.

Table 4.7: Timeline of events recorded during Wall #2 test

Test Time (mm:ss)	Event
00:00	Ignition of fuel trays marked the beginning of the test.
	The initial state of the wall assembly is depicted in Figure 4.27a.
02:38	Softening of vinyl siding panels affixed 305 mm and 610 mm above the bottom of the wall.
03:24	Softening of vinyl siding panel affixed 915 mm above the bottom of the wall.
03:49	Softening of vinyl siding panel affixed at mid–level of the wall.
	Onset of warping of siding panels at bottom of the assembly.
04:22	Siding panels installed at 305 mm wall height started to buckle.
04:51	Softening of vinyl siding panel affixed 1,525 mm and 1,830 mm above the wall base.
	Onset of buckling of siding panels at 610 mm height of the wall assembly.
05:36	Softening of vinyl siding panel affixed 2,135 mm above the wall base.
	Onset of warping of siding panels at 915 mm height of the wall assembly.
05:55	Siding panels affixed up to 915 mm wall height started to to melt and sag towards the bottom of the wall.
	Onset of warping of siding panels at the wall mid–level.
06:48	Siding panels installed at the bottom of the wall warped along their length from edge to edge between the horizontal extremes of the wall.
	Onset of warping of siding panels affixed 1,525 mm above the wall base.
07:03	Onset of warping of siding panels affixed 1,830 mm mm above the wall base.
07:25	Onset of warping of siding panels affixed 2,135 mm mm above the wall base.
	Edge–to–edge warping of all siding panels affixed up to 610 mm of wall height.
07:44	Edge–to–edge warping of all siding panels affixed up to the wall mid–level.
	Siding panels originally affixed 305 mm above the wall base started to melt away from the center of the wall. This recession towards the edges of the wall created tears in the melting vinyl film.
07:59	Edge–to–edge warping of siding panels affixed 1,525 mm and 1,830 mm above the wall base.
	Tears in the melted vinyl siding film appeared as panels affixed at 610 mm wall height receded towards the edges of the wall melting away from the centre of the wall.

Test Time (mm:ss)	Event
08:15	Softening of siding panels at the top of the wall assembly. Tears in the melted siding film appeared as panels affixed at 915 mm wall height receded towards the edges of the wall melting away from the wall centre. Tears in the melted siding film at 305 mm and 610 mm wall heights extended significantly revealing the face of the underlying polyisocyanurate insulation. The state of the wall at this time is depicted in Figure 4.27b.
09:53	Edge–to–edge warping of all siding panels affixed at the fire–side wall surface. Detachment of siding panels from their far–right nailing base at 610 mm and 1,525 mm wall heights. Tears appeared in the melted vinyl film at wall mid–level.
10:47	More tears appeared on the melted siding film at wall mid–level. The tear at the wall centre around 915 mm wall height had extended significantly revealing the exposed face of the underlying polyisocyanurate insulation of an approximate area of 406 mm × 915 mm. The state of the wall at this time is depicted in Figure 4.27c.
11:44	Siding panels originally affixed at 305 mm, 610 mm, and 915 mm wall heights detached at nails. This detachment created a gum–like web of melted film stretching vertically from the wall centre to the bottom of the wall.
12:35	Siding panel originally affixed at 1,525 mm wall height detached at nails and collapsed onto the melted vinyl mass below. Air pockets started to appear beneath the fire–side foil facer surface of the polyisocynurate sheet at 1,525 mm wall height. The state of the wall at this time is depicted in Figure 4.27d.
12:58	Larger sub–surface gas pockets appeared beneath the foil facer of the exposed polyisocyanurate insulation face. Onset of charring of the melted siding panels at the bottom of the wall.
14:19	Sub–foil–facer gas pockets had now covered the entire of the exposed face of polyisocyanurate sheet at the wall mid–level. Siding panel at 1,830 mm wall height melted away from the centre of the wall towards the edges of the wall with small tears appearing on the melting film.

Test Time (mm:ss)	Event
16:13	Complete melting and collapse of siding panel originally affixed at 1,830 mm wall height. The state of the wall at this time is depicted in Figure 4.27e.
17:04	Siding panels at the top of the wall assembly continued to melt and sag towards the centre of the wall assembly. Slight surface charring of the central wood furring strips at 610 mm wall height.
20:08	No further change in the state of the wall regarding thermal damage. The final state of the wall assembly is depicted in Figure 4.27f.

The state of the fire–side (exposed) face of Wall #2 before and after exposure is shown in Figure 4.28. Consistent with small–scale results seen for vinyl siding when tested in Sandwich #2 (Section 3.4.2) scaled assemblies, the layer of vinyl siding on the exposed wall surface softened and buckled shortly after the onset of exposure to radiant heat from the wood crib fire. Under continued exposure, the siding material started to melt and sag towards the bottom of the wall assembly, detaching at the nails. As can be seen from Figure 4.28b, melted siding panels left the underlying polyisocyanurate insulation face partially exposed to the incident heat flux from the design fire, especially along the bottom and middle central portions of the fire–side wall surface. Thermal damage for the siding layer appeared to be greatest across the bottom half of the exposed wall surface supported by significant charring of the melted panels. This was because the value of total heat flux from the fire to the exposed wall face, around 14 kW/m^2 at the peak, was highest across this region (Section 4.6.1). Interestingly, the state of post–exposure wall face also showed a frequent spotting of bubbles beneath the surface of the protective foil facer on the polyisocyanurate insulation board in the middle and upper central portions of its exposed face. This could possibly suggest that the foam core of the insulation material degraded under heating which resulted in expansion of the material and release of gaseous volatiles that remained trapped underneath the foil facer. Similar observations were noted previously when this material was tested under low levels of incident heat flux in the cone calorimeter (Section 3.4.1). There were no noticeable changes in colour or geometry and charring was not evident in the after test state of either the weather resistant barrier or oriented strand board layers since they were shielded from exposure to the fire by to the presence of the 25 mm thick continuous slab of polyisocyanurate insulation that remained intact throughout the test.

(a) Test Time = 00:00

(b) Test Time = 08:15

(c) Test Time = 10:47

(d) Test Time = 12:35

(e) Test Time = 16:13

(f) Test Time = 20:08

Figure 4.27: The extent of damage for Wall #2 at select times for events listed in Table 4.7

(a)

(b)

Figure 4.28: The state of exposed Wall #2 face (a) before and (b) after exposure to the total incident heat flux from the design fire

To further understand the effects of each layer on the overall thermal performance of the wall assembly under exposure from the design fire, it is of interest to examine the time–histories of temperature that were measured through the bulk wall layers. For this, a line plot of temperature versus time is shown in Figure 4.29 for thermocouples T6–2 of the siding layer (Figure 4.3) positioned 25mm away from its exposed surface, T6–4 positioned at the mid-depth of polyisocyanurate insulation (Figure 4.4), and T6–5 at the mid-depth of the oriented strand board (Figure 4.5) where the latter two probes were installed 1,219 mm and 610 mm away from the left edge and bottom of the wall assembly, respectively, locations where highest total incident heat flux to the wall was registered (Section 4.6.1). The total heat flux from the fire incident on the wall face at that position is overlaid with temperature–time traces. It should be noted that thermocouple T6–2 for the siding layer (Figure 4.3) was positioned 1,219 mm and 915 mm away from the left edge and bottom of the wall assembly, respectively, since there was no thermocouple located 1,219 mm and 610 mm on that rake. Discussions regarding the thermal penetration through each layer, its impact on recorded rates of temperature rise and subsequent temperature profiles of the heated exterior wall components are presented and compared with results from the small–scale tests below.

As can be seen from trace "D" in Figure 4.29, after ignition of the starter fuel, the design fire grew in size until the total heat flux experienced at the exposed wall face reached a peak of about 13 kW/m^2 $\pm$ 3 kW/m^2 between 5 and 10 minutes following ignition. During the fire growth phase (prior to 5 minute mark), the vinyl siding panels covering the exposed wall face started to soften and buckle, warping along their length across the entire width of the wall. In the meantime, the thermocouple at the mid–depth of polyisocyanurate insulation, trace "B" in Figure 4.29, registered a gradual increase in temperature, rising from about 26°C two minutes after ignition to around 33°C at 5 minutes. When quasi–steady burning of the design fire established around 5 minutes into test, the siding panels melted, stretching and sagging towards the bottom of the wall assembly, especially along the centerline. At about 8 minutes and 15 seconds, tears started to appear in the melted vinyl around the bottom central portion of the exposed wall surface as noted previously in Table 4.7. At this time, the temperature measured at the insulation mid–depth was about 50°C. A contour plot of temperatures measured by thermocouples positioned across the mid–depth of polyisocyanurate insulation is shown in Figure 4.30a for this time. As can be seen by the vertical and horizontal temperature gradients throughout the mid–depth of the foam insulation, thermal penetration into the depth of the wall was location dependent with maximum thermal penetration occurring along a vertical strip slightly to the left of the wall centerline.

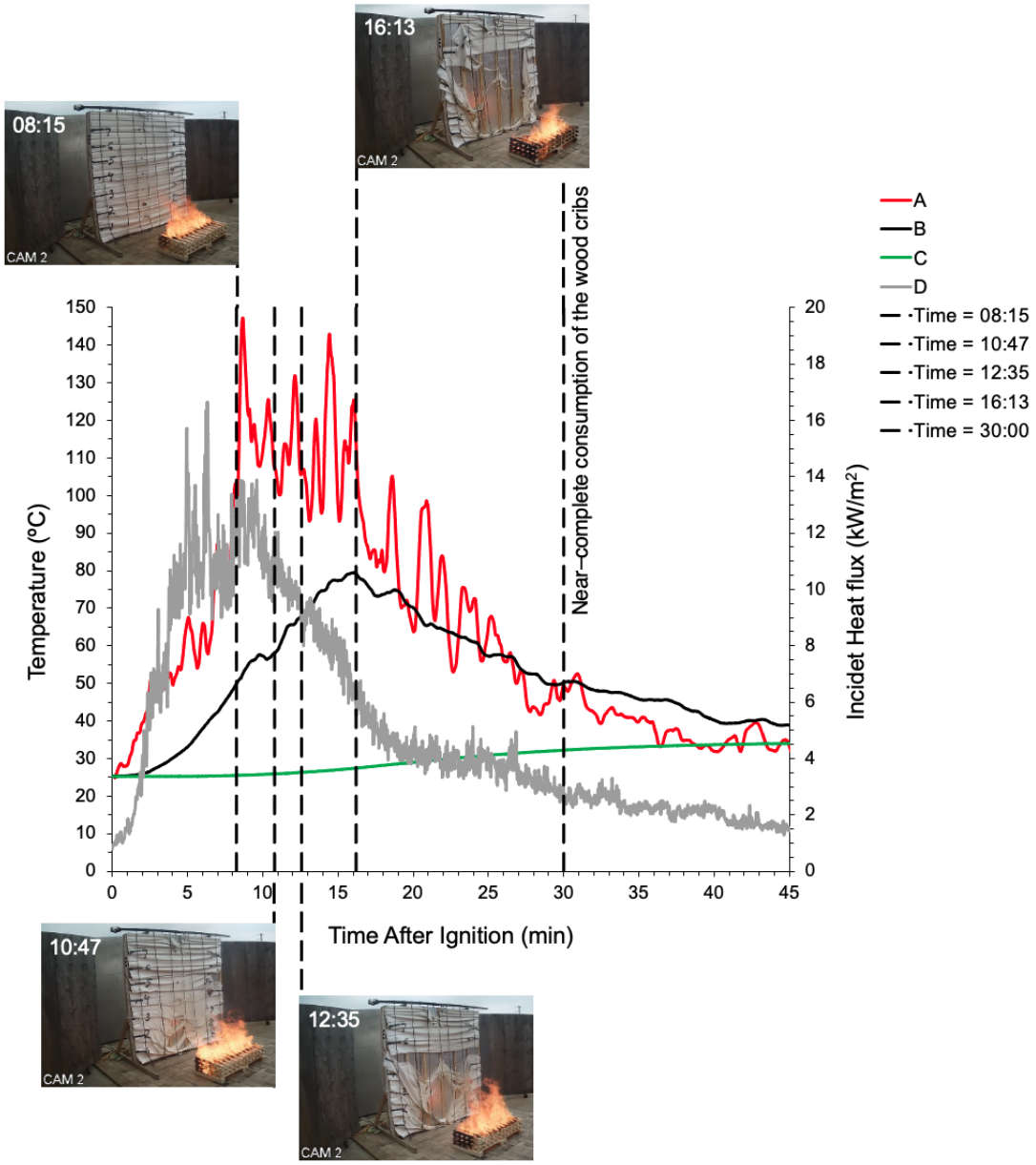

Figure 4.29: Wall #2: Temperature–time traces after ignition recorded from thermocouples T6–2 of the siding layer (A), T6–4 of the extruded polystyrene insulation (B), and T6–5 of the oriented strand board (C) overlaid with total incident heat flux profile from HFG #4 (D)

Under continued exposure, melting of vinyl siding panels intensified, and larger tears appeared around the bottom central portion of the fire–side wall surface. This resulted in partial exposure of the underlying polyisocyanurate face to the radiant heat from the fire as illustrated in the still camera photograph of the fire–side wall face taken at 10 minutes and 47 seconds into the test (Figure 4.27c). As can be seen from Figure 4.29 and consistent with expectations, the temperature recorded at the insulation mid–depth at this time had increased further to approximately 58°C in response to the increased level of direct exposure to the radiant heat from the fire. Another contour plot of temperatures measured across the mid–plane of polyisoyanurate insulation is shown in Figure 4.30b at this time. Please note the difference in limits on the colourbar scales in the subplots of Figure 4.30. As anticipated, the temperatures recorded at the mid–depth of insulation continued rise non–uniformly across the two dimensions at this depth. Interestingly, despite the bottom central portion of the fire–side wall face being exposed to higher levels of radiant heat flux from the fire, the highest interior temperatures in the underlying insulation were recorded across the upper region of polyisocyanurate mid–plane. On average, these upper regions of the foam core were about 15°C higher than those measured at the lower portions along the same vertical strip (slightly to the left of the wall centerline).

To investigate whether such pattern of interior temperature rise continued to hold under continued radiant exposure, additional contour plots for the insulation mid–plane are presented in Figures 4.31a and 4.31b for test times of 12 minutes and 35 seconds and 16 minutes and 13 seconds, respectively. These test times were selected as they corresponded to a greater extent of melting of the vinyl siding across the bottom and middle central portions of the wall and thus a larger area of the underlying insulation face being directly exposed to radiant heat from the fire. These again were supported with the photographs of the exposed wall face shown at these times in Figures 4.27d and 4.27e. As can be seen from trace “B” in Figure 4.29, at 16 minutes and 13 seconds after ignition, a peak temperature of about 80°C was measured at the mid–depth of insulation which is also of interest when examining two–dimensional contour plots of interior temperature at times of peak temperature.

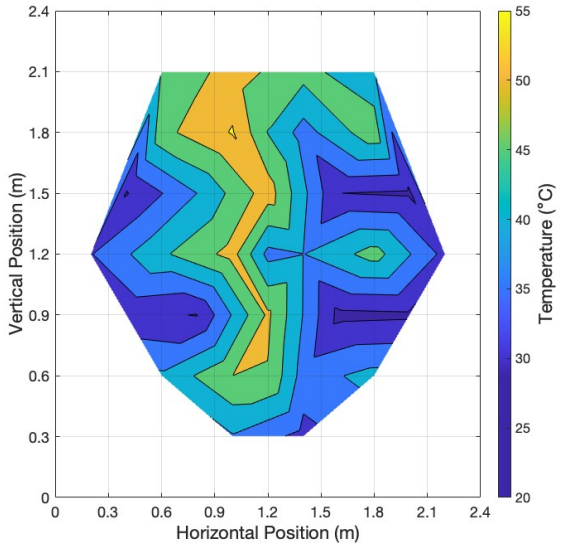

(a)

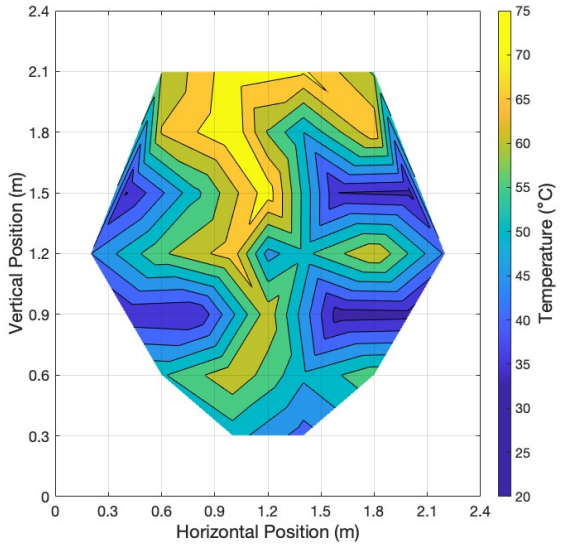

(b)

Figure 4.30: Wall #2: Contour plots of temperatures measured across the mid–depth face of polyisocyanurate insulation at (a) Time = 08:15 and (b) Time = 10:47 after ignition

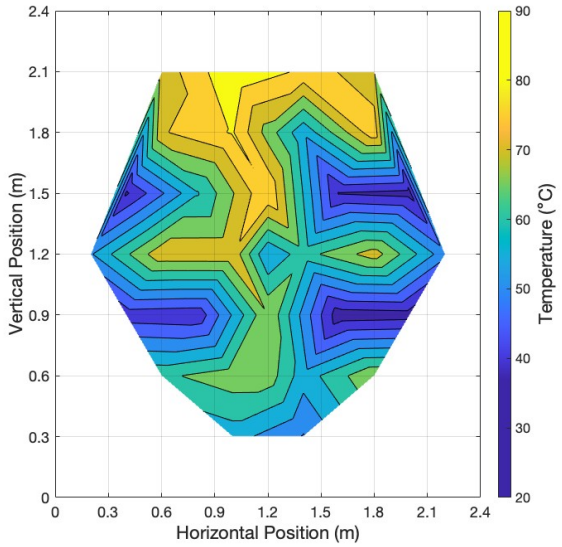

(a)

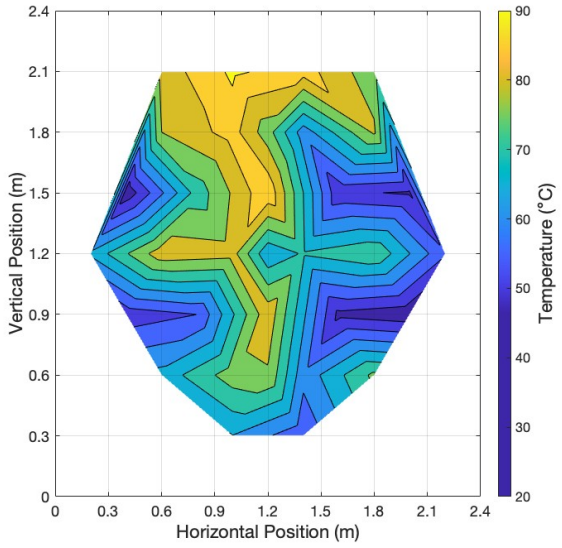

(b)

Figure 4.31: Wall #2: Contour plots of temperatures measured across the mid–depth face of polyisocyanurate insulation at (a) Time = 12:35 and (b) Time = 16:13 after ignition

As can be seen from Figures 4.31a and 4.31b, thermal penetration into the depth of the wall at both times remained location dependent with maximum thermal penetration occurring along the same vertical strip slightly to the left of the wall centerline, specifically, along rake T5 (Figures 4.4 and 4.5). At 12 minutes and 35 seconds into the test, the measured interior temperatures across the upper regions of the insulation mid–plane appeared to be higher than those across the lower portion of the same plane by about 25°C, higher than the difference of 15°C at 16 minutes and 13 seconds. Interestingly, between the two test times, the upper and middle central regions of the polyisocyanurate insulation appeared to cool down, while the bottom portion gradually increased in temperature. The interesting result that there were relatively higher temperature increases in the the upper portions of the insulation mid–plane than in the lower regions (where total heat flux from the fire to the exposed wall face was highest) may be explained by combined effects of radiation and conduction in the material.

Radiation from the fire to the surface of the protective foil facer may have been reflected from the relatively reflective silver surface of the foil, thus re–radiating back to the surroundings, and further heating the hot gases (air) which would convect upward along the foil facer. The reflective nature of the foil can be seen in the photographs of the fire–side wall face shown in Figures 4.27d and 4.27e. The remaining portion of radiant heat would conduct into the foil facer in three dimensions: across and up the face of the slab as well as into the polyisocyanurate foam core of the insulation. Since the foil facer was more thermally conductive than the polyisocyanurate foam core, the extent of heat conduction across the foil facer surface was likely to be higher than that conducted into the bulk of the foam core. Since the foil facer and the exposed surface of the insulation were not instrumented with temperature probes, addressing the exact details of these heat transfer processes warrants further investigation in future.

In addition to the impact of the heat conduction through the foil facer, the relatively high temperatures experienced in the upper portions of the polyisocyanurate insulation could result from the presence of hot gases trapped behind the melted vinyl siding panels, in the air cavity between the backside of siding panels and fire–side insulation face. This is supported by the time–histories of temperature (Figure 4.32) of the hot gases in the vicinity of vinyl siding panels, as well as at the mid–depth of polyisocyanurate insulation at two positions, 305 mm (T5–4) and 2,135 mm (T5–0) above the base of the wall, along rake T5 which was located 203 mm to the left of the wall centerline. As can be seen from the temperature–time profiles, in the upper regions of the wall where siding panels melted but did not detach at the nails, the measured temperatures were consistently higher for both the hot gases and polyisocyanurate insulation during the fire growth and quasi–steady burning phases. The difference in mid–plane insulation temperatures across these two regions of the wall grew larger with time until peak temperatures were attained around 16 minutes into the test. This could also possibly explain the extent of spotting of sub–surface gas pockets beneath the foil facer in the upper regions of the wall. After 16 minutes, the fire started to decay with consequent cooling of the trapped hot gases behind the top vinyl siding panels (trace "A: T5–0" in Figure 4.32) which likely resulted in the gradual decay in temperatures at the insulation mid–depth. Transport of hot gases in the air cavity, however, was not studied in this work and the exact mechanism or impact on the measured interior foam temperatures also warrants further investigation.

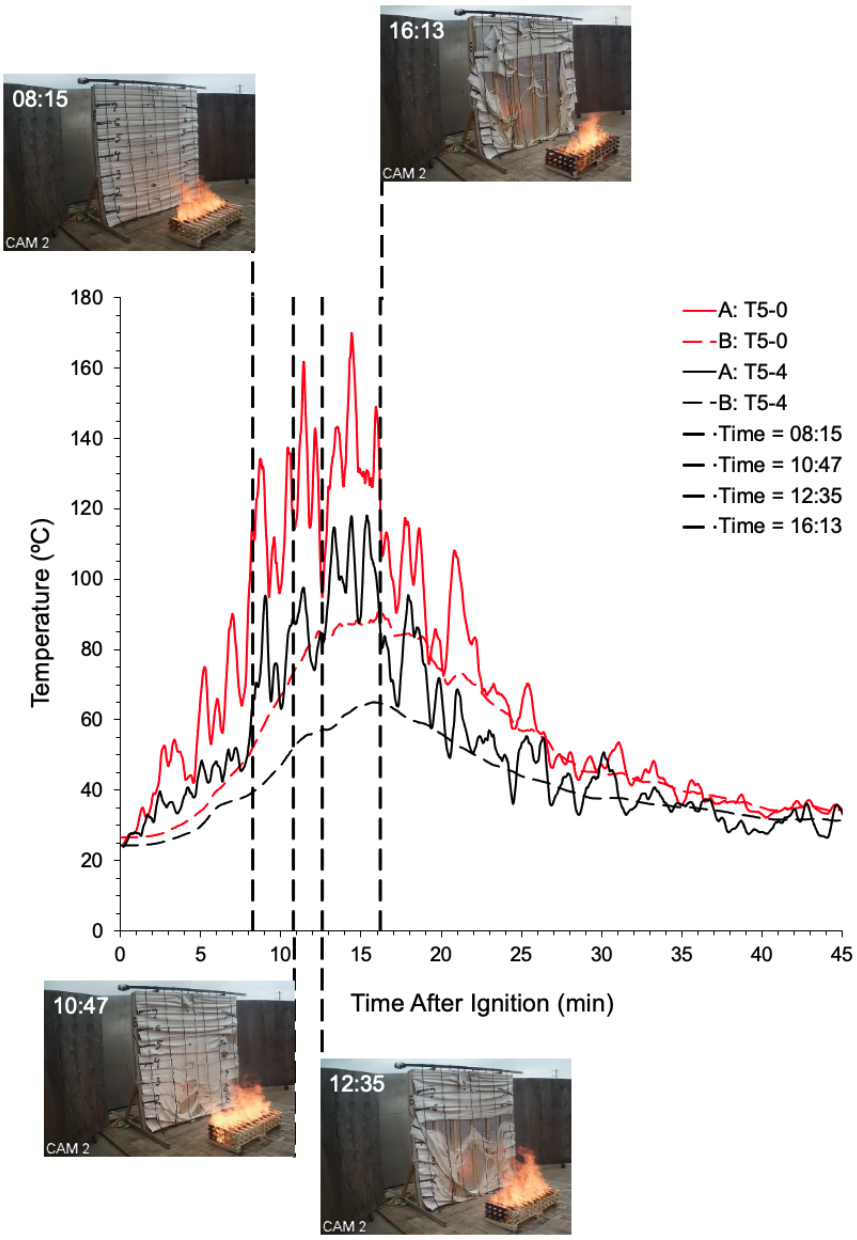

Figure 4.32: Wall #2: Temperature–time traces after ignition recorded from thermocouples T5–0 and T5–4 of the siding layer (trace series "A"), and T5–0 and T5–4 of polyisocyanurate insulation (trace series "B")

Referring back to trace "B" Figure 4.29, after achieving a peak temperate about 80°C at around 16 minutes and 13 seconds into the test, the temperatures measured at the polyisocyanurate mid–depth gradually decayed due to decay of the fire. Interestingly, this time also marked the onset of a temperature rise at the mid–depth of the underlying oriented strand board sheet, trace "C" Figure 4.29. The measured temperatures at the strand board mid–depth continued to rise even after nearly complete consumption of the wood cribs (30 minute mark) while interior temperature of the polyisocyanurate foam gradually decayed. This possibly suggested that heat conducted into and retained in the polyisocyanurate foam core slowly penetrated further into the bulk of the wall assembly towards the unexposed side. Between 30 and 45 minutes following ignition, the temperatures measured at the mid–depth of polyisocyanurate insulation dropped from 50°C to 39°C, while temperature in the oriented strand board rose from around 32°C to 35°C. To further visualize the two dimensional variation of measured temperatures at various depths into the wall, contour plots of recorded temperatures are contained in Figures 4.33a and 4.33b for the mid–planes of polyisocyanurate insulation and oriented strand board, respectively, at 45 minutes following ignition. Again please note the differences in colourbar limits on the subplots of Figure 4.33. As can be seen, maximum thermal penetration into the mid–depth of oriented strand board sheet occurred along the centerline and around the upper central portion of the mid–plane where interior temperatures of polyisocyanurate insulation were historically higher, but had now cooled down significantly. On the backside of the wall, however, at the mid–depth of the in–cavity batt insulation and mid–depth of the wood studs, average temperature increases were minimal; at the end of the test these temperatures had risen by only 0.6°C and 0.5°C, respectively, consistent with these layers remaining insulated from any incident radiation by the polyisocyanurate insulation.

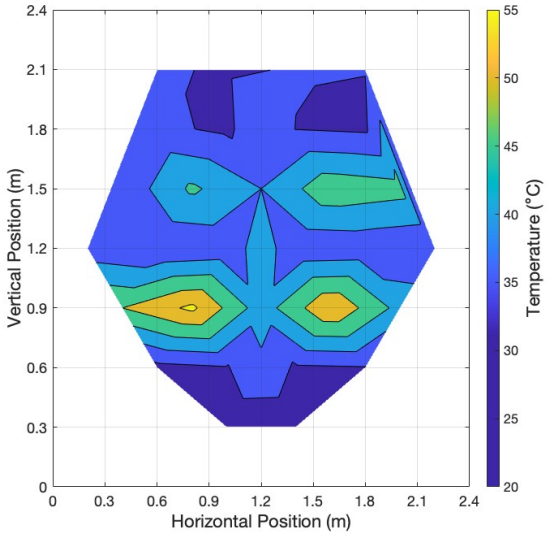

(a)

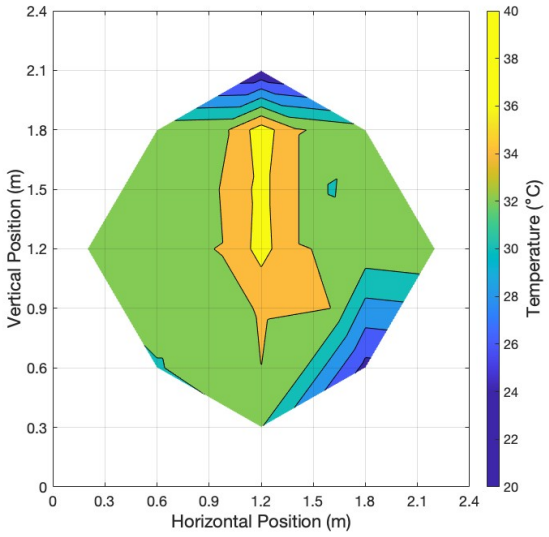

(b)

Figure 4.33: Wall #2: Contour plots of temperatures measured across the mid–depth face of (a) polyisocyanurate insulation and (b) oriented strand board at Time = 45:00 after ignition

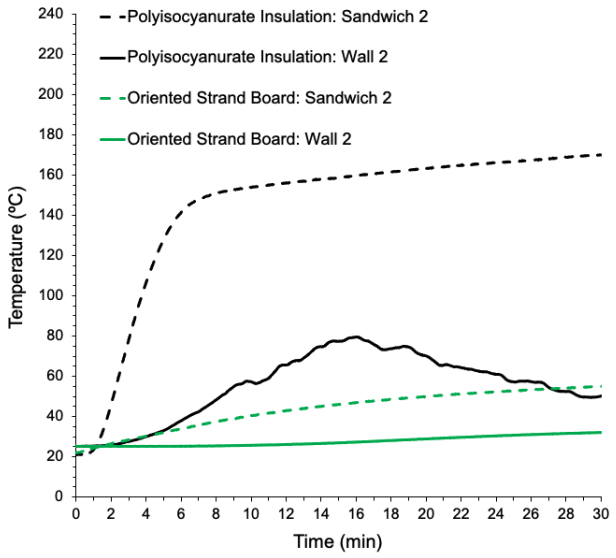

(a)

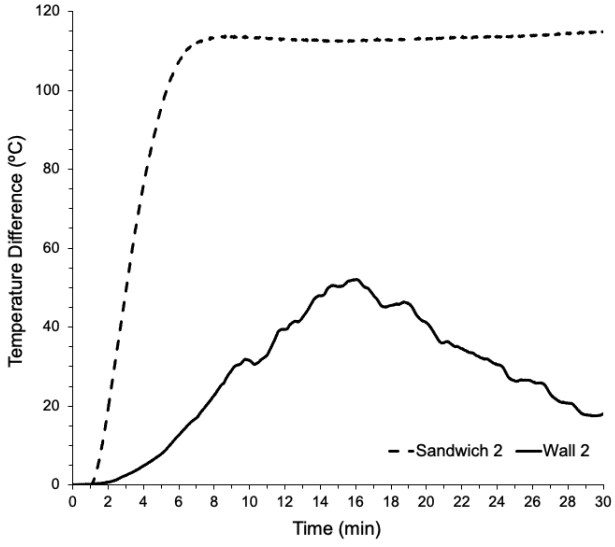

(b)

Figure 4.34: Time–histories of (a) temperatures measured at the mid–depth of polyisocyanurate insulation and mid–depth of oriented strand board sheets across Sandwich #2 and Wall #2 tests, and (b) their difference across the two sets of experiments

In addition to the time evolution of temperatures measured within the Wall #2 assembly, it was also of interest to compare the thermal penetration into the bulk of the wall with results from small–scale testing of Sandwich #2. For this, a line plot of temperature versus time is shown in Figure 4.34a where temperatures recorded at the mid–depth of polyisocyanurate insulation and at the mid–depth of the underlying oriented strand board sheet are overlaid for Sandwich #2 and Wall #2 tests conducted under similar levels of incident radiant heat flux exposure; that is 15 kW/m^2 for Sandwich #2 and 13 kW/m^2 $\pm$ 3 kW/m^2 for Wall #2 experiments. These line plots were previously presented separately for Sandwich #2 and Wall #2 in Figures 3.27a and 4.29, respectively. To illustrate through–wall heat transfer, the time–histories of temperature difference (taken as the difference in temperature across the mid–depth of polyisocyanurate insulation and the mid–depth of the oriented strand board) along the bulk–path of the wall assembly are plotted in Figure 4.34b.

As can be seen from Figure 4.34a, for the Sandwich #2 assembly, the increase in temperature at the centre of polyisocyanurate insulation began around 1.5 minutes following the onset of exposure, rising at a rate of 0.48°C/s until a quasi–steady temperature plateau of 162.6°C $\pm$ 4.7°C was attained after 10 minutes of heating. In contrast, for the Wall #2 assembly, the onset of temperature increase at the mid–depth of polyisocyanurate insulation started around 2 minutes after ignition of the wood cribs. Following this, the insulation in Wall #2 underwent varying rates of interior temperature rise consistent with changes in the size of the test fire. Initially, temperatures rose at a rate of 0.041°C/s between 2 and 5 minutes after ignition, then increased to 0.089°C/s between 5 and 10 minutes, and lastly were 0.07°C/s after 10 minutes until a peak temperature of about 80°C was measured at around 16 minutes and 13 seconds into the test. After 16 minutes, measured temperatures gradually decayed due to decay of the fire. The observed changes were again consistent with results in Section 3.4.1 for individual polyisocyanurate insulation samples heated under different levels of external irradiance, where rates of temperature rise were 0.15°C/s for 15 kW/m^2 and 0.72°C/s at 40 kW/m^2 for example. Further, due to spatial gradients in exposure to the large Wall #2, the heat penetrated into the bulk of insulation sheet from the fire conducted in three dimensions. In contrast for Sandwich #2 assemblies under uniform exposure, heat transfer through the assembly was closer to one–dimensional and thus penetrated through the material at an apparently higher rate than in the multi–dimensional wall situation.

For both sets of small– and large–scale experiments, the time–history of temperature measured at the mid–depth of oriented strand board exhibited a fairly linear profile with increasing time. For Sandwich #2, the rise in measured mid–depth temperature began about 3 minutes after the onset of exposure, increasing at a rate of 0.032°C/s until the end of the test when it had reached about 55°C. For Wall #2, the onset of temperature rise for oriented strand board was significantly delayed, beginning at around 16 minutes after ignition of wood cribs and was still rising until nearly complete consumption of the wood cribs, measuring around 32°C at 30 minute mark, which was lower by 23°C when compared to that recorded in Sandwich #2 at the same time. Consistent with this, the rate of temperature rise at the mid–depth of oriented strand board sheet (0.006°C/s) was also slower for Wall #2, approximately 5 times less than that recorded in Sandwich #2. Regardless of the scale, however, these lower rates of temperature rise at the mid–depth of oriented strand board were due to the insulating effect of the polyisocyanurate insulation which slowed the rate of thermal penetration to those unexposed side layers.

As can be seen from Figure 4.34b, the time–resolved traces of temperature difference across the two measurement points within the assembly bulk (mid–depth of insulation and mid–depth of strand board) followed a similar shape to that of mid–depth insulation temperature–time curve. As such, for the Sandwich #2 assembly, temperature differences increased rapidly with time reaching a peak temperature difference of 113°C around 8 minutes after the onset of exposure. In contrast, for Wall #2, the measured difference along the assembly bulk followed a shallower climb reaching a maximum difference in temperature of 52°C around 16 minutes after ignition of wood cribs. The observed differences in the bulk–path temperature differences across the two scales were consistent with the differing exposure profiles and multi–dimensional heat transfer mechanisms discussed above.

4.6.4 Wall #3 – Extruded Polystyrene Insulation

The third test in the series of large–scale experiments was conducted on Wall #3 which was lined with extruded polystyrene sheets as the continuous exterior insulation layer. The fire–side of the wall assembly was rebuilt with new oriented strand board sheets, wood furring strips and vinyl siding panels. The unexposed side of the wall (wood frame structure, in–cavity batt insulation, and gypsum board finish) was not refurbished since neither thermal nor structural damage was sustained during Test 2. The test rig was instrumented as described in Section 4.3. The exposure fuel load again consisted of two wood cribs placed side by side. New wood had been purchased for this test, so the cribs were heavier than previously, weighing 15.63 kg and 15.65 kg with 6%–11% moisture content. The fire was lit using starter fuel and time–resolved thermocouple data were recorded concurrently with video capture of the state of the wall. Local ambient environmental parameters (temperature, relative humidity, wind speed and direction) were logged at five–minute intervals throughout the test and are presented in Table 4.8. As can be seen from Table 4.8, the local environment remained relatively stable throughout the test duration. The average ambient temperature, relative humidity and wind speed through the test were 26°C, 63%, and 11 km/h, respectively. The test was concluded 33 minutes after ignition, at the time of extinction of the design fire. The remaining smouldering fuel was manually extinguished.

Table 4.8: Local ambient environment throughout Wall #3 test duration

Test Time (mm:ss)	Ambient Temperature (°C)	Relative Humidity (%)	Wind Speed, Direction (km/h), Cardinal Direction
00:00	26	63	11, Northwest
05:00	26	63	11, Northwest
10:00	26	63	11, North–Northwest
15:00	26	63	11, North–Northwest
20:00	26	62	11, North–Northwest
25:00	26	63	11, North–Northwest
30:00	26	63	11, North–Northwest

Table 4.9 lists the timeline of experimental observations (events) during the test. These describe the thermal response of the wall as observed on the fire–side surface. Events marked in **bold** in Table 4.9 are paired with video images and still camera photographs that depict the extent of thermal damage in Figure 4.35.

Table 4.9: Timeline of events recorded during Wall #3 test

Test Time (mm:ss)	Event
00:00	Ignition of fuel trays marked the beginning of the test.
	The initial state of the wall assembly is depicted in Figure 4.35a.
02:00	Softening of siding panels affixed 305 mm and 610 mm above the base of the wall assembly.
02:11	Softening of siding panels affixed 915 mm above the base of the wall.
02:27	Softening of siding panels affixed at mid–level of the wall.
	Onset of buckling of siding panels affixed at the bottom of the wall assembly.
02:47	Onset of buckling of siding panels at 305 mm and 610 mm wall heights.
03:55	Softening of siding panels mounted at 1,525 mm and 1,830 mm wall heights.
04:40	Onset of buckling of siding panels at 915 mm and mid–level wall heights.
05:40	Siding panels installed up to 915 mm of the wall height were warped along their length from edge to edge between the horizontal extremes of the wall.
06:06	Edge–to–edge warping of vinyl panels installed up to the mid wall height.
06:36	Softened siding panels originally affixed 610 mm and 915 mm above the wall base started to melt away from the center of the wall. This recession towards the edges of the wall created tears in the melting vinyl film.
07:17	Softening of vinyl panels affixed 2,135 mm above the wall base.
	Edge–to–edge warping of vinyl panels affixed at 1,830 mm wall height.
	Softened and melted siding panels originally affixed up to mid wall height collapsed and sagged towards the bottom of the wall assembly.
	Tear in the melted vinyl film at 915 mm wall height had expanded exposing the underlying extruded polystyrene insulation face to radiant heat from the fire.
	The state of the wall at this time is depicted in Figure 4.35b.
08:09	The exposed extruded polystyrene insulation at 915 mm wall height started to melt.
08:30	Detachment of siding panels at nails at 1,220 mm as well as 1,525 mm wall heights.
	Siding panels at the bottom half of the wall assembly continued to melt and receded towards the edge of the wall.

Test Time (mm:ss)	Event
09:07	At 1,220 mm and 1,525 mm wall heights, vinyl panels as well as the exposed extruded polystyrene insulation melted away from the fire–side surface of the wall. This recession revealed the underlying layer of weather resistant barrier at mid wall height. Slight charring of melted siding panels as well as wood furring strips at 610 mm wall height. Edge–to–edge warping of vinyl panels affixed at 2,135 mm wall height. The state of the wall at this time is depicted in Figure 4.35c.
09:15	Extensive melting of siding panels and polystyrene insulation revealed a larger area of weather resistant barrier face at 1,525 mm wall height directly exposing this layer to radiant heat from the fire. At the bottom half of the wall, 610 mm above the wall base, the weather resistant barrier started to melt revealing the exposed face of the underlying oriented strand board sheet.
09:36	Warping of siding panels at the top of the wall assembly. Previously visible weather resistant barrier segments melted away partially exposing the underlying oriented strand board face to the fire.
10:02	Unshielded oriented strand board face at the mid wall level now occupied an approximately 812 mm wide × 610 mm tall area at the wall center Slight surface charring of oriented strand board sheet at 610 mm height above the base of the wall. Onset of charring of melted vinyl siding panels across the lower portion of the wall. Melted siding panels and polystyrene insulation receded towards the right edge of the wall revealing some weather resistant barrier at 1,525 mm wall height. The state of the wall at this time is depicted in Figure 4.35d.
12:26	Virtually all of the siding panels, polystyrene insulation, and weather resistant barrier had melted away from the center of the wall. Significant surface charring of oriented strand board face at 610 mm wall height. Slight charring of the central wood furring strip from 610 mm to 915 mm wall heights. The state of the wall at this time is depicted in Figure 4.35e.
12:58	Surface charring of the exposed strand board face extended to the wall mid–level.
15:50	No further change in the state of the wall regarding thermal damage. The final state of the wall assembly is depicted in Figure 4.35f.

(a) Test Time = 00:00

(b) Test Time = 07:17

(c) Test Time = 09:07

(d) Test Time = 10:02

(e) Test Time = 12:26

(f) Test Time = 15:50

Figure 4.35: The extent of damage for Wall #3 at select times for events listed in Table 4.9

(a)

(b)

Figure 4.36: The state of exposed Wall #3 face (a) before and (b) after exposure to the total incident heat flux from the design fire

The state of the fire–side (exposed) face of Wall #3 before and after exposure is shown in Figure 4.36. Consistent with small–scale results seen for vinyl siding when tested in Sandwich #3 (Section 3.4.2) scaled assemblies, the layer of vinyl siding on the exposed wall surface softened and buckled shortly after the onset of exposure to radiant heat from the wood crib fire. Under continued exposure, the siding material started to melt and sag towards the bottom of the wall assembly, detaching at the nails. This left the underlying extruded polystyrene insulation partially exposed to the incident heat flux from the design fire. As a result, the bottom central portion of the insulation face first softened and then melted on the fire–side. This in turn left the underlying house wrap and oriented strand board face partially exposed to the radiant heat from the fire, leading to melting of the house wrap and significant surface charring of the strand board as well. As can be seen from Figure 4.36, thermal damage to the outermost layers of the wall assembly was greatest across the bottom half of the exposed wall surface since the value of heat flux from the fire to the exposed wall face, around 14 kW/m^2 at the peak, was highest across this region (Section 4.6.1).

To further understand the effects of each layer on the overall thermal performance of the wall assembly under exposure from the design fire, it is of interest to examine the time–histories of temperature that were measured through the bulk wall layers. For this, a line plot of temperature versus time is shown in Figure 4.37 for thermocouples T6–2 of the siding layer (Figure 4.3) positioned 25 mm away from its exposed surface, T6–4 positioned at the mid–depth of extruded polystyrene insulation (Figure 4.4), and T6–5 at the mid–depth of the oriented strand board (Figure 4.5) where the latter two probes were installed 1,219 mm and 610 mm away from the left edge and bottom of the wall assembly, respectively, locations where highest total incident heat flux to the wall was registered (Section 4.6.1). The total heat flux from the fire incident on the wall face at that position is overlaid with temperature–time traces. It should be noted that thermocouple T6–2 for the siding layer (Figure 4.3) was positioned 1,219 mm and 915 mm away from the left edge and bottom of the wall assembly, respectively, since there was no thermocouple located 1,219 mm and 610 mm on that rake. Discussions regarding the thermal penetration through each layer, its impact on recorded rates of temperature rise and subsequent temperature profiles of the heated exterior wall components are presented and compared with results from the small–scale tests below.

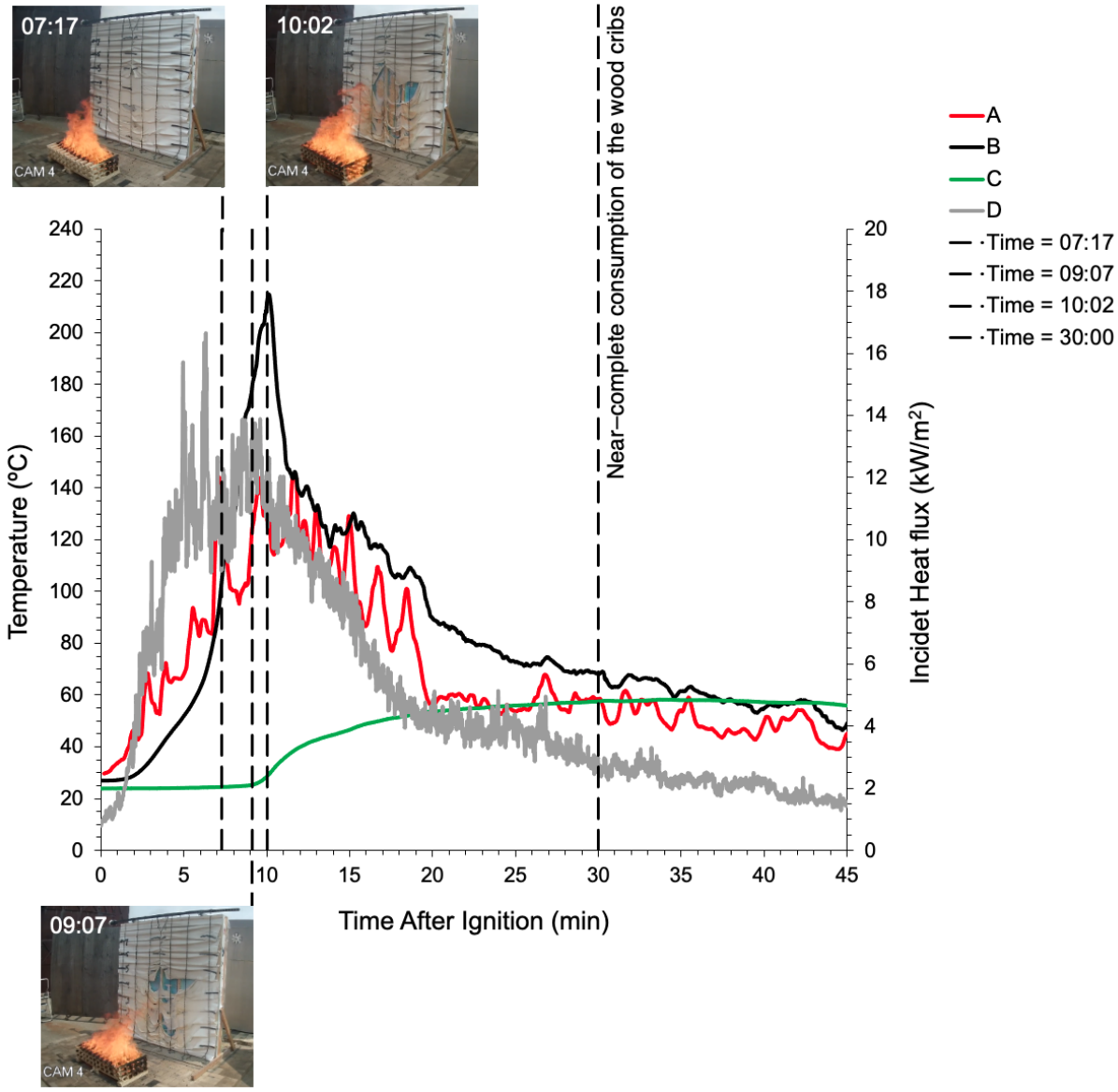

Figure 4.37: Wall #3: Temperature–time traces after ignition recorded from thermocouples T6–2 of the siding layer (A), T6–4 of the extruded polystyrene insulation (B), and T6–5 of the oriented strand board (C) overlaid with total incident heat flux profile from HFG #4 (D)

As can be seen from trace "D" in Figure 4.37, after ignition of the starter fuel, the design fire grew in size until the total heat flux experienced at the exposed wall face reached a peak of about 14 kW/m^2 $\pm$ 3 kW/m^2 between 5 and 10 minutes following ignition. During the fire growth phase (prior to 5 minute into the test), the vinyl siding panels covering the exposed wall face started to soften and buckle, warping along their length across the entire width of the wall. In the meantime, the thermocouple at the mid–depth of the extruded polystyrene insulation, trace "B" in Figure 4.37, registered a gradual increase in temperature, rising from about 26°C two minutes after ignition to around 51°C at 5 minutes. When quasi–steady burning of the design fire established around 5 minutes into test, the siding panels melted, stretching and sagging towards the bottom of the wall assembly, especially along the centerline. At about 7 minutes and 17 seconds, tears started to appear in the melted vinyl around the bottom central portion of the exposed wall surface as noted previously in Table 4.5. At this time, the temperature measured at the insulation mid–depth was about 104°C, a twofold increase compared to that recorded just a little over 2 minutes before. A contour plot of temperatures measured by thermocouples positioned across the mid–depth of the extruded polystyrene insulation is shown in Figure 4.38a for this time. As can be seen by the vertical and horizontal temperature gradients throughout the mid–depth of the foam insulation, thermal penetration into the depth of the wall was very location dependent. As anticipated, maximum thermal penetration occurred in the lower region of the wall, slightly off–center and to the left of the wall centerline, close to where the incident heat flux was greatest. In contrast, in the middle and upper regions, temperature gradients varied both with height above the bottom of the wall and horizontally across the mid–plane insulation face marking the three-dimensional nature of heat penetration into the insulation layer.

Under continued exposure, melting of vinyl siding panels intensified, resulting in partial exposure of the underlying extruded polystyrene face to the radiant heat from the fire. This is illustrated with the still camera photograph of the fire–side wall face taken at 9 minutes and 7 seconds into the test as shown in Figure 4.35c. As can be seen from Figure 4.37 and consistent with expectations, the temperature recorded at the insulation mid–depth at this time had increased further to approximately 180°C in response to the increased level of direct exposure to the radiant heat from the fire. The rise in measured temperatures across the mid–depth of the solid foam insulation was further supported by the contour plot of temperatures registered at 9 minutes at 7 seconds into the test (Figure 4.38b). Please note the difference in the colourbar scale limits on the subplots of Figure 4.38.

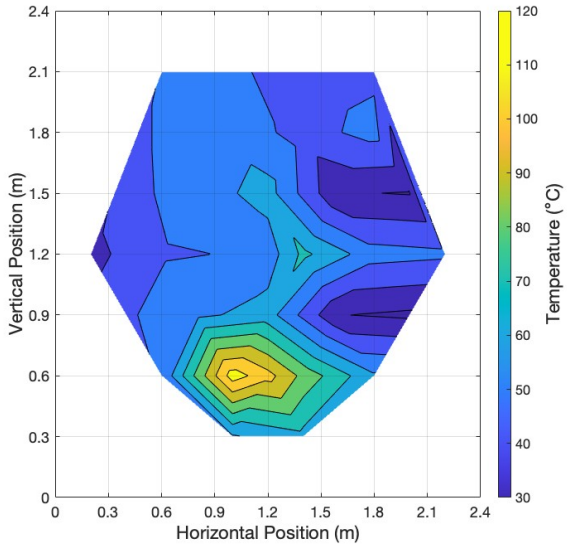

(a)

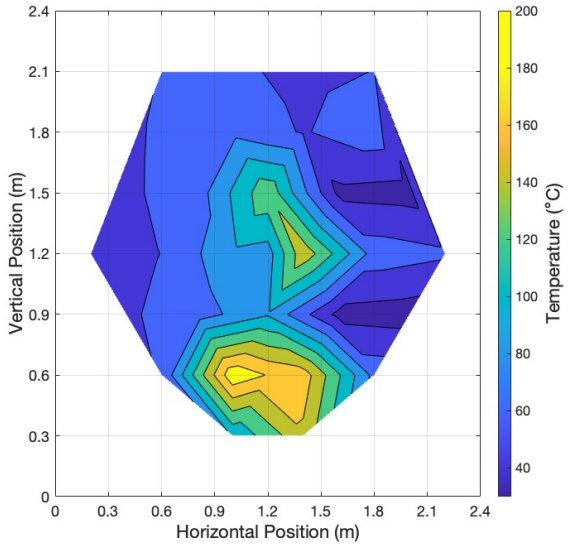

(b)

Figure 4.38: Wall #3: Contour plots of temperatures measured across the mid–depth face of extruded polystyrene insulation at (a) Time = 07:17 and (b) Time = 09:07 after ignition

The accelerated increase in temperature at the mid–depth of the polystyrene insulation occurred in regions corresponding to significant melting of the vinyl siding panels (Figure 4.35c) where the shielding effect of the siding material had failed. As such, at 9 minutes and 7 seconds into the test, the temperatures around the bottom central, middle central and upper portions of the exposed insulation face were higher by around 80°C – 100°C, 60°C – 70°C and 20°C – 30°C, respectively, compared to temperatures recorded at 7 minutes and 17 seconds, when only a few small tears were evident on the vinyl siding. Interestingly, minimal differences in measured temperatures (< 10°C) were recorded over this same time period at regions closer to the horizontal edges of the wall, possibly suggesting that during quasi–steady burning, the fire plume was anchored to the center of the fuel bed with its "footprint" projected centrally onto the exposed wall face.

Around 10 minutes into the test, both the vinyl siding panels and extruded polystyrene insulation had undergone significant melting along the bottom and middle central portions of the wall. While still affixed in the polystyrene insulation, the thermocouple measured a peak temperature of 215°C, but it detached from the insulation shortly afterwards as the foam melted down past the thermocouple location. Similar observations were recorded during small–scale tests for this same material. Upon detachment, the thermocouple recorded the temperature of the hot gases instead, thus yielding a similar temperature–time profile to trace "A" after 10 minutes as shown in Figure 4.37. The melting of the vinyl siding panels and polystyrene foam insulation left the underlying oriented strand board face partially exposed to the radiant heat from the wood crib fire as shown by the photograph of the fire–side wall face taken at 10 minutes and 2 seconds after ignition (Figure 4.35d). This time also marked the onset of temperature rise at the mid–depth of the oriented strand board sheet, trace "C" in Figure 4.37, as the combined result of earlier heat penetrated from the solid polystyrene foam into the outer layers of the oriented strand board and the sudden exposure to higher heat flux from the fire. To further visualize the two dimensional variation of temperature at this depth into the wall, contour plots of temperature for the mid–plane of oriented strand board at this time are presented in Figure 4.39a. As can be seen, locations of maximum thermal penetration into this layer of the wall assembly aligned with regions of highest incident heat flux across the lower region of the wall and temperatures across the mid–depth of the oriented strand board plane varied both horizontally and vertically.

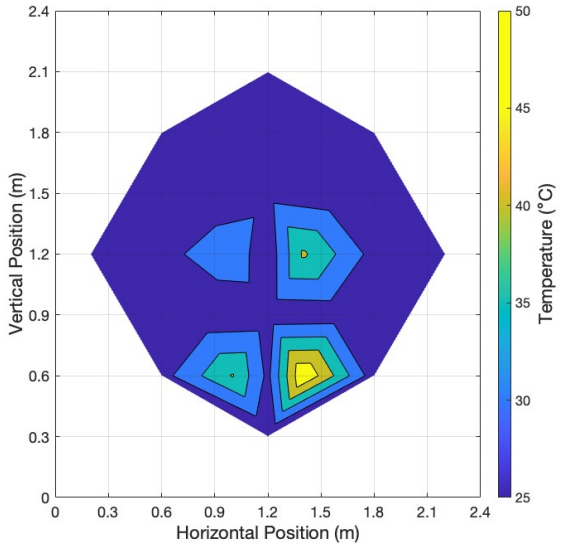

(a)

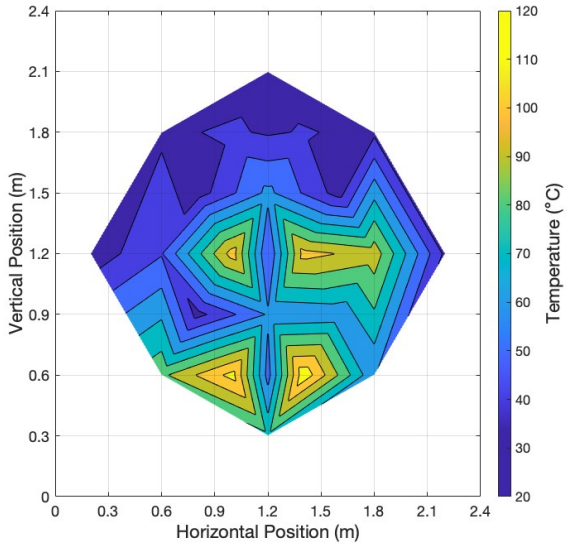

(b)

Figure 4.39: Wall #3: Contour plots of temperatures measured across the mid–depth plane of oriented strand board sheet at (a) Time = 10:02 and (b) Time = 25:00 after ignition

Under continued exposure to the radiant heat from the fire, the temperatures recorded at the strand board mid–depth continued to rise attaining a peak temperatures of 58°C ± 0.2°C at around 25 minutes into the test as shown in Figure 4.39b for this time. Again it is important to note the difference in colourbar scales on subplots of Figure 4.39. As can be seen from Figure 4.39b, the highest temperatures at this plane in the strand board occurred where there was significant melting of the vinyl siding and foam insulation. In select regions around the bottom and middle portions of this layer, measured temperatures were higher than $\sim$ 98°C which would promote evaporation of water from the material as well. On the backside of the wall, at the mid–depth of the in–cavity batt insulation and mid–depth of the wood studs, average temperature increases were higher than those recorded from previous wall tests. Although temperatures in the strand board mid–depth gradually decayed with decay of the fire, temperatures into the batt insulation and wood studs had risen by 14°C and 6°C, respectively, after failure of the extruded polystyrene foam.

One of the main objectives of this work was to complement the previously conducted small–scale experiments with a limited set of larger–scale tests in order to investigate the fire performance of full exterior walls under a more realistic fire exposure. Therefore, in addition to the time evolution of temperatures measured within the wall assembly, it was also of interest to compare the thermal penetration into the bulk of the wall assemblies across the two scales. For this, a line plot of temperature versus time is shown in Figure 4.40a where temperatures recorded at the mid–depth of the extruded polystyrene insulation and at the mid–depth of the underlying oriented strand board sheet are overlaid for Sandwich #3 and Wall #3 tests conducted under similar levels of incident radiant heat flux exposure; that is 15 kW/m^2 for Sandwich #3 and 14 kW/m^2 ± 3 kW/m^2 for Wall #3 experiments. These line plots were previously presented separately for Sandwich #3 and Wall #3 in Figures 3.30a and 4.37, respectively. To further illustrate through–wall heat transfer, the time–histories of temperature differences (taken as the difference in temperature across the mid–depth of the extruded polystyrene insulation and the mid–depth of the oriented strand board) are plotted in Figure 4.40b. For both sets of plots in Figure 4.40, the time–resolved traces of measured temperature and temperature difference are presented for periods during which the thermocouple affixed at the mid–depth extruded polystyrene was measuring the temperature of the solid foam. Thus, temperature–time profiles for Sandwich #3 are shown until a minute and a half (90 seconds) following the onset of exposure, and for Wall #3 until 10 minutes after ignition of the wood cribs.

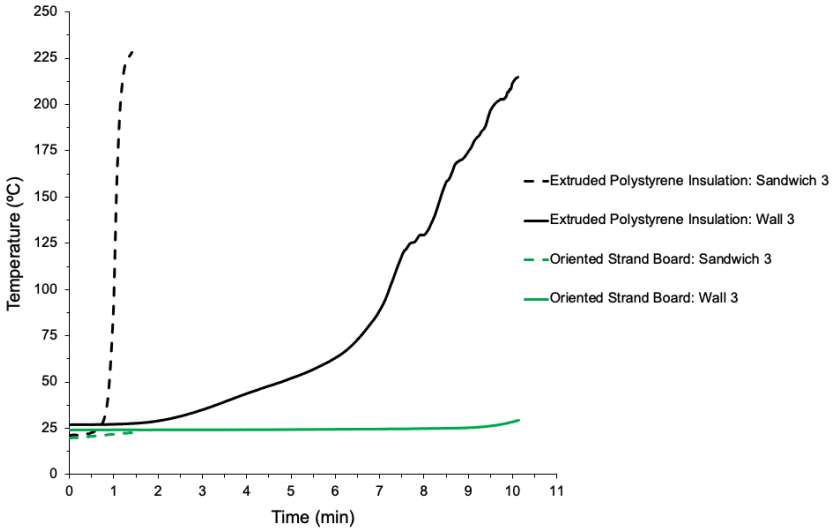

(a)

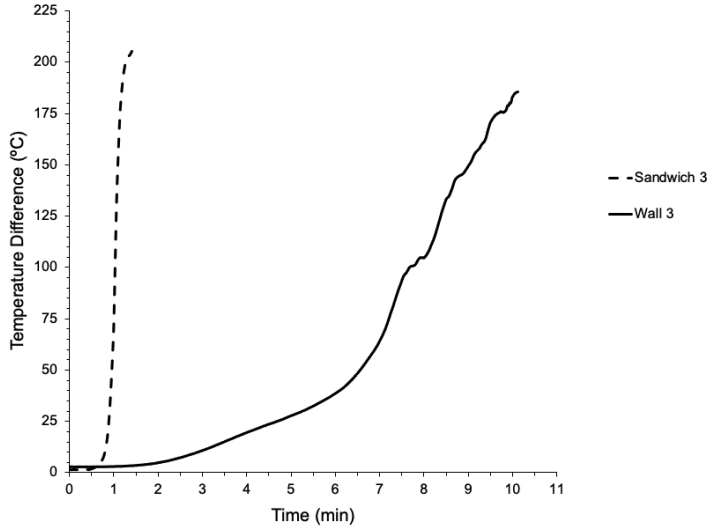

(b)

Figure 4.40: Time–histories of (a) temperatures measured at the mid–depth of extruded polystyrene foam and mid–depth of oriented strand board across Sandwich #3 and Wall #3 tests, and (b) their difference across the two sets of experiments

As can be seen from Figure 4.40a, for Sandwich #3 assembly, the increase in temperature at the centre of the solid foam slab began around one minute following the onset of exposure, rising rapidly with a constant rate of 4.7°C/s until around 230°C at which point the extruded polystyrene insulation melted. In contrast, for Wall #3 assembly, the increase in temperature at the centre of solid polystyrene foam started around 2 minutes after ignition of wood cribs, and again exhibited varying rates of interior temperature rise consistent with the growth and decay of the exposure fire. Initially, temperatures in the wall increased at a rate of 0.14°C/s between 2 and 5 minutes, then at 0.34°C/s between 5 and 7 minutes, and lastly at 0.67°C/s between 7 minutes and 10 minutes after ignition after which the foam reached temperatures around 215°C and melted. The temperatures corresponding to melting of the insulation were similar for Sandwich #3 and Wall #3 (230°C vs. 215°C), but due to differences in fire exposure profiles with time across the two tests, the rates of temperature rise leading to this point were significantly different. Such changes were again consistent with results in Section 3.4.1 for individual polystyrene samples heated under different levels of external irradiance, where rates of temperature rise were 4.4°C/s for 15 kW/m^2 and 7.2°C/s at 30 kW/m^2 for example. Further, due to spatial gradients in exposure to the large Wall #3, the heat penetrated into the bulk of extruded polystyrene insulation from the fire conducted in three dimensions. In contrast for Sandwich #3 assemblies under uniform exposure, heat transfer through the assembly was closer to one–dimensional and thus penetrated through the material at an apparently higher rate than in the multi-dimensional wall situation.

Interestingly, for both Sandwich #3 and Wall #3 assemblies, the rise in temperature at the mid–depth of oriented strand board sheet was minimal prior to melting of extruded polystyrene foam. Consistent with this, the time–resolved traces of temperature difference across the two measurement points within the assembly bulk (mid–depth of insulation and mid–depth of strand board) followed a similar shape to that of mid–depth insulation temperature–time curve. For Sandwich #3 assembly, the temperature difference curve increased rapidly with time (Figure 4.40b) reaching a peak difference of 205°C around 1.5 minutes after the onset of exposure. For Wall #3, the measured difference followed a shallower climb reaching a maximum difference in temperature of 185°C 10 minutes after ignition and during steady exposure from the wood crib fire, consistent with the differing exposure profiles discussed above.

Chapter 5

Closure

At present, in Canada, multi–layered and highly–insulated building envelopes are taking centre stage in construction due to their demonstrated ability to meet building energy efficiency, acoustic and hygrothermal requirements. Predicting fire performance of these complex assemblies, however, is challenging and must be carefully addressed to ensure occupant and firefighter safety as well as minimize property damage in the event of fire. To address this, the present research outlined results from a series of experiments conducted to characterize the thermal and fire performance of common Canadian exterior wall materials, alone and in combination with underlying layers, via complementary small– and large–scale experiments. The conclusions and key observations made from the results of the multi–scale approach for testing adopted in this research are contained in the next section, followed by topics identified for further investigation based on the work performed within this thesis framework.

5.1 Conclusions

5.1.1 Small–Scale Fire Tests

A total of 145 tests were conducted in the cone calorimeter to characterize the fire performance of six building materials (vinyl siding, stone wool insulation, polyisocyanurate insulation, extruded polystyrene insulation, weather resistant barrier, and oriented strand board) commonly used in a typical Canadian exterior wall assembly. These layers were then stacked to form a (scaled) section of an exterior wall assembly and additional 18 tests were conducted on three composite (sandwich) assemblies at the small–scale, with each sandwich lined with one type of insulation: stone wool for Sandwich #1, polyisocyanurate for Sandwich #2, and extruded polystyrene for Sandwich #3. The results presented in Section 3.4 are a refined subset of the experimental data, which are most useful for characterization of the thermal response of building materials, alone and in combination with underlying layers, found in a typical residential building envelope. For example, when testing exterior wall components individually, Section 3.4.1, time–histories of temperatures measured on the backside of decorative vinyl siding, at the mid–depth of exterior continuous insulation as well as at the mid–depth of oriented strand board sheets in conjunction with time–resolved traces of mass remaining and heat release rate profiles demonstrated that a wide range of thermal degradation phenomena unique to a particular material could be captured and studied systematically when the representative samples of these materials were subjected to increasing levels of external heat flux ranging from low values of 15 kW/m^2 to high levels of 75 kW/m^2 irradiance. In the case of the sandwich assemblies, Section 3.4.2, thermal degradation phenomena unique to each sandwich component was again observed under two exposure levels (low of 15 kW/m^2 and high of 50 kW/m^2 heat flux) and their impact on the performance of the underlying layers was assessed relative to temperatures measured at several locations across each layer of a composite sample. In general, measurements of unexposed side and interior temperatures at the backside of vinyl siding, at the mid–depth of insulation and at the mid–depth of oriented strand board sheets, respectively, can be used to identify the impact of thermal degradation phenomena on the overall performance of a sandwich assembly, as was done here, and also to validate the predictions of temperature rise rates, peak temperatures attained and the succession of thermal decomposition events in future models of thermal degradation of exterior wall components and composite assemblies.

From the results, the following conclusions could be drawn:

- Simultaneous measurement of temperatures, time–varying mass loss and heat release rates when representative samples of wall materials were exposed to varying levels of external irradation allowed investigation of a broad range of thermal degradation phenomena unique to each material, including
  - Extent of distortion in sample geometry for vinyl siding and extruded polystyrene insulation; charring nature of vinyl siding, polyisocyanurate insulation, and oriented strand board;
  - Melting of extruded polystyrene insulation and weather resistant barrier;
  - Pyrolysis and oxidation of organic binder and oxidation of siliceous species in stone wool;
  - Discoloration across the exposed surface and lateral sides of stone wool insulation relating to different internal phenomena that occurred for various levels of incident heat flux.
- The sequence of observed thermal degradation processes for each material was similar independent of the level of incident heat flux and regardless of whether the materials were tested individually or in combination with underlying layers in a sandwich assembly.
- In tests of individual materials, the rates of temperature rise on the unexposed side and the interior, as well as the rates of mass loss and heat release per unit area, strongly depended on the level of imposed incident heat flux and typically increased with increasing level of external irradiance. Likewise, the values of peak temperature attained, total mass loss at the end of thermal exposure and peak heat release rate during sustained flaming combustion were also higher at higher levels of external incident heat flux.
- In tests of sandwich assemblies, the rates of temperature rise and values of peak temperature attained at the measurement locations depended on multiple factors including the level of external heat flux, the interactions of the stacked layers and the flame heat feedback from the fire in case of positive ignition.
- Due to the size of the cone calorimeter test samples, and the uniform heat flux to the surface, heat conducted primarily in one dimension through the sandwich assemblies at this small–scale of testing.

5.1.2 Large–Scale Fire Tests

Three tests were conducted on large–scale exterior wall assemblies constructed of the same materials used in the Sandwich assembly tests and representative of typical residential building envelopes, with each wall lined with one type of exterior continuous insulation: stone wool for Wall #1, polyisocyanurate for Wall #2, and extruded polystyrene for Wall #3. For each test, thermal damage on the fire–side wall face was observed and its impact on the performance of the underlying layers was assessed relative to temperatures measured at the mid–depth of the insulation and mid–depth of the oriented strand board sheets as well as on the unexposed of the wall, at the mid–depth of the in–cavity batt insulation and mid–depth of the framing wood studs. The results presented in Section 4.6 are a refined subset of the experimental data, which are most useful for demonstrating the time–histories of temperature measured across each layer of an exterior wall assembly as well as for illustrating through–wall heat transfer in a given assembly when subjected to temperature and heat flux conditions from a realistic, yet confined, fire exposure. Measured temperatures were then compared to the results from previously conducted small–scale experiments to demonstrate the utility of multi–scale studies into the thermal degradation of building materials and construction assemblies in the context of energy–efficient building envelopes. At large-scale, measurements of interior temperature at the mid–depth of the fire–side wall components can be used to identify and define threshold values related to thermal damage phenomena on the wall, as was done here, and also to validate the predictions of temperature rise rates, peak temperatures attained and the occurrence of damage events in future models of thermal degradation of wall assemblies.

From the results, the following more specific conclusions can be drawn:

- Temperature slices taken at times when values of heat flux from the fire to the wall were highest indicated that the highest internal temperatures covered a region across which thermal damage to the outermost layers of the wall assembly was greatest.
- Contour plots of temperature from thermocouples positioned across the mid–depth of the insulation and underlying oriented strand board sheets showed that the thermal penetration into the depth of the wall was location dependent marking the three–dimensional nature of heat penetration into the bulk of a wall assembly.
- Measurement of temperatures at each layer in the wall, combined with visual observation of the tests, allowed identification of thermal decomposition phenomena such as pyrolysis of organic binder in stone wool, expansion of polyisocyanurate foam core, melting of extruded polystyrene insulation and surface charring of the oriented strand board sheet.

- The rate of interior temperature rise at the insulation mid–depth followed changes in heat exposure to the wall during the various phases of fire growth. Temperatures increased at lower rates as the fire grew in size, after which the rates of temperature rise increased during more steady burning periods. Such changes also related to the structural integrity of the fire–side wall covering since as the vinyl siding panels melted, it left the underlying insulation face partially exposed to radiant heat from the fire also leading to increased rates of interior temperature rise.

- Under real fire exposure, heat transfer through a wall assembly was characterized by significant three dimensional processes with maximum thermal penetration into all layers of a wall assembly typically aligned with the highest incident heat flux and significant variations in temperature both horizontally and vertically across the mid–planes of both the insulation and oriented strand board sheets.

- Thermal penetration through the bulk of the wall assembly appeared to continue after decay and even extinguishment of the fire suggesting that heat conducted into and retained in the insulation during fire exposure tended to slowly penetrate further into the bulk of the wall assembly towards the unexposed side.

- Provided that the layer of exterior continuous insulation remained physically intact (i.e. unlike melting of extruded polystyrene foam in Wall #3), average temperature increases on the backside of the wall, at the mid–depth of the in–cavity batt insulation and mid–depth of the wood studs, were minimal: typically these temperatures had risen by $< 1°C$ at the end of the fire exposure.

5.2 Recommendations

A series of recommendations to continue and extend the detailed work presented in this thesis are noted below:

1. Complement and extend data and protocols from the small–scale testing of individual wall materials and sandwich assemblies through to intermediate–scale experiments.

The results of this thesis research demonstrated that due to the practical size of the cone calorimeter test samples, the heat transfer through the sandwich assemblies conducted primarily in one dimension at the small–scale. While it provides insight into thermal degradation processes that will also occur at the large–scale, it was also evident that heat transfer through full sections of exterior wall assemblies occurred in three dimensions. This resulted in challenges with direct comparison of the temperature–time data obtained across the two scales. Therefore, further work at an intermediate–scale is recommended to assess some of the more detailed differences between tests performed at different scales. Intermediate–scale tests should allow capture of the multi–dimensional heat transfer mechanisms seen in the large wall tests that were not necessarily evident at the small–scale, but at greatly reduced cost. A phenomenon of particular interest would include the transport of hot gases in the air cavity between the backside of the siding layer and the exposed face of exterior continuous insulation and its impact on the measured interior temperatures at the insulation mid–depth.

2. Conduct additional experiments which utilize different levels of fire exposure severity and wall configurations.

In the present work, the severity of fire exposure was determined by consulting the guidelines of the Australian Standard, AS 3959:2018, and Bushfire Attack Level of 19 was selected as an adequate level of exposure for the purposes of this study. The experiments outlined in this work can easily be modified to incorporate fires of greater intensity, such as Bushfire Attack Level of 40 or above, by modifying the fuel load. This would provide additional insight into the thermal degradation phenomena that might occur in exterior wall assemblies under severe fire exposures and also guide formulation of advanced numerical simulation and design tools for predicting fire performance of building materials and their interactions in exterior wall assemblies across a wider range of realistic fire exposures. In related work, it would be of interest to study different configurations of exterior wall assemblies, specifically, those lined with other types of exterior continuous insulation emerging in construction of building envelopes such as spray polyurethane foam (SPF), phenolic foam (PF) and expanded polystyrene foam (EPS).

3. Utilize the data presented in this work to support development and validation of the next generation of fire models.

Building on the present results and in parallel to any future experimental work, it is recommended to develop and formulate detailed models for predicting thermal performance, response and endurance of exterior wall assemblies when subject to temperature and heat flux conditions from a fire. Three levels of validation data are required in support of such work:

1. thermophysical properties of the building materials of interest: some of these can be obtained from the collection of published and emerging pertinent literature, other would need to be determined in separate studies;

2. characterization of fire exposure: this can be obtained from the collection of available literature (such as this work) and test standards (e.g. Australian Standard, AS 3959:2018) that specify the temperature and heat flux conditions encountered in various fire scenarios and provide information regarding the total heat flux from the fire experienced at the wall surface, although the existing information would still need to be translated into specification of realistic boundary conditions; and

3. data from thermal degradation experiments: these include information regarding succession of thermal degradation events, their impact on the measured temperatures and the onset of fire damage phenomena, through work similar to that described here.

Such models, when developed, could later be applied to different situations where data exists (e.g. heat transfer from fire to highly–insulated exterior wall assemblies), as well as to a broad range of new fire scenarios and assembly designs as recommended above.

References

[1] United Nations Environment Programme, "Global Status Report for Buildings and Construction: Towards a Zero-emission, Efficient and Resilient Buildings and Construction Sector," 2020.

[2] Environment and Climate Change Canada, "A Healthy Environment and a Healthy Economy: Canada's Strengthened Climate Plan to Create Jobs and Support People, Communities and the Planet," 2020.

[3] A. Huynh, R. D. Barkokebas, M. Al-Hussein, C. Cruz-Noguez, and Y. Chen, "Energy-Efficiency Requirements for Residential Building Envelopes in Cold-Climate Regions," *Atmosphere*, vol. 12, p. 405–425, 2021.

[4] G. Desmarais, "Impact of Added Insulation on the Hygrothermal Performance of Leaky Exterior Wall Assemblies," Master's thesis, Concordia University, 2000.

[5] M. A. Lacasse, H. H. Saber, W. Maref, G. Ganapathy, and M. Nicholls, "Evaluation of Thermal and Moisture Response of Highly Insulated Wood-Frame Wall Assemblies - Part I: Experimental Trials in the Field Exposure of Walls Test Facility Phase 1 and Phase 2," National Research Council Canada Report A1-000444.5, 2016.

[6] M. Bartko, R. Jonkman, M. A. Lacasse, T. Moore, A. Parekh, and S. Plescia, "An Overview of Studies to Assess the Thermal and Hygrothermal Performance of Highly Insulated and Zero Energy Ready Wall Assemblies," *Proceedings of the 15 th Canadian Conference on Building Science and Technology*, 2017.

[7] M. Bonner and G. Rein, "Flammability and Multi-objective Performance of Building Façades: Towards Optimum Design," *International Journal of High-Rise Buildings*, vol. 7(4), p. 363–374, 2018.

[8] N. White, M. Delichatsios, M. Ahrens, and A. Kimball, "Fire Hazards of Exterior Wall Assemblies Containing Combustible Components." MATEC Web of Conferences 9, 02005, 2013.

[9] National Research Council of Canada, "Housing Research Summary for 2017."

[10] J. Valiulis, "Building Exterior Wall Assembly Flammability: Have We Forgotten the Past 40 Years?." Fire Engineering Magazine, 2015.

[11] P. Hayes, "How Lacrosse and Grenfell Have Dramatically Altered the Litigation and Regulatory Landscape," *Journal of Building Survey, Appraisal and Valuation*, vol. 7(1), p. 48–60, 2018.

[12] "The New York Times: Northern California Fires Have Destroyed at Least 5,700 Buildings," 2017.

[13] "Global News: Fort McMurray Wildfire Named Canada's News Story of 2016," 2016.

[14] "CBC News: A Look Back at the 2021 B.C. Wildfire Season," 2021.

[15] M. Hamdy, A. Hasan, and K. Siren, "Applying a Multi-Objective Optimization Approach for Design of Low-Emission Cost-Effective Dwellings," *Journal of Building and Environment*, vol. 46(1), p. 109–123, 2011.

[16] M. Fesanghary, S. Asadi, and Z. W. Geem, "Design of Low-Emission and Energy-Efficient Residential Buildings Using a Multi-Objective Optimization Algorithm," *Journal of Building and Environment*, vol. 49, p. 245–250, 2012.

[17] H. Islam, M. Jollands, S. Setunge, and M. A. Bhuiyan, "Optimization Approach of Balancing Life Cycle Cost and Environmental Impacts on Residential Building Design," *Journal of Energy and Buildings*, vol. 87, p. 282–292, 2015.

[18] C. Croitoru, I. Nastase, F. Bode, A. Meslem, and A. Dogeanu, "Thermal Comfort Models for Indoor Spaces and Vehicles - Current Capabilities and Future Perspectives," *Journal of Renewable and Sustainable Energy Reviews*, vol. 44, p. 304–318, 2015.

[19] W. Yu, B. Li, H. Jia, M. Zhang, and D. Wang, "Application of Multi-Objective Genetic Algorithm to Optimize Energy Efficiency and Thermal Comfort in Building Design," *Journal of Energy and Buildings*, vol. 88, p. 135–143, 2015.

[20] N. G. Vardaxis, D. Bard, and K. P. Waye, "Review of Acoustic Comfort Evaluation in Dwellings - Part 1: Associations of Acoustic Field Data to Subjective Responses from Building Surveys," *Journal of Building Acoustics*, vol. 25(2), p. 151–170, 2018.

[21] G. K. Oral, A. K. Yener, and N. T. Bayazit, "Building Envelope Design with the Objective to Ensure Thermal, Visual and Acoustic Comfort Conditions," *Journal of Building and Environment*, vol. 39(3), p. 281–287, 2004.

[22] R. R. David and V. E. Sanvido, "Patterns of Construction-Space Use in Multistory Buildings," *Journal of Construction Engineering and Management*, vol. 121(4), p. 464–473, 1995.

[23] T. Hamidavi, S. Abrishami, and M. R. Hosseini, "Towards Intelligent Structural Design of Buildings: A BIM-Based Solution," *Journal of Building Engineering*, vol. 32, p. 101685, 2020.

[24] C. Maluk, M. Woodrow, and J. L. Torero, "The Potential of Integrating Fire Safety in Modern Building Design," *Fire Safety Journal*, vol. 88, pp. 104–112, 2017.

[25] V. Kodur, P. Kumar, and M. M. Rafi, "Fire Hazard in Buildings: Review, Assessment and Strategies for Improving Fire Safety," *Prince Sultan University Research Review*, vol. 4(1), pp. 1–23, 2020.

[26] J. Vijayalaxmi, "Concept of Overall Thermal Transfer Value (OTTV) in Design of Building Envelope to Achieve Energy Efficiency," *International Journal of Thermal and Environmental Engineering*, vol. 1(2), pp. 75–80, 2010.

[27] T. Van Renterghem, M. Hornikx, J. Forssen, and D. Botteldooren, "The Potential of Building Envelope Greening to Achieve Quietness," *Journal of Building and Environment*, vol. 61, pp. 34–44, 2013.

[28] National Research Council of Canada, "National Building Code of Canada 2020," 2022.

[29] CAN/ULC-S134-13, "Standard Method of Fire Test of Exterior Wall Assemblies." ULC Standards of Canada, Ottawa, ON, Canada, 2013.

[30] A. K. Persily, "Envelope Design Guidelines for Federal Office Buildings: Thermal Integrity and Airtightness," NISTIR 4821, National Institute of Standards and Technology, 1993.

[31] D. T. Damery and P. Fisette, "Decision Making in the Purchase of Siding: A Survey of Architects, Contractors, and Homeowners in the U.S. Northeast," *Forest Products Journal*, vol. 51(7-8), pp. 29–36, 2001.

[32] J. P. Bradtmueller and S. P. Foley, "Historical Trends of Exterior Wall Materials used in U.S. Residential Construction," *Proceedings of the 50 th Associated Schools of Construction Annual International Conference*, 2014.

[33] S. Ilomets and T. Kalamees, "Evaluation of the Criticality of Thermal Bridges," *Journal of Building Pathology and Rehabilitation*, vol. 1(11), 2016.

[34] M. S. Al-Homoud, "Performance Characteristics and Practical Applications of Common Building Thermal Insulation Materials," *Building and Environment*, vol. 40, p. 353–366, 2005.

[35] R. W. Dazel, "Exterior Continuous Insulation and the Positive Impact on Building Envelope Performance-Achieving New Energy Code Wall Insulation Metrics," *Exterior Insulation and Finish Systems (EIFS): Performance, Progress, and Innovation, ASTM STP1585, P. E. Nelson and B. Egan, Eds., ASTM International, West Conshohocken, PA*, p. 67–79, 2016.

[36] T. A. Weston, "Innovating Continuous Exterior Insulation," *Proceedings of the 3 rd Residential Building Design and Construction Conference*, pp. 114–127, 2016.

[37] T. A. Weston, "A Review of Housewrap Performance and Its Implications for Energy Savings," *Proceedings from the American Council for an Energy-Efficient Economy Summer Studies on Energy Efficiency in Buildings*, pp. 327–338, 2006.

[38] S. Agarwal and R. K. Gupta, "29 - Plastics in Buildings and Construction," in *Applied Plastics Engineering Handbook* (M. Kutz, ed.), pp. 635–649, 2 nd ed., 2017.

[39] T. Ojanen and A. Jarkko, "Moisture Performance Properties of Exterior Sheathing Products Made of Spruce Plywood or OSB," VTT Working Papers 1459 7683, 2005.

[40] C. Maier and T. Calafut, "16 - Extrusion," in *Polypropylene* (C. Maier and T. Calafut, eds.), Plastics Design Library, pp. 205–221, 1998.

[41] S. Selke and R. Hernandez, "Packaging: Polymers in Flexible Packaging," in *Encyclopedia of Materials: Science and Technology* (K. J. Buschow, R. W. Cahn, M. C. Flemings, B. Ilschner, E. J. Kramer, S. Mahajan, and P. Veyssière, eds.), pp. 6652–6656, 2001.

[42] A. Shaidle, "Compound Requirements for Vinyl Siding," *Journal of Vinyl Technology*, vol. 1(2), p. 64–67, 1979.

[43] L. W. Weaver, "Weatherability of Rigid Vinyl Siding," *Journal of Vinyl Technology*, vol. 1(2), p. 72–75, 1979.

[44] C. Wu, C. Chang, J. Hor, S. Shih, L. Chen, and F. Chang, "On the Thermal Treatment of Plastic Mixtures of MSW: Pyrolysis Kinetics," *Waste Management*, vol. 13(3), pp. 221–235, 1993.

[45] H. Bockhorn, A. Hornung, U. Hornung, S. Teepe, and J. Weichmann, "Investigation of the Kinetics of Thermal Degradation of Commodity Plastics," *Combustion Science and Technology*, vol. 116-117(1-6), pp. 129–151, 1996.

[46] R. Miranda, J. Yang, C. Roy, and C. Vasile, "Vacuum Pyrolysis of PVC Part I: Kinetic Study," *Polymer Degradation and Stability*, vol. 64(1), pp. 127–144, 1999.

[47] G. Matuschek, N. Milanov, and A. Kettrup, "Thermoanalytical Investigations for the Recycling of PVC," *Thermochimica Acta*, vol. 361(1), pp. 77–84, 2000.

[48] M. Mehl, A. Marongiu, T. Faravelli, G. Bozzano, M. Dente, and E. Ranzi, "A Kinetic Modeling Study of the Thermal Degradation of Halogenated Polymers," *Journal of Analytical and Applied Pyrolysis*, vol. 72(2), pp. 253–272, 2004.

[49] Y. Soudais, L. Moga, J. Blazek, and F. Lemort, "Coupled DTA–TGA–FT-IR Investigation of Pyrolytic Decomposition of EVA, PVC and Cellulose," *Journal of Analytical and Applied Pyrolysis*, vol. 78, p. 46–57, 2007.

[50] S. Bocchini and G. Camino, "Halogen-Containing Flame Retardants," *Fire Retardancy of Polymeric Materials*, p. 75–105, 2010.

[51] J. Yu, L. Sun, C. Ma, Y. Qiao, and H. Yao, "Thermal Degradation of PVC: A Review," *Waste Management*, vol. 48, p. 300–314, 2016.

[52] M. Werth, G. Curran, P. Ascani, and S. Paing, "Materials Fire and Thermal Properties: Low-E Windows." Worcester Polytechnic Institute, 2017.

[53] N. Nagy, "Determination of Thermal Properties of Mineral Wool Insulation Materials for Use in Full-Scale Fire Modelling," Master's thesis, University of Waterloo, 2020.

[54] J. Sjöström and R. E. Jansson, "Measuring Thermal Material Properties for Structural Fire Engineering," *15 th International Conference on Experimental Mechanics*, 2012.

[55] N. Nagy, M. J. DiDomizio, E. J. Weckman, and R. Roos, "Determination of Thermochemical Properties of Stone Wool Insulation Materials," *Proceedings of the 15 th International Fire and Materials Conference*, pp. 491–502, 2017.

[56] C. Clauser and E. Huenges, "Thermal Conductivity of Rocks and Minerals, Rock Physics and Phase Relations," *A Handbook of Physical Constants, American Geophysical Union*, pp. 105–126, 1995.

[57] K. Livkiss, B. Andres, A. Bhargava, and P. van Hees, "Characterization of Stone Wool Properties for Fire Safety Engineering Calculations," *Journal of Fire Sciences*, vol. 36(3), pp. 202–223, 2018.

[58] I. Poljanšek, U. Šebenik, and M. Krajnc, "Characterization of Phenol-Urea-Formaldehyde Resin by Inline FTIR Spectroscopy," *Journal of Applied Polymer Science*, vol. 99(5), pp. 2016–2028, 2006.

[59] M. Moesgaard, H. Pedersen, Y. Yue, and E. Nielsen, "Crystallization in Stone Wool Fibres," *Journal of Non-Crystalline Solids*, vol. 353, p. 1101–1108, 2007.

[60] Y. Yue, M. Korsgaard, L. F. Kirkegaard, and G. Heide, "Formation of a Nanocrystalline Layer on the Surface of Stone Wool Fibers," *Journal of the American Ceramic Society*, vol. 92(1), pp. 62–67, 2009.

[61] M. Kaasgaard, P. A. L. Jacobsen, and Y. Yue, "Influence of Oxygen Partial Pressure on Crystallization Behaviour and High-Temperature Stability of Stone Wool Fibres," *Glass Science and Technology*, vol. 78(2), pp. 63–68, 2005.

[62] M. Modesti, A. Lorenzetti, F. Simioni, and M. Checchin, "Influence of Different Flame Retardants on Fire Behaviour of Modified PIR/PUR Polymers," *Polymer Degradation and Stability*, vol. 74(3), pp. 475–479, 2001.

[63] K. Ashida, K. Saiki, J. Goto, and K. Sasaki, "Polyisocyanurate Foams Modified by Thermally Stable Linkages," *American Chemical Society Symposium Series*, vol. 669, p. 81–100, 1997.

[64] E. Asimakopoulou, J. Zhang, M. McKee, K. Wieczorek, A. Krawczyk, M. Andolfo, M. Scatto, M. Sisani, and M. Bastianini, "Assessment of Fire Behaviour of Polyisocyanurate (PIR) Insulation Foam Enhanced with Lamellar Inorganic Smart Fillers," *Journal of Physics: Conference Series 1107*, p. 032004, 2018.

[65] J. P. Hidalgo, J. L. Torero, and S. Welch, "Fire Performance of Charring Closed-Cell Polymeric Insulation Materials: Polyisocyanurate and Phenolic Foam," *Fire and Materials*, vol. 42(4), pp. 358–373, 2018.

[66] S. Mehta, S. Biederman, and S. Shivkumar, "Thermal Degradation of Foamed Polystyrene," *Journal of Materials Science*, vol. 30, p. 2944–2949, 1995.

[67] J. B. Butler, "Degradation of Polystyrene Foam under Radiant Heat Flux," Master's thesis, University of Arkansas, 2011.

[68] L. Jiao and S. J., "A Thermal Degradation Study of Insulation Materials Extruded Polystyrene," *Procedia Engineering*, vol. 71, p. 622–628, 2014.

[69] C. T. Aire, M. J. DiDomizio, D. A. Torvi, and E. J. Weckman, "Investigation of the Fire Performance of Building Enclosure Assemblies," NSERC Engage Grant Project Report 461391-13, 2015.

[70] K. Chrissafis, K. M. Paraskevopoulos, I. Tsiaoussis, and D. Bikiaris, "Comparative Study of the Effect of Different Nanoparticles on the Mechanical Properties, Permeability, and Thermal Degradation Mechanism of HDPE," *Journal of Applied Polymer Science*, vol. 114(3), pp. 1606–1618, 2009.

[71] Y. S. Oh and J. M. Kim, "Properties of Oriented Strand Board Bonded with Phenol-Urea-Formaldehyde Resin," *Journal of Tropical Forest Science*, vol. 27(2), p. 222–226, 2015.

[72] P. Basu, "Chapter 14 - Analytical Techniques," in *Biomass Gasification, Pyrolysis and Torrefaction: Practical Design and Theory, (Third Edition)* (P. Basu, ed.), pp. 479–495, 2018.

[73] A. Salari, T. Tabarsa, A. Khazaeian, and A. Saraeian, "Improving Some of Applied Properties of Oriented Strand Board (OSB) Made from Underutilized Low Quality Paulownia (Paulownia Fortunie) Wood Employing Nano-SiO_2," *Industrial Crops and Products*, vol. 42, pp. 1–9, 2013.

[74] M. Brebu and C. Vasile, "Thermal Degradation of Lignin - A Review," *Cellulose Chemistry and Technology*, vol. 44(9), pp. 353–363, 2010.

[75] J. Gong, H. Zhu, H. Zhou, and S. I. Stoliarov, "Development of a Pyrolysis Model for Oriented Strand Board - Part I: Kinetics and Thermodynamics of the Thermal Decomposition," *Journal of Fire Sciences*, vol. 39(2), pp. 190–204, 2021.

[76] H. Yang, R. Yan, H. Chen, D. H. Lee, and C. Zheng, "Characteristics of Hemicellulose, Cellulose and Lignin Pyrolysis," *Fuel*, vol. 86(12/13), p. 1781–1788, 2007.

[77] I. Jiří, L. Hasalová, V. Šálek, M. Jahoda, and V. Vystrčil, "Thermal Analysis and Cone Calorimeter Study of Engineered Wood with an Emphasis on Fire Modelling," *Fire Technology*, vol. 56, p. 1099–1132, 2020.

[78] D. R. Tallant and R. L. Simpson, "The Thermal History of Charred Materials by Raman Spectroscopy," Sandia National Laboratories Report SAND2001-0131, 2001.

[79] O. Chiantore and M. Lazzari, "Thermal Decomposition of Phenol-Formaldehyde Foundry Resins," *International Journal of Polymer Analysis and Characterization*, vol. 1, pp. 119–130, 1995.

[80] M. J. DiDomizio, *Experimental Study of Thermal Degradation of Fire Resisting Compartment Partitions in Fires*. PhD thesis, University of Waterloo, 2017.

[81] L. Bustamante Valencia, *Experimental and Numerical Investigation of the Thermal Decomposition of Materials at Three Scales: Application to Polyether Polyurethane Foam Used in Upholstered Furniture*. PhD thesis, École Nationale Supérieure de Méchanique et d'Aérotechnique, Poitiers, 2009.

[82] D. M. Marquis, M. Pavageau, and E. Guillaume, "Multi-Scale Simulations of Fire Growth on a Sandwich Composite Structure," *Journal of Fire Sciences*, vol. 31(1), pp. 3–34, 2012.

[83] J. L. Torero, "Scaling-Up Fire," *Proceedings of the Combustion Institute*, vol. 34(1), pp. 99–124, 2013.

[84] A. Camillo, *Multi-Scale Investigation of Fire behaviour of a Seat and a Wall Panel from European Railway Transport System*. PhD thesis, École Nationale Supérieure de Méchanique et d'Aérotechnique, Poitiers, 2013.

[85] S. I. Stoliarov and J. Li, "Parameterization and Validation of Pyrolysis Models for Polymeric Materials," *Fire Technology*, vol. 52(1), pp. 79–91, 2016.

[86] F. Richter and G. Rein, "A Multiscale Model of Wood Pyrolysis in Fire to Study the Roles of Chemistry and Heat Transfer at the Mesoscale," *Combustion and Flame*, vol. 216, pp. 316–325, 2020.

[87] B. Andrés Valiente, *A Multi-Scale Approach for Predicting the Fire Response of Building Barriers*. PhD thesis, Lund University, 2021.

[88] C. Wilkie, "TGA-FTIR an Extremely Useful Technique for Studying Polymer Degradation," *Polymer Degradation and Stability*, vol. 66, p. 301–306, 1999.

[89] C. Branca and C. Di Blasi, "Global Intrinsic Kinetics of Wood Oxidation," *Fuel*, vol. 83, p. 81–87, 2004.

[90] M. Fang, D. Shen, Y. Li, C. Yu, Z. Luo, and K. Cen, "Kinetic Study on Pyrolysis and Combustion of Wood Under Different Oxygen Concentrations by Using TG-FTIR Analysis," *Journal of Analytical and Applied Pyrolysis*, vol. 77, pp. 22–27, 2006.

[91] F. Chuang, "Analysis of Thermal Degradation of Diacetylene Containing Polyurethane Copolymers," *Polymer Degradation and Stability*, vol. 92, pp. 1393–1407, 2007.

[92] C. Di Blasi, "Modeling Chemical and Physical Processes of Wood and Biomass Pyrolysis," *Progress in Energy and Combustion Sciences*, vol. 34, p. 47–90, 2008.

[93] W. Richard and M. A.S., "Quantitative Flash Pyrolysis Fourier Transforms Infrared Spectroscopy of Organic Materials," *Analytica Chimica Acta*, vol. 639, pp. 62–66, 2009.

[94] R. Mehrabian, R. Scharler, and I. Obernberger, "Effects of Pyrolysis Conditions on the Heating Rate in Biomass Particles and Applicability of TGA Kinetic Parameters in Particle Thermal Conversion Modeling," *Fuel*, vol. 90, pp. 567–575, 2012.

[95] T. Fateh, T. Rogaume, and F. Richard, "Multi-Scale Modeling of the Thermal Decomposition of Fire Retardant Plywood," *Fire Safety Journal*, vol. 64, pp. 36–47, 2014.

[96] L. J. Goff, "Investigation of Polymeric Materials Using the Cone Calorimeter," *Polymer Engineering and Science*, vol. 33(8), p. 497-500, 1993.

[97] A. B. Morgan and M. Bundy, "Cone Calorimeter Analysis of UL-94 V-Rated Plastics," *Fire and Materials*, vol. 31, p. 257-283, 2007.

[98] Q. Xu, C. Jin, M. Zachar, and A. Majlingova, "Test Flammability of PVC Wall Panel with Cone Calorimetry," *Procedia Engineering*, vol. 62, p. 754-759, 2013.

[99] S. Bakhtiyari, L. Taghi-Akbari, and M. J. Ashtiani, "Evaluation of Thermal Fire Hazard of 10 Polymeric Building Materials and Proposing a Classification Method Based on Cone Calorimeter Results," *Fire and Materials*, vol. 39(1), p. 1-13, 2015.

[100] M. M. Hirschler, "Poly(Vinyl Chloride) and Its Fire Properties," *Fire and Materials*, vol. 41(8), p. 993-1006, 2017.

[101] C. Wen, "A Laboratory Scale Study of Particulates Generation from Charring and Non-Charring Polymers," Master's thesis, Case Western Reserve University, 2019.

[102] L. Ang, B. Huang, H. Wu, W. Zhang, R. Zhou, and Y. Ding, "Effects of Sample Thickness on the Combustion and Smoke Characteristics of Chlorinated Polyvinyl Chloride," *Journal of Applied Polymer Science*, vol. 139(4), p. 51541, 2022.

[103] J. P. Hidalgo, J. L. Torero, and S. Welch, "Experimental Characterisation of the Fire Behaviour of Thermal Insulation Materials for a Performance-Based Design Methodology," *Fire Technology*, vol. 53, pp. 1201–1232, 2017.

[104] S. T. McKenna, *The Fire Hazards of Insulation Materials*. PhD thesis, University of Central Lancashire, 2019.

[105] M. Modesti and A. Lorenzetti, "Flame Retardancy of Polyisocyanurate–Polyurethane Foams: Use of Different Charring Agents," *Polymer Degradation and Stability*, vol. 78(2), pp. 341–347, 2002.

[106] M. Modesti, A. Lorenzetti, F. Simioni, and G. Camino, "Expandable Graphite as an Intumescent Flame Retardant in Polyisocyanurate–Polyurethane Foams," *Polymer Degradation and Stability*, vol. 77(2), pp. 195–202, 2002.

[107] M. Modesti and A. Lorenzetti, "Improvement on Fire Behaviour of Water Blown PIR–PUR Foams: Use of an Halogen-Free Flame Retardant," *European Polymer Journal*, vol. 39(2), pp. 263–268, 2003.

[108] J. Urbas, "Effects of Retainer Frame, Irradiance Level and Specimen Thickness on Cone Calorimeter Test Results," *Fire and Materials*, vol. 29, pp. 1–13, 2005.

[109] M. Kurańska, U. Cabulis, M. Auguścik, A. Prociak, J. Ryszkowska, and M. Kirpluks, "Bio-Based Polyurethane-Polyisocyanurate Composites with an Intumescent Flame Retardant," *Polymer Degradation and Stability*, vol. 127, pp. 11–19, 2016.

[110] W. An, L. Jiang, and J. Sun, "Correlation Analysis of Sample Thickness, Heat Flux, and Cone Calorimetry Test Data of Polystyrene Foam," *Journal of Thermal Analysis and Calorimetry*, vol. 119, p. 229–238, 2015.

[111] Q. Xu, C. Jin, and Y. Jiang, "Compare the Flammability of Two Extruded Polystyrene Foams with Micro-Scale Combustion Calorimeter and Cone Calorimeter Tests," *Journal of Thermal Analysis and Calorimetry*, vol. 127, p. 2359–2366, 2017.

[112] L. D. Tsantaridis and B. A. L. Östman, "Communication: Retainer Frame Effects on Cone Calorimeter Results for Building Products," *Fire and Materials*, vol. 17, p. 43–46, 1993.

[113] B. A. L. Östman and L. D. Tsantaridis, "Smoke Data from the Cone Calorimeter for Comparison with the Room Fire Test," *Fire and Materials*, vol. 17, p. 191–200, 1993.

[114] R. H. White and K. Sumathipala, "Cone Calorimeter Tests of Wood Composites," *Proceedings of the 13 th International Conference on Fire and Materials Conference*, pp. 401–412, 2013.

[115] J. Gong, H. Zhou, H. Zhu, C. G. McCoy, and S. I. Stoliarov, "Development of a Pyrolysis Model for Oriented Strand Board - Part II: Thermal Transport Parameterization and Bench-Scale Validation," *Journal of Fire Sciences*, vol. 39(6), p. 477–494, 2021.

[116] N. Ayrilmis, Z. Candan, and R. White, "Physical, Mechanical, and Fire Properties of Oriented Strandboard with Fire Retardant Treated Veneers," *European Journal of Wood and Wood Products*, vol. 65, pp. 449–458, 2007.

[117] K. Carpenter and M. Janssens, "Using Heat Release Rate to Assess Combustibility of Building Products in the Cone Calorimeter," *Fire Technology*, vol. 41, p. 79–92, 2005.

[118] R. H. White and J. E. Winandy, "Fire Performance of Oriented Strandboard," *Proceedings of the Conference on Recent Advances in Flame Retardancy of Polymeric Materials: Applications, Research and Industrial Development Markets*, vol. 17, pp. 297–309, 2006.

[119] N. Ayrilmis, S. N. Kartal, T. L. Laufenberg, J. E. Winandy, and R. H. White, "Physical and Mechanical Properties and Fire, Decay, and Termite Resistance of Treated Oriented Strandboard," *Forest Products Journal*, vol. 55(5), pp. 74–81, 2005.

[120] J. Park and J. Lee, "Ignition and Heat Release Rate of Wood-Based Materials in Cone Calorimeter Tests," *Journal of the Korean Wood Science and Technology*, vol. 36(2), pp. 1–8, 2008.

[121] L. E. Hasburgh, R. H. White, M. A. Dietenberger, and C. R. Boardman, "Comparison of the Heat Release Rate from the Mass Loss Calorimeter to the Cone Calorimeter for Wood-Based Materials," *Proceedings Fire and Materials 2015, 14 th International Conference and Exhibition*, pp. 116–126, 2015.

[122] S. Hirle and K. Balog, "The Effect of the Heat Flux on the Self-Ignition of Oriented Strand Board," *Research Papers Faculty of Materials Science and Technology Slovak University of Technology*, vol. 25(40), p. 123–129, 2017.

[123] B. G. Mustafa, M. H. Mat Kiah, J. Al-Nahdi, G. E. Andrews, H. N. Phylaktou, and H. Li, "Toxic Emissions from Processed Wood in Cone Calorimeter Tests," *Proceedings of the 15 th International Conference on Fire Science and Engineering: Interflam 2019*, 2019.

[124] H. Zhou, "Development of a Pyrolysis Model for Oriented Strand Board," Master's thesis, University of Maryland, 2021.

[125] I. Tureková, I. Marková, M. Ivanovičová, and J. Harangózo, "Experimental Study of Oriented Strand Board Ignition by Radiant Heat Fluxes," *Polymers*, vol. 13(5), pp. 709–722, 2021.

[126] W. K. Chow, "Fire Hazard Assessment on Polyurethane Sandwich Panels for Temporary Accommodation Units," *Polymer Testing*, vol. 23, pp. 973–977, 2004.

[127] S. McKenna, N. Jones, G. Peck, K. Dickens, W. Pawelec, S. Oradei, S. Harris, A. A. Stec, and T. Hull, "Fire Behaviour of Modern Façade Materials – Understanding the Grenfell Tower Fire," *Journal of Hazardous Materials*, vol. 368, pp. 115–123, 2019.

[128] A. A. Khan, S. Lin, X. Huang, and A. Usmani, "Façade Fire Hazards of Bench-Scale Aluminum Composite Panel with Flame-Retardant Core," *Fire Technology*, pp. 1–24, 2021.

[129] M. D. Hossain, S. Saha, M. K. Hassan, A. C. Y. Yuen, C. Wang, W. Hittini, L. George, and R. Wuhrer, "Testing of Aluminium Composite Panels in a Cone Calorimeter: A New Specimen Preparation Method," *Polymer Testing*, vol. 106, p. 107454, 2022.

[130] E. Mikkola, T. Hakkarainen, and A. Matala, "Fire Safety of EPS ETICS in Residential Multi-Storey Buildings," VTT-R-04632-13, VTT Technical Research Centre of Finland, 2013.

[131] E. Mikkola, T. Hakkarainen, and A. Matala, "Fire Safety of EPS Insulated Façades in Residential Multi-Storey Buildings," *MATEC Web of Conferences*, vol. 9, p. 04002, 2013.

[132] B. Zhou, H. Yoshioka, T. Noguchi, and T. Ando, "Numerical Prediction of Mass Loss Rate of Expanded Polystyrene (EPS) Used for External Thermal Insulation Composite Systems(ETICS) in Cone Calorimeter," *Fire and Materials*, vol. 42, p. 517–526, 2018.

[133] B. Zhou, H. Yoshioka, T. Noguchi, K. Wang, and X. Huang, "Fire Performance of EPS ETICS Façade: Effect of Test Scale and Masonry Cover," *Fire Technology*, 2021.

[134] R. Nilica and H. Harmuth, "Mechanical and Fracture Mechanical Characterization of Building Materials Used for External Thermal Insulation Composite Systems," *Cement and Concrete Research*, vol. 35(8), p. 1641-1645, 2005.

[135] C. T. Aire, "Experimental and Numerical Modeling of Heat Transfer in Wall Assemblies," Master's thesis, University of Saskatchewan, 2014.

[136] H. Yoshioka, H. C. Yang, M. Tamura, M. Yoshida, T. Noguchi, M. Kanematsu, K. Koura, and Y. Ozaki, "Study of Test Method for Evaluation of Fire Propagation along Façade Wall with Exterior Thermal Insulation," *Fire Science and Technology*, vol. 30(1), pp. 27–44, 2011.

[137] I. Kotthoff and J. Riemesch-Speer, "Mechanism of Fire Spread on Facades and the New Technical Report of EOTA "Large-Scale Fire Performance Testing of External Wall Cladding Systems"." MATEC Web of Conferences 9, 02010, 2013.

[138] H. Xin, N. Zhaopeng, P. Lei, and Z. Ping, "Experimental Study of Fire Barriers Preventing Vertical Fire Spread in ETISs." MATEC Web of Conferences 9, 04003, 2013.

[139] B. A. L. Östman and L. D. Tsantaridis, "Fire Performance of Multi-Storey Wooden Facades." MATEC Web of Conferences 9, 06001, 2013.

[140] P. Lei, Z. Ni, and H. Xin, "Review on the Fire Safety of Exterior Wall Claddings in High-Rise Buildings in China," *Procedia Engineering*, vol. 62, p. 663–670, 2013.

[141] H. Yoshioka, Y. Nishio, M. Tamura, M. Yoshida, T. Noguchi, Y. Ohmiya, M. Kanematsu, T. Ando, K. Koura, T. Tomatsu, and Y. Ozaki, "Façade Tests on Fire Propagation along Combustible Exterior Wall Systems," *Fire Science and Technology*, vol. 33(1), pp. 1–15, 2014.

[142] D. Bjegović, I. B. Pečur, B. Milovanović, M. J. Rukavina, and M. Bagarić, "Comparative Full-Scale Fire Performance Testing of ETICS Systems," *Journal of the Croatian Association of Civil Engineers*, vol. 68(5), pp. 357–369, 2016.

[143] I. Kotthoff, S. Hauswaldt, O. Riese, and J. Riemesch-Speer, "Investigations of the Performance of Facades Made of ETICS with Polystyrene Under External Fire Exposure and Fire Safety Measures for Their Improvement." MATEC Web of Conferences 46, 02007, 2016.

[144] L. Zhou, A. Chen, X. Liu, and F. Zhang, "The Effectiveness of Horizontal Barriers in Preventing Fire Spread on Vertical Insulation Panels Made of Polystyrene Foams," *Fire Technology*, vol. 52, p. 649–662, 2016.

[145] J. Anderson, L. Boström, R. Jansson McNamee, and B. Milovanović, "Modeling of Fire Exposure in Facade Fire Testing," *Fire and Materials*, vol. 42, pp. 475–483, 2018.

[146] A. Čolić and I. B. Pečur, "Influence of Horizontal and Vertical Barriers on Fire Development for Ventilated Façades," *Fire Technology*, vol. 56, p. 1725–1754, 2020.

[147] P. Cancelliere, P. Canzani, S. Sassi, A. Lucchini, S. Messa, and E. Anselmi, "A New Test Method to Determine the Fire Behavior of Façades with ETIC System," *Fire and Materials*, vol. 45(5), pp. 624–637, 2021.

[148] BS 8414-1:2015, "Fire Performance of External Cladding Systems: Test Method for Non-Load Bearing External Cladding Systems Applied to the Masonry Face of a Building." British Standards Institute, London, the United Kingdom, 2015.

[149] BS 8414-2:2015, "Fire Performance of External Cladding Systems: Test Method for Non-Load Bearing External Cladding Systems Fixed to and Supported by a Structural Steel Frame." British Standards Institute, London, the United Kingdom, 2015.

[150] NFPA 285, "Standard Fire Test Method for Evaluation of Fire Propagation Characteristics of Exterior Wall Assemblies Containing Combustible Components." National Fire protection Association, Quincy, MA, United States, 2019.

[151] JIS A 1310, "Test Method for Fire Propagation over Building Façades." Japanese Standards Association, Tokyo, Japan, 2015.

[152] ISO 13785-2, "Reaction-to-Fire Tests for Façades — Part 2: Large-Scale Test." International Organization for Standardization, Geneva, Switzerland, 2002.

[153] C. A. Wade and J. C. Clampett, "Fire Performance of Exterior Claddings," BRANZ Report FCR 1, Building Research Association of New Zealand. Judgeford, New Zealand, 2000.

[154] J. P. Hidalgo-Medina, *Performance–Based Methodology for the Fire Safe Design of Insulation Materials in Energy Efficient Buildings*. PhD thesis, University of Edinburgh, 2015.

[155] D. P. Wilson, "Numerical Simulations of Small-Scale and Full-Scale Fire Experiments," Master's thesis, University of Waterloo, 2018.

[156] M. J. DiDomizio, "On the Potential Use of Small Scale Fire Tests for Screening Steiner Tunnel Results for Spray Foam Insulation," Master's thesis, University of Waterloo, 2013.

[157] F. T. Technology, "ConeCalc5 Software," 2009.

[158] W. Thornton, "The Relation of Oxygen to the Heat of Combustion of Organic Compounds," *Philosophical Magazine and Journal of Science*, vol. 33(196), 1917.

[159] C. Huggett, "Estimation of the Rate of Heat Release by Means of Oxygen Consumption," *Fire and Materials*, vol. 12, pp. 61–65, 1980.

[160] M. Janssens, "SFPE Handbook of Fire Protection Engineering, 5 th Ed. Volume 1, Chapter 10: Calorimetry," *National Fire Protection Association, Quincy, Massachusetts*, pp. 905–952, 2016.

[161] ASTM E1354–17, "Standard Test Method for Heat and Visible Smoke Release Rates for Materials and Products Using and Oxygen Consumption Calorimeter." ASTM International, West Conshohocken, PA, United States, 2017.

[162] L. Zhao and N. A. Dembsey, "Measurement Uncertainty Analysis for Calorimetry Apparatuses," *Fire and Materials*, vol. 32, pp. 1–26, 2008.

[163] C. F. Cullis and M. M. Hirschler, "The Combustion of Organic Polymers." Oxford University Press, Oxford, United Kingdom, 1982.

[164] Hirschler, M.M., "Flammability and Fire Performance," *PVC Handbook*, pp. 419–481, 2005.

[165] A. Karamanos, S. Hadiarakou, and A. M. Papadopoulos, "The Impact of Temperature and Moisture on the Thermal Performance of Stone Wool," *Energy and Buildings*, vol. 40, pp. 1401–1411, 2008.

[166] D. Paudel, A. Rinta-Paavola, H.-P. Mattila, and S. Hostikka, "Multiphysics Modelling of Stone Wool Fire Resistance," *Fire Technology*, vol. 57, pp. 1283–1312, 2021.

[167] B. Jones, "Sampling-Window Based Approach for Fire Gas Analysis of Rigid Foams," Master's thesis, University of Waterloo, 2013.

[168] AS 3959:2018, "Construction of Buildings in Bushfire-Prone Areas." Standards Australia Limited, 2018.

[169] M. R. Obach, "Effects of Initial Fire Attack Suppression Tactics on the Firefighter and Compartment Environment," Master's thesis, University of Waterloo, 2011.

[170] ASTM E3057–16, "Standard Test Method for Measuring Heat Flux Using Directional Flame Thermometers with Advanced Data Analysis Techniques." ASTM International, West Conshohocken, PA, United States, 2016.